ACS SYMPOSIUM SERIES 1064

Fluorine-Related Nanoscience with Energy Applications

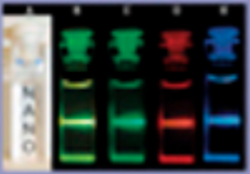

EDITED BY

Donna J. Nelson and
Christopher N. Brammer

Downloaded by 89.163.35.42 on June 5, 2012 | http://pubs.acs.org
Publication Date (Web): April 27, 2011 | doi: 10.1021/bk-2011-1064.fw001

Fluorine-Related Nanoscience with Energy Applications

Downloaded by 89.163.35.42 on June 5, 2012 | http://pubs.acs.org
Publication Date (Web): April 27, 2011 | doi: 10.1021/bk-2011-1064.fw001

Downloaded by 89.163.35.42 on June 5, 2012 | http://pubs.acs.org
Publication Date (Web): April 27, 2011 | doi: 10.1021/bk-2011-1064.fw001

ACS SYMPOSIUM SERIES **1064**

Fluorine-Related Nanoscience with Energy Applications

Donna J. Nelson, Editor
University of Oklahoma

Christopher N. Brammer, Editor
University of Oklahoma

Sponsored by the
ACS Division of Fluorine Chemistry

American Chemical Society, Washington, DC

Distributed in print by Oxford University Press, Inc.

Downloaded by 89.163.35.42 on June 5, 2012 | http://pubs.acs.org
Publication Date (Web): April 27, 2011 | doi: 10.1021/bk-2011-1064.fw001

Library of Congress Cataloging-in-Publication Data

Library of Congress Cataloging-in-Publication Data

Fluorine-related nanoscience with energy applications / Donna J. Nelson, editor, Christopher N. Brammer, editor ; sponsored by the ACS Division of Fluorine Chemistry.
p. cm. -- (ACS symposium series ; 1064)
Includes bibliographical references and index.
ISBN 978-0-8412-2610-4 (alk. paper)
1. Fluorine compounds. 2. Nanocomposites (Materials) I. Nelson, Donna J. II. Brammer, Christopher N. III. American Chemical Society. Division of Fluorine Chemistry.
QD181.F1F56 2010
546′.731--dc23
2011013621

The paper used in this publication meets the minimum requirements of American National Standard for Information Sciences—Permanence of Paper for Printed Library Materials, ANSI Z39.48n1984.

Copyright © 2011 American Chemical Society

Distributed in print by Oxford University Press, Inc.

All Rights Reserved. Reprographic copying beyond that permitted by Sections 107 or 108 of the U.S. Copyright Act is allowed for internal use only, provided that a per-chapter fee of $40.25 plus $0.75 per page is paid to the Copyright Clearance Center, Inc., 222 Rosewood Drive, Danvers, MA 01923, USA. Republication or reproduction for sale of pages in this book is permitted only under license from ACS. Direct these and other permission requests to ACS Copyright Office, Publications Division, 1155 16th Street, N.W., Washington, DC 20036.

The citation of trade names and/or names of manufacturers in this publication is not to be construed as an endorsement or as approval by ACS of the commercial products or services referenced herein; nor should the mere reference herein to any drawing, specification, chemical process, or other data be regarded as a license or as a conveyance of any right or permission to the holder, reader, or any other person or corporation, to manufacture, reproduce, use, or sell any patented invention or copyrighted work that may in any way be related thereto. Registered names, trademarks, etc., used in this publication, even without specific indication thereof, are not to be considered unprotected by law.

PRINTED IN THE UNITED STATES OF AMERICA

Downloaded by 89.163.35.42 on June 5, 2012 | http://pubs.acs.org
Publication Date (Web): April 27, 2011 | doi: 10.1021/bk-2011-1064.fw001

Foreword

The ACS Symposium Series was first published in 1974 to provide a mechanism for publishing symposia quickly in book form. The purpose of the series is to publish timely, comprehensive books developed from the ACS sponsored symposia based on current scientific research. Occasionally, books are developed from symposia sponsored by other organizations when the topic is of keen interest to the chemistry audience.

Before agreeing to publish a book, the proposed table of contents is reviewed for appropriate and comprehensive coverage and for interest to the audience. Some papers may be excluded to better focus the book; others may be added to provide comprehensiveness. When appropriate, overview or introductory chapters are added. Drafts of chapters are peer-reviewed prior to final acceptance or rejection, and manuscripts are prepared in camera-ready format.

As a rule, only original research papers and original review papers are included in the volumes. Verbatim reproductions of previous published papers are not accepted.

ACS Books Department

Downloaded by 89.163.35.42 on June 5, 2012 | http://pubs.acs.org
Publication Date (Web): April 27, 2011 | doi: 10.1021/bk-2011-1064.ch001

Chapter 1

Introduction

Donna J. Nelson* **and Dragan Nikic**

Department of Chemistry and Biochemistry, University of Oklahoma,
Norman, OK 73019
***djnelson@ou.edu**

The Introduction (Chapter 1) provides an overview of *Fluorine-Related Nanoscience with Energy Applications*, relating its significance and pertinence to current global grand challenges. The Introduction discusses the differences among sections of the book, as well as the relationship between chapters within a section. This book contains seven additional chapters, each describing energy application of the unique nanomaterials presented.

The Chapters 2 and 3 describe graphene and how its properties can be engineered by fluorination; fluorination of graphene can change the band gap, producing desired properties. Fluorinated graphene applications create the possibility of replacing silicon in electronics. Comparing the effects of fluorination upon single-walled carbon nanotubes (SWCNTs) versus graphene reveals that fluorination damages the structure of SWCNTs but does not damage the structure of graphene. Chapter 3 describes SWCNTs and their interactions with diverse small organic molecules using ^{1}H NMR spectroscopy, as a powerful method of characterizing these non-covalent complexes.

Chapter 4 discusses the synthesis of new highly fluorinated porphyrin nanomaterials and their properties as nanomaterials used to prepare ultra thin-films which have applications in solar cells energy conversion. This includes the use of highly fluorinated porphyrin materials as catalysts for oxidation under "green" conditions.

Chapters 5 and 6 describe fluorinated inorganic compounds of the lanthanide family doped with other lanthanides, which

are used in light harvesting, sunlight conversion, and low-cost lighting.

Chapter 7 describes nanomaterials which are fluorinated ionomer membrane -Nafion films; these are essential parts of fuel cells. New energy nanomaterial like an alane (AlH3)n embedded in Nafion films were discussed. Chapter 8 discusses the catalytic properties of noble metal nanoparticles (Pt, Au, and Ag) as a function of particle morphology and composition. Potential applications in fuel cells of these nanoparticle catalysts with different morphologies of nanoparticle catalysts were compared, such as solid, porous, hollow, supported or unsupported, mono-versus bi-metallic composition.

Downloaded by 89.163.35.42 on June 5, 2012 | http://pubs.acs.org
Publication Date (Web): April 27, 2011 | doi: 10.1021/bk-2011-1064.ch001

The conditions of our overpopulated planet with ever-growing energy needs, fossil fuels in limited supplies, and inefficient energy use world-wide, are creating a global crisis. Science has a responsibility, as well as a grand opportunity, to solve these energy-based problems of society. Science's new nanotechnologies, and the creativity they bring, are particularly appropriate to solve these problems. For example, energy-saving lighting, coupled with improved harvesting and conversion of sunlight into electric energy, will have a great impact on society's energy needs. Also, development of energy efficient and low cost fuel cells, which could eventually replace car engines, has a potential to improve everyday life greatly.

Nanomaterials offer an opportunity to develop new low-cost materials as environmentally friendly solutions and renewable energy sources, in order to meet society's energy needs. Fortunately, a wide spectrum of the scientific community has become interested in developing these nanomaterials in order to solve the above energy challenges. Nanomaterials offer unique mechanical, catalytic, electronic, and optical features, which are different from those of the analogous bulk material (*1*). This is because nanomaterials have scale-dependent properties, due to quantum size effects, which means the nanomaterial size (10 – 100 nm) is smaller than the mean free path of their electrons. Thus, nanomaterials have great promise for use in harvesting solar energy, hydrogen production and storage, fuel cells, catalysis, chemical, optical sensors, drug delivery systems (such as liposomes), and nanothermite reactions (*2–4*).

Fluorine-containing nanomaterials generally have certain unique properties which are often improved relative to the analogous non-fluorinated nanomaterials, and which therefore could be engineered. Although fluorine has the highest electronegativity of all the elements, which means that bonds to fluorine are generally quite polar, it is also in the second period of the periodic table, so it also has a small atomic radius and forms strong bonds. This produces the following properties, which also are characteristic of and bring great advantages to fluorine nanomaterials: high thermal and chemical stability, resistance to degradation by solvents, low flammability, low moisture absorption, low surface tension or energy, low dielectric constant, and serving as a strong oxidant under high energy

Downloaded by 89.163.35.42 on June 5, 2012 | http://pubs.acs.org
Publication Date (Web): April 27, 2011 | doi: 10.1021/bk-2011-1064.ch001

conditions (*5*). However, little attention has been given to fluorine-containing organic and inorganic nanomaterials, which are predicted to have these unusual characteristics. This book presents examples of four diverse classes of these nanomaterials.

The first class of nanomaterial is that of low-dimensional carbon structures, with two pertinent chapters. In Chapter 2, fluorinated graphene, generated by XeF_2–fluorination of graphene films on copper foils or SiO_2 substrates, is presented as a nanomaterial of interest for uses in electronics components. In this study, fluorination was carried out on one side and on both sides of the graphene sheet. When fluorination is done from one side, fluorine coverage reaches saturation at 20% (C_4F). Fluorinating both sides of the graphene film on the SiO_2 substrate gave a fluorine coverage of 50% (CF). Single-side fluorinated graphene is optically transparent, with interesting nanoproperties, such as being six orders of magnitude more resistive than graphene itself. The material obtained can be easily patterned (*6*). These unique characteristics of modified graphene enable the possibility of replacing silicon with graphene in electronics (*7*).

Single-walled carbon nanotubes (SWCNTs) are another nanomaterial which has been used to construct new energy conversion architectures, due to its high solar energy conversion efficiency. Exceptional optical and electronic properties of SWCNTs make it is a promising platform for photovoltaic devices and sensors (*8*). For example, a transistor has been constructed using non-fluorinated SWCNT (*9*). These characteristics and examples might lead one to predict that fluorinating SWCNTs would produce an improvement in their electronic properties, analogously to the fluorination of graphite above.

However, when SWCNTs were analogously fluorinated under the same reaction conditions, a maximum of only 5% fluorination was obtained (*6*). In an earlier study, it was found that when using fluorinated SWCNTs instead of unmodified SWCNTs in C_{60} paper (buckypaper), the conductivity also decreased, but only by up to two orders of magnitude at room temperature (*11*). Comparing the effects of fluorination upon SWCNTs versus graphene, reveals that fluorination damages the structure of SWCNTs, but does not damage the structure of graphene (*10*).

Understanding the above differences in degree of fluorination of SWCNTs versus graphene could be facilitated by a better understanding of the interactions between SWCNTs and common solvents or other organic molecules (*12*). These are determined by studying SWCNT sidewall interactions with simple molecules, each containing only one or two different organic functional groups, as described in Chapter 3. Typical molecules are ketones, amides, oximes, aminoalcohols, and aminoketones. NMR spectra reveal varying degrees of association of functional groups with SWCNTs, measured by the downfield shifts of the protons in or around each functional group. The strength of association is represented by the magnitude of ^1H NMR shift change upon SWCNT:organonitrogen complex formation. Some findings are: (1) in amides and aminoketones, SWCNT association with carbonyls is generally stronger than with nitrogen, (2) in aminoalcohols, SWCNT association with nitrogen is generally stronger than with oxygen, and (3) protons bonded to heteroatoms generally experience greater changes in their chemical shifts than those bonded to carbons, upon SWCNT association (*13*).

The fourth chapter describes the synthesis of two new highly-fluorinated porphyrins and their properties as nanomaterials used in the synthesis of thin films, which have applications in solar cell energy conversion. The two porphyrins are 5,10,15,20-tetrakis-(2,3,4,5,6-pentafluorophenyl) porphyrin ($TPPF_{20}$) and $TPPF_{100}$, a compound prepared from $TPPF_{20}$. These highly fluorinated porphyrin nanoparticles catalyze oxidation of compounds such as cyclohexane (*14*), constituting a conversion which is greener than other typical methods, because the oxidation is carried out in a solvent containing 89 % water and O_2 as the oxidizing agent, instead of synthetic oxygen sources. Such porphyrins are also being used to prepare other nanomaterials, such as nanorods, nanoparticles, nanowires, and nanotubes (*15*).

The synthetic value of these fluorinated porphyrins is due to the fluorine at position 4 in the phenyl ring, which can be easily substituted by nucleophiles, enabling further derivatization. Fluorinated porphyrin derivatives which were further derivatized with perfluoro alkyl chains as well as fullerene (C_{60}) were used to prepare self–assembled thin films on an indium–tin–oxide electrode. This new nanomaterial is remarkably stable, being robust to oxidative damage, if used as a film on surfaces (*16*); it can be used for solar energy conversion and energy storage, because the complexes can form long-lived charge-separated states.

In Chapters 5 and 6, fluorinated inorganic compounds of the Lanthanide family are used for light harvesting, sunlight conversion, and other energy-related purposes. In the first part of this chapter, colloidal $NaYF_4$:Yb, Er up conversion nanophosphors (UCNPs) are one type of Lanthanide family nanomaterial explored. Instead of using oleic acid in a classical synthesis of these colloidal materials, this study uses a combination of stearic acid, lauric acid, and a trioctylphosphine ligand. The following parameters were studied and analyzed: a strong dependence upon nanophosphor monodispersity and crystallinity, synthesis temperature, and precursor concentration. Synthesis and characterization of core/shell structured phosphors - UCNP/$NaYF_4$, DCNP/$NaYF_4$:Eu/UCNP, and UCNP/DCNP (DC = down conversion) - are presented. Making the correct host material selection for doping Ln^{3+} was critical to achieving efficient luminescence. Two of the most commonly used and successful types of host are fluorides, such as $NeYF_4$ and LaF_3 and oxides, such as Y_2O_3 and Y_2O_2S.

Furthermore, the classical synthesis of these fluoride- and oxide-based phosphors uses solid state reactions and hydrothermal methods. Synthesis of colloidal inorganic nanocrystals via a thermal decomposition of organometallic precursors had been studied (*17*, *18*). However, this usually produces particles with irregular morphology and broad size distribution, difficulties which hinder correlating the photophysical properties of the ensemble particles to the synthetic conditions, especially for nanoscale syntheses. For the above-mentioned reasons, there is a need for the controllable synthesis of lanthanide-doped UC and DC nanophosphors. Work by Shan, et al., describes the effect of surfactants, precursor ratios, and reaction time and temperature upon the synthesis of fluoride-based hydrophobically–ligated NaYF4 :Yb, Er UCNPs, as well as the synthesis of core/shell structured NPs both UCNP and DCNPs (*19*).

Another inorganic fluorinated nanomaterial included is lanthanide fluorides, which are used in lighting and solar cells. These lanthanide fluorides have unique

Downloaded by 89.163.35.42 on June 5, 2012 | http://pubs.acs.org
Publication Date (Web): April 27, 2011 | doi: 10.1021/bk-2011-1064.ch001

properties, such as low photon frequencies, high index of refraction, thermal stability, and other related photophysical properties. When a fluoride host material is doped with lanthanides, the newly-formed material has excited states of long lifetime and high luminescence efficiency. Nanomaterials, such as $YF_3:Pr^{3+}$ and $NaYF_4:Pr^{3+}$, produce direct sequential emission of two photons, with a quantum efficiency over 100 % (*20*, *21*). Industrially very important white light producing hexagonal Yb^{3+}- Ho^{3+}- Tm^{3+} triply doped $NaYF_4$ nanorods were recently prepared via hydrothermal route using oleic acid as a stabilizing ligand (*22*). Thus, these lanthanide doped nanofluorides are suitable materials for improving fluorescent lamps and solar cells, which have advantages over classical solar cells (*23*).

The fourth type of nanomaterial, which is covered in Chapters 7 and 8 of this book, is fluorinated ionomer membranes, such as commercially available Nafion films. These perfluoro membranes are robust nanomaterials which are thermally and chemically stable, while retaining their mechanical properties even in highly corrosive and oxidative environments. The Nafion membrane is made via copolymerization of tetrafluoroethylene and a perfluoro-alkyl vinyl ether derivative with sulfonyl acid fluoride, followed by conversion of the sulfonyl fluoride into the sulfonate, and then conversion into the acid form. Finally, thin films are obtained by heating the polymer solution in aqueous solution at 250 ºC in an autoclave and casting (*24*) Nafion can serve as host for a wide range of redox mediators and nanoparticles, which produces more efficient catalytic and energy applications.

Recently a highly energy-efficient nanomaterial was made by embedding alane $(AlH_3)_n$ in Nafion (Al-in-Nafion) film (*25*). Al-in-Nafion films are very stable at room temperature in air, and the reactive Al content is changed insignificantly over time. The Al-in-Nafion membrane structure is not permeable to oxygen, avoiding any significant oxidation of embedded Al nanoparticles. The nanocomposite configuration of AlH_3 polymer particles in Nafion film could serve as a platform for efficient hydrogen generation under ambient conditions. In the future, possible regeneration of the Al nanoparticles, which are inside nano-cavities within the Nafion membrane, may be achieved, which would enable the production of rechargeable nano-Al material for energy storage and hydrogen production. A nanosemiconductor could be embedded in this and used as photocatalyst for energy conversion. Nanofluoromembranes, in which reactive metals are embedded, are a useful nanomaterial for hydrogen generation in fuel cells.

Recent advances in synthesis characterization, as well as catalytic and physicochemical properties of nanoscale materials, with potential applications in fuel cells are also presented. The research described primarily focuses on the catalytic properties of noble metal nanoparticles (Pt, Au, Ag) as a function of particle morphology and composition. Pt and Pt alloy based metals (Ag, Au, Ru, etc.) are currently the best electrochemical catalysts for proton exchange membrane fuel cells (*26*). Because Pt is a rare and costly metal, one way to increase the efficiency of the catalytic properties of Pt is to downsize particle's size; this is done by creating the corresponding nanomaterial - a nanocatalyst which will have a different morphology, such as solid, porous, hollow, supported, or unsupported material. These Pt nanocatalysts can boost the catalytic power

Downloaded by 89.163.35.42 on June 5, 2012 | http://pubs.acs.org
Publication Date (Web): April 27, 2011 | doi: 10.1021/bk-2011-1064.ch001

of Pt catalysts and simultaneously reduce the material cost and weight of the fuel cell. Therefore, the nanoscale Pt material is more electrochemically active than the corresponding bulk Pt catalyst. The size of Pt clusters, decreased to sub-nanoscale dimensions, such as a Pt cluster of 12 Pt atoms only, significantly increases the Pt catalytic activity in fuel cells. This increase of catalytic activity is attributed to the quantum size rather than a simple increase in surface area (*27*). Thus, nanoscale materials are promising in the development of future energy conversion technologies.

Wide-ranging and important characteristics of nanocomposite materials, as potential fuel cell components, have been compared in this work, such as isotropic versus anisotropic, hollow versus solid or core structures, mono– versus bi–metallic compositions, and supported versus unsupported nanoparticles. The nanomaterials were characterized by methods such as transmission electron microscopy and dispersive X–ray analysis (*28*). Both Ag–Pt nanowires and Pt nanotubes were prepared; the product nanomaterials are stable and can be isolated without core aggregation and decomposition.

Downloaded by 89.163.35.42 on June 5, 2012 | http://pubs.acs.org
Publication Date (Web): April 27, 2011 | doi: 10.1021/bk-2011-1064.ch001

References

1. Hunyadi Murph, S. E.; Serkiz, S. M.; Fox, E. B.; Colon-Mercado, H.; Sexton, L.; Siegfried, M. In *Fluorine-Related Nanoscience with Energy Applications*; Nelson, D. J., Brammer, C. N., Eds.; ACS Symposium Series 1064; American Chemical Society: Washington, DC, 2011; Chapter 8.
2. Lee, C. Y.; Strano, M. S. *J. Am. Chem. Soc.* **2008**, *130*, 1766–1773.
3. Kabata, N.; Serizawa, C. *J. Propul. Power* **1987**, *4*, 303–307.
4. Lips, H. R. *J. Spacecr. Rockets* **1977**, *14* (9), 539–545.
5. Gladysz, J. A., Curran, D. P., Horvath, I. T.; Eds.; *Handbook of Fluorous Chemistry*; Wiley/VCH: Weinheim, Germany, 2004.
6. Fuhrer, M. S.; Lau, C. N.; McDonald, A. H. *MRS Bull.* **2010**, *35*, 289–295.
7. Robinson, J. T.; Burgess, J. S; Junkermeier, C. E.; Badescu, S. C.; Reinecke, T. L.; Perkins, F. K.; Zalalutdniov, M. K.; Baldwin, J. W.; Colbertson, J. C.; Sheehan, P. E.; Snow, E. S. *Nano Lett.* **2010**, *10*, 3001–3005.
8. Kongkanand, A.; Kamat, P. V. *ACS Nano* **2007**, *1*, 13–21.
9. Jong, S.; Jong, H.; Suh, D.; Bark, S.; Hang, H. B.; Ahn, J.-H. *Nanotechnology* **2010**, *21*, 425105.
10. Dai, L. *Intelligent Macromolecules for Smart Devices*; Springer-Verlag: London, 2004, p 179.
11. Dettlaff-Weglikowska, U.; Skakalova, V.; Meter, J.; Cech, J.; Mueller, B. G.; Roth, S. *Curr. Appl. Phys.* **2007**, *7* (1), 42–46.
12. Nelson, D. J.; Brammer, C. N.; Nagarajan, P. S.; Perumal, P. T. In *Fluorine-Related Nanoscience with Energy Applications*; Nelson, D. J., Brammer, C. N., Eds.; ACS Symposium Series 1064; American Chemical Society: Washington, DC, 2011; Chapter 3.
13. Nelson, D. J.; Nagarajan, P. S.; Brammer, C. N.; Perumal, P. T. *J. Phys. Chem. C* **2010**, *114*, 10140–10147.

Downloaded by 89.163.35.42 on June 5, 2012 | http://pubs.acs.org
Publication Date (Web): April 27, 2011 | doi: 10.1021/bk-2011-1064.ch001

14. Varotto, A.; Smeureanu, G.; Aggarwal, A.; Drain, C. M. In *Fluorine-Related Nanoscience with Energy Applications*; Nelson, D. J., Brammer, C. N., Eds.; ACS Symposium Series 1064; American Chemical Society: Washington, DC, 2011; Chapter 4.
15. Drain, C. M.; Varotto, A.; Radivojevic, I. *Chem. Rev.* **2009**, *109* (3), 1630–1658.
16. Varotto, A.; Todoro, L.; Vinodu, M.; Koehne, J.; Liu, G.-yu; Drain, M. C. *Chem. Commun.* **2008**, 4921–4923.
17. Yin, Y.; Alivisatos, A. P. *Nature* **2005**, *437*, 664–670.
18. Peng, X.; Wickham, J.; Alivisatos, A. P. *J. Am. Chem. Soc.* **1998**, *120*, 5343–5344.
19. Shan, J.; Yao, N.; Ju, Y. In *Fluorine-Related Nanoscience with Energy Applications*; Nelson, D. J., Brammer, C. N., Eds.; ACS Symposium Series 1064; American Chemical Society: Washington, DC, 2011; Chapter 5.
20. Sommerdijk, J. L.; Bril, A.; de Jager, A. W. *J. Lumin.* **1974**, *8*, 341–343.
21. Piper, W. W.; De Luca, J. A.; Ham, F. S. *J. Lumin.* **1974**, *8*, 344–348.
22. Yong, L. W.; Han, H. L.; Zhang, Y. Y.; Zhong, J. X. *J. Phys. Chem. C* **2009**, *113*, 18995–18999.
23. Ghosh, P.; Lorbeer, C.; Mudring, A.-V. In *Fluorine-Related Nanoscience with Energy Applications*; Nelson, D. J., Brammer, C. N., Eds.; ACS Symposium Series 1064; American Chemical Society: Washington, DC, 2011; Chapter 6.
24. Heitner-Wirguin, C. *J. Memb. Sci.* **1996**, *120* (1), 1–33.
25. Li, H.; Meziani, M. J.; Lu, F.; Burker, C. E.; Guliants, E. A.; Sun, Y.-P. *J. Phys. Chem. C* **2009**, *113* (48), 20539–20542.
26. Somorjai, G. A.; Park, J. Y. *Angew. Chem., Int. Ed.* **2008**, *47*, 9212–9228.
27. Yamamoto, K.; Imaoka, T.; Chun, W.-J.; Enoki, O.; Katoh, H.; Takenaga, M.; Sonoi, A. *Nature Chem.* **2009**, *1*, 397–402.
28. Hunyadi, S. E.; Murphy, C. J. *J. Cluster Sci.* **2009**, *20* (2), 319–330.

Chapter 2

Fluorinated Carbon Nanomaterials: XeF_2 Fluorination of Graphene

James S. Burgess,*[,a] Jeffrey W. Baldwin,[a] Jeremy T. Robinson,[a] Felipe A. Bulat,[b] and Brian H. Houston[a]

[a]Naval Research Laboratory, Washington, DC 20375, United States
[b]Global Defense Technology and Systems, Inc., Crofton, Maryland 21114, United States
***james.burgess.ctr@nrl.navy.mil**

The material properties of graphene, such as electrical conductivity, optical transmission, and chemical reactivity, can be drastically altered with fluorination, enabling new utility from this already promising material. Stoichiometric control of the fluorination of graphene was made possible by controlled exposure of graphene films on various substrates (copper, silicon dioxide, and silicon on insulator (SOI)). Reacting XeF_2 gas to a single side of the graphene sheet, with the underside protected by a copper or SiO_2 substrate, results in a fluorine content of 20% in the film (C_4F) as determined by x-ray photoelectron spectroscopy (XPS). XeF_2 gas exposure to both sides of graphene on a silicon on insulator (SOI) substrate results in fully fluorinated graphene (50% in the film, CF). Quantum mechanical calculations are presented that demonstrate the stability of single- and double-sided fluorinated graphene. To compare this fluorination method to other relevant carbon materials, single-walled carbon nanotubes (SWNTs) were exposed under the same reaction conditions, where the maximum fluorine content is 5% ($C_{19}F$). The chemical reactivity and stability of fluorinated graphene was explored by thermal desorption and hydrazine reduction. For single-side fluorine addition, fluorine begins to dissociate from the material at less than 100 °C and is completely removed at 300 °C. Hydrazine reduction showed complete removal of the fluorine

In Fluorine-Related Nanoscience with Energy Applications; Nelson, D., et al.; ACS Symposium Series; American Chemical Society: Washington, DC, 2011.

for single-sided fluorination, but with nitrogen incorporation in the graphene.

Fluorinated Carbon Materials

The fluorination of carbon materials dates back to the 1930s with the formation of graphite fluoride using fluorine gas at 300 °C (*1*, *2*). Graphite fluoride has vastly different electrical, thermal, and mechanical properties than graphite, opening possibilities for uses as solid lubricants (*3*) and lithium ion battery cathodes (*4*). Many routes have been used to fluorinate graphite and other carbon materials, such as single-walled carbon nanotubes (SWNTs), utilizing CF_4, SF_6, F_2, and HF gasses (*5–7*). These methods require either elevated temperatures, as with the graphite fluoride, or plasmas to react with the materials. Recently, XeF_2 has been used as a room temperature fluorinating agent for multi-walled carbon nanotubes (MWNTs), with a fluorine content of 5% giving the stoichiometry ($C_{19}F$) (*8*). The fluorination of the most recent member of the carbon family, graphene, was first accomplished using a SF_6 plasma, yielding 18% fluorine on the graphene film (*9*). Complete fluorination of monolayer graphene was only recently accomplished utilizing XeF_2 gas as the fluorinating agent (*10*). XeF_2 was found to be a much better fluorinating agent for graphene than for the MWNTs with a fluorination of 50% (CF) possible by exposing both sides of the graphene film to XeF_2 gas (*10–12*). General interest in graphene began in 2004 when a simple synthesis technique was developed to exfoliate single sheets of graphene from graphite (*13*). It was found that this material has unique electrical and mechanical properties, including electron mobilities that rival silicon (15,000 $cm^2V^{-1}s^{-1}$) and a thermal conductivity of 5,000 W/m·K (*14*, *15*). These properties make graphene attractive as a replacement for silicon in the semiconductor industry. Graphene's high thermal conductivity should enable higher density circuits and faster processor speeds without the need for additional heat management schemes. However, a barrier to graphene replacing silicon arises from the absence of a band gap in the material, being essential to logic applications in circuits. Opening a band gap in graphene is possible through functionalization with fluorine and other substituent groups (*10*, *16–20*). Indeed, it has been shown in multilayer graphene that fluorination induces semiconducting properties (*20*). Additionally, calculations have shown that the band gaps of these materials can be varied, allowing one to 'tune' the band gap to the desired level, e.g. 1.4 eV for C_8F , 2.8 eV for C_4F , and 3.07 eV for CF (*10*). Together, these unique characteristics fuel interest in utilizing graphene as a possible replacement for silicon in the electronics industry (*21*), with the possibility of attaining more efficient devices with less energy dissipation.

Besides use in field-effect transistors, graphene and carbon nanotubes have been investigated as electrode materials for a variety of devices, including ultracapacitors, fuel cells, and solar cells (*22–30*). The mechanical robustness, transparency, and high conductance of graphene make it an ideal transparent electrode for optical devices and may allow for the replacement of indium tin oxide in such applications (*22*). Fluorinated graphene could also have a variety of applications in the field of energy storage, including electrodes for ultracapacitors. Due to their fast charge/discharge rates, ultracapacitors are sought after for secondary batteries, with graphene being a desirable material as an electrode since energy storage is inversely proportional to film thickness (*23*). In fact, such devices fabricated from chemically modified graphene and graphene yield specific capacities ranging from 135 to 480 F/g (*23*, *26*). Since carbon nanotubes used as electrodes for lithium batteries have a higher specific capacity when fluorinated (797 mAh/g) than ones that are not fluorinated (200 mAh/g), fluorination of graphene films for electrode applications may improve their performance (*31*, *32*). In addition to higher specific capacity, low level fluorination (< 10 %) of anodes in secondary batteries improve their first Coulombic efficiencies by a factor of 12 to 25 %, thus causing less degradation of the electrolyte layer in the cell (*32–34*). These concepts, high specific capacity and first Coulombic efficiency, could be combined in an improved ultracapacitive cell.

Fluorination of Single Walled Carbon Nanotubes (SWCNTs) Using XeF_2

In the experiments described here we used a commercially available XeF_2 etching system (Xactix®) to fluorinate SWCNTs. XeF_2 gas has long been known to fluorinate alkenes across the double bond (*35*). The reaction is also known to occur in MWCNTs, which were placed in a container with XeF_2 gas for a period of 30 hours, yielding fluorine contents of 5.4 % (*8*). In contrast to the method for MWCNTS in the literature, our SWCNTs were exposed for short periods of time, between 30 and 150 seconds, at a partial pressure of 1 Torr XeF_2 in 35 Torr N_2 carrier gas.

The XPS spectra (Figure 1) of a SWNT film (a) and a SWNT film exposed to XeF_2 for 150s (b) confirms fluorine is present in the film after XeF_2 exposure. Furthermore, the binding energy of 688 eV is expected for covalently bound fluorine to carbon nanotubes (*7*). Analysis of the peak areas from the survey spectra (not shown) gives a relative ratio of 5% fluorine to carbon.

Raman spectra (Figure 2) of the SWNT film (a) and the same film after XeF_2 exposure for 150 s (b) confirm structural changes occur after fluorination. In the region of the Raman spectrum from 1,100 to 2,000 cm^{-1}, two of the most important *sp*^{2} carbon-carbon stretching modes are present. The mode at 1343 cm^{-1} corresponds to disorder (called the D-mode) in *sp*^{2}-carbon compounds and arises from the breaking of the carbon-carbon double bounds (*36–38*). The G-mode (1584 cm^{-1}) is associated with graphite and other materials with networked aromatic rings. The intensity ratio (I_D/I_G) of these two modes is often used to determine disorder in graphitic materials (*36–38*). This ratio is related to the aromatic *sp*^{2}-domain size and is normally associated with a shift in the frequency of the G-mode. However, the lack of shift of the G-mode here points to some interesting differences in the morphology between disordered carbon systems and fluorinated SWNTs.

In Fluorine-Related Nanoscience with Energy Applications; Nelson, D., et al.;
ACS Symposium Series; American Chemical Society: Washington, DC, 2011.

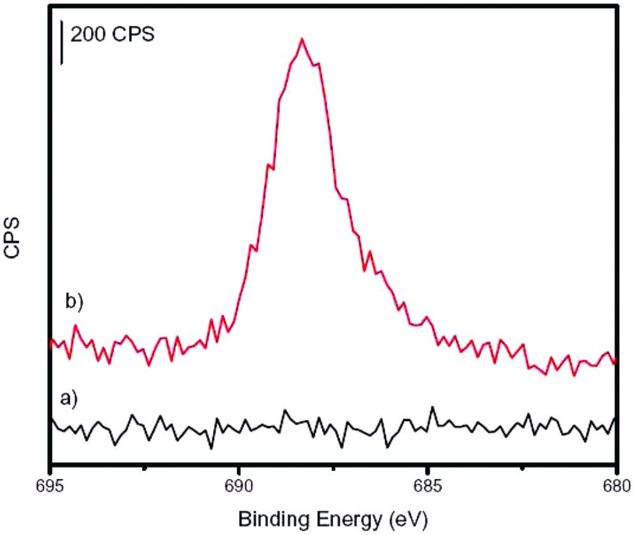

Figure 1. XPS Spectra of F 1s region for an unreacted SWCNT (a) and a SWCNT exposed to XeF_2 for 150 s (b).

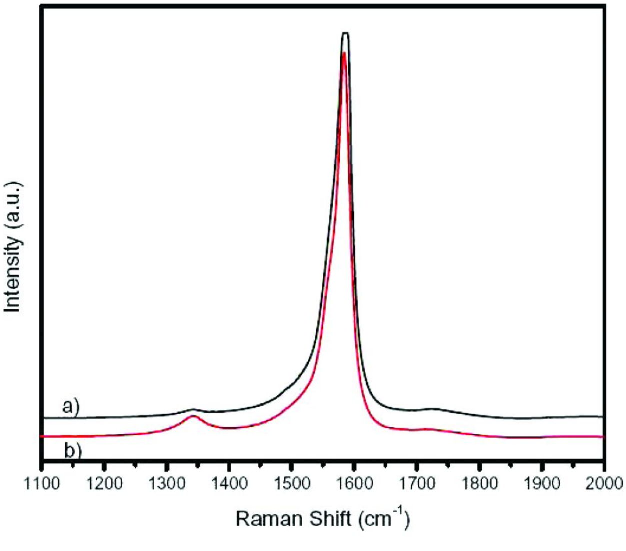

Figure 2. Raman Spectra of an unreacted SWNT (a) and a SWNT exposed to XeF_2 for 150 s (b).

In Fluorine-Related Nanoscience with Energy Applications; Nelson, D., et al.;
ACS Symposium Series; American Chemical Society: Washington, DC, 2011.

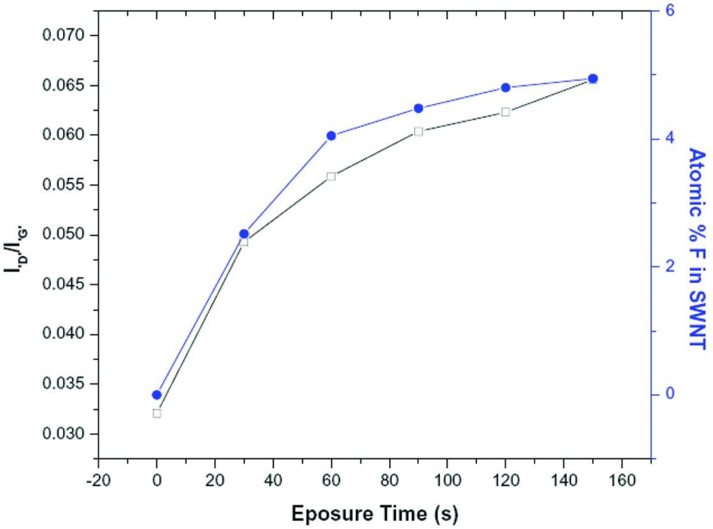

Figure 3. Plot of the relationship between I_D/I_G ratio (left axis, squares), % fluorine in the film (right axis, circles), and the exposure time.

The I_D/I_G ratio increases with exposure time (Figure 3, left axis) up to 60 seconds of exposure. After this time, the I_D/I_G ratio remains relatively unchanged, indicating a maximum fluorine content using the XeF_2. This is further evidenced by the %F in the film (Figure 3, right axis) which approaches a maximum of 5% after one minute exposure. The rate of fluorination using XeF_2 is, therefore, quite fast with most of the reaction proceeding in the first minute of exposure. However, in terms of percent fluorination, this method does not procede as far as other methods such as exposure to F_2 at elevated temperatures, which has yields approaching 50% fluorine in the SWNTs (i.e. CF) (*6*).

Fluorination of Graphene Using XeF_2: Perfluorographane

Graphene films were produced using chemical vapor deposition (CVD) growth on Cu foils as described elsewhere (*39*). A flow chart of the growth and transfer processes is shown in Figure 4. Briefly, Cu foils are heated to 1,000 °C under H_2 flow (~600 mTorr), then the partial pressure of H_2 is reduced to (<50 mTorr) and methane is introduced (P_{total} ~500 mTorr) for 20 minutes, after which the sample is quenched to room temperature. Graphene films are transferred to various substrates using a poly(methyl methacrylate) (PMMA) protective film, while the Cu substrate is dissolved in acid. The PMMA/Graphene film is then transferred to either SiO_2 or silicon-on-insulator (SOI) substrates and rinsed with acetone to remove the PMMA protective layer. Finally, PMMA residues are removed by thermal annealing up to 400 °C for 30 minutes in H_2/Ar (5%/95%). The graphene samples are then reacted with XeF_2 gas under the same conditions as the aforementioned SWNTs samples.

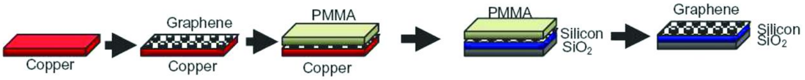

Figure 4. Schematic of graphene transfer.

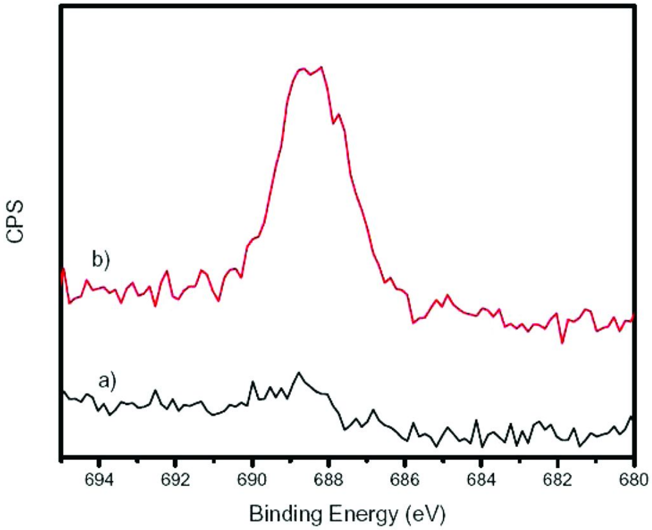

Figure 5. XPS spectra of the F 1s region for an untreated sample (a) and a sample exposed to XeF_2 for 600s (b) on the copper substrate.

Graphene films on copper were exposed to the XeF_2 gas. XPS was used to investigate the fluorination of the films based on its ability to determine atomic percents and to observe chemical shifts of fluorine-bound carbons. The high electronegativity of fluorine shifts the carbon 1s binding energy to the extent that C-CF, CF, CF_2, and CF_3 bonding moieties are distinguishable. The F 1s region of the XPS spectra (Figure 5) for the untreated (a) and XeF_2 exposed (b) sample resembles results from fluroinated SWCNTs, with the location of the fluorine binding energy being consistent with fluorine covalently bound to carbon, i.e. not bound to the copper substrate. The carbon binding energy spectra was also analyzed for these samples (Figure 6). The untreated sample (a) showed a single peak in the XPS at 284.5 eV, consistent with *sp*^{2} carbon-carbon bonds. Upon exposure to XeF_2 for 30s (b) and 600s (c), a shoulder appears at 286 eV, indicating carbons adjacent to fluorine bound carbons ($\underline{C}$-CF), and a peak at 289 eV, indicating carbons bound directly to a single fluorine atom (C-F) (*5*). When the %F in the film is plotted against exposure time (Figure 7), it becomes apparent that the reaction saturates after one minute, much the same as what was seen in the SWNT material. However, the maximum fluorine content is much higher by comparison, about 20% or C_4F. This value is in good agreement with calculations for single-sided fluorination of graphene (*cis* additions across the double bonds in the film) already in the literature (*40*).

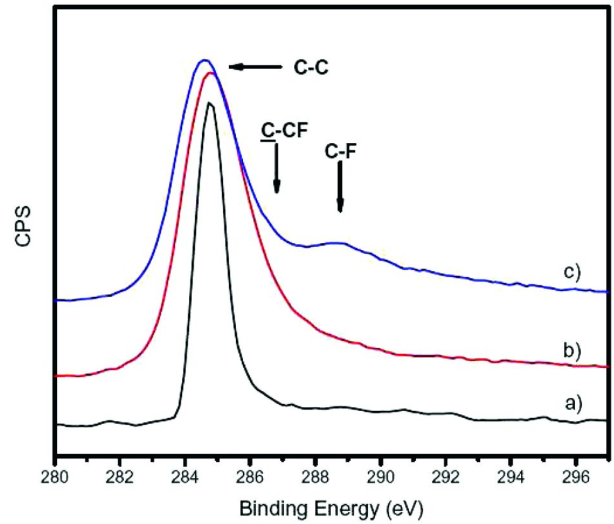

Figure 6. XPS spectra of the C 1s region for an untreated sample (a), a sample exposed to XeF_2 for 30s (b), and a sample exposed to XeF_2 for 600s (c) on the copper substrate. Arrows indicate location of carbon types (10).

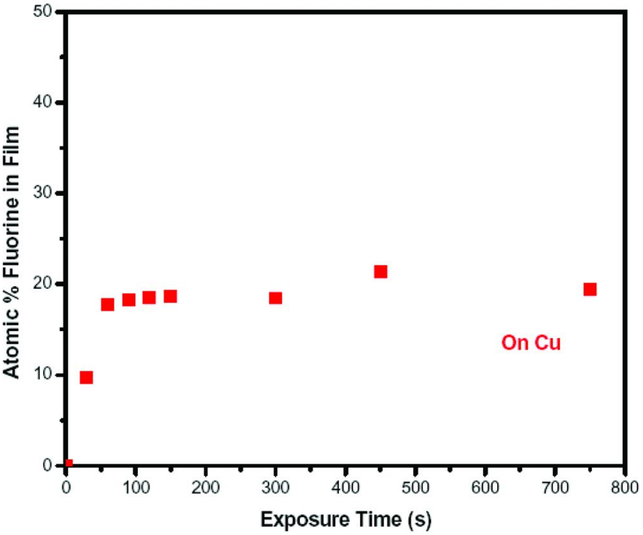

Figure 7. Atomic % of fluorine in the fluorinated graphene film on the copper substrate reaching a maximum of 20% fluorine (i.e. C_4F) (10).

Graphene samples were also transferred onto silicon on insulator (SOI) substrates. These substrates consist of 400 nm of crystalline silicon on a 400 nm layer of SiO_2 on a Si wafer and were processed under the same conditions as the graphene on copper and the SWNTs. The fluorine region of the XPS spectra of the graphene films on SOI (Figure 8a) exhibits fluorination in the 60 seconds of exposure (Figure 8b), much like the SWCNTs and graphene on copper, but with one main difference: there is a large increase in the amount of fluorine in the film after the 600 seconds of exposure (Figure 8c). XPS analysis of the carbon binding energy region of a clean graphene film (Figure 9a) shows a major feature occurring at 284.5 eV, indicating sp^2 C-C bonds on the surface. After a 30s XeF_2 exposure (Figure 9b) a large C-CF peak (286 eV) appears, indicating that fluorine is reacting with the carbon in the lattice. At longer exposures (600 seconds, Figure 9c), a dramatic change is seen in the films. The sp^2 C-C bonding decreases close the same intensity as the C-CF bonding, while the signal from C-F bonds has the highest intensity, indicating that a majority of the carbon is covalently bound fluorine.

A full picture emerges when we examine what is happening to the silicon layer supporting the graphene film. An important difference between the Cu, SiO_2, and SOI substrates is the fact that XeF_2 gas effectively etches silicon, while it has a very low reactivity with SiO_2 or Cu. XPS analysis of the silicon binding energy region for a graphene/SOI sample exposed to XeF_2 for 150 s (Figure 10a) shows two major features at 99 eV and 103.5 eV, which corresponds to Si-Si and Si-O bonding, respectively. The observation of the Si-O peak indicates some of the top Si layer in the SOI stack has been etched, exposing the buried oxide. After only 30 s more exposure (Figure 10b), the majority of the Si-Si signal has disappeared indicating that XeF_2 is indeed etching the silicon underlayer. This reaction occurs when XeF_2 gas diffuses through pinholes naturally occurring in the graphene film and forms volatile $Si\text{-}F_x$ products. XeF_2 etching is highly selective between Si and SiO_x, which results in Si-O intensity increasing while the Si-Si intensity disappears. By 240s exposure, the silicon layer is entirely etched leaving only the SiO_2 underlayer and the fluorinated graphene film intact (Figure 10c).

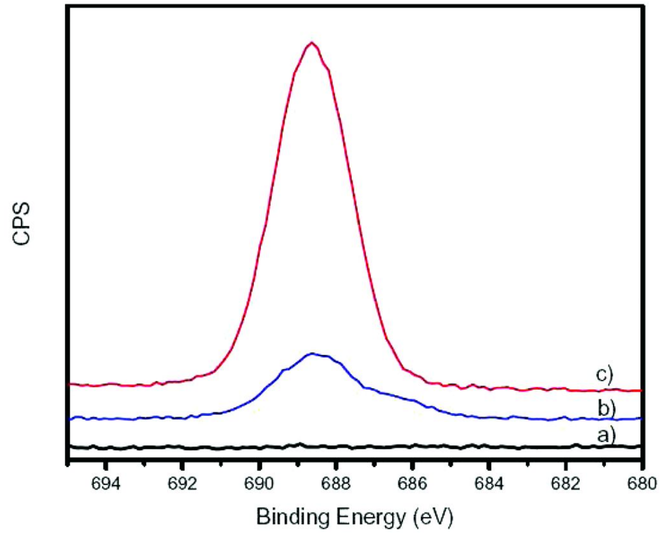

Figure 8. XPS spectra of F 1s region of fluorinated graphene films on SOI substrates of samples exposed to XeF_2 for 0s (a), 60s (b), and 600s (c).

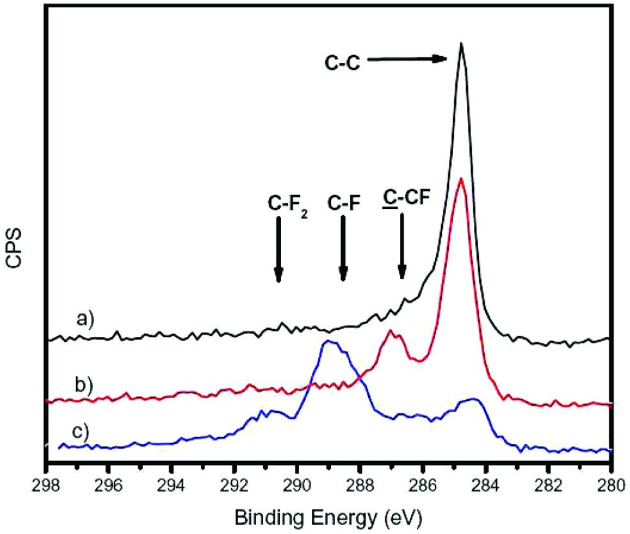

Figure 9. XPS spectra of C 1s region of fluorinated graphene films on SOI substrates of samples exposed to XeF$_2$ for 0s (a), 30s (b), and 600s (c) (10).

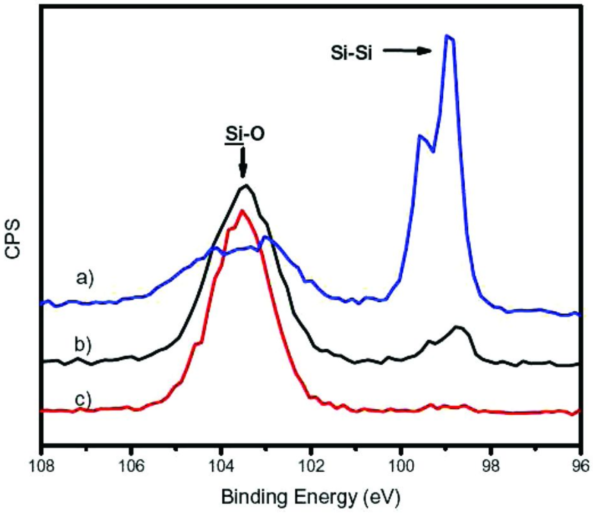

Figure 10. XPS spectra of Si 2p region of fluorinated graphene films on SOI substrates exposed to XeF$_2$ for 150 (a), 180 (b), and 240s (c) (10).

The XPS survey spectra (not shown) were utilized to determine the atomic %F in the graphene films (Figure 11, left axis, circles). The films behave much the same as the samples on the copper substrates reaching 20 % (C_4F) in the first minute of reaction and saturating the surface. However, between 150 s and 200 s the fluorine content reaches 50 % (CF, termed perfluorographane) and the reaction saturates at this value. We use the term perfluorographane to describe this new material; this naming scheme arises from a combination of the common nomenclature using perfluoro- to indicate the replacement of hydrogen with fluorine, and graphane, which is the accepted name for fully hydrogenated graphene. The amount of pure silicon remaining in the SOI layer was determined using the following relationship:

$$\%Si - Si = \frac{A_{Si-Si}}{A_{Si-Si} + A_{Si-O}} \times 100\%$$

using the area of the Si-Si feature ($A_{Si\text{-}Si}$) and the area of the Si-O ($A_{Si\text{-}O}$) as determined using a Gaussian-Lorentzian fit to the peaks. This data was plotted against exposure time (Figure 10, right axis, squares). As can be seen, between 0 and 150 s the silicon layer remained intact and began to decrease to zero by 200 s.

A physical picture of the etching and fluorination process is shown in figure 12. At first, when the silicon layer is still intact, only the top side of graphene is exposed to the XeF_2, similiar to the films on copper. This single-sided exposure results in a fluorine concentration of C_4F, which is comparable to graphene films on copper. As the XeF_2 gas etches silicon through pinholes in the graphene film, the underside of the graphene film is exposed to the gas. The exposure of both sides of graphene to the XeF_2 enables fluorine addition in the *trans*- position, allowing for a stable CF structure that has been predicted by calculations (*41*).

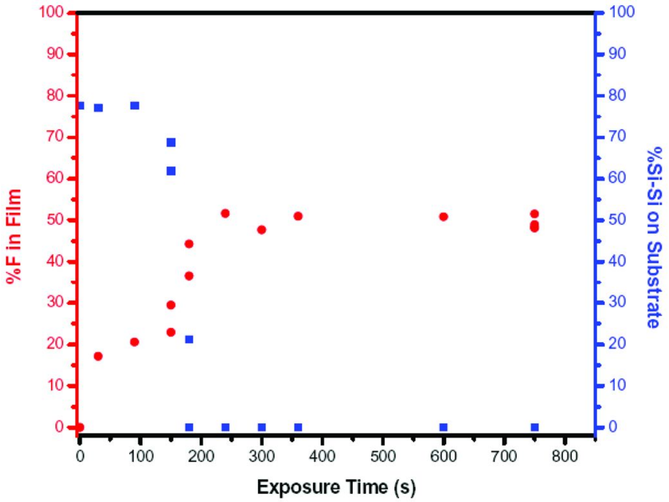

Figure 11. Chart showing the % fluorine (left axis, red circles) and the percent of crystalline silicon (right axis, blue squares) in the film versus exposure time (10).

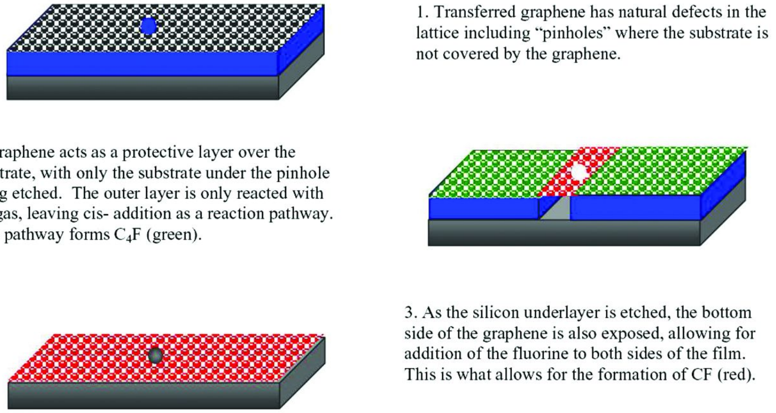

1. Transferred graphene has natural defects in the lattice including "pinholes" where the substrate is not covered by the graphene.

2. Graphene acts as a protective layer over the substrate, with only the substrate under the pinhole being etched. The outer layer is only reacted with the gas, leaving cis- addition as a reaction pathway. This pathway forms C_4F (green).

3. As the silicon underlayer is etched, the bottom side of the graphene is also exposed, allowing for addition of the fluorine to both sides of the film. This is what allows for the formation of CF (red).

Figure 12. Schematic of the fluorination pathway for perfluorographane with the top layer being graphene, the middle layer being crystalline silicon, and the bottom layer being silicon dioxide.

Relative Stabilities of *Cis* and *Trans* Fluorines on Coronene

In order to further understand the fluorination of graphene, we performed quantum mechanical calculations of the relative stabilities of the single- and double-sided fluorine addition products on a cluster model were calculated. Coronene (**1**, $C_{24}H_{12}$), a polycyclic aromatic molecule consisting of 6 fused benzene rings, was chosen as a model to study the fluorination of the central ring.

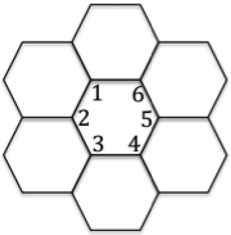

(1)

We have considered all possible conformations for the cases on which the central ring (atoms labeled 1-6) is substituted with one to six fluorine atoms. For conformations with an even number of fluorine atoms we considered both the singlet and triplet spin states, while for the conformations with odd number of fluorine atoms we considered both the doublet and quadruplet spin states. We found that in all cases the most stable geometries correspond to the singlet and doublet spin states, so we shall limit the discussion to these. All geometries were fully optimized using the B3LYP (*42*, *43*) energy functional and a triple-zeta basis containing polarization functions, 6-311G(d,p). Frequency analysis for each of the optimized geometries was also performed to ensure that they indeed correspond to energy minima (no imaginary frequencies). All calculations were performed with the Gaussian 09 (*44*) suite.

Figure 13 displays the relative stability of the products when 2 fluorine atoms are added to the central ring of coronene. Note that regardless of whether the addition results in a *cis* or *trans* product, the most stable geometries are those corresponding to a 1,2 addition. The *trans* product, however, is roughly 12 kcal/mol more stable than the *cis* product. This difference is likely not only due to the F-F repulsion but partially to the added strain caused by the “buckling up” of the otherwise rather rigid planar geometry of coronene (induced by the longer C-C single bond in FC-CF compared to the shorter C=C double bonds). The *trans* and *cis* 1,4 products are only ~3 kcal/mol from each other, likely a consequence of the large distance separating the fluorine atoms. Finally, the 1,3 products are almost degenerate (separated from each other by less than 1 kcal/mol), but significantly less stable than the 1,4 products (by roughly ~23 kcal/mol). These observations indicate a clear preference toward maintaining electronic conjugation by breaking as few double bonds as possible, which takes clear precedence over positioning 2 fluorine atoms in close proximity.

The preference toward breaking as few double bonds as possible, even at the expense of close F-F proximity, is also observed for the products of the addition of 3 fluorine atoms to the central ring of coronene. The stability of the products is 1,2,3 > 1,2,4 > 1,3,5, regardless of whether the addition is on a single side or on both sides of the molecular plane. Similarly, the most stable products for the addition of 4 fluorine atoms to the central ring of coronene are the 1,2,3,4 products over any other possible configuration (again, regardless of the positioning of the atoms with respect to the molecular plane).

It is clear from the results above that there is a strong preference toward clustering of the fluorine atoms for both the single- and double-sided additions. However, the double-side addition is seen to be increasingly favorable over the single-sided addition as the number of fluorine atoms in a ring increases. Figure 14 shows the binding energy for the subsequent addition of fluorine atoms when the addition occurs on a single side (red squares) and on both sides (blue diamonds) of the molecular plane. For the latter situation all possibilities were considered, and it was found that the most stable configuration was invariably the one on which the fluorine atoms alternate sides and are clustered together, as noted earlier. Figure 14 indicates that the double sided addition of a second F atom to the ring, leading to the *trans*-1,2 product, is ~12 kcal/mol more favorable than the single sided addition, as also seen in Figure 13. The double-sided additions of the third and fourth fluorine are more favorable by ~6 kcal/mol and ~8 kcal/mol, respectively, than the single sided. This effect is also cumulative; by the time the fourth atom has been added, the double-sided configuration is ~26 kcal/mol (12+6+8) more stable than the single-sided configuration. The binding energies for the fifth and sixth fluorine atoms present even larger differences, indicating that as the degree of fluorination increases, the difference in stability becomes increasingly larger. Also, the binding energy is still negative even after the addition of the sixth fluorine atom, indicating that the process is energetically favored and perhaps also thermodynamically favorable. If so, why does the single-side fluorination stop at ~20% coverage? The final piece of the puzzle is provided by the underlying surface. When six fluorine atoms are added to a single ring on the same side, the carbon-carbon bonds "buckle up" significantly. However, this buckling is impeded by the interaction between the layer and the underlying (silicon) surface. The combined effect of the less favorable single-side binding and the constraints imposed by the substrate are thus responsible for the limitations to the coverage rates on the single side case.

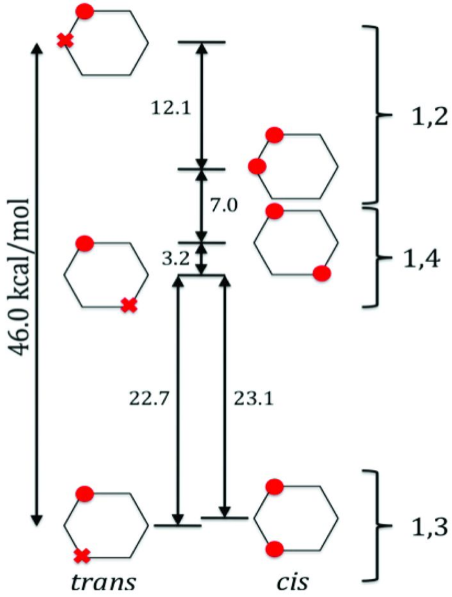

Figure 13. Relative stability of the 1,2 addition products computed using a B3LYP/6-311G(d,p) model chemistry. Full circles denote fluorine atoms on one side, and crosses on the opposite one.

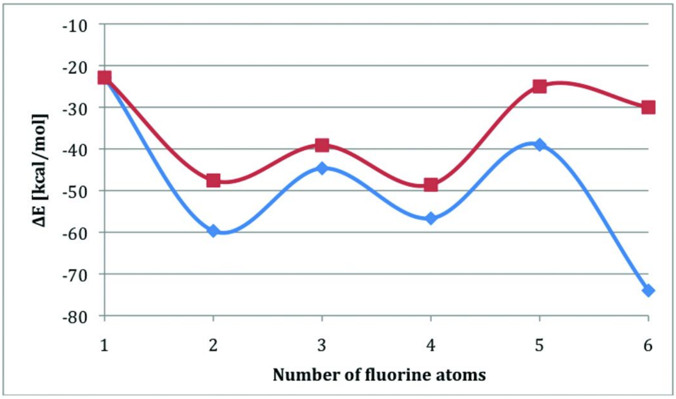

Figure 14. Binding energy for the subsequent addition (double side, blue diamonds; single side, red squares) of fluorine atoms to the central ring of coronene.

Removal of Fluorine from the Carbon Lattice

A common property of graphane (fully hydrogenated graphene) and perfluorographane is the ability to thermally reverse the reaction. It has been shown in both experiments (*45–47*) and predicted in calculations (*48*) that hydrogen leaves the film beginning as low as 300 °C and the material returns to graphene. We have also explored the thermal reversibility of fluorinated graphene. Two substrates were chosen for comparison: graphene on SiO_2 and on SOI. Both samples were treated with XeF_2 for 350 s, which is full saturation for both single- and double-sided fluorination. The %F for the graphene film on the SiO_2 wafer was 23% (~C_4F), a value expected for single-sided fluorination as evidenced from the copper experiments. The %F for the SOI is consistent with the prior experiments at about 47 %F (~CF). The dependence of the fluorine in the film with temperature (Figure 15) shows a linear dependence up to 300 °C, whereupon the concentration remains unchanged for both samples with 10 atomic %F still left in the perfluorographane, possibly due to fluorine trapped between the substrate and the graphene film. This indicates that the C-F bonds in fluorinated graphene can begin breaking between 200 and 300 °C. The Raman spectra (Figure 16) of the fluorinated graphene (a) and after heating to 120 °C (b) and 400 °C (c) shows a small change in the disorder in the film at lower temperatures, but no change at higher temperatures. No Raman active C-F stretching mode was observed due to either the mode being Raman inactive or masked by a relatively broad, intense mode from this SiO_2 substrate located around 900 cm^{-1}. Moreover, XPS analysis of annealed samples suggests the carbon content in fluorinated graphene, before and after thermal treatment, remains constant. This is illustrated in Figure 17, where the silicon/carbon ratio for the untreated graphene sample is about one (Figure 17, triangle) and this ratio remains constant during the defluorination.

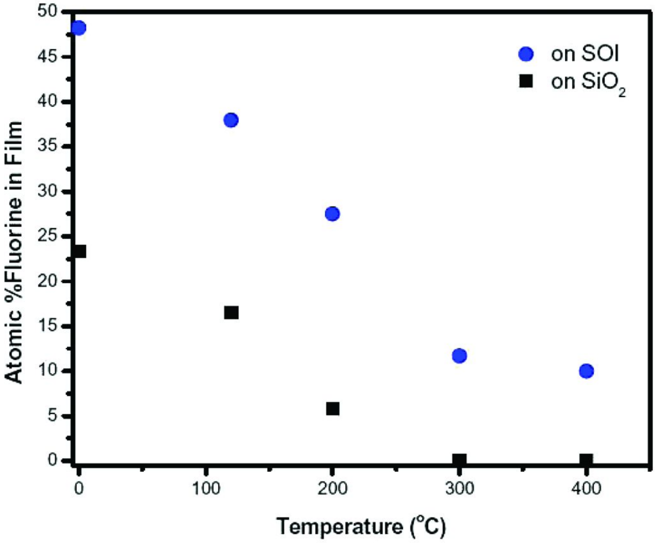

Figure 15. Chart of the % fluorine in films as a function of temperature for samples on SOI (blue circles) and SiO_2 (black squares).

In Fluorine-Related Nanoscience with Energy Applications; Nelson, D., et al.;
ACS Symposium Series; American Chemical Society: Washington, DC, 2011.

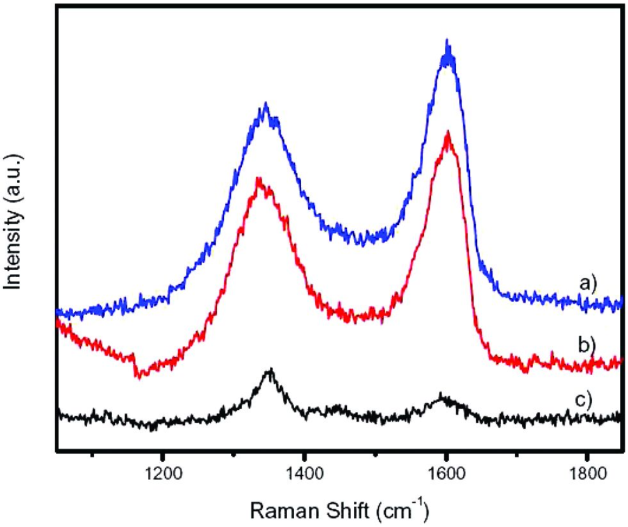

Figure 16. Raman spectra of a fluorinated film (a) and films heated to 120 °C (b) and 400 °C (c).

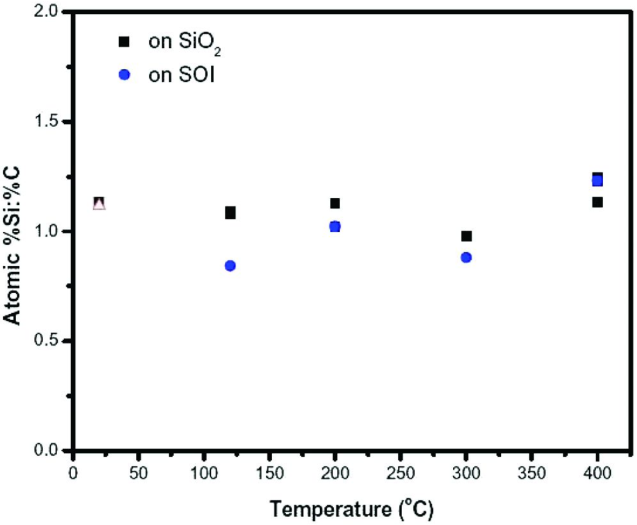

Figure 17. Chart illustrating the relative amount of carbon on the surface of the samples on an untreated sample (triangle), SOI (blue circles), and SiO_2 (black squares) after thermal treatment.

Hydrazine (N_2H_2) has been successfully used to reduce graphene oxide (*49*) to graphene, so this route was tested as a means to remove fluorine from fluorinated graphene films. Hydrazine reduction was carried out by bubbling N_2 gas through liquid hydrazine and then exposing the samples to the hydrazine-rich

N_2 vapor, as described elsewhere (*50*). Since hydrazine contains reactive nitrogen groups which can bond to graphene, we also monitored the nitrogen content during hydrazine reduction. Figure 18 demonstrates that hydrazine removes fluorine for both single-side (C_4F, left panel-circles) and double-side (CF, right panel-circles) fluorinated films down to a concentration of 5% fluorine. However, as the fluorine level decreases, the nitrogen level increases (figure 18, squares, both panels), indicating that some nitrogen is undergoing a replacement reaction on the fluorinated graphene film. The maximum nitrogen incorporation for both films was approximately 15% after ~44 hours of exposure. The film does not appear to etch in this process as evinced by the lack of change in carbon to silicon atomic percent ratios (Figure 19).

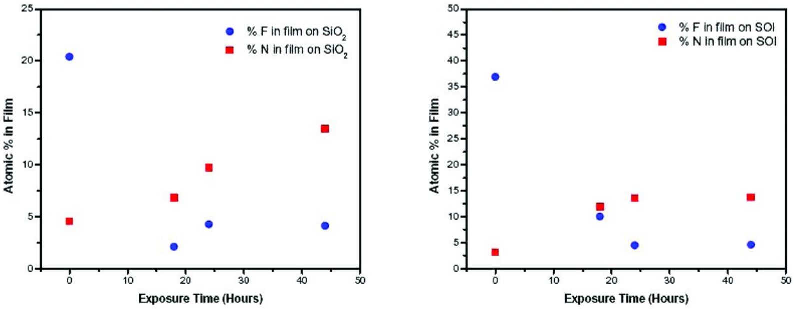

Figure 18. Charts of the % fluorine (blue circles) and % nitrogen (red squares) in films as a function of hydrazine exposure time for samples on SiO_2 (left chart) and SOI (right chart).

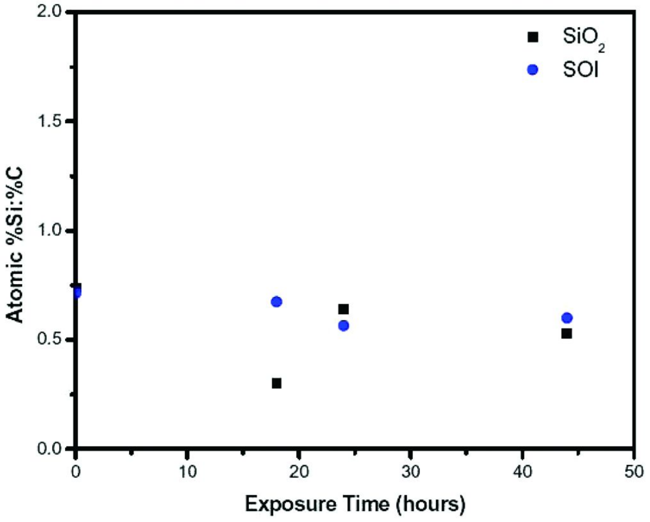

Figure 19. Chart illustrating the relative amount of carbon on the surface of the samples on SOI (blue circles) and SiO_2 (black squares) after hydrazine treatment.

Recently, it has been proposed that an intermediate step could possibly aide in the removal of the fluorine to form graphene (*11*). It was suggested that potassium iodine (KI) could be used with perfluorographane to form periodographane, or graphene iodide. This intermediate was found to be thermodynamically unstable and decomposed into graphene and iodide gas. This data was supported by atomic force microscopy and infrared spectroscopy (*11*). Thus, while the direct removal of fluorine from the carbon lattice may be thermodynamically unfavorable, intermediate steps may achieve defluorination.

Conclusion for the Formation of Perfluorographane (CF) and Fluorinated Graphene (C_xF)

The successful fluorination of graphene resulted from room temperature exposure to XeF_2 gas. XeF_2 fluorination of graphene and SWNTs show a structural dependence, as seen by the variation of the extent of fluorination seen in SWNTs ($C_{19}F$), single-sided graphene (C_4F), and double-sided graphene (CF). Both SWNTs and graphene have a graphitic structure consisting of conjugated pi-bonds in a honeycomb lattice; however, the bond angles in SWNTs are slightly smaller than those for graphite or graphene. Bond angles may play an important role in the fluoriantion process, including the reaction between a single side or double side of graphene. As fluorine reacts with the graphene surface, buckling occurs due to the different bond angles in the *sp*^{2} graphitic carbons (120°) and the fluorinated carbons (approximately 109.5°). This change in bond angle likely makes further addition of fluorine thermodynamically unfavored, leading to a maximum composition of C_4F when only a single side of the graphene is exposed to XeF_2. Both the reaction of the SWNTs and the single-sided graphene rely on fluorine radicals reacting with only one side of the material. Graphene on SOI has no such restrictions, since XeF_2 gas can access both sides. Double-sided exposure allows for fluorine to be added above and below the graphite plane, a configuration that is calculated to be 12 kcal/mol more stable than when added to the same side for the first 2 fluorine atoms per ring. These calculations are consistent with a clear preference towards clustering of the F atoms and a minimal disruption of the pi-electron network.

Fluorination of *sp*^{2} carbon materials using XeF_2 gas has the advantage of being controlled at room temperature, and does not rely on plasmas to form fluorine ions and radicals, which can damage graphene. For example, oxygen plasmas are routinely used to etch graphene during lithography and it has been shown that even hydrogen plasmas can etch graphene. Functionalization utilizing F_2 and HF gasses will also encounter problems due to the elevated temperatures required for the reactions (300 °C being the lowest temperature found to react fluorine with nanotubes or graphite). These higher processing temperatures can lead to carbon-carbon disorder and structural damage during fluorination, plus we note that defluorination begins at temperatures above 200 °C.

XeF_2 gas fluorination enables stoichiometric control of fluorine on graphene as evinced by the fluorine content in films exposed on one side (C_4F) or both sides (CF). The fluorine content changes the electrical (conducting to insulating), optical (opaque to transparent), and chemical properties (*10*). These properties may be tailored and integrated into novel graphene/perfluorographane systems leading to better nanoelectromechanical systems (NEMS), electrodes for ultracapacitors, and dielectric materials for graphene-based electronic devices.

Acknowledgments

The authors gratefully acknowledge the members of the technical staff of the Institute for Nanoscience at NRL, Darrell King, Dean St. Amand, and David Zapotok. James Burgess performed research courtesy of a National Research Council postdoctoral fellowship. This work was supported by the Office of Naval Research.

References

1. Ruff, O.; Bretschneider, O.; Ebert, F. *Z. Anorg. Allg. Chem.* **1934**, *217* (1).
2. Rüdorff, W.; Rüdorff, G. *Chem. Ber./Recl.* **1947**, *80* (5), 417–423.
3. Fusaro, R. L.; Sliney, H. E. *Tribol. Trans.* **1970**, *13* (1), 56–65.
4. Watanabe, N.; Hagiwara, R.; Nakajima, T.; Touhara, H.; Ueno, K. *Electrochem. Acta* **1982**, *27* (11), 1615–1619.
5. Felten, A.; Bittencourt, C.; Pireaux, J. J.; Van Lier, G.; Charlier, J. C. *J. Appl. Phys.* **2005**, *98*, 074308.
6. Pehrsson, P. E.; Zhao, W.; Baldwin, J. W.; Song, C.; Liu, J.; Kooi, S.; Zheng, B. *J. Phys. Chem. B* **2003**, *107* (204), 5690–5695.
7. Lee, J.-M.; Kim, S. J.; Kim, J. W.; Kang, P. H.; Nho, Y. C.; Lee, Y.-S. *J. Ind. Eng. Chem.* **2009**, *15*, 66–71.
8. Unger, E. *Chem. Phys. Lett.* **2004**, *399*, 280–283.
9. Baraket, M.; Walton, S. G.; Lock, E. H.; Robinson, J. T.; Perkins, F. K. *Appl. Phys. Lett.* **2010**, *96*, 231501.
10. Robinson, J. T.; Burgess, J. S.; Junkermeier, C. E.; Badescu, S.; Reinecke, T.; Perkins, K.; Zalalutinov, M.; Baldwin, J. W.; Culbertson, J.; Sheehan, P. E.; Snow, E. S. *Nano Lett.* **2010**, *10* (8), 3001–3005.
11. Zbořil, R.; Karlický, F.; Bourlinos, A. B.; Steriotis, T. A.; Stubos, A. K.; Georgakilas, V.; Šafářová, K.; Jančík, D.; Trapalis, C.; Otyepka, M. *Small* **2010**, *6* (24), 2885–2891.
12. Nair, R. R.; Ren, W.; Jalil, R.; Riaz, I.; Kravets, V. G.; Britnell, L.; Blake, P.; Schedin, F.; Mayorov, A. S.; Yuan, S.; Katsnelson, M. I.; Cheng, H.-M.; Strupinski, W.; Bulusheva, L. G.; Okotrub, A. V.; Grigorieva, I. V.; Grigorenko, A. N.; Novoselov, K. S.; Geim, A. K. *Small* **2010**, *6* (24), 2877–2884.
13. Novoselov, K. S.; Geim, A. K.; Morozov, S. V.; Jiang, D.; Zhang, Y.; Dubonos, S. V.; Grigorieva, I. V.; Firsov, A. A. *Science* **2004**, *306*, 666–669.
14. Novoselov, K. S.; Geim, A. K.; Morozov, S. V.; Jiang, D.; Katsnelson, M. I.; Dubonos, S. V. *Nature* **2005**, *438*, 197–200.
15. Shedin, F.; Geim, A. K.; Morozov, S. V.; Hill, E. W.; Blake, P.; Novoselov, K. S. *Nat. Mater.* **2007**, *6*, 652–655.

16. Flores, M. Z. S.; Autreto, P. A. S.; Legoas, S. B.; Galvao, D. S. *Nanotechnology* **2009**, *20*, 465704.
17. Sofo, J. O.; Chaudhari, A. S.; Barber, G. D. *Phys. Rev. B* **2007**, *75*, 153401.
18. Leenaerts, O.; Partoens, B.; Peeters, F. M. *Phys. Rev. B* **2009**, *80*, 245422.
19. Lu, N.; Li, Z.; Yang, J. *J. Phys. Chem. C* **2009**, *113*, 16741–16746.
20. Cheng, S.-H.; Zuo, K.; Okino, F.; Gutierrez, H. R.; Gupta, A.; Shen, N.; Eklund, P. C.; Sofo, J. O.; Zhu, J. *Phys. Rev. B* **2010**, *81*, 205435.
21. Fuhrer, M. S.; Lau, C. N.; MacDonald, A. H. *MRS Bull.* **2010**, *35*, 289–295.
22. Wallace, G. G.; Chen, J.; Li, D.; Moulton, S. E.; Razal, J. M. *J. Mater. Chem.* **2010**, *20*, 3553–3562.
23. Stoller, M. D.; Park, S.; Zhu, Y.; An, J.; Ruoff, R. S. *Nano Lett.* **2008**, *8* (10), 3498–3502.
24. Zhao, X.; Tian, H.; Zhu, M.; Tian, K.; Wang, J. J.; Kang, F.; Outlaw, R. A. *J. Power Sources* **2009**, *194*, 1208–1212.
25. Wu, Q.; Xu, Y.; Yao, Z.; Liu, A.; Shi, G. *ACS Nano* **2010**, *4* (4), 1963–1970.
26. Zhang, K.; Zhang, L. L.; Zhao, X. S.; Wu *J. Chem. Mater.* **2010**, *22*, 1392–1401.
27. Mori, T.; Kikuzawa, Y.; Takeuchi, H. *Org. Electron.* **2008**, *9*, 328–332.
28. Verma, V. P.; Das, S.; Lahiri, I.; Choi, W. *Appl. Phys. Lett.* **2010**, *96*, 203108.
29. Yu, L.; YanFang, C.; YiYu, F.; ShengLing, Z.; Peng, L.; XiaoYan, Y.; Wei, F. *Sci. China* **2010**, *53* (5), 1225–1233.
30. Kim, K. S.; Ryu, J. H.; Lee, C. S.; Jang, J.; Park, K. C. *J. Mater. Electron.* **2009**, *20*, S120–S124.
31. Yazami, R.; Hamwi, A.; Guerin, K.; Ozawa, Y.; Dubois, M.; Giraudet, J.; Masin, F. *Electrochem. Comm.* **2007**, *9*, 1850–1855.
32. Nakajima, T. J. *Fluorine Chem.* **2007**, *128*, 277–284.
33. Nakajima, T. *Solid State Sci.* **2007**, *9*, 777–784.
34. Matsuo, Y In *Fluorinated Materials for Energy Conversion*; Nakajima, T., Groult, H., Eds.; Elsevier: Amsterdam, 2005; Vol. 1, pp 397−417
35. Anand, S. P.; Quarterman, L. A.; Christian, P. A.; Hyman, H. H.; Filler, R. *J. Org. Chem.* **1975**, *40* (25), 3796–3797.
36. Tunistra, F.; Koeng, J. L. *J. Chem. Phys.* **1970**, *53* (3), 1126–1130.
37. Ferrari, A. C.; Robertson, J. *Phys. Rev. B* **2000**, *61* (20), 14095–14107.
38. Ferrari, A. C.; Robertson, J. *Philos. Trans. R. Soc., A* **2004**, *362*, 2477–2512.
39. Li, X.; Zhu, Y.; Weiwei, C.; Borysiak, M.; Han, B.; Chen, D.; Piner, R. D.; Colombo, L.; Ruoff, R. S.; et al. *Nano Lett.* **2009**, *9* (12), 4359–4363.
40. Osuna, S.; Torrent-Sucarrat, M.; Solà, M.; Geerlings, P.; Ewels, C. P.; Lier, G. V. *J. Phys. Chem. C* **2010**, *114*, 3340–3345.
41. Elias, D. C.; Nair, R. R.; Mohiuddin, T. M. G.; Morozov, S. V.; Blake, P.; Halsall, M. P.; Ferrri, A. C.; Boukhvalov, D. W.; Katsnelson, M. I.; Geim, A. K.; Novoselov, K. S. *Science* **2009**, *323*, 610–613.
42. Becke, A. *J. Chem. Phys.* **1993**, *98*, 5648.
43. Lee, C; Yang, W; Parr, R G. *Phys. Rev. B* **1988**, *37*, 785.
44. Frisch, MJ. Gaussian 09.
45. Ewels, C. P.; Lier, G. V.; Charlier, J.-C.; Heggie, M. I.; Briddon, P. R. *Phys. Rev. Lett.* **2006**, *96*, 216103.

46. Ryu, S.; Han, M. Y.; Maultzsch, J.; Heinz, T. F.; Kim, P.; Steigerwald, M. L.; Brus, L. E. *Nano Lett.* **2008**, *8* (12), 4597–4602.
47. Luo, Z.; Yu, T.; Kim, K.; Ni, Z.; You, Y.; Lim, S.; Shen, Z. *ACS Nano* **2009**, *3* (7), 1781–1788.
48. Openov, L. A.; Podlivaev, A. I. *Technol. Phys. Lett.* **2010**, *36* (1), 31–33.
49. Stankovich, S.; Dikin, D. A.; Piner, R. D.; Kohlhaas, K. A.; Kleinhammes, A.; Jia, Y.; Wu, Y.; Nguyen, S. T.; Ruoff, R. S. *Carbon* **2007**, *45*, 1558–1565.
50. Robinson, J. T.; Perkings, F. K.; Snow, E. S.; Wei, Z.; Sheehan, P. E. *Nano Lett.* **2008**, *8* (10), 3137–3140.

Downloaded by UNIV OF GUELPH LIBRARY on June 5, 2012 | http://pubs.acs.org
Publication Date (Web): April 27, 2011 | doi: 10.1021/bk-2011-1064.ch003

Chapter 3

Association of Representative Amides and Aminoalcohols with SWCNT As Revealed by ^{1}H NMR

Donna J. Nelson,* Christopher N. Brammer,
Panneer Selvam Nagarajan, and Paramasivan T. Perumal

Department of Chemistry and Biochemistry, University of Oklahoma,
Norman, Oklahoma 73019
***djnelson@ou.edu**

Select amides have been widely used to suspend nanoarchitectures in organic solvents. In order to determine factors enabling these suspensions, interactions of single walled carbon nanotubes (SWCNTs) with representative amides, aminoalcohols, an aminoketone, and an oxime were examined. ^{1}H NMR spectra gave evidence for two types of associations, formed after evaporation of the reaction mixture to either a concentrated solution or a wet paste, and followed by sonication in NMR solvent. NMR spectra after evaporation to concentrated solution show broadening and small downfield changes, suggesting weak interactions. Evaporation to a wet paste causes larger spectral changes, predominantly in aldehydic and a proton signals. These are often 10 times those in concentrated solution, especially when R has small steric requirements, which suggests a stronger interaction with SWCNTs under wet paste conditions. The magnitude of ^{1}H NMR chemical shift change upon SWCNT:organonitrogen complex formation represents the strength of the association. Magnitudes of changes in NMR signals of different protons in the organonitrogen reveal which protons are in close proximity to SWCNTs. Results reveal that (1) in amides and aminoketones, SWCNT association with carbonyls is stronger than with nitrogen, (2) in aminoalcohols, SWCNT association with nitrogen is stronger than with oxygen, and (3) protons bonded to heteroatoms have greater changes in their chemical shifts than those bonded to carbons. Changes (broadening and downfield shifts) in ^{1}H NMR signals of these compounds, which accompany SWCNT association, depend upon (1) degree of evaporation of residual amide and organic solvent, (2) organic and NMR solvent combination, (3) type of proton in R, (4) proximity effects to the carbonyl (R-CO versus NR_2), (5) steric requirements of R, (6) electronic effects of alkyls, and (7) effects of tethering two ends of a molecule. These data have important uses in SWCNT solvation, adsorption of molecules, and characterization by NMR.

Downloaded by UNIV OF GUELPH LIBRARY on June 5, 2012 | http://pubs.acs.org
Publication Date (Web): April 27, 2011 | doi: 10.1021/bk-2011-1064.ch003

Recently, carbon nanomaterials such as nanotubes and fullerenes were utilized to construct novel energy conversion architectures due to their high solar energy conversion efficiency (*1*). Especially single-walled carbon nanotubes (SWCNTs) have recently gained considerable attention due to their unusual semiconducting and metallic character (*2*). Extraordinary optical and electronic properties of SWCNT make it is a promising platforms for photovoltaic devices (*3*). Extended π-electron conjugation of SWCNT foster it act as good electron acceptors. Combining these innovative materials with photosensitive electron donors (dyes) would attain high efficient photochemical solar cells or dye-sensitized solar cells (DSSC). Photo induced electron transfer between excited electron donor (dyes) (*4*) and SWCNT has been successfully implemented in dye-sensitized solar cells. In a typical dye-sensitized solar cell inorganic complex, organic or mixed organic/inorganic materials were preferred for dyes (*4*). Recent scanning electron microscopy (SEM) analyses reveal that in combined photo energy harvesting materials SWCNT were not uniformly distributed or aligned and some portions of electron donating material (organic or inorganic or mixed) were not attached to SWCNT and contaminated with residual metal impurities (*5*). Unevenly distributed or aligned or not properly combined nanomaterials and the impurities present will reduce the efficiency of solar energy conversion devices. The molecular organization between photo induced donor and SWCNT, and purity of SWCNT were found to be the constrained gaps for the construction of photochemical cells with improved performance.

Due to strong van der Waals interactions between SWCNT sidewalls, generally they exist as bundles (*6*), so a key challenge for exploiting SWCNTs widely is overcoming their nonpolar nature, which fosters a solvation problem and restricts their stable dispersion, solubilization, and purification (*7–9*). Different and improved dispersal techniques are needed in order to increase SWCNT solubility, take advantage to attain higher purities (*9d,f*), and enable their alignment for molecular device development (*10*).

Much recent effort has been committed to improving SWCNT solubility by using ionic (*11a,c*) or nonionic surfactants (*11b,c*), frequently combined with covalent (*12*) or noncovalent (*13*) side-wall functionalization. However, many of these procedures (*11–13*) can disrupt the electronic structure of SWCNTs

Downloaded by UNIV OF GUELPH LIBRARY on June 5, 2012 | http://pubs.acs.org
Publication Date (Web): April 27, 2011 | doi: 10.1021/bk-2011-1064.ch003

and cause problems in their subsequent applications. A better understanding of the interactions of molecules with SWCNT surfaces would benefit some important applications of SWCNTs, such as molecular sensing (*14*), which involve adsorption of molecules onto SWCNT surfaces, as well as their dispersal in solvent.

SWCNTs display exceptional adsorption properties because of their high surface area to volume ratio (*15*). Recent adsorption studies of SWCNTs with molecules, such as amines (*16*), aminoacids (*17*), ketones (*18*), amides (*19*), CO_2 (*20*), NH_3 (*15*), hydroxyl (*21*), and water (*22*), show that the functionalities in those molecules have a great tendency to associate with SWCNTs. Understanding associations with these simple groups will help understand and design interactions with other molecules containing such functional groups, such as surfactants, which disperse SWCNTs in solvent by forming a lamellar pattern on their surfaces (*23*). Larger molecules such as DNA (*24*) and polymers (*25*) are reported to interact with SWCNT either by wrapping (*24*, *25b−d*) or linear associations (*25*).

The organic solvents *N*,*N*-dimethylformamide (DMF) (*26a−e*) and 1-methyl-2-pyrrolidone (NMP) (*26*) are known to increase the solubility of SWCNTs, and both have been used as solvent in ultrasonic debundling of SWCNTs (*26*). Recently, the effect of SWCNT association upon amides was investigated (*8b*), in order to ascertain the molecular characteristics giving rise to the unusual capability of amides, especially DMF, to solvate SWCNTs. It is desirable to compare and contrast these characteristics of DMF versus those of NMP and other related organonitrogen compounds. Recent studies reveal that the solvating capability of NMP is not restricted to SWCNTs, but that solubilities of nanomaterials in general are increased in the presence of NMP (*26b,g,h*) as was the case for DMF (*26a−e*). Therefore, identifying and comparing such molecular characteristics of both NMP and related organonitrogen compounds, which facilitate complexing with and solvating SWCNTs, could be applicable to nanomaterials generally. However, the role of NMP has not been fully investigated in any of the above systems (*26*). The unusual solvating capabilities of DMF and other amides upon SWCNTs were explored (*8b*) in two physical states of samples; the organic solvent and amide were evaporated from the reaction mixture to give either a concentrated solution or a wet paste, followed by sonication in an NMR solvent. NMR value differences between pure amide and wet past sample were up to 10 times those observed in concentrated solution samples, suggesting that the wet paste sample preparation method effects a stronger SWCNT:amide association, which would be more conducive to solvation (*8b*).

A major deterrent to the use of NMR to analyze SWCNTs has been peak broadening, which most likely arises from residual paramagnetic metal catalysts used in the SWCNT synthesis (*13b*). However, NMR can be a powerful tool in SWCNT characterization, with advantages, such as that over Raman spectroscopy for quantifying the degree of SWCNT functionalization (*27*). Nevertheless, there are reports of achieving narrower signals in liquid phase NMR spectra (*8b*, *16c*). Therefore, NMR is a promising tool, undergoing further developments for SWCNT characterization.

Downloaded by UNIV OF GUELPH LIBRARY on June 5, 2012 | http://pubs.acs.org
Publication Date (Web): April 27, 2011 | doi: 10.1021/bk-2011-1064.ch003

Accordingly, we report the use of ^{1}H NMR spectroscopy to explore the effect of SWCNTs upon NMP and related organonitrogen compounds. The degree and type of SWCNT complexation was measured by comparing NMR spectra of NMP and related organonitrogen compounds in the presence and absence of SWCNTs. The wet paste conditions and methodology, which were shown to afford the strongest interactions between SWCNTs and amides (*8b*), are used in the studies reported herein.

Results and Discussion

Representative organonitrogen compounds **1–5** in this study are shown in Figure 1. SWCNTs associated with these organonitrogens can be compared among themselves in order to explore differences in the effects of a range of structural variations. (1) Compounds **1** and **2c** are isoatomic in C, O, and N; their comparison gives the effects of tethering together the ends of **2c**. (2) Increasing the steric requirements of groups bonded to C=O in compounds **2** has been reported (*8b*), but some pertinent data and information are reproduced here for convenience. (3) Comparing compounds **2b** and **3** contrasts the effects of having the carbonyl bonded to nitrogen versus isolated from nitrogen by 3 methylene units. (4) The series represented by **4** explores the effects of increasing steric requirements of groups bonded to nitrogen. (5) Comparing compounds **4** and **5** gives the effects of having hydroxyl isolated from nitrogen by 2 methylene units versus bonded to nitrogen. NMR spectra of organonitrogen compounds **1** – **5** in NMR solvent, with and without SWCNTs, enables exploring the above effects upon and trends in these associations, SWCNT:**1** – **5**. These NMR data are shown in Table 1.

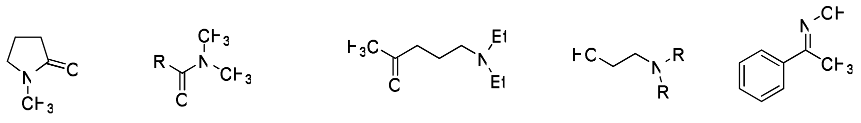

1 **2** **3** **4** **5**

R = H (**a**), Me (**b**), Et (**c**),
i-Pr (**d**), *t*-Bu (**e**), Ph (**f**)

R = H (**a**), Me (**b**), Et (**c**)

Figure 1. Representative organonitrogen compounds used in SWCNT associations: 1-methyl-2-pyrrolidone (NMP) ***1****; N,N-dimethylamides* ***2****, in which R = H (**2a**), Me (**2b**), Et (**2c**), i-Pr (**2d**), t-Bu (**2e**), Ph (**2f**); 5-diethylamino-2-pentanone* ***3****; 2-aminoethanols* ***4*** *in which R = H (**4a**), Me (**4b**), Et (**4c**); acetophenone oxime* ***5****.*

Forming SWCNT:1 – 5

SWCNT:**1 – 5** associations were effected by sonicating the SWCNT and amide in an organic solvent (toluene), and reaction mixtures were then evaporated to achieve each of two solvent conditions, concentrated solution and wet paste. Each resulting concentrated solution or wet paste sample was sonicated in an NMR solvent ($CDCl_3$), and the intermolecular interactions were then measured by using ^1H NMR; results are detailed below. Changes (broadening and downfield shifts) in ^1H NMR signals of **1**, which accompany SWCNT:**1** association, are dependent upon (1) degree of residual amide and organic solvent evaporation, (2) solvent combination, (3) type of proton within R (aldehydic, α, etc.), (4) proximity effects to the carbonyl (R versus NMe_2), and (5) steric requirements of R.

Some potential complications to the ^1H NMR study of SWCNT:**1** – **5)** interactions were (1) accidental coincidence of NMR signals for any of the following: free organonitrogen **1 – 5**, reaction solvent, and NMR solvent, (2) the small size of the NMR signals, which results from the small amount of organonitrogen associated with SWCNT, relative to the signals for other species present, and (3) the simultaneous effects of different types of association upon NMR shifts. Most of these were addressed by judicious choice of complexing agent, reaction solvent, and NMR solvent; others were addressed by appropriate reaction design.

For example, suspending SWCNTs in only the complexing agent **1** would cause the signal for free **1** to swamp the signal for SWCNT:**1**, which would preclude differentiating between NMR signals of free versus associated **1**. This was particularly important, because differentiating between them was essential to appropriate analysis. Consequently, in order to explore the nature of SWCNT:**1 – 5** associations, two procedures were used to produce the concentrated SWCNT:**1 – 5** product, which was then suspended in an NMR solvent. Then comparing the NMR of free versus associated **1 – 5** measured the effects upon NMR shift, which were caused by association. These methods were developed in order to minimize residual amide and organic solvent in the sample, in order to minimize their complicating NMR signals and to expose maximally the SWCNT:**1 – 5** NMR signals.

Downloaded by UNIV OF GUELPH LIBRARY on June 5, 2012 | http://pubs.acs.org
Publication Date (Web): April 27, 2011 | doi: 10.1021/bk-2011-1064.ch003

Forming Concentrated Solution of SWCNT:Organonitrogens (SWCNT:1 – 5)

SWCNTs and a small amount of organonitrogen **1 – 5** were suspended in a small amount of solvent (toluene) by sonication, in order to achieve SWCNT debundling, dispersion, and association with **1 – 5**. The SWCNT:**1 – 5** solution was allowed to stand at room temperature, evaporating organic solvent and some excess **1 – 5**; a small aliquot of the resulting mixture was sonicated in NMR solvent ($CDCl_3$) for analysis. MR data for SWCNT:**1** concentrated solution samples are compared to those for organonitrogen **1 – 5** in Table 1. The NMR of each SWCNT:amide (SWCNT:**1**) showed that proton peaks due to methyls on nitrogen, which are typically sharp and distinct in the free amide **1**, generally broaden and coalesce slightly. However, association with SWCNTs also has a relatively small effect upon NMR values (~≤ 0.1 ppm) of all protons, usually a small downfield shift.

Table 1. ^{1}H NMR Chemical Shift Values for Organonitrogens 1 – 5 in the Absence of SWCNTs and in Their Presence as a Concentrated Solution

complexing agent	SWCNT brand	chemical shift (ppm)											
		protons near C=O or COH						NR_2 protons				OH protons	
		α	Δα	β	Δβ	γ	Δγ	amino/α′	Δα′	β′	Δβ′	α	Δα
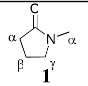 **1**	none	2.28		1.94		3.30		2.76					
	SWeNT	–		–		–		–					
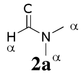 **2a**	none	7.98						2.88					
	SWeNT	7.95	-0.03					2.85	-0.03				
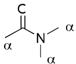 **2b**	none	2.02						2.92					
	SWeNT	2.06	0.04					2.96	0.04				
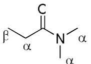 **2c**	none	2.24		1.03				2.88					
	SWeNT	2.35	0.11	1.10	0.07			2.99	0.11				
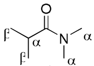 **2d**	none	2.79		1.08				2.97					
	SWeNT	2.86	0.07	1.15	0.07			3.04	0.07				
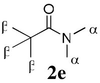 **2e**	none			1.28				3.04					
	SWeNT			1.30	0.02			3.05	0.01				
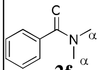 **2f**	none			7.44				3.08					
	SWeNT			7.46	0.02			3.11	0.03				
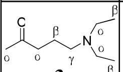 **3**	none	2.08		1.65		2.39		2.43		0.93			
	SWeNT	–		–		–		–		–			
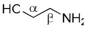 **4a**	none	3.48		2.70				2.55				2.55	
	SWeNT	3.65	0.17	2.89	0.19			5.45	2.90			5.45	2.90
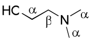 **4b**	none	3.53		2.39				2.19				3.53	
	SWeNT	–		–				–				–	
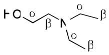 **4c**	none	3.48		2.53				2.50		0.97		3.20	
	SWeNT	3.57	0.09	2.59	0.06			2.59	0.09	1.05	0.08	4.78	1.58
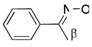 **5**	none									2.29		7.00[a]	
	SWeNT									2.32	0.03	7.35	0.35

[a] Ref. 28a.

Downloaded by UNIV OF GUELPH LIBRARY on June 5, 2012 | http://pubs.acs.org
Publication Date (Web): April 27, 2011 | doi: 10.1021/bk-2011-1064.ch003

Downloaded by UNIV OF GUELPH LIBRARY on June 5, 2012 | http://pubs.acs.org
Publication Date (Web): April 27, 2011 | doi: 10.1021/bk-2011-1064.ch003

Forming Wet Paste of SWCNT:Organonitrogens (SWCNT:1 – 5)

The remaining solution of SWCNTs, complexing agent, and organic solvent, from the above procedure, was allowed to evaporate for 3-5 more days at ambient temperature, giving a wet paste. A small amount of the wet paste sample was then dissolved by sonication in the NMR solvent $CDCl_3$, and the proton chemical shift values (ppm) were then measured by using ^1H NMR. The results are compiled in Table 2. The NMR spectra of compound **1** are shown in Figure 2 as representative examples of the NMR spectra of compounds **1 – 5**. NMR data for SWCNT:**1** – **5** wet paste samples are compared to NMR data for free organonitrogen compounds **1** – **5** in Table 1. The near-complete removal of solvent and free complexing agent from SWCNT:**1** – **5** samples simplify their NMR spectra, but signals for SWCNT:**1 – 5** are nevertheless small and somewhat obscure. Similarly to the previous report (*8b*), changes (broadening and downfield shifts) in ^1H NMR signals of the organonitrogen compounds, which accompany SWCNT:organonitrogen association, were found to be dependent upon (1) type of proton within R (α, β, etc.), (2) proximity to the carbonyl (R-CO versus NR_2), (3) steric effects of alkyl substituents, (4) electronic effects of alkyl substituents, and (5) tethering effects.

Effect of NMP Concentration upon NMR Chemical Shift

Differentiating among and assigning NMR signals of free, unassociated organonitrogen compounds versus those associated with SWCNTs was essential to this study. NMR signal shifts of amides are dependent upon their concentrations (*26*). A threshold concentration of NMP in NMR solvent, below which a constant NMR signal shift would be obtained, was previously established (*8b*). This concentration of 1:40 (v:v) was used in taking NMR spectra of **1– 5,** and a more dilute concentration (1:150,000) was used for SWCNT:**1 – 5**.

*A. Compounds **1** and **2**: Steric Effects and Cyclization*

Compounds **1** and **2c** are isoatomic in C, H, and O; their structural difference is that the two ends of **1** forms **2c** are tethered, as shown in Figure 3. The difference in magnitudes of downfield NMR shift changes of these compounds, upon association with SWCNT, explores the differences in their interactions with SWCNTs and the origins for the differences. Therefore, ^1H NMR signals for organonitrogens **1** and **2** were measured in the absence and in the presence of HiPco or SWeNT brand SWCNT. Downfield chemical shift changes upon association were calculated and compared. Values for **2a, 2b, 2d, 2e** and **2f** were used for comparison when appropriate.

NMR chemical shift values of protons α to carbonyl in SWCNT:**1** are shifted downfield 0.08 ppm (2.28 – 2.36 ppm) for HiPco, and 0.09 ppm (2.28 – 2.37 ppm) for SWeNT SWCNTs. In SWCNT:**2c**, NMR signals for protons α to carbonyl are shifted downfield 0.08 ppm (2.24 – 2.32 ppm) for HiPco and 0.10 ppm (2.24 – 2.34 ppm) for SWeNT SWCNTs. In SWCNT:**2d,** NMR signals of protons α to carbonyl are shifted downfield 0.01 ppm (2.79 – 2.80 ppm) for HiPco and 0.06 ppm (2.79 – 2.85 ppm) for SWeNT. All of these chemical shift changes upon complexation are rather small.

Table 2. ^{1}H NMR Chemical Shift Values for Organonitrogens 1 – 5 in the Absence of SWCNTs and in Their Presence as a Wet Paste

complexing agent	SWCNT brand	chemical shift (ppm)											
		protons near C=O or COH						NR$_2$ protons				OH protons	
		α	Δα	β	Δβ	γ	Δγ	amino/α′	Δα′	β′	Δβ′	α	Δα
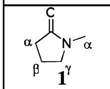 **1**	none	2.28		1.94		3.30		2.76					
	HiPco	2.36	0.08	2.01	0.07	3.37	0.07	2.83	0.07				
	SWeNT	2.37	0.09	2.01	0.07	3.37	0.07	2.84	0.08				
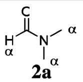 **2a**	none	7.98						2.88					
	HiPco	–						–					
	SWeNT	8.28	0.30					3.08	0.20				
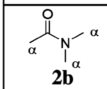 **2b**	none	2.02						2.92					
	HiPco	2.08	0.06					2.97	0.05				
	SWeNT	2.15	0.13					3.03	0.11				
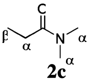 **2c**	none	2.24		1.03				2.88					
	HiPco	2.32	0.08	1.13	0.10			2.96	0.08				
	SWeNT	2.34	0.10	1.26	0.23			2.90	0.02				
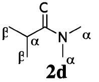 **2d**	none	2.79		1.08				2.97					
	HiPco	2.80	0.01	1.10	0.02			2.99	0.02				
	SWeNT	2.85	0.06	1.28	0.20			3.07	0.10				
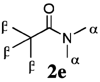 **2e**	none			1.28				3.04					
	HiPco			–				–					
	SWeNT			1.32	0.04			3.08	0.04				
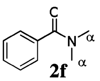 **2f**	none			7.44				3.08					
	HiPco			–				–					
	SWeNT			7.44	0.00			3.09	0.01				
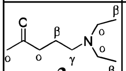 **3**	none	2.08		1.65		2.39		2.43		0.93			
	HiPco	2.55	0.47	1.89	0.24	2.69	0.30	2.81	0.38	1.20	0.27		
	SWeNT	2.16	0.08	1.73	0.08	2.41	0.02	2.50	0.07	1.01	0.08		
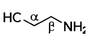 **4a**	none	3.48		2.70				2.55				2.55	
	HiPco	3.60	0.12	2.85	0.15			4.46	1.91			4.46	1.91
	SWeNT	3.65	0.17	2.89	0.19			6.18	3.63			6.18	3.63
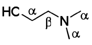 **4b**	none	3.53		2.39				2.19				3.53	
	HiPco	3.64	0.11	2.55	0.16			2.34	0.15			4.26	0.73
	SWeNT	4.16	0.63	3.48	1.09			3.33	1.14			b	–
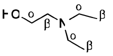 **4c**	none	3.48		2.53				2.50		0.97		3.20	
	HiPco	3.76	0.28	2.88	0.35			2.86	0.36	1.23	0.26	7.16	3.96
	SWeNT	4.12	0.64	3.40	0.87			3.38	0.88	1.35	0.38	b	–
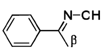 **5**	none									2.29		7.00[a]	
	HiPco									2.28	-0.01	b	–
	SWeNT									2.66	0.37	7.90	0.90

[a]Ref. 28a. [b]No signal observed.

The protons β and γ to carbonyl in SWCNT:**1** are each shifted downfield 0.07 ppm (1.94 – 2.01 ppm, 3.30 – 3.37 ppm) for both HiPco and SWeNT, and NMe

Downloaded by UNIV OF GUELPH LIBRARY on June 5, 2012 | http://pubs.acs.org
Publication Date (Web): April 27, 2011 | doi: 10.1021/bk-2011-1064.ch003

protons are shifted downfield 0.07 ppm (2.76 – 2.83 ppm) for HiPco and 0.08 ppm (2.76 – 2.84 ppm) for SWeNT brands. The β protons of SWCNT:**2c** are shifted downfield 0.10 ppm (1.03 – 1.13 ppm) for HiPco and 0.23 ppm (1.03 – 1.26 ppm) for SWeNT brands, and NMe_2 protons are shifted downfield 0.08 ppm for HiPco and 0.02 ppm for SWeNT respectively. The β protons of SWCNT:**2d** are shifted downfield 0.02 ppm (1.08 – 1.10 ppm) for HiPco and 0.20 ppm (1.08 – 1.28 ppm) for SWeNT samples, and NMe_2 protons are shifted downfield 0.02 ppm (2.97 – 2.99) for HiPco and 0.10 ppm (2.97 – 3.07 ppm) for SWeNT SWCNTs. The β protons in **2c** and **2d** show more change in chemical shift upon association of **2c** and **2d** with SWCNTs than do the other protons in **2c** and **2d**, especially when using the SWeNT brand.

Downloaded by UNIV OF GUELPH LIBRARY on June 5, 2012 | http://pubs.acs.org
Publication Date (Web): April 27, 2011 | doi: 10.1021/bk-2011-1064.ch003

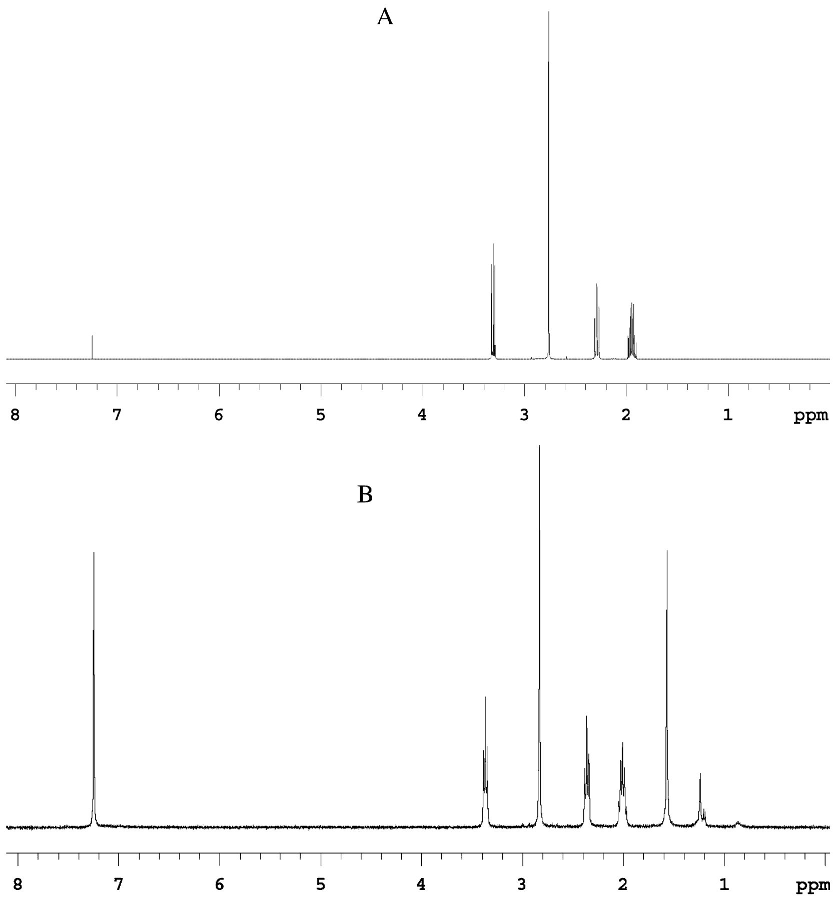

Downloaded by UNIV OF GUELPH LIBRARY on June 5, 2012 | http://pubs.acs.org
Publication Date (Web): April 27, 2011 | doi: 10.1021/bk-2011-1064.ch003

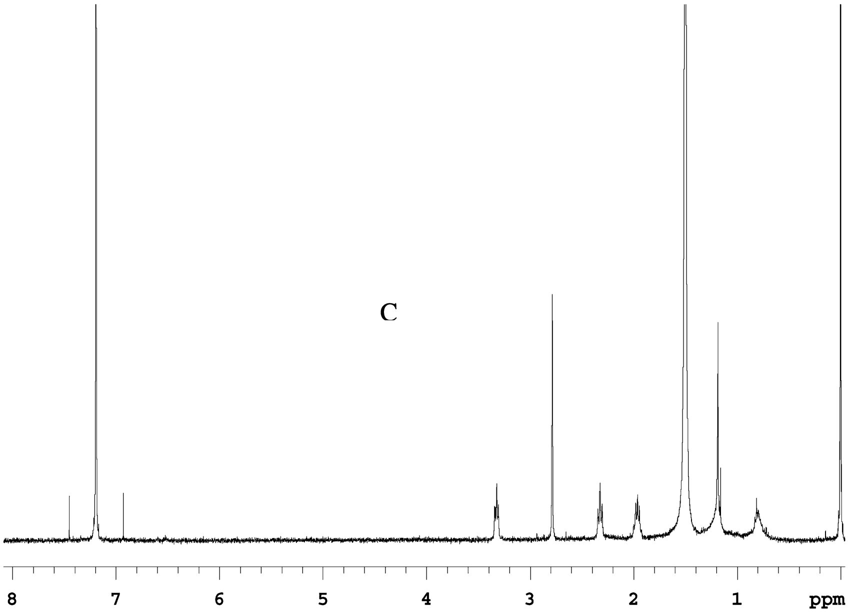

*Figure 2. ^{1}H NMR spectra of (A) 1-methyl-2-pyrrolidone NMP **1** in CDCl$_3$, (B) HiPco SWCNT:**1** wet paste sample using toluene and CDCl$_3$ solvents, and (C) SWeNT SWCNT:**1** wet paste sample using toluene and CDCl$_3$ solvents.*

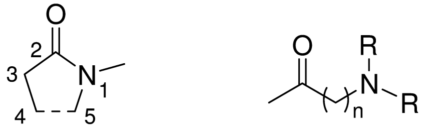

1: 4,5 bonded
2c: 4,5 nonbonded

2b: n = 0, R = Me
3: n = 3, R = Et

*Figure 3. Structural similarities in tethering (**1** vs **2c**) and functional group proximity (**2b** vs **3**).*

Chemical shift changes, for β protons in **1**, **2c,** and **2d** upon association with SWCNTs, are 0.07 ppm, 0.10 ppm and 0.02 ppm respectively for the HiPco brand, and 0.07 ppm, 0.23 ppm, and 0.20 ppm respectively for the SWeNT brand. The general trend for chemical shift upon SWCNT association is in the order **1** < **2d** < **2c**. This indicates that the heteroatom corresponding to the β protons of **1** associates less than those of **2c** and **2d** with SWCNTs, suggesting that the conformational freedom of **2c** and **2d** enables them to be more accommodating sterically and enabling a stronger association than in cyclic, rigid **1**. Therefore, in compounds **2c** and **2d** the heteroatoms corresponding to the β protons can more effectively associate with SWCNTs than that of **1**.

In SWCNT:**2** wet paste samples, downfield changes (Table 1) in amide NMR values are greatest for aldehydic protons (**1a**, R= H, 0.30 ppm), compared to protons α to C=O (**2b**, R=Me, 0.13 ppm), protons β to C=O (**2c**, R=Et, 0.23 ppm), and NMe_2 protons (**2a**, R=H, 0.20 ppm). This interaction in SWCNT:DMF (**2a**, R = H) was so strong, that the aldehydic proton signal (8.28 ppm, compared to 7.98 ppm for free DMF) broadened sufficiently to obfuscate the NMR chemical shift value. NMR signals for protons in SWCNT:**2b – 2f** (R = Me, Et, *i*-Pr, *t*-Bu, and Ph) were less broadened than those for SWCNT:**2a** (R = H); broadening decreased with increasing steric requirements of R and with increasing distance of the proton from C=O. Downfield changes for protons α to C=O generally show a decreasing trend in the order R = Me (**2b**) > Et (**2c**) > *i*-Pr (**2d**). When there are no α protons, R = *t*-Bu (**2e**) or Ph (**2f**), the β and phenyl protons are changed only slightly upon association of the molecule with SWCNTs. NMe_2 signals of SWCNT:amides with larger NMR value changes (≥ ~0.10 ppm) coalesced into one broader peak. Relative to the unassociated amide **2**, most signals of NMe_2 in SWCNT:**2** are moved downfield by ≤ ~0.10 ppm.

B. Compounds ***1*** *and* ***3****: Cyclic versus Acyclic*

Comparing **1** and **3** also explores the effects of SWCNT:organonitrogen formation upon the three methylene units of these cyclic and acyclic analogs. In Table 1, ^1H NMR chemical shift changes of free versus SWCNT-associated **3** are compared versus those for compound **1** above. NMR signals of SWCNT:**3** protons α to carbonyl are shifted downfield 0.47 ppm for HiPco and 0.08 ppm for SWeNT brands, protons β to carbonyl are shifted 0.24 ppm for HiPco and 0.08 ppm for SWeNT. Protons γ to carbonyl are shifted 0.30 ppm for HiPco and 0.02 ppm for SWeNT SWCNT. Similarly, protons α′ to nitrogen are shifted 0.38 ppm for HiPco and 0.07 ppm for SWeNT, and β′ protons are shifted 0.27 ppm for HiPco and 0.08 ppm for SWeNT SWCNT. Position labels α, β, γ, α′, β′ in **3** are identified in Table 1.

The ^1H NMR chemical shift change differences in compound **1** upon association with SWCNTs of either brand, are downfield ~ 0.07 – 0.09 ppm. Association with SWeNT SWCNTs produces a similarly small downfield shift in compound **3**. These small changes indicate a weak association of **1** and **3** with the SWeNT brand. But greater NMR signal changes for all protons of compound **3** as compared to **1,** upon HiPco SWCNT association, indicates more association with (1) increased separation between the carbonyl and amino functionalities and (2) greater conformational freedom of the acyclic molecule. Thus, association with HiPco SWCNTs effects the greatest change in NMR shifts upon protons α to carbonyl. Again, acyclic **3** has conformational freedom which enables it to be more accommodating sterically and have a stronger association with SWCNTs than **1** does.

Downloaded by UNIV OF GUELPH LIBRARY on June 5, 2012 | http://pubs.acs.org
Publication Date (Web): April 27, 2011 | doi: 10.1021/bk-2011-1064.ch003

Downloaded by UNIV OF GUELPH LIBRARY on June 5, 2012 | http://pubs.acs.org
Publication Date (Web): April 27, 2011 | doi: 10.1021/bk-2011-1064.ch003

*C. Compounds **1**, **2b**, **2c**, and **3**: Carbonyl versus Nitrogen Complexation*

Compounds **2b** and **3** have the same functionalities, but differ in intervening methylene groups (**2b**, n = 0; **3**, n = 3) (Figure 3). Compound **1** is analogous to **2c**, with the ends tethered. These compounds offer the opportunity to compare changes in NMR chemical shifts of protons α to carbonyl versus those α to nitrogen. Upon association with SWCNTs, compounds **1, 2b,** and **2c** show only a marginally greater proton chemical shift change at protons α to carbonyl rather than α to nitrogen. The same trend is observed in compounds **3**, but much larger in magnitude, 0.47 ppm for protons α to carbonyl versus 0.38 ppm for those α to nitrogen. Hence, these results reveal that protons closer to the carbonyl functionality are closer to the major point of association with SWCNTs than those near nitrogen, regardless of SWCNT brand. This supports the hypothesis that amide compounds show a marginally greater association with SWCNTs at the carbonyl end under wet paste conditions, as found previously for simple amides (*8b*). Compound **3** experiences the greatest change upon association with SWCNTs, probably due to its conformational flexibility.

It should be mentioned that compound **3** has no protons β to the carbonyl, which are remote to nitrogen, as do compounds **2c** and **2d**. In compounds **2c** and **2d**, it is these β protons, remote to nitrogen, which show the greatest NMR shift changes.

*D. Compounds **4**: Association with Carbonyl and/or Nitrogen Electron Pairs*

The 2-aminoethanol series **4** (Figure 1) explores steric effects due to increasing substituents in NR_2 (R = H **4a**, Me **4b**, E **4c**). For each, NMR proton shift changes in **4a – c** were measured upon association with SWCNTs. The greatest changes in NMR shifts upon SWCNT association were in hydroxyl and amino protons. The ^1H NMR shift for the hydroxyl functionality in each compound **4** at 1:40 concentration (**4a**, 2.55 ppm; **4b**, 3.53 ppm; **4c**, 3.20 ppm) is comparable to its literature value (*28*) (**4a**, 2.76 ppm; **4b**, 3.67 ppm; **4c**, 3.41 ppm). It should be noted that an alternate literature report (*25a*) for **4c** incorrectly assigns the hydroxyl proton to the spurious signal at 7.35 ppm, which is actually due to the typically-observed slight $CHCl_3$ contamination in $CDCl_3$ NMR solvent. Similarly to the literature reports, NMR spectra of the uncomplexed hydroxyl compounds herein usually do not show a well-defined separate hydroxyl proton signal. One reason for this is because the NMR signals for hydroxyl protons in compounds **4** often accidently coincide with or overlap another signal. For example, in compound **4a,** the signal for OH overlaps that for NH_2, as revealed by the signal integration values.

In compound **4a**, hydroxyl and amino proton signals accidently coincide, and both are shifted downfield upon complexation with SWCNT: 1.91 ppm (2.55 – 4.46 ppm) for HiPco, and 3.63 ppm (2.55 – 6.18 ppm) for SWeNT. The hydroxyl proton signal for neither **4b** nor **4c** associated with SWeNT SWCNT was observed, but they were shifted 0.73 ppm and 3.96 ppm respectively, upon HiPco complexation. The other protons experienced considerably smaller

NMR shift changes, as discussed below. The greater chemical shift changes of heteroatom-bonded protons, is due to these protons being closer to the points of associated with SWCNTs than are those bonded to carbons.

Changes in NMR chemical shifts of the protons α to OH in the presence, versus the absence, of SWCNTs can also be compared to those α to NR_2 (β to OH). This can reveal the relative contributions of lone pairs on O, versus lone pairs on N, to SWCNT:**4** association. Protons α to nitrogen experience greater chemical shift change regardless of substituents on nitrogen and regardless of SWCNT brand, which indicates a stronger SWCNT association with N lone pairs than with O lone pairs. Signals for protons α to hydroxyl in **4a** are shifted downfield 0.12 ppm (3.48 – 3.60 ppm) for HiPco and 0.17 ppm (3.48 – 3.65 ppm) for SWeNT brands; β protons are shifted downfield 0.15 ppm (2.70 – 2.85 ppm) for HiPco and 0.19 ppm (2.70 – 2.89 ppm) for SWeNT. In **4b**, protons α to OH are shifted downfield 0.11 ppm (3.53 – 3.64 ppm) for HiPco and 0.63 ppm (3.53 – 4.16 ppm) for SWeNT; β protons are shifted 0.16 ppm (2.39 – 2.55 ppm) for HiPco and 1.09 ppm (2.39 – 3.48 ppm) for SWeNT. Dimethyl protons in **4b** are shifted 0.15 ppm (2.19 – 2.34 ppm) for HiPco and 1.14 ppm (2.19 – 3.33 ppm) for SWeNT. Protons α to OH in **4c** are shifted downfield 0.28 ppm (3.48 – 3.76 ppm) for HiPco and 0.64 ppm (3.48 – 4.12 ppm) for SWeNT; β protons 0.35 ppm (2.53 – 2.88 ppm) for HiPco and 0.87 ppm (2.53 – 3.40 ppm) for SWeNT. In **4c**, both sets of methylene protons α to N are shifted downfield 0.36 ppm (2.50 – 2.86 ppm) for HiPco and 0.88 ppm (2.50 – 3.38 ppm) for SWeNT and methyl protons are shifted downfield 0.26 ppm (0.97 – 1.23 ppm) for HiPco and 0.38 ppm (0.97 – 1.35 ppm) for SWeNT.

Thus, the trend in NMR chemical shift changes for CH protons in free versus HiPco SWCNT associated with **4a**, **4b**, and **4c** (R = H, Me, and Et respectively) is 0.12 ppm, 0.11 ppm, and 0.28 ppm for α to OH, and 0.15 ppm, 0.16 ppm, and 0.35 ppm for β protons. Similarly, magnitudes of NMR signal changes of SWeNT SWCNT associated with **4** are 0.17 ppm, 0.63 ppm, and 0.64 ppm respectively for protons α to OH, and 0.19 ppm, 1.09 ppm, and 0.87 ppm respectively for β protons. Protons α to NR_2 experience greater chemical shift change than those α to OH, in order to determine the relative degrees of association of the two functionalities. However, the changes in CH protons both near OH and near N are significant, suggesting that both groups are associating with SWCNT, as portrayed in Figure 4.

Downloaded by UNIV OF GUELPH LIBRARY on June 5, 2012 | http://pubs.acs.org
Publication Date (Web): April 27, 2011 | doi: 10.1021/bk-2011-1064.ch003

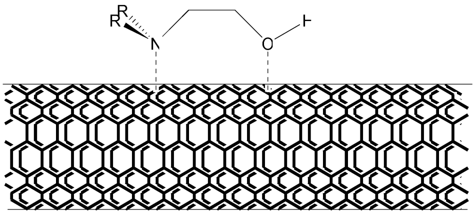

*Figure 4. Association of 2-aminoethanol **4** involving SWCNT with lone pairs of both N and O.*

Changes in chemical shifts of protons bonded to carbon generally increase with increasing size of the group on nitrogen, in the order Et > Me > H. These associations with SWCNTs might be expected to be increasingly hindered by increasing steric requirements, as they were in series **2** , but the opposite is observed in series **4**. Upon association with SWCNTs, greater changes in NMR proton shifts are observed for **4b** and **4c** which have larger substituents than **4a** regardless of SWCNT brand. This indicates that electronic effects of groups on nitrogen are overriding the steric effects of these substituents here, increasing donation of electrons by R to N in the general order Et > Me > H. Note that this is opposite to the results found for amides (*8b*), in which steric effects outweighed electronic effects in these wet paste samples of SWCNT complexes.

Downloaded by UNIV OF GUELPH LIBRARY on June 5, 2012 | http://pubs.acs.org
Publication Date (Web): April 27, 2011 | doi: 10.1021/bk-2011-1064.ch003

*E. Compounds **4c** and **5**: Effects of O to N Proximity*

It was desirable to compare interactions with SWCNTs of both N and O, when they are remote versus directly bonded to each other. NMR data for compound **5,** both SWCNT-associated and unassociated, are shown in Table 1. The NMR signals for **5** after complexation with SWCNTs are somewhat approximate or undetectable, due to signal broadening, as well as accidental coincidence and signal overlapping, as discussed earlier for **4c**. In **5,** the hydroxyl peak overlaps those of the aromatic protons, in both this study and the literature report (*25a*).

In SWCNT:**5**, the proton directly attached to oxygen is shifted 0.90 ppm (7.00 – 7.90 ppm) for SWeNT tubes, but this is not observed with HiPco tubes. The relative magnitudes of chemical shift changes in **4c** versus **5** upon complexation will compare the effects of proximity to O and to N in **4c** versus **5**. However, it is very hard to draw any comparison, because neither SWeNT nor HiPco tubes produced OH signals with both **4c** and **5** upon association. SWCNT:**4c** gave no OH signal with SWeNT tubes, and SWCNT:**5** gave no OH signal with HiPco tubes. Thus, the only comparison available uses observations with different types of SWCNTs; SWCNT:**4c** is with HiPco, while SWCNT:**5** is with SWeNT. Nevertheless, a very rough approximation is possible by considering data from SWCNT:**4a**, which gave a OH signal both with SWeNT and with HiPco tubes. Upon complexation, the OH signal of **4a** was shifted downfield more with SWeNT (3.63 ppm) than HiPco (1.91 ppm) nanotubes. This raises the possibility that complexation with the SWeNT brand may usually effect greater change in the NMR signal shifts, because this is the case with compounds studied herein, except **3**.

Comparing **4c** vs **5**, the chemical shift change for hydroxyl in **4c** (3.96 ppm with HiPco) is greater than that of **5** (0.90 ppm with SWeNTs). The observations from SWCNT:**4a** with both types of tubes indicates that SWeNT effects greater change than HiPco upon complexation. Therefore, because the SWeNT effected change in **5** is so much less than that of HiPco, one could predict that complexation of OH in **5** will be less than in **4c**. This suggests a possibility that heteroatoms separated by 2 methylene units are more associated than when they are directly bonded. However, suggestions from these data are tentative, due to incorporating a approximation, which is based on a correction that has not been shown to be general.

NMR chemical shift changes of protons β to nitrogen in **4c** and **5**, upon association of the molecules with SWCNTs, were compared. Their values of 0.26 ppm and -0.01 ppm respectively for HiPco SWCNTs and 0.38 ppm and 0.37 ppm for SWeNT SWCNT; the NMR chemical shift of protons β to nitrogen marginally less than that of **4c**. It raises the question whether remote heteroatoms (as in **4c**) generally enhance the association of organonitrogen compounds more than directly-bonded ones (as in **5**). One more reason for this is that **4c** has more conformational flexibility than rigid **5**, which allows the organonitrogen to associate effectively. This strengthens the concept that conformational flexibility enhances the association of heteroatoms in the molecule.

SWCNT:1 – 5 Raman Studies

The Raman spectrum of each compound studied herein, SWCNT:**1,** SWCNT:**2**, SWCNT:**3** SWCNT:**4** and SWCNT:**5**, has both D-band and G-band identical in appearance to those of pristine SWCNT (p-SWCNT). They evidence no covalent bond formation to SWCNT and support the concept that the interaction between SWCNTs and complexing agents **1** – **5** herein are associations, similar to those reported previously (*8b*, *13a*).

Association

The previous report (*8b*) on the effect of SWCNT association upon representative dimethylamides **2**, (R = H (**a**), Me (**b**), Et (**c**), *i*-Pr (**d**), *t*-Bu (**e**), and Ph (**f**)) indicates that chemical shift change is a measure of degree of adsorption. A stronger association with SWCNTs produces a larger NMR chemical shift change; a small change indicates weak association with SWCNTs. Raman spectral analysis of the SWCNT:complexing agent reveals that there is no bond formation, which confirms the interaction between these two is purely association.

The proton chemical shift change upon association of compounds **2b** and **2c** with SWCNTs is larger for protons β to carbonyl than in compound **1**, indicating a greater degree of association with SWCNTs. This suggests that molecules with greater conformational freedom generally associate more strongly with SWCNTs. Another example of this can be seen by comparing the proton shift changes of compounds **1** versus **3**, which has more conformational flexibility; the greater change in **3** upon association reveals that the effect of separation by a long chain between the functionalities permits greater functional group association with SWCNTs.

In compound **4**, protons bonded to the heteroatoms show a greater change than other carbon bonded protons. This is because they are closer to the heteroatoms, which are the points at which the association occurs. It is possible to determine if the association involves only one region of a molecule by examining relative magnitudes of NMR chemical shift changes for different protons in a molecule upon SWCNT association. SWCNT:**4a**, SWCNT:**4b**, and SWCNT:**4c** show greater change in shifts of protons α to the amino group than those α to

Downloaded by UNIV OF GUELPH LIBRARY on June 5, 2012 | http://pubs.acs.org
Publication Date (Web): April 27, 2011 | doi: 10.1021/bk-2011-1064.ch003

the alcohol functionality. This indicates that 2-aminoalcohols **4** form stronger associations at nitrogen than at oxygen. However, in SWCNT:**4a** the changes in the chemical shifts of the protons α to nitrogen are only marginally greater than of those α to oxygen. Increasing the size of R on nitrogen in **4** increases its association. This is because increasing the size of an alkyl group on N has a significant inductive effect; it increases the availability of the nonbonding pair on N and outweighing the steric effect.

It is these associations which enable these compounds to disperse SWCNTs and effect SWCNT debundling and dispersion.

Effecting Dispersion

Recent studies of the degree of a compound's association with SWCNTs conclude that it directly relates to the degree of SWCNT dispersion (*8b*, *29*). Forming stronger associations of compounds **1** – **5** with SWCNTs is accompanied by greater NMR value changes, which are caused by an increased SWCNT:organonitrogen interaction. Therefore, the magnitude of change in an NMR spectrum of a compound, after its association with SWCNTs, also helps predict its capability to disperse SWCNTs and effect SWCNT debundling. Thus, association of SWCNTs with the carbonyl end in **1, 2,** and **3**, with both oxygen and nitrogen in **4,** and with oxygen in **5** enables those compounds to disperse SWCNTs, which effects SWCNT debundling and dispersion. Because NMP is known to increase nanomaterial solvation generally (*26b*, *26g,h*), a similar phenomenon may also occur with other nanostructures in order to disperse them as individual molecules.

Conclusion

Magnitudes of changes in NMR chemical shift values indicate the degree to which SWCNTs associate with compounds such as amino alcohols and amides. NMR data for amides **1 – 3** indicate that that carbonyl association with SWCNTs is a stronger interaction. Changes in NMR shifts of aminoalcohols, which occur upon association with SWCNTs, reveal that SWCNTs interact with nitrogen lone pairs in **4a – c**. In amides, steric effects appear to be more important to forming a stronger association, while electronic effects are more important in aminoalcohols. Therefore, compounds with these structural characteristics are expected to associate more strongly and better disperse nanostructures generally as individual molecules.

In compounds associated with SWCNTs, three characteristics generally have the greatest effect on NMR chemical shifts and therefore are predicted to disperse SWCNTs best: (1) having multiple atoms and π bonds, which possess lone pairs for donation to the SWCNT surface, (2) having such functional groups separated by a number of methylene units, so they can associate with SWCNTs independently of each other, and (3) having a linear molecular framework, as opposed to a cyclic one, in order to enable greater conformational freedom in the molecule, increasing its ability to interact and associate with the SWCNT surface.

Downloaded by UNIV OF GUELPH LIBRARY on June 5, 2012 | http://pubs.acs.org
Publication Date (Web): April 27, 2011 | doi: 10.1021/bk-2011-1064.ch003

Downloaded by UNIV OF GUELPH LIBRARY on June 5, 2012 | http://pubs.acs.org
Publication Date (Web): April 27, 2011 | doi: 10.1021/bk-2011-1064.ch003

Experimental Section

Chemicals

Complexing agents **1** – **5** were purchased from Aldrich Chemical Co. Purified powder p-SWCNTs were purchased from Unidym, Inc (HiPco PO 269) . and donated from Southwest Nanotechnologies, Inc. All were used without further treatment.

Evaporation of SWCNT:1 – 5 Samples to Wet Paste

The procedure for formation of SWCNT:NMP is given as an example. Adapting procedures reported previously (*8b*) , NMP association with SWCNTs was explored by horn sonicating (30 min) p-SWCNT (0.5 mg), NMP (30 mg), and toluene solvent (4 mL). The p-SWCNT/NMP solution was evaporated to wet paste consistency (~5 days). Then a solution of the residual wet paste (~0.1 mg) in *d*-chloroform (10 mL) was prepared by horn sonication (30 min). SWCNT:**5** contains a mixture of the complex and starting materials.

NMR Spectra

Each sample of free **1 − 5** was prepared for NMR spectrum acquisition by dissolving a small amount (0.25 mL) in *d*-chloroform (10 mL). Each sample of SWCNT:**1 − 5** was prepared by dissolving a small amount of the wet paste (~0.1 mg) in *d*-chloroform (10 mL). The resulting solution was added by pipette into a 5 mm NMR tube (Wilmad, 503-PS). NMR measurements of free **1 – 5** (1:40 concentration (v:v) of sample:solvent) and SWCNT:**1 – 5** (1:150,000 concentration (w:w)) were acquired on a Varian VXR-300 or a Varian VMX-400 Spectrometer, with a typical run time of about 30 min (~1000 transients). The typical error in NMR shifts reported herein is ≤ ±0.00098 ppm.

Raman Spectra

Raman spectra were measured using microscope laser Raman spectroscopy with a Jobin Yvon-LabRam spectrometer. The laser excitation wavelength was 632 nm with a spectral resolution of 4 cm^{-1}.

Acknowledgments

We acknowledge the National Science Foundation and National Institute of Health for support of this research. We are grateful to SouthWest NanoTechnologies for a donation of pristine single-walled carbon nanotubes.

References

1. O'Regan, B.; Gratzel, M. *Nature* **1991**, *353*, 737.
2. (a) Chiu, P. W.; Duesberg, G. S.; Dettlaff-Weglikowska, U.; Roth, S. *Appl. Phys. Lett.* **2002**, *80*, 3811. (b) Zhu, H.; Zeng, H.; Subramanian, V.; Masarapu, C.; Hung, K. –H.; Weil, B. *Nanotechnology* **2008**, *19*, 465204. (c) Guldi, D. M.; Rahman, G. M. A.; Sgobba, V.; Kotov, N. A.; Bonifazi, D.; Prato, M. *J. Am. Chem. Soc.* **2006**, *128*, 2315. (d) Wei, J.; Jia, Y.; Shu, Q.; Gu, Z.; Wang, K.; Zhuang, D.; Zhang, G.; Wang, Z.; Luo, J.; Cao, A.; Wu, D. *Nano Lett.* **2007**, *7*, 2317. (e) Kongkanand, A.; Kamat, P. V. *ACS Nano* **2007**, *1*, 13.
3. (a) Huang, Z.; Liu, X. H.; Li, K. X.; Li, D. M.; Luo, Y. H.; Li, H.; Song, W. B.; Chen, L. Q.; Meng, Q. B. *Electrochem. Commun.* **2007**, *9*, 596. (b) Suzuki, K.; Yamaguchi, M.; Kumagai, M.; Yanagiday, S. *Chem. Lett.* **2003**, *32*, 28. (c) Guldi, D. M.; Rahman, G. M. A.; Sgobba, V.; Kotov, N. A.; Bonifazi, D.; Prato, M. *J. Am. Chem. Soc.* **2006**, *128*, 2315. (d) Kongkanand, A.; Kamat, P. V. *ACS Nano* **2007**, *1*, 13. (e) Itoh, E.; Suzuki, I.; Miyairi, K.; *Jpn. J. Appl. Phys.* **2005**, *44*, 636. (f) Ago, H.; Petrisch, K.; Shaffer, M. S. P.; Windle, A. H.; Friend, R. H. *Adv. Mater.* **1999**, *11*, 1281. (g) Geng, J.; Zeng, T. *J. Am. Chem. Soc.* **2006**, 128, 16827. (h) Barazzouk, S.; Hotchandani, S.; Vinodgopal, K.; Kamat, P. V. *J. Phys. Chem. B* **2004**, *108*, 17015. (i) Hirsch, A. *Angew. Chem., Int. Ed.* **2002**, *41*, 1853. (j) Bahr, J. L.; Tour, J. M. *J. Mater. Chem.* **2002**, *12*, 1952. (k) Niyogi, S.; Hamon, M. A.; Hu, H.; Zhao, B.; Bhomwik, P.; Sen, R.; Itkis, M. E.; Haddon, R. C. *Acc. Chem. Res.* **2002**, *35*, 1105. (l) Sun, Y. –P.; Fu, K.; Lin, Y.; Huang, W. *Acc. Chem. Res.* **2002**, *35*, 1096. (m) Banerjee, S.; Kahn, M. G. C.; Wang, S. S. *Chem. Eur. J.* **2003**, *9*, 1899. (n) Tasis, D.; Tagmatarchis, N.; Georgakilas, V.; Prato, M. *Chem. Eur. J.* **2003**, *9*, 4000. (o) Tagmatarchis, N.; Prato, M. *J. Mater. Chem.* **2004**, *14*, 437.
4. (a) Robertson, N. *Angew. Chem., Int. Ed.* **2006**, *45*, 2338. (b) Cherepy, N. J.; Smestad, G. P.; Gratzel, M.; Zhang, J. Z. *J. Phys. Chem. B* **1997**, *101*, 9342. (c) Zhu, H.; Zeng, H.; Subramanian, V.; Masarapu, C.; Hung, K. –H.; Weil, B. *Nanotechnology* **2008**, *19*, 465204. (d) Jung, K.-H.; Hong, J. S.; Vittal, R.; Kim, K.-J. *Chem. Lett.* **2002**, *31*, 864. (e) Jung, K.-H.; Jang, S.-R.; Vittal, R.; Kim, D.; Kim, K.-J. *Bull. Korean Chem. Soc.* **2003**, *24*, 1501. (f) Wang, Z. S.; Yamaguchi, T.; Sugihara, H.; Arakawa, H. *Langmuir* **2005**, *21*, 4272.
5. (a) Jang, S.-R.; Vittal, R.; Kim, K.-J. *Langmuir* **2004**, *20*, 9807. (b) Jung, K.-H.; Hong, J. S.; Vittal, R.; Kim, K.-J. *Chem. Lett.* **2002**, *31*, 864. (c) Jung, K.-H.; Jang, S.-R.; Vittal, R.; Kim, D.; Kim, K.-J. *Bull. Korean Chem. Soc.* **2003**, *24*, 1501.
6. (a) Zhu, H.; Zeng, H.; Subramanian, V.; Masarapu, C.; Hung, K.-H.; Weil, B. *Nanotechnology* **2008**, *19*, 465204. (b) Priya, B. R.; Byrne, H. J. *J. Phys. Chem. C* **2008**, *112*, 332. (c) Mao, S.; Kleinhammes, A.; Wu, Y. *Chem. Phys. Lett.* **2006**, *421*, 513. (d) Gotovac, S.; Hattori, Y.; Noguchi, D.; Miyamoto, J.-I.; Kanamaru, M.; Utsumi, S.; Kanoh, H.; Kaneko, K. *J. Phys. Chem. B* **2006**, *110*, 16219. (e) Harutyunyan, A. R.; Pradhan, B. K.; Chang, J.; Chen,

Downloaded by UNIV OF GUELPH LIBRARY on June 5, 2012 | http://pubs.acs.org
Publication Date (Web): April 27, 2011 | doi: 10.1021/bk-2011-1064.ch003

In Fluorine-Related Nanoscience with Energy Applications; Nelson, D., et al.;
ACS Symposium Series; American Chemical Society: Washington, DC, 2011.

Downloaded by UNIV OF GUELPH LIBRARY on June 5, 2012 | http://pubs.acs.org
Publication Date (Web): April 27, 2011 | doi: 10.1021/bk-2011-1064.ch003

G.; Eklund, P. C. *J. Phys. Chem. B* **2002**, *106*, 8671. (f) Pulikkathara, M. X.; Kuznetsov, O. V.; Khabashesku, V. N. *Chem. Mater.* **2008**, *20*, 2685.

7. (a) Fu, K.; Kitaygorodskiy, A.; Rao, A. M.; Sun, Y.-P. *Nano Lett.* **2002**, *2*, 1165. (b) Sun, Y.-P.; Fu, K.; Lin, Y.; Huang, W. *Acc. Chem. Res.* **2002**, *35*, 1096. (c) Banerjee, S.; Kahn, M. G. C.; Wang, S. S. *Chem. Eur. J.* **2003**, *9*, 1898. (d) Tasis, D.; Tagmatarchis, N.; Georgakilas, V.; Prato, M. *Chem. Eur. J.* **2003**, *9*, 4000. (e) Dyke, C. A.; Tour, J. M. *Chem. Eur. J.* **2004**, *10*, 812.
8. (a) Nelson, D. J.; Rhoads, H.; Brammer, C. *J. Phys. Chem. C.* **2007**, *111*, 17872. (b) Nelson, D. J.; Perumal, P. T.; Brammer, C.; Selvam, N. P. *J. Phys. Chem. C.* **2009**, *113*, 17378.
9. (a) Georgakilas, V.; Kordatos, K.; Prato, M.; Guldi, D. M.; Holzinger, M.; Hirsch, A. *J. Am. Chem. Soc.* **2002**, *124*, 760. (b) Holzinger, M.; Abraham, J.; Whelan, P.; Graupner, R.; Ley, L.; Hennrich, F.; Kappes, M.; Hirsch, A. *J. Am. Chem. Soc.* **2003**, *15*, 8566. (c) Murakami, H.; Nomura, T.; Nakashima, N. *Chem. Phys. Lett.* **2003**, *378*, 481. (d) Guldi, D. M.; Marcaccio, M.;Paolucci, D.; Paolucci, F.; Tagmatarchis, N.; Tasis, D.; Vazquez, E.; Prato, M. *Angew. Chem., Int. Ed.* **2003**, *42*, 4206.
10. Rueckes, T.; Kim, K.; Joselevich, E.; Tseng, G. Y.; Cheung, C.-L.; Lieber, C. M. *Science* **2000**, *289*, 94.
11. (a) O'Connell, M. J.; Bachilo, S. M.; Huffman, C. B.; Moore, V. C.; Strano, M. S.; Haroz, E. H.; Rialon, K. L.; Boul, P. J.; Noon, W. H.; Kittrell, C.; Ma, J.; Hauge, R. H.; Weisman, R. B.; Smalley, R. E. *Science* **2002**, *297*, 593. (b) Islam, M. F.; Rojas, E.; Bergey, D. M.; Johnson, A. T.; Yodh, A. G. *Nano Lett.* **2003**, *3*, 269. (c) Moore, V. C.; Strano, M. S.; Haroz, E. H.; Hauge, R. H.; Smalley, R. E.; *Nano Lett.* **2003**, *3*, 1379.
12. (a) Giordani, S.; Bergin, S.; Nicolosi, V.; Lebedkin, S.; Blau, W. J.; Coleman, J. N. *Phys. Stat. Sol.* **2006**, *243*, 3058. (b) Hirsch, A. *Angew. Chem., Int. Ed.* **2002**, *41*, 1853. (c) Niyogi, S.; Hamon, M. A.; Hu, H.; Zhao, B.; Bhowmik, P.; Sen, R.; Itkis, M. E.; Haddon, R. C. *Acc. Chem. Res.* **2002**, *35*, 1105. (d) Dyke, C. A.; Tour, J. M. *J. Phys. Chem. A* **2004**, *108*, 11151. (e) Banerjee, S.; Hemraj-Benny, T.; Wong, S. S. *Adv. Mater.* **2005**, *17*, 17. (f) Tasis, D.; Tagmatarchis, N.; Bianco, A.; Prato, M. *Chem. Rev.* **2006**, *106*, 1105.
13. (a) O'Connell, M. J.; Boul, P.; Ericson, L. M.; Huffman, C.; Wang, Y.; Haroz, E.; Kuper, C.; Tour, J. M.; Ausman, K. D.; Smalley, R. E. *Chem. Phys. Lett.* **2001**, *342*, 265. (b) Star, A.; Stoddart, J. F.; Steuerman, D.; Diehl, M.; Boukai, A.; Wong, E. W.; Yang, X.; Chung, S.-W.; Choi, H.; Heath, J. R. *Angew. Chem., Int. Ed.* **2001**, *40*, 1721. (c) Nakashima, N.; Tomonari, Y.; Murakami, H. *Chem. Lett.* **2002**, 638. (d) Richard, C.; Balavoine, F.; Schultz, P.; Ebbesen, T. W.; Mioskowski, C. *Science* **2003**, *300*, 775. (e) Numata, M.; Asai, M.; Kaneko, K.; Bae, A.-H.; Hasegawa, M.; Sakurai, K.; Shinkai, S. *J. Am. Chem. Soc.* **2005**, *127*, 5875.
14. (a) Qi, P.; Vermesh, O.; Grecu, M.; Javey, A.; Wang, Q.; Dai, H.; Peng, S.; Cho, K. J. *Nano Lett.* **2003**, *3*, 347. (b) Star, A.; Han, T.-R.; Gabriel, J.-C. P.; Bradley, K.; Grüner, P. *Nano Lett.* **2003**, *3*, 459.
15. Lee, C. Y.; Strano, M. S. *J. Am. Chem. Soc.* **2008**, *130*, 1766.
16. (a) Maeda, Y.; Kimura, S.; Hirashima, Y.; Kanda, M.; Lian, Y.; Wakahara, T.; Akasaka, T.; Hasegawa, T.; Tokumoto, H.; Shimizu, T.; Kataura, H.;

Miyauchi, Y.; Maruyama, S.; Kobayashi, K.; Nagase, S. *J. Phys. Chem. B* **2004**, *108*, 18395. (b) An, K. H.; Jeong, S. Y.; Hwang, H. R.; Lee, Y. H. *Adv. mater.* **2004**, *16*, 1005. (c) Ju, S.-Y.; Utz, M.; Papadimitrakopoulos, F. *J. Am. Chem. Soc.* **2009**, *131*, 6775. (d) Brown, J. M.; Anderson, D. P.; Justice, R. C.; Lafdi, K.; Belfor, M.; Strong, K. L.; Schaefer, D. W. *Polymer* **2005**, *46*, 10854. (e) Maeda, Y.; Kimura, S.-I.; Kanda, M.; Hirashima, Y.; Hasegawa, T.; Wakahara, T.; Lian, Y.; Nakahodo, T.; Tsuchiya, T.; Akasaka, T.; Lu, J.; Zhang, X.; Gao, Z.; Yu, Y.; Nagase, S.; Kazaoui, S.; Minami, N.; Shimizu, T.; Tokumoto, H.; Saito, R. *J. Am. Chem. Soc.* **2005**, *127*, 10287. (f) Zhou, Y.-K.; He, B.-L.; Zhou, W.-J.; Liz, H.-L. *J. Electrochem. Soc.* **2004**, *151*, A1052.

17. Leon, A. D.; Jalbout, A. F.; Basiuk, V. A. *Chem. Phys. Lett.* **2008**, *457*, 185.
18. (a) Kuznetsova, A.; Popova, I.; Yates, J. T., Jr.; Bronikowski, M. J.; Huffman, C. B.; Liu, J.; Smalley, R. E.; Hwu, H. H.; Chen, J. G. *J. Am. Chem. Soc.* **2001**, *123*, 10699. (b) Koshio, A.; Yudasaka, M.; Zhang, M.; Iijima, S. *Nano Lett.* **2001**, *1*, 361. (c) Koshio, A.; Yudasaka, M.; Iijima, S. *Chem. Phys. Lett.* **2001**, *341*, 461.
19. (a) Yan, L. Y.; Poon, Y. F.; Chan-Park, M. B.; Chen, Y.; Zhang, Q. *J. Phys. Chem. C* **2008**, *112*, 7579. (b) Czerw, R.; Guo, Z.; Ajayan, P. M.; Sun, Y.-P.; Carroll, D. L. *Nano Lett.* **2001**, *1*, 423.
20. (a) Matranga, C.; Bockrath, B. *J. Phys. Chem. B* **2005**, *109*, 4853. (b) Matranga, C.; Chen, L.; Bockrath, B.; Johnson, *J. Phys. Rev. B* **2004**, *70*, 165416.
21. (a) Harada, A.; Takashima, Y.; Yamaguchi, H. *Chem. Soc. Rev.* **2009**, *38*, 875. (b) Liu, Y.; Gao, L.; Zheng, S.;Wang, Y.; Sun, J.; Kajiura, H.; Li, Y.; Noda, K. *Nanotechnology* **2007**, *18*, 365702. (c) Satishkumar, B. C.; Doorn, S. K.; Baker, G. A.; Dattelbaum, A. M. *ACS Nano* **2008**, *2*, 2283. (d) Zhang, X.; Liu, T.; Sreekumar, T. V.; Kumar, S.; Moore, V. C.; Hauge, R. H.; Smalley, R. E. *Nano Lett.* **2003**, *3*, 1285. (e) Liu, N.; Cai, X.; Zhang, Q.; Lei, Y.; Chan-Park, M. B. *Electroanalysis* **2008**, *20*, 558. (f) Ikeda, A.; Hayashi, K.; Konishi, T.; Kikuchi, J.-I. *Chem. Commun.* **2004**, 1334. (g) Kim, O.-K.; Je, J.; Baldwin, J. W.; Kooi, S.; Pehrsson, P. E.; Buckley, L. J. *J. Am. Chem. Soc.* **2003**, *125*, 4426.
22. Kim, P.; Zheng, Y.; Agnihotri, S. *Ind. Eng. Chem. Res.* **2008**, *47*, 3170.
23. Ago, H.; Azumi, R.; Ohshima, S.; Zhang, Y.; Kataura, H.; Yumura, M. *Chem. Phys. Lett.* **2004**, *383*, 469.
24. (a) Malik, S.; Vogel, S.; Rösner, H.; Arnold, K.; Hennrich, F.; Köhler, A.-K.; Richert, C.; Kappes, M. *Compos. Sci. Technol.* **2007**, *67*, 916. (b) Gigliotti, B.; Sakizzie, B.; Bethune, D. S.; Shelby, R. M.; Cha, J. N. *Nano Lett.* **2006**, *6*, 159.
25. (a) Chen, J.; Liu, H.; Weimer, W. A.; Halls, M. D.; Waldeck, D. H.; Walker, G. C. *J. Am. Chem. Soc.* **2002**, *124*, 9034. (b) Steuerman, D. W.; Star, A.; Narizzano, R.; Choi, H.; Ries, H. S.; Nicolini, C.; Stoddart, J. F.; Heath, J. R. *J. Phys. Chem. B* **2002**, *106*, 3124. (c) Miyako, E.; Nagata, H.; Hirano, K.; Hirotsu, T. *Angew. Chem., Int. Ed.* **2008**, *47*, 3610. (d) Nativ-Roth, E.; Shvartzman-Cohen, R.; Bounioux, C.; Florent, M.; Zhang, D.; Szleifer, I.; Yerushalmi-Rozen, R. *Macromolecules* **2007**, *40*, 3676. (e) Ju, S.-Y.; Utz,

Downloaded by UNIV OF GUELPH LIBRARY on June 5, 2012 | http://pubs.acs.org
Publication Date (Web): April 27, 2011 | doi: 10.1021/bk-2011-1064.ch003

M.; Luo, Z.; Papadimitrakopoulous, F. *Polym. Prepr. (Am. Chem. Soc., Div. Polym. Chem.)* **2005**, *46*, 209.

26. (a) Furtado, C. A.; Kim, U. J.; Gutierrez, H. R.; Pan, L.; Dickey, E. C.; Eklund, P. C. *J. Am. Chem. Soc.* **2004**, *126*, 6095. (b) Giordani, S.; Bergin, S.; Nicolosi, V.; Lebedkin, S.; Blau, W.; Coleman, J. *Phys. Stat. Sol. B* **2006**, *243*, 3058. (c) Bahr, J.; Mickelson, E.; Bronikowski, M.; Smalley, R.; Tour, J. *Chem. Commun.* **2001**, *2*, 193. (d) Landi, B.; Ruf, H.; Worman, J.; Raffaelle, R. *J. Phys. Chem. B* **2004**, *108*, 17089. (e) Krupke, R.; Hennrich, F.; Hampe, O.; Kappes, M. *J. Phys. Chem. B* **2003**, *107*, 5667. (f) Ausman, K. D.; Piner, R.; Lourie, O.; Ruoff, R. S.; Korobov, M. *J. Phys. Chem. B* **2000**, *104*, 8911. (g) Wang, J.; Blau, W. *J. Phys. Chem. C* **2008**, *112*, 2298. (h) Hasan, T.; Scardaci, V.; Tan, P. H.; Rozhin, A. G.; Milne, W. I.; Ferrari, A. C. *J. Phys. Chem. C* **2007**, *111*, 12594.
27. Alemany, L. B.; Zhang, L.; Zeng, L. L.; Edwards, C. L.; Barron, A. R. *Chem. Mater.* **2007**, *19*, 735.
28. (a) Spectral Database for Organic Compounds, National Institute of Advanced Industrial Science and Technology (AIST). http://riodb01.ibase.aist.go.jp/sdbs/cgi-bin/cre_index.cgi?lang=eng (accessed January 20, 2010). (b) Spectral Database for Products, Sigma-Aldrich, Inc. http://www.sigmaaldrich.com/technical-service-home/product-catalog.html (accessed January 20, 2010).
29. Matarredona, O.; Rhoads, H.; Li, Z.; Harwell, J.; Balzano, L.; Resasco, D. *J. Phys. Chem. B* **2003**, *107*, 13357.
30. (a) Purified HIPCO® Single-Wall Carbon Nanotubes properties. http://www.unidym.com/products/materials.html (accessed January 20, 2010). (b) SWeNT SG 65 Typical Properties. SouthWest NanoTechnologies, Inc. http://www.swnano.com/tech/docs/Final_SG_65_Data_Sheet.pdf (accessed June 2, 2009).

Downloaded by UNIV OF GUELPH LIBRARY on June 5, 2012 | http://pubs.acs.org
Publication Date (Web): April 27, 2011 | doi: 10.1021/bk-2011-1064.ch003

Chapter 4

Highly Fluorinated Porphyrins: From Ultra-Thin Films to Nanoparticles in Catalysis

Alessandro Varotto,[1,*] Gabriela Smeureanu,[1] Amit Aggarwal,[1] and Charles Michael Drain[1]

[1]Department of Chemistry and Biochemistry, Hunter College of The City University of New York, 695 Park Avenue, New York, NY, 10065
[*]alessandro.varotto@gmail.com

Porphyrins are heterocyclic macrocycles that are extensively studied as functional materials and components of devices in several fields of science because of their unique and tunable characteristics. The periphery of the ring can be functionalized with a variety of substituents that modulate both the photophysical and the materials properties. Because of their exceptional and tunable opto-electronic properties, porphyrins have been studied for energy related applications ranging from energy storage to materials for organic photovoltaics and to catalysis. Substitution with perfluoro-alkane moieties and perfluoro-phenyl groups improve their supramolecular self-organizing properties as well as the robustness of porphyrinic materials. The preparation of highly fluorinated porphyrins and formation of thin films for studies of their photonic properties are discussed. The fabrication of stable nanoparticles of iron perfluorophenylporphyrin, the derivative with para fluorous alkanes, and the performance of these systems as catalysts is introduced. For all of these materials, the presence of fluorines stabilizes the nanocomposites and increases their resistance towards oxidation.

1. Porphyrins

A porphyrin is a planar heterocyclic macrocycle derived from four pyrrole subunits interconnected via their *α* carbon atoms with methine bridges (=CH–).

Many porphyrins occur in nature, such as the chlorophylls in green leaves and hemes in red blood cells. The chemistry to synthesize both the natural and non-naturally occurring derivatives is well established (*1*). Porphyrins bind metals to form complexes. The metal ion, usually with a charge of 2+ or 3+, resides in the central N4 dianion cavity formed by the loss of two protons. Most metals can be inserted in this cavity. The periphery of the ring can also be functionalized with a variety of susbstituents that modulate both the photophysical properties and the materials properties. Because of their exceptional and tunable opto-electronic properties, porphyrins have been extensively studied for energy related applications ranging from energy storage to materials for organic photovoltaics and to catalysis (*2*). Porphyrins are also investigated for the preparation of nanomaterials, such as nanoparticles, nanowires, and nanotubes which, due to the size, often display enhanced or unexpected properties (*2*). Figure 1 shows the structures of the core porphyrin macrocycle, and 5,10,15,20-tetrakis-(2,3,4,5,6-pentafluorophenyl)porphyrin ($TPPF_{20}$), a porphyrin functionalized with four perfluorophenyl groups.

Porphyrins are deeply colored and their UV-visible spectra consist of several absorptions, one in the near UV to blue (ca. 380 nm to 430 nm, called Soret or B-band) with absorptivities around 10^5 $M^{-1}cm^{-1}$ and several others in the visible (between ca. 500-700 nm, Q-bands). The location and intensity depend on several factors, such as substitution of the macrocycle, metallation, protonation, and environment (solvent, pH). Martin Gouterman successfully described the electronic spectra of porphyrins refered to as four-orbital model, which uses two HOMOs and two LUMOs generated by Hückel theory. The electronic transition from the HOMO to the LUMO accounts for the spectral characteristics of porphyrins and depend on the symmetry of the macrocycle. The dominant spectral feature appears between 400-430 nm because it is an allowed transition, whereas the Q-bands are weakly allowed because of vibronic coupling and therefore less intense (*3*).

1.1. $TPPF_{20}$

$TPPF_{20}$ (Fig. 1) is extensively studied because of the unique properties imparted by the pentafluorphenyl groups. For example, the remarkable properties have been exploited for the preparation of catalysts (*4*), nanoparticles (*5*, *6*), photonic devices (*7*) and fullerene co-crystals (*8*). Due to the easy substitution of the para fluorines with nucelophiles, $TPPF_{20}$ can also be employed for the synthesis of a variety of derivatives ranging from sugars (*9*) to polyamines (*10*) and as a core platform for the formation of combinatorial libraries (*9*) These click-like reactions generally proceed in high yields and the by-product is HF. In this discussion, we will focus first on the use of $TPPF_{20}$ functionalized with perfluoroalkane moieties to grow ultrathin films containing fullerene C_{60} (*11*) and secondly on the preparation of stable nanoparticles along with the description of their catalytic properties (*4*).

In Fluorine-Related Nanoscience with Energy Applications; Nelson, D., et al.;
ACS Symposium Series; American Chemical Society: Washington, DC, 2011.

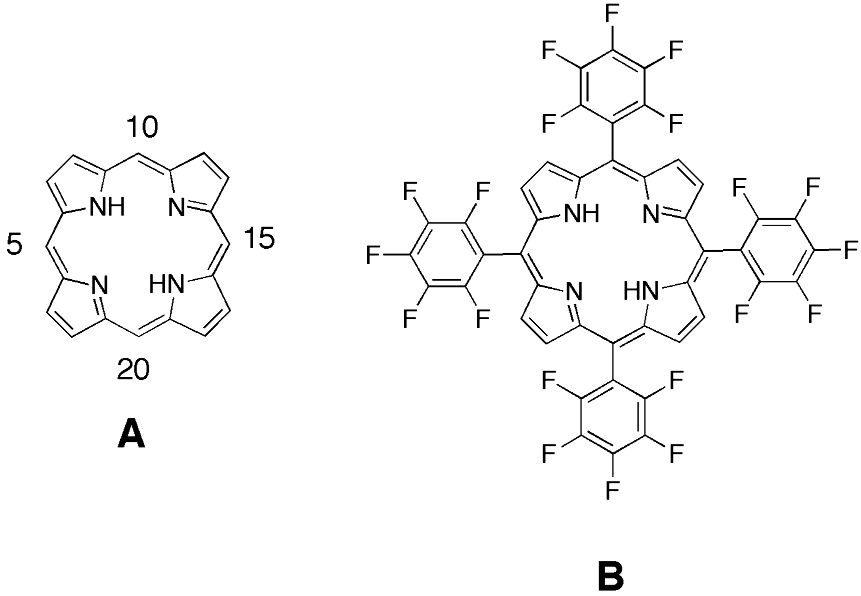

Figure 1. (A) The porphine macrocycle and (B) $TPPF_{20}$, a porphyrin functionalized with four perfluorophenyl groups.

2. $TPPF_{20}$ and C_{60}

The supramolecular chemistry of porphyrins and fullerenes is well established and in the literature there are several examples of porphyrins and fullerenes co-crystals. There are at least two kinds of attractive non-covalent interactions that hold the chromophores in close proximity: π- π intermolecular interactions between the curved surface of a fullerene and the center of a porphyrin (*8*), and electrostatic interactions between the electropositive center of the porphyrin and a 6:6 ring juncture of the fullerene. These forces synergistically decrease the distance between the molecules which would be expected to be larger for π-π interactions alone (*12*). Because of the excellent properties of fullerenes as electron acceptors that arise from their symmetry and minimal reorganization energies, and the optimum alignment between their orbitals and those of porphyrins, porphyrin-C_{60} constructs are interesting for the preparation of adducts that form long-lived charge-separated states (*13*). Thus, these constructs can be useful for the fabrication of a variety of photonic devices such as solar cells and optical sensors. There are a large variety of covalently attached porphyrin-fullerene molecules (*13*) and fullerenes modified with ligands that can axially bind to metal centers in metalloporphyrins (*14*) but strategies that involve making derivatives of C_{60} diminish its quality as an electron acceptor (*15*).

Supramolecular chemistry allows formation of porphyrin-fullerene materials without making derivatives of the C_{60}. Recently $TPPF_{20}$ has been co-crystallized with fullerene C_{60} and C_{70}, revealing non classic interactions (Figure 2). The spontaneous attraction between fullerenes and porphyrins described above is augmented by the presence of the four pentafluorophenyl groups that provide additional interactions that contributes to the stabilization of the crystal lattice. An attractive C–F···C (fullerene), mostly C–F···π, has been observed independently by two groups examining co-crystals of $TPPF_{20}$ and fullerenes (*12*, *16*). Crystal structures are essential for understanding the 3-dimensional arrangement of molecules in the space and intermolecular interactions; however, supramolecularly self-organized materials used for the preparation of devices, especially based on relatively weak interactions such as van der Waals forces, may undergo significant re-organization and phase separation upon deposition on surfaces from solution. Surface deposition from solution is a complex process wherein solvent evaporation, fluid dynamics, surface interactions, and intermolecular interactions evolve with time. Chemical vapor deposition can also lead to quite different structures on surfaces than found in crystals due to the interaction with a surface and differentiated intermolecular interactions

Since we found that simple porphyrins and C_{60} indeed phase separate and form poor quality films on surfaces when drop cast from solution, further modification of the porphyrin is necessary. A simple modification of the $TPPF_{20}$ facilitates growth of robust, high-quality thin films supramolecularly self-organized with pristine fullerene C_{60} with no phase separation.

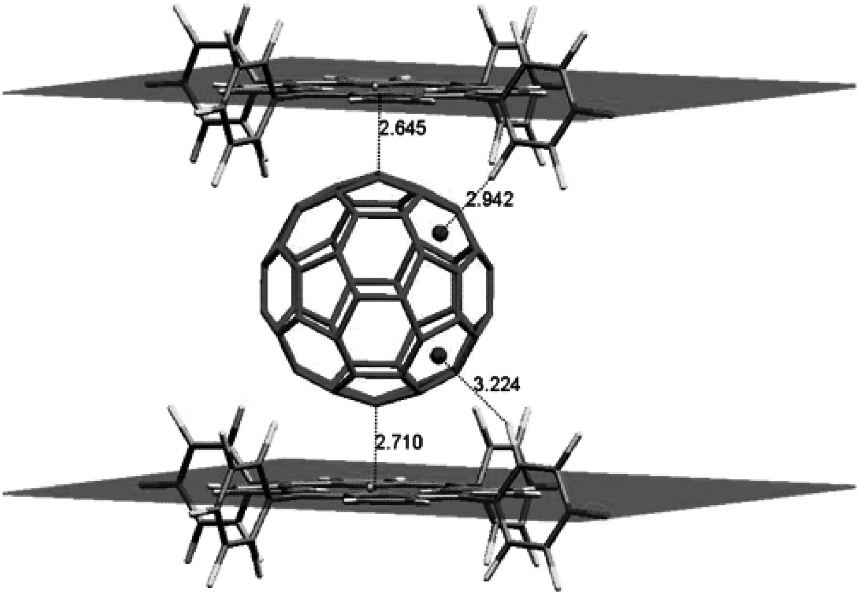

Figure 2. $TPPF_{20}$-C_{60} co-crystal structure showing the short distance between the chromophores. Fullerene approaches the porphyrin core from the 6:6 (C=C) junction. Reproduced with permission from reference (12). Copyright 2006.

2.1. $TPPF_{100}$

We reported the synthesis of $TPPF_{100}$, prepared from substitution of the four *para*-F's on the phenyl groups with a thio group attached to a fluorous alkane bearing twelve carbons (1H,1H,2H,2H-perfluorododecanethiol) (*11*). The fluoro-alkane substituents impart remarkable properties to the macrocycle due to a combination of polar and steric effects, and due to the great strength of the C-F bond, which confers chemical stability, especially to oxidation, to fluoro-substituted compounds. High density, excellent adhesion properties, and low permeability of perfluoro compounds have made possible their applications in many fields, such as in coating and in thin films technology (*17–20*). In our work, we have taken advantage of the extraordinary properties of the fluoroalkane moieties to form films and to reinforce the non-covalent interactions between $TPPF_{20}$ and C_{60} to grow ultra-thin films (7-12 nm) from a solution phase mixture of the two chromophores. This is accomplished simply by dipping an indium-tin-oxide (ITO) electrode into a solution of the two compounds.

The synthesis of $TPPF_{100}$ is described in detail elsewhere and it is based on the reaction of $TPPF_{20}$ with perfluorododecanethiol (*11*). This reaction proceeds in five minutes at room temperature and quantitatively yields the tetra-*para*-substituted adduct ($TPPF_{100}$). $TPPF_{100}$ precipitates from the solution and therefore is easy to recover by filtration without the need for purification by chromatography. The X-ray crystal structural analysis of $TPPF_{100}$ indicated that the perfluoroalkane moieties prefer to adopt an all extended conformation, possibly suggesting a rigid framework in the deposited films (Figure 3).

The films were prepared by dipping a slide of ITO in a solution of $TPPF_{100}$ and C_{60} in CCl_4 with a molar ratio 1:1. After one hour of immersion in solution, the substrate was removed and let dry in the air. During this process self-organized thin films containing both chromophores formed. Similar deposition conditions with control molecules, $TPPF_{20}$ and the corresponding non-fluorous alkylated version of $TPPF_{100}$, did not form similar films or have similar properties. The $TPPF_{100}$-C_{60} blended films were characterized using a combination of spectroscopic techniques to probe their photonic properties: fluorescence and UV-vis spectroscopy, laser scan confocal microscopy (LSCM) and atomic force microscopy (AFM) (Figure 4). The UV-vis spectra of the 1:1 blend, both in solution and as a film on ITO, was the sum of the spectra of the chromophores taken individually. This indicates weak electronic interactions in the ground state, which is consistent with previous reports (*21*). Nevertheless, both fluorescence spectroscopy (Figure 5) and LSCM confirmed that the fluorescence of the $TPPF_{100}$ was significantly quenched in presence of C_{60}. Fluorescence spectroscopy provides information about the properties of bulk film material, whereas LSCM offers information about the local photonic properties of the films at the micro scale. LSCM was combined with an AFM so that the same area of the films could be analyzed by two different techniques. AFM analysis revealed very different morphologies for the films formed from $TPPF_{100}$ alone versus the films of $TPPF_{100}/C_{60}$. $TPPF_{100}$ forms large, flat islands that have minimal surface roughness, while a granular morphology, similar to ones reported for polymers (*22*) are consistently observed for the films formed from the 1:1 mixture (Figure

4). Additionally, as anticipated above, the fluorescence of the porphyrin was quenched in the blend by the presence of fullerene. All these data, taken together, suggests that the C_{60} is in close proximity to the porphyrin and that electron transfer from the porphyrin to the C_{60} is the cause of the fluorescence quenching.

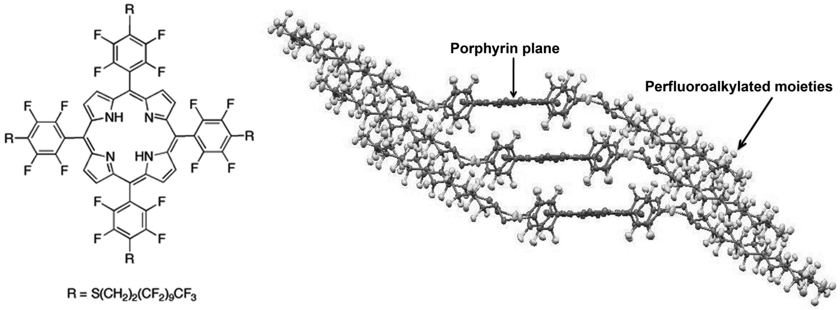
R
F
NH
N
HN
R = $S(CH_2)_2(CF_2)_9CF_3$
Porphyrin plane
Perfluoroalkylated moieties

Figure 3. Structure (left) and crystal packing (right) of $TPPF_{100}$.

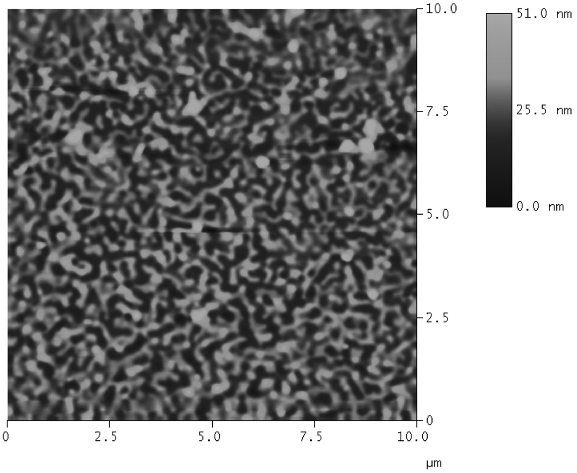
10.0
7.5
5.0
2.5
0
0
2.5
5.0
7.5
10.0
µm
51.0 nm
25.5 nm
0.0 nm

Figure 4. AFM height mode image of a film formed from blended $TPPF_{100}$ and C_{60} solution (1:1 molar ratio) on ITO. Adapted with permission from reference (11). Copyright 2008 RSC Publishing.

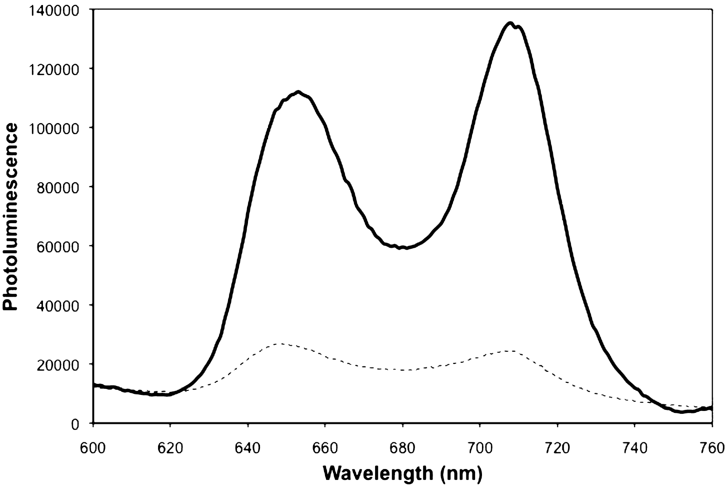

Figure 5. Photoluminescence of TPPF$_{100}$ *deposited on ITO (solid black line) is quenched when co-deposited with fullerene C*$_{60}$ *pre-mixed in CCl*$_{4}$ *with molar ratio 1:1 (dashed line). Adapted with permission from reference (11). Copyright 2008 RSC Publishing.*

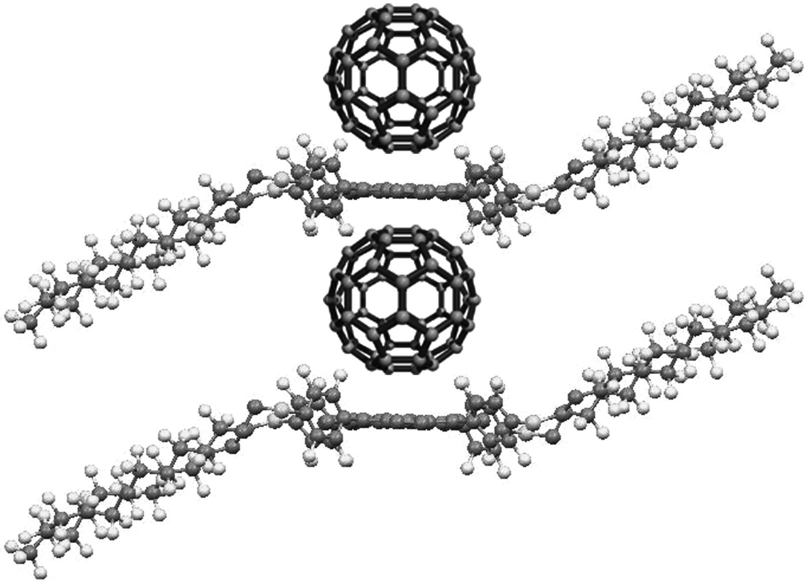

Figure 6. A possible arrangement of the 1:1 blend of TPPF$_{100}$*/C*$_{60}$ *into stacked multi layers.*

Not only do the fluorous alkanes on the porphyrin drive the formation of thin films but they also keep the chromophores held together within the film. The films are resistant to sonication in water. More than 70% of the control molecules deposited on the surface was removed together with C_{60} in the first two minutes of sonication, whereas the $TPPF_{100}/C_{60}$ blended films persisted even after 30 minutes. Based on the crystal structure shown in figure 3, the fluorines between adjacent molecules are separated by channels as small as 0.272 nm. Hydrocarbon chains similarly arranged would leave much bigger channels which could be more permeable to oxygen and water. A scheme is presented in figure 6 for a possible arrangement of the chromophores when multilayers are deposited on ITO. This is based both on the crystal structure of $TPPF_{100}$ and the structures of co-crystals of $TPPF_{20}$ and C_{60}. This would account for the robustness of the film driven by the fluorous alkanes cooperatively with the porphyrin-fullerene interactions. The C_{60} could also reside between the fluorous alkane chains, but this would likely diminish the interactions that form the film.

3. Nanoparticles in Catalysis

Nanoparticles (NPs), an unique subset of the broad field of nanotechnology, play an important role in a wide variety of applications, including advanced and smart materials, medicinal chemistry, and detection of pollutants and toxins in the environment (*23*). Porphyrin NPs can be considered supramolecularly self-organized systems that are governed by many non-covalent interactions that depend on the porphyrin structure, the metal ion, and the mode of preparation. Like the inorganic counterparts, porphyrin and metalloporphyrin NPs are promising components for advanced material chemistry because of their remarkable photochemical and catalytic properties, stability, and ease of preparation.

Recenly, we reported a method to successfully prepare a variety of porphyrin and metalloporphyrin NPs (*6*, *24*). This method includes the use of porphyrins containing different redox active transition metals (Fe, Co, Zn and Cr) that exhibit enhanced and/or unexpected properties. A detailed description of the NPs preparation is described elsewhere (*4*–*6*), but in general, they can be obtained by controlled aggregation of porphyrins from different host/guest solvents via sonication and stabilization with polyethylene glycols (PEGs). For example, hydrophobic porphyrins in water miscible solvents such as tetrahydrofuran or acetonitrile form < 100 nm NPs when slowly added to water containing a few percent tetraethyleneglycol monomethylether. The mode of mixing the solvent, e.g. stirring or sonication, is one of the factors the dictates the size of the resulting NP. These NPs are aggregated into 10-300 nm spheres and we observed that, in addition to the processing conditions, the sizes can be tuned by appending different hydrocarbon functionalitites to the porphyrin, and by insertion of different metal ions in the core. These nanoparticles were characterized using DLS (dynamic light scattering) in solution and AFM on glass surfaces (Table 1). All the particles were made by adding a large volume of an insoluble guest solvent to a small volume of the porphyrin in a soluble host solvent, mixed with poly(ethylene glycol) derivative (*6*) (Figure 7).

Table 1. Examples of size distribution for few free bases and metalated porphyrin nanoparticles

Compound	*DLS (nm)*	*AFM (nm)*
Tetra-phenyl-porphyrin (TPP)	5-6	3-10
Tetra-tolyl-porphyrin (tolylPP)	5-7	7-10
Tetra-*t*-butyl-phenyl- porphyrin (TtbutylPP)	6-8	12-20
$TPPF_{20}$	5-8	5-15
Fe(III)tetra-phenyl- porphyrin	20-30	7-15
Co(III)tetra-tolyl-porphyrin	30-35	5-12
Zn(III)tetra-*t*-butyl phenyl-porphyrin	30-40	8-15
Fe(III)$TPPF_{20}$	7-10	6-12

Data are from reference (*6*).

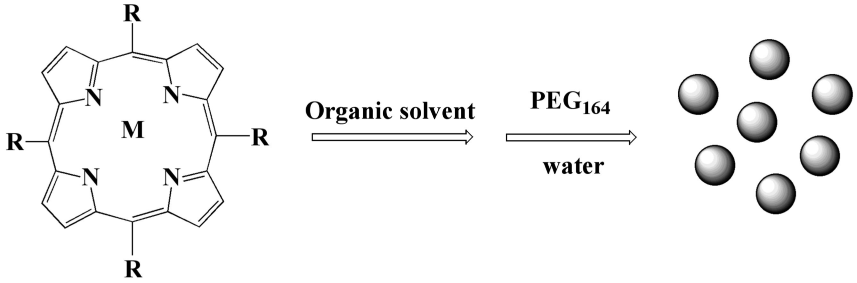
R
R
R
R
N
N
N
N
M
Organic solvent
PEG164
water

Figure 7. Preparation of different hydrophobic metalloporphyrin nanoparticles in water.

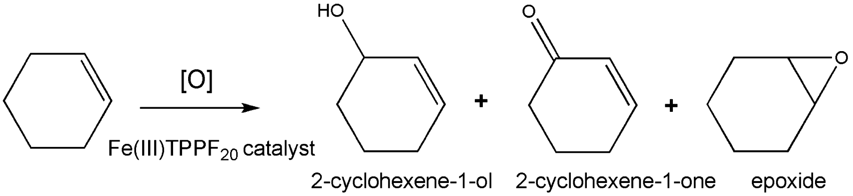
[O]
Fe(III)TPPF20 catalyst
HO
O
O
+
+
2-cyclohexene-1-ol
2-cyclohexene-1-one
epoxide

Figure 8. Oxidation of cyclohexene.

The advantages of these self-organized nanoparticles arise from the use of commercially available pigments, ease of preparation, and high stability. There is a variety of possible applications of porphyrin NPs that originate from the photonic properties of both the specific dye molecule, e.g. fluorescence and phosphorescence, and the nanoscaled dimensions of the particle. When the porphyrin contains a redox-active transition metal, many of these NPs are more efficient catalysts on a per porphyrin basis than the individual porphyrins in solution (*4*, *24*) Recently we reported the enhanced catalytic activity and unexpected products from the oxidation of cyclohexene by NPs of Fe(III)TPPF$_{20}$ in water using O_2 (*4*). Though this iron porphyrin has been extensively studied by many researchers, this pioneering study demonstrated that the oxidation of cyclohexene can be accomplished under mild conditions using organic Fe(III)TPPF$_{20}$ nanoparticles as a catalyst that activates oxygen. At room temperature the catalytic oxidation of alkenes by most iron porphyrins using a variety of synthetic oxygen sources, yields the epoxide with only minor quantities of other possible products. The turnover numbers (TON) for these catalysts are modest, ranging from a few hundreds to a few thousands depending on the degree of halogenation of the porphyrin, the substrate, catalysts ratio, solvent, temperatures, axial ligands, and other conditions (*25*). Though the details are still under discussion, halogenation of the macrocycle makes the metalloporphyrin catalyst more robust to oxidative degradation and/or increases the rate of reaction, and/or distorts the otherwise planar macrocycle thereby altering the relative energy of the d-orbitals. The epoxide accounts for more than 99% of the product with TON of ca. 350 when Fe(III)TPPF$_{20}$ is used to affect the oxidation of cyclohexene (*4*). The catalytic oxidation of a variety of olefins by Fe(III)-tetra-aryl porphyrins is a standard reaction that has been thoroughly investigated over the last few decades (*27*). The epoxide is the major product under a range of experimental conditions irrespective of the peripheral substituents on the aryl moiety. In general the TON is a few hundreds because of the degradation of the iron porphyrin catalyst, but when using Fe(III)TPPF$_{20}$ the TON is increased to about ca. 350 because this is more resistant to oxidative degradation and is more active, so the kinetic competition between catalyst decomposition and product formation is different than with the non-halogenated aryl groups (*28*). There are numerous studies on the catalytic activity of this porphyrin including the recent reports on the catalytic oxidation of cyclooctene by Fe(III)TPPF$_{20}$ in acetonitrile/methanol, which yielded over 98% of the epoxide and traces of the 2-cyclooctene-1-one and the 2-cyclooctene-1-ol (*26*, *29*–*31*).

Under the same conditions, we found similar reactivity for cyclohexene (Figure 8). Aqueous suspensions of NPs of commercially available Fe(III)TPPF$_{20}$ chloride, formed by the methods described above, have significantly enhanced the catalytic properties compared to the component molecules, and those on supports, and results in different product distributions (*4*). Specifically, NPs of Fe(III)TPPF$_{20}$ yielded exclusively the ketone and the alcohol (Table 2). Examination of the mechanism of the catalytic activity of this system also allows studying the fundamental differences in the chemistry of nanoscaled aggregates versus solvated molecules or solid-state materials.

Table 2. Fe(III)TPPF$_{20}$ NPs catalysis of cyclohexene oxidation

solution or NP	*conditions*	*% oxide*	*% ene-1-ol*	*% ene-1-one*	*TON#*	*Reaction time*
solution	CH_3CN/CH_3OH H_2O_2	98	<1	<1	350	15 min
solution	CH_3CN/CH_3OH H_2O_2	95 ±5	5±1	<1	not reported	cyclooctene, 15 min
10 nm NP	H_2O_2	<1	30	70	175	ca. 5 min
10 nm NP	6.5 mL O_2	<1	26	74	500	O_2 limiting reagent 16 hrs
10 nm NP	125 mL O_2	<1	28	72	3500	16 hrs

Data are from reference (*4*).

A solution of Fe(III)TPPF$_{20}$ in acetonitrile/methanol catalytically oxidizes cyclohexene to the epoxide using H_2O_2 with a TON of ca. 350. Previous reports using cyclooctene as a substrate parallel these results in that only the epoxide is formed and hydrogenperoxide is required (*26*, *29–31*). In contrast, 10 nm diameter Fe(III)TPPF$_{20}$ NPs catalytically oxidize cyclohexene using O_2 to yield only the 2-cyclohexene-1-one and the 2-cyclohexene-1-ol with ca. 10-fold greater TON than the completely solvated metalloporphyrin (Table 2).

These catalytic NPs of Fe(III)TPPF$_{20}$ demonstrate that greener chemical transformations can be accomplished because the reaction solvent is 89% water and the (ultimate) oxidizing agent is O_2 in place of a synthetic oxygen source. Whether or not this reaction is general for other metalloporphyrins is currently under investigation. Nonetheless, the observed reactivity is unexpected because the metalloporphyrins are in close proximity and oxidative degradation of the catalyst should be enhanced, thereby reducing the TON. The allylic products suggest a different oxidative mechanism compared to that of the solvated metalloporphyrins. The mechanisms of hydrocarbon oxidation by iron porphyrins and other metalloporphyrins depends on both the specific molecule under investigation and the conditions used. The dominant proposed mechanisms are: (1) a radical hydrogen-abstraction–oxygen-rebound mechanism, and (2) an oxygen (or hydroxyl) insertion reaction that proceeds through a cationic ROH_2^+ species. In the case of the Fe(III)TPPF$_{20}$ NPs, our working hypothesis is that the close proximity of the iron porphyrins in the NP facilitates the formation of μ-dioxo-bridged dimers and/or μ-oxo-bridged dimers which have known catalytic activity only at elevated temperature (*28*), and may contribute to the overall stability of the NPs. A plausible mechanism for the increased TON is that the metalloporphyrins on the outermost surface of the NPs are held in a supramolecular organization that diminishes the rate of oxidation of one macrocycle by another. When the porphyrins on the exterior of the NPs eventually decompose, they fall off because of the greatly increased polarity of the oxidized product, thereby exposing the next layer of catalytically active molecules. This '*onion-type*' called mechanism and the presence of the oxo-bridged dimers may account for the slow rates of catalysis by the present NPs since fewer catalytic sites are available at a given time. A second consideration is the local concentration of the substrate. Since cyclohexene is hydrophobic and the reaction solvent is mostly water, the organic substrate can rapidly partition into the NPs containing the organic solvent and the PEG. The partitioning significantly increases the concentration of the substrate proximal to the catalytic sites.

The organization of the metalloporphyrin molecules in the NPs may allow the local structure to adapt to a variety of substrates with different topologies. Preliminary work shows that the allylic ketones and alcohols of d-limonene are formed under the same conditions.

Clearly, a variety of inorganic and metallic NP systems can be superior alkene oxidation catalysts compared to the present metalloporphyrin NPs in terms of TON (*32*). Though the epoxide is versatile intermediate, there are numerous organic transformations requiring mild allylic oxidation (*33*). However, given the great variety of porphyrins and their metal complexes, the full potential of self-organized organic nanoparticles of these systems has to be ascertained. Since the Fe(III)TPPF$_{20}$ NPs catalyst system represents an advance in green chemistry research, because there are only few molecule-based catalysts that operate in water and activate oxygen under mild conditions, there is significant motivation to develope these types of catalysts. The halogenations of the phenyl group and/or on the periphery of the porphyrin ring is known to increase the catalytic activity but not the stability towards their self oxidative degradation (*26*). We synthesized Fe(III)TPPF$_{84}$ using our previously reported method (*11*) on the synthesis of free base TPPF$_{100}$. The detailed catalytic properties of this new synthesized porphyrin are under investigation. Initial findings shows that 12 nm diameter nanoparticles of Fe(III)TPPF$_{84}$ are catalytically active for the oxidation of cyclohexene under similar conditions (using O_2 with NPs in ca. 89% water) and gives the same allylic oxidation products as for the Fe(III)TPPF$_{20}$ nanoparticles. The yields are about half, 670 TON, but in contrast to the previously reported system, the Fe(III)TPPF$_{84}$ was found to be stable towards self-oxidative degradation when the catalytic oxidation reaction is run exhaustively such that about 26% of the porphyrin remains. The nanoparticles of Fe(III)TPPF$_{84}$ are presently found to be less active than NPs of Fe(III)TPPF$_{20}$ which may be because of the formation of their μ-oxo and/or μ-dioxo dimers which are reported to be catalytically inactive (*34*, *35*). The low catalytic activity may also be because of the presence of the long fluorinated alkyl chains on the para positions of the phenyl group, which may block access to the central iron, where the oxygen is activated. The Fe(III)TPPF$_{84}$ catalyst system needs to be optimized.

4. Conclusion

The ability of making devices by using purely supramolecular chemistry is desirable because of the ease of preparation and commercial viability, along with the added benefit of a potentially reduced environmental impact. The remarkable properties of porphyrin dyes can be improved by functionalization with perfluoroalkanes which foster the formation of robust ultra-thin films and by taking advantage of a variety of non-covalent interactions to form nanoparticles. The properties of these materials with fluorous porphyrins at the nanoscale are yet to be fully explored. These and similar systems open the route for burgeoning opportunities to new studies in the field of fluorinated nanomaterial for catalysts, sensors, photonics, and energy applications.

Acknowledgments

Supported by the National Science Foundation (CHE-0847997 to CMD); Hunter College Science infrastructure: NSF, National Institutes of Health, including (RCMI, G12-RR-03037) and CUNY.

References

1. Smith, K. M. In *The Porphyrin Handbook*; Kadish, K.; Smith, K.; Guilard, R., Eds.; Academic Press of Elsevier Science: New York, 1999; Vol. 1, pp 1−40.
2. Drain, C. M.; Varotto, A.; Radivojevic, I. *Chem. Rev.* **2009**, *109*, 1630–1658.
3. Rio, Y.; Rodrıguez-Morgade, M. S.; Torres, T. *Org. Biomol. Chem.* **2008**, *6*, 1877–1894.
4. Smeureanu, G.; Aggarwal, A.; E. Soll, C.; Arijeloye, J.; Malave, E.; Drain, C. M. *Chem. Eur. J.* **2009**, *15*, 12133–12140.
5. Cheng, K. F.; Thai, N. A.; Grohmann, K.; Teague, L. C.; Drain, C. M. *Inorg. Chem.* **2006**, *45*, 6928–6932.
6. Drain, C. M.; Smeureanu, G.; Patel, S.; Gong, X.; Garno, J.; Arijeloye, J. *New J. Chem.* **2006**, *30*, 1834–1843.
7. Umeyama, T.; Imahori, H. *Photosynt. Res.* **2006**, *87*, 63–71.
8. Boyd, P. D. W.; Reed, C. A. *Acc. Chem. Res.* **2005**, *38*, 235–242.
9. Samaroo, D.; Vinodu, M.; Chen, X.; Drain, C. M. *J. Comb. Chem.* **2007**, *9*, 998–1011.
10. Samaroo, D.; Soll, C. E.; Todaro, L. J.; Drain, C. M. *Org. Lett.* **2006**, *8*, 4985–4988.
11. Varotto, A.; Todaro, L.; Vinodu, M.; Koehne, J.; Liu, G.-y.; Drain, C. M. *Chem. Commun.* **2008**, 4921–4923.
12. Hosseini, A.; Hodgson, M. C.; Tham, F. S.; Reed, C. A.; Boyd, P. D. W. *Cryst. Growth Des.* **2006**, *6*, 397–403.
13. Guldi, D. M. *Chem. Soc. Rev.* **2001**, *31*, 22–36.
14. D'Souza, F.; Ito, O. *Coord. Chem. Rev.* **2005**, *249*, 1410–1422.
15. Guldi, D. M.; Prato, M. *Acc. Chem. Res.* **2000**, *33*, 695–703.
16. Olmstead, M. M.; Nurco, D. J. *Cryst. Growth Des.* **2006**, *6*, 109–113.
17. Kirsch, P. *Modern Fluoroorganic Chemistry: Synthesis, Reactivity, Applications*; Wiley-VCH: Weinheim, Germany, 2004; pp 203−277.
18. Sandford, G. *Tetrahedron* **2003**, *59*, 437–454.

19. Carstens, P. A. B.; Marais, S. A.; Thompson, C. J. *J. Fluorine Chem.* **2000**, *104*.
20. Johns, K.; Stead, G. *J. Fluorine Chem.* **2000**, *104*, 5–18.
21. Hosseini, A.; Taylor, S.; Accorsi, G.; Armaroli, N.; Reed, C. A.; Boyd, P. D. W. *J. Am. Chem. Soc.* **2006**, *128*, 15903–15913.
22. Kim, H.-C.; Park, S.-M.; Hinsberg, W. D. *Chem. Rev.* **2010**, *110*, 146–177.
23. Masciangioli, T.; Zhang, W.-X. *Environ. Sci. Technol.* **2003**, *37*, 102–108.
24. Gong, X.; Milic, T.; Xu, C.; Batteas, J. D.; Drain, C. M. *J. Am. Chem. Soc.* **2002**, *124*, 14290–14291.
25. Battioni, P.; Renaud, J. P.; Bartoli, J. F.; Reinaartiles, M.; Fort, M.; Mansuy, D. *J. Am. Chem. Soc.* **1988**, *110*, 8462–8470.
26. Stephenson, N. A.; Bell, A. T. *J. Am. Chem. Soc.* **2005**, *127*, 8635–8643.
27. Lyons, J. E.; Ellis, P. E.; Myers, H. K. *J. Catal.* **1995**, *155*, 59–73.
28. Evans, S.; Smith, J. R. L. *J. Chem. Soc., Perkin Trans. 2* **2001**, 174–180.
29. Stephenson, N. A.; Bell, A. T. *Inorg. Chem.* **2007**, *46*, 2278–2285.
30. Stephenson, N. A.; Bell, A. T. *Inorg. Chem.* **2006**, *45*, 2758–2766.
31. Stephenson, N. A.; Bell, A. T. *Inorg. Chem.* **2006**, *45*, 5591–5599.
32. Andrus, M. B.; Lashley, J. C. *Tetrahedron* **2002**, *58*, 845–866.
33. Shing, T. K. M.; Yeung, Y.-Y.; Su, P. L. *Org. Lett.* **2006**, *8*, 3149–3151.
34. Meunier, B. *Chem. Rev.* **1992**, *92*, 1411–1456.
35. Merlau, M. L.; Cho, S. H.; Sun, S. S.; Nguyen, S. T.; Hupp, J. T. *Inorg. Chem.* **2005**, *44*, 5523–5529.

Chapter 5

Ligand Effects and Synthesis of $NaYF_4$ Based Up and Downconversion Colloidal Nanophosphors

Jingning Shan,*,[1] Nan Yao,[2] and Yiguang Ju[1]

**[1]Department of Mechanical and Aerospace Engineering,
Princeton University, Princeton, New Jersey 08544
[2]Princeton Institute for the Science and Technology of Materials,
Princeton University, Princeton, New Jersey 08544
*jshan@princeton.edu**

The effects of ligands on the synthesis of colloidal $NaYF_4$:Yb,Er upconversion nanophosphors (UCNPs) are reviewed. New results of using stearic acid (SA) and lauric acid (LA) and their combination with trioctylphosphine (TOP) as the ligands are compared with the commonly used oleic acid (OA). The strong dependence of crystallinity and monodispersity of nanophosphors (NPs) on the steric effect of ligands as well as the synthesis temperature and precursor concentrations are summarized. Synthesis and characterization of the core/shell structured UCNP/$NaYF_4$, DCNP (downconversion nanophosphors, $NaYF_4$:Eu)/UCNP, and UCNP/DCNP NPs are also presented.

The lanthanide ions (Ln^{3+}) doped phosphors have received much attention in many areas of modern science and technology including lighting and display, security, solar cells, laser, and bionanotechnology owing to their unique *f-f* orbital electronic transitions (*1*, *2*). Visible emissions from these phosphors can be excited via either an upconversion (UC) process using near infrared source (e.g., 980 nm diode laser) or a downconversion (DC) process employing UV (or X-ray) source. Selection of a proper host material for doping Ln^{3+} has been playing one of the key roles to achieve efficient luminescence. Fluorides, e.g.,

In Fluorine-Related Nanoscience with Energy Applications; Nelson, D., et al.;
ACS Symposium Series; American Chemical Society: Washington, DC, 2011.

$NaYF_4$ and LaF_3 and oxides, e.g., Y_2O_3 and Y_2O_2S are the two most widely used hosts. Traditional syntheses have been focused on the solid state reaction and hydrothermal method to prepare these fluoride and oxides based phosphors, which usually produce the particles with broad size distribution and irregular morphology. As a result, it is difficult to correlate the photophysical properties of the ensemble particles with the synthetic conditions, especially when the synthesis is down to the nanoscale. This further limits the fundamental studies and research design to achieve efficient nanophosphors (NPs) for the above mentioned energy and biological applications. There has been therefore increasing need on the controllable synthesis of lanthanides doped UC- and DC-NPs.

Synthesis of colloidal inorganic nanocrystals via a thermal decomposition of organometallic precursors in coordination solvents with or without non-coordination solvents has been actively studied in the past two decades (*3*, *4*). It has been found that surfactant molecules can significantly affect nucleation and growth of a nanocrystal and photophysical properties of the final ensemble particles. During the past five years, the same co-thermolysis method was introduced to prepare colloidal lanthanides doped NPs (*5*, *6*). These NPs can be prepared in either hydrophilic or hydrophobic ligation. Key factors controlling the synthesis are surfactants, precursor ratios, and reaction time and temperature. In this work, the ligand (or surfactant) effects on the synthesis of the fluoride based hydrophobically-ligated $NaYF_4$:Yb,Er UCNPs are reviewed and new results are presented for the first time. Synthesis of core/shell structured NPs combining both UCNPs and DCNPs are also reported.

Experimental Details

Synthesis

The UCNPs were synthesized according to our previous work (*7*, *8*). A typical procedure is following: Synthesis of OA-TOP coated β-NaYF4:Yb,Er UCNPs was carried out using the standard oxygen-free procedures. For example, for 100 nm $NaYF_4$:Yb(20%),Er (2%) UCNPs, a mixture of 2.81 mmol Na(TFA), 1.46 mmol $Y(TFA)_3$, 0.375 mmol $Yb(TFA)_3$, and 0.0375 mmol $Er(TFA)_3$ was dissolved in OA/TOP/ODE (Octadecene, non-coordination solvent) (2 mL/2 mL/16 mL). Under vigorous stirring in a 50 mL flask, the mixture was first heated in an oil bath at 100 °C under vacuum for 30 min to remove water, and then nitrogen was purged into the solution periodically. In the presence of nitrogen, the solution was then heated with a heating mantle to reflux temperature (~ 315 °C) within 10 - 15 min, and the reaction was stopped after one hour heating at reflux. The cooled solution was divided into two centrifuge tubes (45 mL) and added by ethanol (30 mL) to precipitate UCNPs. The UCNPs were isolated by centrifugation and were washed by excess ethanol at least three times. After washing, the product was left to dry at atmosphere and the yield was between 250 – 300 mg. Na/Re ratios were varied to prepare *β*-UCNPs in different size, and we found the yield was slightly increased with Na/Re ratios. Synthesis performed in other ligands or ligand combination followed the same routes above and all reactions were heated at refluxing. Minor changes on ligand and precursor ratios were shown in the Figure captions.

Core/shell synthesis followed two-step synthesis according to the literatures (*9*). A typical procedure synthesizing UCNP/$NaYF_4$ core/shell is: ca. 50 mg core UCNPs were dissolved in OA/TOP/ODE (2 mL/2 mL/16 mL) with 2 mmol of Na(TFA) and 1.0 mmol $Y(TFA)_3$. The mixture was heated to reflux temperature and maintained for 2 hrs. After that, the same purification processes were performed as those of core NPs.

Characterization

TEM images of UCNPs were obtained using a LEO/Zeiss 910 TEM equipped with a PGT-IMIX EDX system (100 KeV). With a field-emission-gun, this microscope provides a point-to-point resolution of 0.2 nm and uses an electron probe of 0.7 nm with energy up to 200 KeV. Powder X-ray diffractometer (XRD, 30 kV and 20 mA, CuKα, Rigaku) was used for crystal phase identification. The powders were pasted on an alumina substrate and the scan was performed in the 2θ range of 10° to 70°.

The UCL intensities and UC emission spectra were measured and compared on a thin solid sample pellet. The samples were excited using a Thorlabs F240FCB collimated Qphotonics 975 nm diode laser, driven with a Thorlabs LDC3065-488 High Power Laser Diode Driver. The beam was focused (50 mm focal length) on a spot size of approximately 1 mm in diameter. The UCL signal was focused again by a spherical lens and then collected by a monochromator (SP-2500i, Princeton Instruments) with a 2400 g/mm grating (holographic, 400-700 nm). The signal was detected by a photomultiplier module (H6780-04, Hamamatsu) and was amplified by a lock-in amplifier (SR510, Stanford Research Systems) together with an optical chopper (SR540, Stanford Research Systems). The signal was recorded under computer control using the SpectraSense software data acquisition/analyzer system (Princeton Instruments, Trenton, New Jersey).

Ligand Effects

Single Ligand and Combination Ligands

Colloidal $NaYF_4$:Yb,Ln (Ln = Er, Ho, and Tm) UCNPs have been prepared via the co-thermolysis of trifluoroacetate precursors in the presence of various coordinating ligands to control synthesis and UC luminescence. $NaYF_4$ based NPs can be produced as cubic (α) or hexagonal (β) phase crystalline structures, but the β-phase $NaYF_4$ is the most efficient host for UC photoluminescence (*10*, *11*). The selection of a proper coordinating ligand or ligand combinations dictates the particle nucleation and growth, and is one of the key factors for achieving monodisperse and size-tunable colloidal UCNPs. In the co-thermolysis method, oleic acid (OA) (*12–15*), oleylamine (OM) (*16*, *17*), trioctylphosphine (TOP) (*18*), trioctylphosphine oxide (TOPO) (*8*), and OA-TOP (*18*, *19*) ligands have been studied and proved to be effective in coating the $NaYF_4$ based NPs to prevent particle aggregation and control the particle nucleation and growth. Considering the particle sizes of β-UCNPs achieved using these ligands, reaction in OA could produce plate-shaped particles as large as 300 nm in a two step synthesis (*15*);

a more size tunable and shape controllable synthesis can be achieved by using OA-TOP combination ligand via a single-step co-thermolysis in which the prims-shaped β-UCNPs ranging from 18 nm to 200 nm were achieved (*7*). In both OA and OA-TOP ligands, precursor ratios were shown to be crucial in controlling the NP size and shape.On the other hand, synthesis in OM and TOPO ligands has only produced β-UCNPs less than 20 nm and meanwhile required reaction temperature above 330 °C (*8*, *16*). Since the boiling point of the OM is ca. 330 °C, the temperature window to achieve β-UCNPs in OM is very narrow. In our work using OM as the ligand, we observed that the UCNPs were usually in mixed α and β crystalline phases. A prolonged heating would result aggolomerated particles in a broad size distribution (*8*). TOPO has allowed synthesis to be conducted as high as 370 °C and produced particles in a high monodispersity. However, the organic solubility of the TOPO coated UCNPs were not satisfactory and there were still in short of reports on surface modifications. Using both OM and TOPO ligands, precursor ratios did not show observable effects on the synthesis. Although the synthesis using TOP only produced α-UCNPs, which could be be attributed to the low boiling point of TOP, ca. 280 °C, the combination of TOP with OA ligand has presented interesting effects in controlling and growing β-UCNPs (*18*).

Overall, it is unknown how ligand properties (e.g., molecular structure) affect particle size and crystalline structure. The ligand combination of OA-TOP has been proved in our work to affect the synthesis, while whether the other ligands have the combination effect has no report. Therefore at here, we examine the effects of ligand molecular structure, such as the alkyl chain length and saturation, on the morphology and crystallinity of $NaYF_4$:Yb,Er UCNPs prepared from colloidal co-thermolysis. Two fully hydrogenated ligands with different chain lengths, stearic acid (SA, 18 C) and lauric acid (LA, 12 carbon) and their combinations with TOP (SA-TOP and LA-TOP) were compared with partially unsaturated ligand, OA, and its combination with TOP (OA-TOP). Potential combination effects of the OM-TOPO, OA-TOP-OM, and OA-TOP-TOPO were also examined.

The molecular structures of the ligands used in the synthesis are shown in Fig 1. OA and SA have the same C18 chain length, but OA has double bond at C-9, which increases the steric hindrance in the molecular structure (*20*). On the other hand, LA has a shorter chain length than OA and has no carbon-carbon double bond. Our previous work used OA and OA-TOP ligands to synthesize UCNPs at precursor ratios of 2.5 (Na/Re, Re = Y, Yb and Er) (*7*). When using OA, we observed hexagonal (β) phase UCNPs with a plate shape (140 nm × 70 nm); while using OA-TOP ligand, we obtained β prism UCNPs (~ 50 nm × 50 nm). We ascribed the results to the bidentate structure formed between OA and TOP, which changed the coordination properties of OA by increasing steric hindrance of this combined ligand. In this work, we conducted synthesis by using SA, LA and combination ligands of SA-TOP and LA-TOP to gain more detailed understanding of the ligand effects, especially the steric effects. TEM images and XRD patterns of the UCNPs synthesized with the above ligands are shown in Fig. 2 and Fig. 3, respectively.

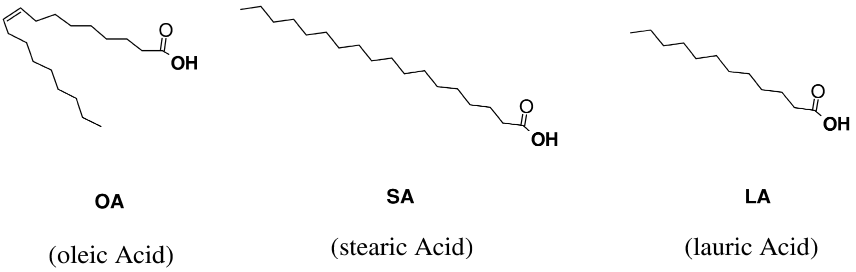
O
OH
O
OH
O
OH
OA
(oleic Acid)
SA
(stearic Acid)
LA
(lauric Acid)

Figure 1. The coordination ligands used for the synthesis of UCNPs.

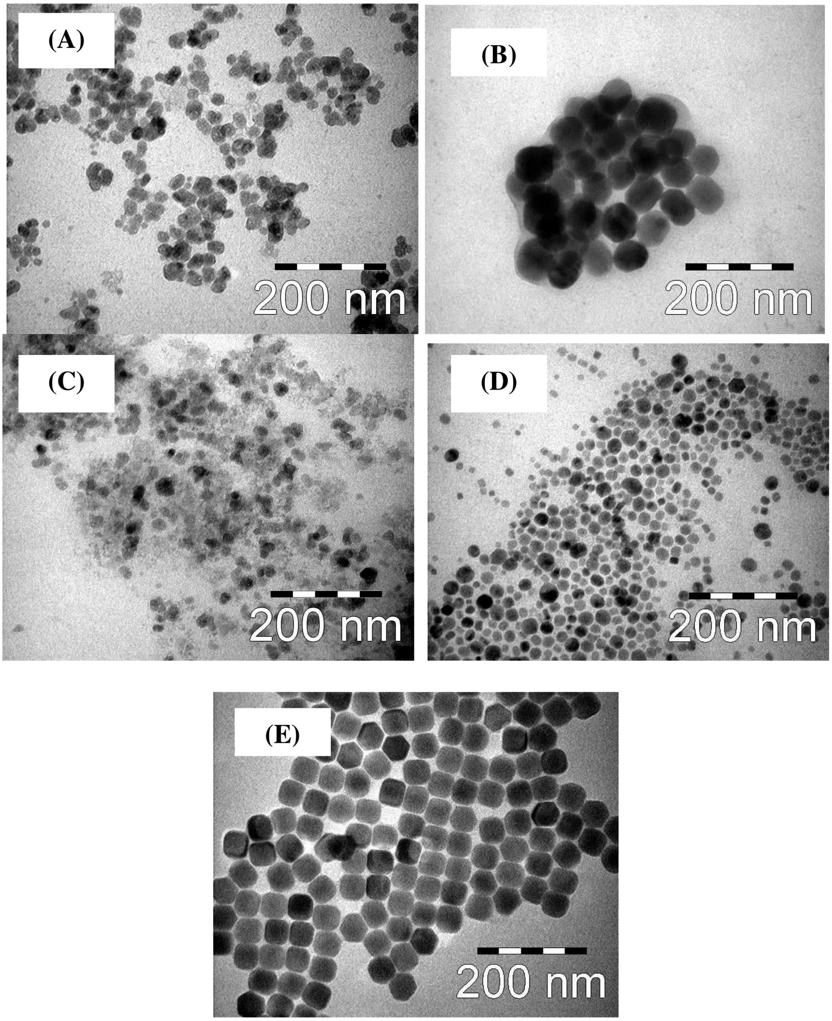
(A)
200 nm
(B)
200 nm
(C)
200 nm
(D)
200 nm
(E)
200 nm

Figure 2. TEM images of the UCNPs synthesized in (A) SA, (B) SA-TOP, (C) LA, (D) LA-TOP and (E) OA-TOP.

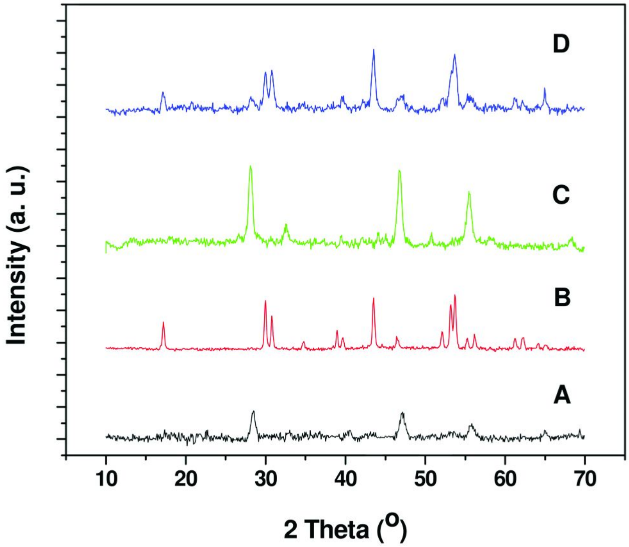

Figure 3. XRD patterns of the UCNPs synthesized in ligands of (A) SA, (B) SA-TOP, (C) LA, and (D) LA-TOP. (A) and (C) match the cubic phase of NaYF$_4$ (JCPDS File No. 6-0342), (B) matches hexagonal phase of NaYF$_4$ (JCPDS File No. 28-1192). (D) shows the mixed cubic and hexagonal phases.

TEM images (Fig. 2) of the UCNPs synthesized in SA (2A) and LA (2C) show irregular particle shapes with a broad size distribution, which indicates that the growth of the NPs underwent a “burst of nucleation” during formation of the cubic (α) phase NPs without α→β phase transition (*15*, *19*). The α-phase NPs were proved by the XRD diffraction patterns in Fig. 3 (3A) and (3C). When using the combination ligand of SA-TOP, pure β-phase UCNPs were obtained (3B), while in LA-TOP, mixed α and β phase NPs resulted (3D). For comparison, a TEM image of the β-phase UCNPs synthesized in OA-TOP is shown in Fig. 2 (2E).

The growth of colloidal β-NaYF$_4$:Yb,Er UCNPs in this work can be classified into three stages: i) formation of α-phase UCNPs, ii) α→β phase transition, and iii) formation of β-phase UCNPs. The observations suggest that there are strong ligand effects on the second stage of α→β phase transition process.

The ligand effects on the nucleation, growth, and properties of colloidal nanocrystals were classified as two types, effects on monomers and effects on nanocrystals (*4*, *21*). The bonding strength between ligands and cations affected surface energy of the crystals and the entire phase transition process. In this work, since the α-phase NPs were produced via “burst of nucleation”, the bonding strength between ligands and fluoride monomers (NaF and ReF$_3$, Re = Y, Yb and Er) that were produced by decomposition of trifluoroacetate precursors had little effect in the first stage. In the second stage, ligands with longer hydrocarbon chains have more steric hindrance and, therefore they introduce greater steric stabilization than ligands with short chains, resulting in easier for the α→β phase transitions. For the ligands used in this work, a double bond at C-9 in OA gives it more steric protection on UCNPs than SA (*20*), meanwhile both OA and SA have longer chains than LA. The addition of TOP ligand into SA and LA produces more steric stabilization than the single ligands alone (*19*). Our experimental results confirm that the α-phase NPs were more easily transformed to the β phase when the larger ligands were being used. The greater steric structure decreases the bonding strength, while on the other hand, increases exchange rates between the monomers/NPs and ligands over the course of crystal growth. Since the formation of the β-phase UCNPs involves the re-dissolving of the α-phase UCNPs (*15*, *19*), the more sterically structured ligands should facilitate the transition process, which explains why the synthesis in OA-TOP, the most sterically structured combination ligand, produced the best UCNPs, with respect to their crystallinity and monodispersity (Figure 2 (2E)). It should be mentioned that besides ligand effects, reaction temperature and precursor ratios (Na/Re) can also affect the α→β phase transition process synergetically, so these have been held constant for all of these UCNP syntheses.

The UC emission spectra of the UCNPs synthesized in SA, LA, SA-TOP and LA-TOP ligands are shown in Fig. 4. The UC spectra of both α and β-phase UCNPs display emission peaks at 520.8, 545, and 658.8 nm for the Er doped UCNPs excited at 980 nm, which were ascribed to $^4H_{11/2}$ to $^4I_{15/2}$, $^4S_{3/2}$ to $^4I_{15/2}$, and $^4F_{9/2}$ to $^4I_{15/2}$ transitions for Er^{3+}, respectively (*5*). The two phases have different green/red intensity ratios for the UCNPs synthesized in SA, LA, SA-TOP and LA-TOP ligands with the same stoichoimetric precursors, which are 0.29, 0.24, 2.21 and 1.96, respectively. The results indicate that SA and LA ligands can be used to prepare $NaYF_4$:Yb,Er UCNPs in addition to the previously reported OA ligand. The UCNPs in α-phase show good red emissions while the β-phase UCNPs have strong green emissions.

Other Combination Ligands

Although the combination ligand of OA-OM has been used to synthesize $NaYF_4$ based UCNPs, the role of OM was more like a stabilizer (*14*). To explore more effects of combination ligand studied in this work, we performed the synthesis using the systems of OA-TOP-OM/ODE and OM-TOPO/ODE, OA-TOP-TOPO, and results are shown in Fig. 5.

Results in Fig. 5 (A) show two distinct particles, indicating that OM and OA-TOP ligands have controlled the synthesis separately. The bigger NPs are the typical α-UCNPs produced from "burst of nucleation". After reducing the OM down to 0.5 mL, the particles due to the OM controlling were not observed (Fig. 5 (B)). However, the α-UCNPs were still present in the solution without transforming into β-UCNPs even after two more hours reaction. By performing the synthesis using OM-TOPO combination ligands and reaction was heated at 330 °C, there were only α-UCNPs observed (proved by XRD, data not shown) and the particles were extremely small, ca. 2-3 nm. The above results confirmed that OM in a ligand combination system had the role of hindering the growth of α-UCNPs (*14*). Since the formation of β-UCNPs needs first to form and then re-dissolve the α-UCNPs, it is then not surprising that the OM found to retard the α→β phase transition in this work.

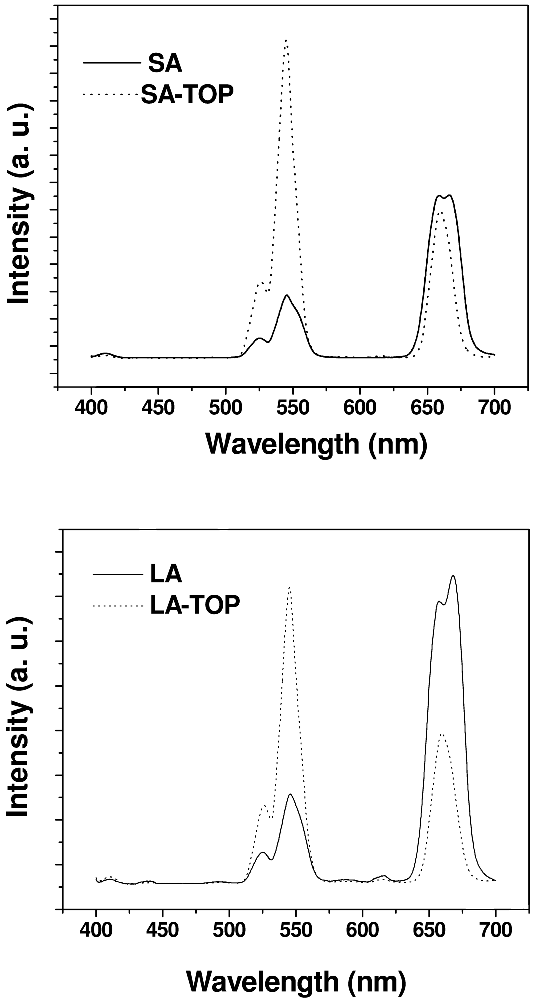

Figure 4. UC emission spectra of the UCNPs synthesized in SA, LA and combination ligands. Intensity was adjusted for comparison.

When adding TOPO in OA-TOP system, we did not observe the hindrance effect of TOPO. If TOPO was added in a large amount, the growth of UCNPs was controlled by OA-TOP and TOPO separately (Fig. 6 (A)). When TOPO was added in smaller amount (Fig. 6(B)), the reaction was only controlled by OA-TOP combination ligand.

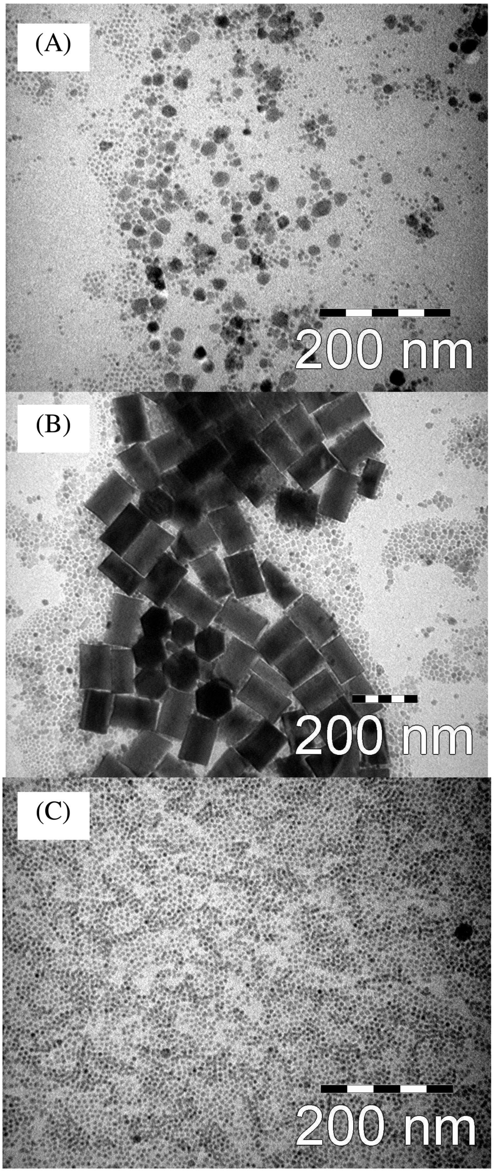

Figure 5. TEM images of the UCNPs synthesized in (A) OA/TOP/OM (6 mL/4 mL/2 mL), (B) OA/TOP/OM (6 mL/4 mL/0.5 mL), and (C) TOPO/OM (6 g/4 g) at Na/Re = 1.2/1. In reaction (A) and (B),ODE was added to adjust the total volume to 20 mL.

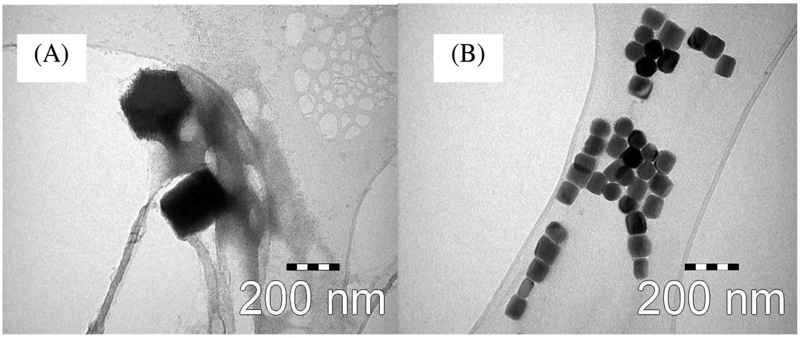

Figure 6. TEM images of UCNPs synthesized in (A) OA/TOP/TOPO (2.5 mL/2 mL/8g) and (B) OA/TOP/TOPO (2.5 mL/2 mL/2g) at Na/Re = 1.2/1.

Synthesis and Characterization of Core/Shell Structured NPs

UCNPs/NaYF$_4$ Core/Shell NPs

Growing a shell of NaYF$_4$ onto NaYF$_4$:Yb,Ln UCNPs was first reported by Yi and Yan et al. on OM and OA coated UCNPs, respectively (*17*, *22*). Later, Zhang et al. developed multilayer core/shell/shell structured NPs (*9*). A two-step core/shell growth, viz., isolating the core UCNPs and then reacting with the shell precursors has been employed. So far, indirect methos were applied to prove the successful shell growth, such as using XPS to detect elemental compositions of the NPs or simply comparing the UC luminescence efficiency of the core and core/shell NPs. On the other hand, we noice that that synthesis of the core/shell NPs have been focused on the particle sizes smaller than 50 nm. In this work, to find direct and in-situ proof of the shell growth, we followed the two-step synthesis route to synthesize core/shell structured NPs using OA-TOP combination ligand. TEM images of the NPs collected from the synthesis are shown in Fig. 7.

From Fig. 7 (B), it can be seen that there are small particles, which are most probably the α-NaYF$_4$ particles, attaching onto the large core UCNP surface (Fig. 7 (A)). After prolonged heating, these small particles grew larger and formed a solid thin layer. The layer contrast between the core and shell is clearly shown in Fig. 7 (C). It should be mentioned if excess shell precursors were added at the beginning, there would be more independent shell particles produced. More experimentation is required to to find the right precursor amounts for the shell growth.

DCNP and UCNP Core/Shell NPs and Fluorescence Spectroscopy

After figuring out conditions to grow core/shell NPs using OA-TOP ligand, we synthesized a series of core/shell structured NPs by combining UCNPs and DCNPs, and then investigated their photophysical properties. Table 1 summaries the core and core/shell NPs combining DCNPs and UCNPs in this work. Fig.

8 shows the corresponding TEM images in Table 1. Fig. 9 and 10 present the fluorescence spectroscopy of the UC and DC emission spectra.

In Fig. 8, a clear core/shell formation is seen from the size difference before and after the two step shell growth. For the synthesis of core NPs (Fig. 8 (A) and (C)), and mixed DC-UC NPs, although a strict Na/Re (Re = Eu, Yb, Er and Y) ratio of 2.5 was added, the particle sizes have a large difference, which indicating that Eu and Yb/Er ions have different mechanism in controlling the nucleation and growth of the NPs. Fluorescence data in Fig. 9 and 10 show that the core/shell NPs have significant effects on the UC emission efficiency, but not on DC emission. In Fig. 9, it can be seen that growing a layer of DCNPs onto UCNPs increases the UC emission intensity over 100% in comparison with the core NPs. This could be attributed to the removing of the surface defect on UCNPs after growing a shell layer. While the mixed DC-UC NPs, on the other hand, have much decreased UC emission intensity. The reason might be due to the increased non-radiative inter-ion cross relaxation. In Fig. 10, interestingly, all DC emission luminescent efficiency does not shown much difference. This indicates that the surface properties have little influence on the down conversion emission for the energy transfer in Eu ions.

The deeper photophysical fundamental studies are still needed to address the above photophysical observations, while the experimental results at here should be instructive for the future synthesis of core/shell structured NPs aimed at potential energy and biological applications.

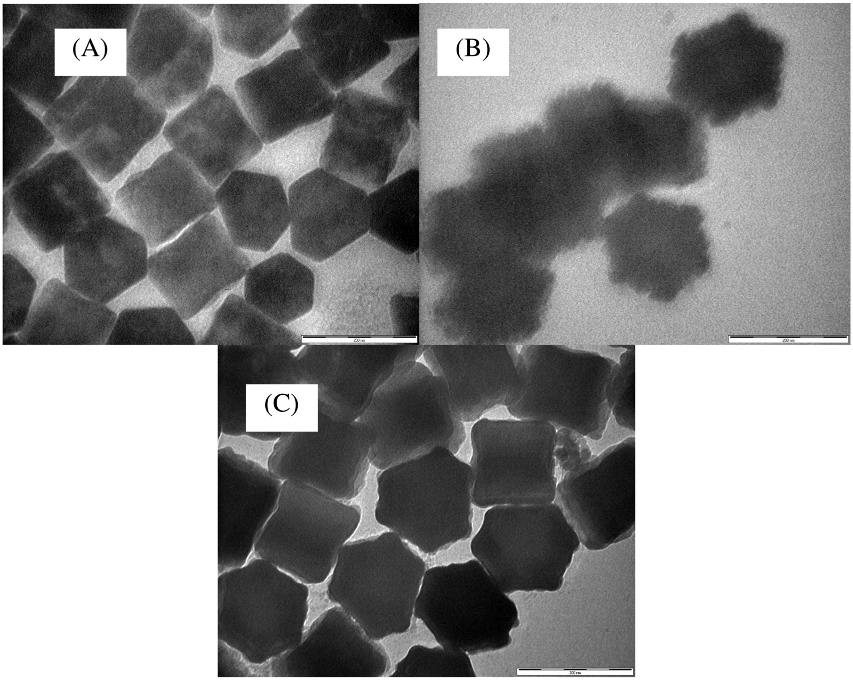

Figure 7. TEM proof of a two-step growth of core/shell NaYF$_4$:Yb,Er/NaYF4 nanophosphors (Scalar bar = 200 nm).(A) Core UCNP, (B) After 1 hr growth of NaYF4 shell, and (C) After 2 hrs growth.

Table 1. Summary of NP sizes

NPs	*UCNPs*	*UCNP/ DCNP*	*DCNP*	*DCNP/ UCNP*	*Mixed (DC+UC)NPs*
Size (nm) (± 1.7)	45.2	66.1	69.6	87.0	83.5
Fig. 8	A	B	C	D	E

UCNPs = $NaYF_4$:Yb(20%),Er(2%). DCNPs = $NaYF_4$:Eu(5%).

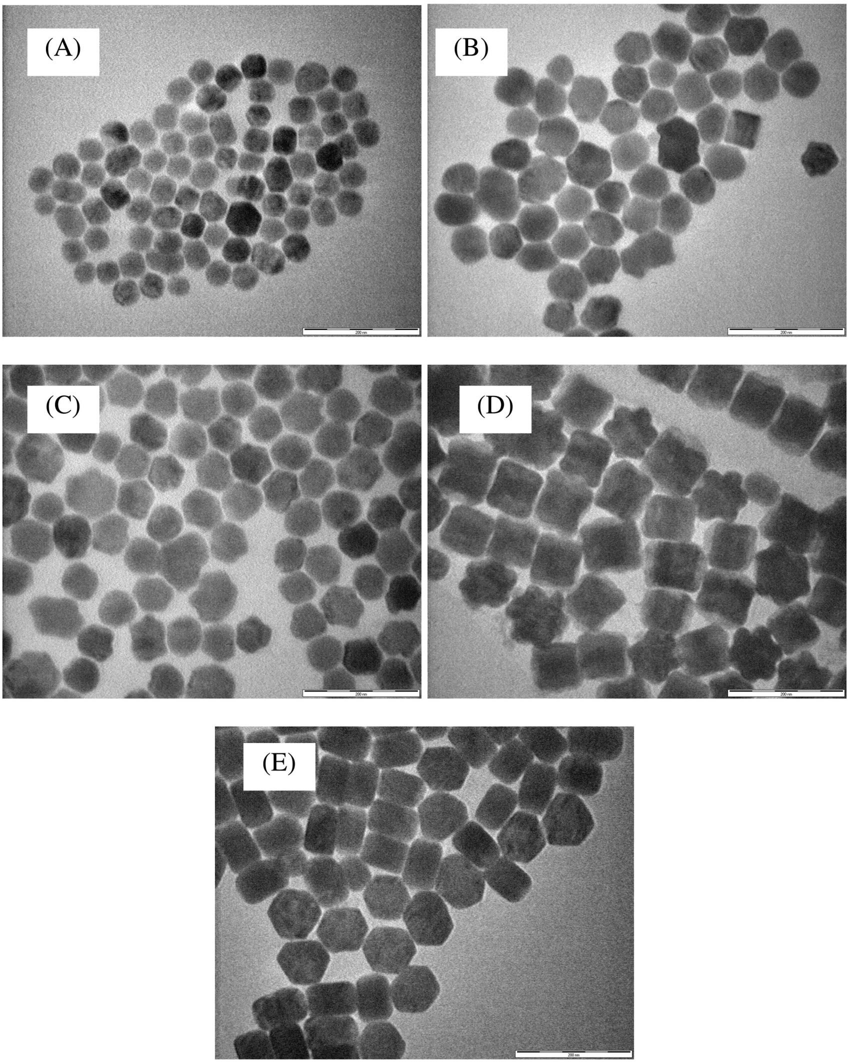

Figure 8. TEM images of core and core/shell combining DCNPs ($NaYF_4$:Eu) and UCNPs ($NaYF_4$:Yb,Er). (A) Core DCNPs, (B) Core/shell DCNP/UCNP, (C) Core UCNPs, (D) Core/shell UCNP/DCNP, and (E) Mixed (DC+UC)NPs. (Scalar bar = 200 nm).

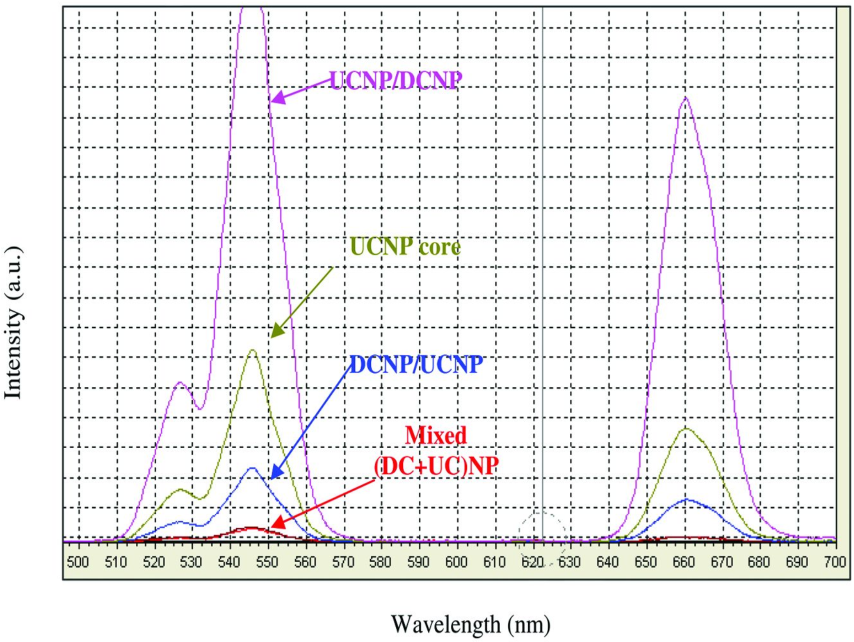

Figure 9. Upconversion emission spectra of the NPs from Figure 8 at excitation of 980 nm.

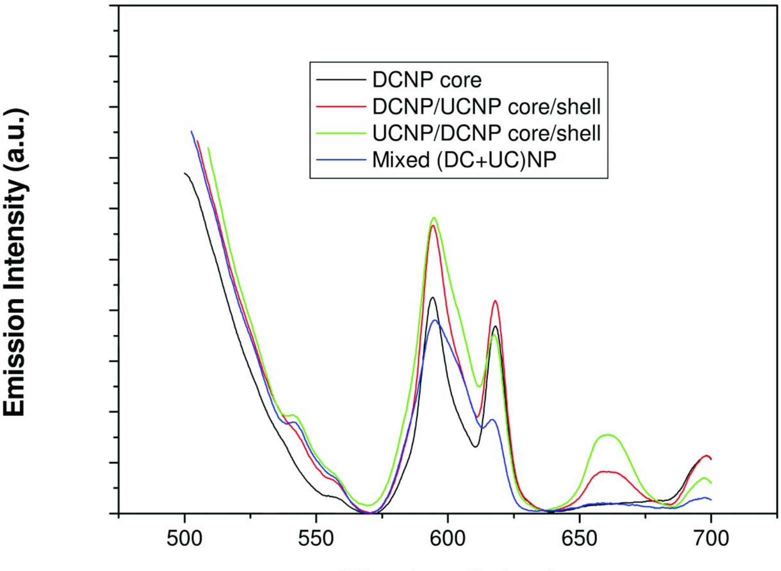

Figure 10. Downconversion emission spectra of the NPs from Figure 8 at excitation wavelength of 365 nm.

Concluding Remarks

Synthesis of hydrophobically-ligated $NaYF_4$ based NPs have been shown to be successful concerning the particle size and shape controllability. We have assessed the ligand effects and demonstrated that the molecular structure of ligands has strong effects on the morphology and crystallinity of hydrophobic $NaYF_4$:Yb,Er UCNPs. The results show that the steric structure afforded by the ligand chain length, carbon-carbon double bond and combination of ligands is important to synthesize hexagonal phase hydrophobic UCNPs. TOP has combination effect due to its lone pairs. OM has the effect to hinder the NP growth, while TOPO was not found to have combination effect.

The fluorescence spectroscopy studies show that UC emission efficiency of the UCNPs is significant affected by the surface properties, while there are no surface and size effects observed on the DCNPs. The work presented here is of both fundamental understanding and technical interests.

Acknowledgments

This work was supported by the National Science Foundation MRSEC Program through the Princeton Center for Complex Materials (DMR-0819860), AFSOR and NSF NIRT.

References

1. Feldmann, C.; Justel, T.; Ronda, C. R.; Schmidt, P. J. *Adv. Funct. Mater.* **2003**, *13*, 511–516.
2. Wang, F.; Liu, X. G. *Chem. Soc. Rev.* **2009**, *38*, 976–989.
3. Peng, X. G.; Wickham, J.; Alivisatos, A. P. *J. Am. Chem. Soc.* **1998**, *120*, 5343–5344.
4. Yin, Y.; Alivisatos, A. P. *Nature* **2005**, *437*, 664–670.
5. Heer, S.; Kompe, K.; Gudel, H. U.; Haase, M. *Adv. Mater.* **2004**, *16*, 2102–2105.
6. Zhao, F.; Yuan, M.; Zhang, W.; Gao, S. *J. Am. Chem. Soc.* **2006**, *128*, 11758–11759.
7. Shan, J.; Ju, Y. *Nanotechnology* **2009**, *20*, 275603.
8. Shan, J.; Qin, X.; Yao, N.; Ju, Y. *Nanotechnology* **2007**, *18*, 445607.
9. Qian, H. S.; Zhang, Y. *Langmuir* **2008**, *24*, 12123–12125.
10. Kramer, K. W.; Biner, D.; Frei, G.; Gudel, H. U.; Hehlen, M. P.; Luthi, S. R. *Chem. Mater.* **2004**, *16*, 1244–1251.
11. Suyver, J. F.; Grimm, J.; van Veen, M. K.; Biner, D.; Kramer, K. W.; Gudel, H. U. *J. Lumin.* **2006**, *117*, 1–12.
12. Boyer, J. C.; Cuccia, L. A.; Capobianco, J. A. *Nano Lett.* **2007**, *7*, 847–852.
13. Boyer, J. C.; Vetrone, F.; Cuccia, L. A.; Capobianco, J. A. *J. Am. Chem. Soc.* **2006**, *128*, 7444–7445.
14. Mai, H. X.; Zhang, Y. W.; Si, R.; Yan, Z. G.; Sun, L. D.; You, L. P.; Yan, C. H. *J. Am. Chem. Soc.* **2006**, *128*, 6426–6436.

15. Mai, H. X.; Zhang, Y. W.; Sun, L. D.; Yan, C. R. *J. Phys. Chem. C* **2007**, *111*, 13730–13739.
16. Yi, G. S.; Chow, G. M. *Adv. Funct. Mater.* **2006**, *16*, 2324–2329.
17. Yi, G. S.; Chow, G. M. *Chem. Mater.* **2007**, *19*, 341–343.
18. Shan, J. N.; Ju, Y. G. *Appl. Phys. Lett.* **2007**, *91*, 123103.
19. Shan, J. N.; Chen, J. B.; Meng, J.; Collins, J.; Soboyejo, W.; Friedberg, J. S.; Ju, Y. G. *J. Appl. Phys.* **2008**, *104*, 094308.
20. Yordanov, G. G.; Gicheva, G. D.; Bochev, B. H.; Dushkin, C. D.; Adachi, E. *Colloid Surf., A* **2006**, *273*, 10–15.
21. Yu, W. W.; Wang, Y. A.; Peng, X. G. *Chem. Mater.* **2003**, *15*, 4300–4308.
22. Mai, H. X.; Zhang, Y. W.; Sun, L. D.; Yan, C. H. *J. Phys. Chem. C* **2007**, *111*, 13721–13729.

Chapter 6

Nanofluorides for Environmentally Benign Lighting and Energy Conversion in Solar Cells

Pushpal Ghosh, Chantal Lorbeer, and Anja-Verena Mudring*

Anorganische Chemie I – Festkörperchemie und Materialien,
Ruhr-Universität Bochum, D-44780 Bochum, Germany
***anja.mudring@rub.de**

Energy-saving lighting and the conversion of sunlight into electric energy by solar cells are both topics that are receiving a constantly growing interest both in their respective scientific communities as well as in society due to rising environmental awareness and the seek for a responsible handling of energy. Interestingly for both, lighting and solar cells, lanthanide fluorides as photonic materials are of high importance.

Fluoride materials as photonic materials provide some distinct advantages compared to other materials because of their outstanding properties such as very low phonon frequencies, high refractive index, high thermal stability and sometimes tunable crystal phases and related photo physical properties. Lanthanide ions doped into fluoride host materials display low probabilities for multiphonon relaxation resulting in long lifetimes of their excited states and high luminescence quantum efficiencies. Such properties are needed for example for quantum-cutting phosphors for improved compact fluorescent lamps or solar cells. The spectral region of sunlight, not directly available for a classical solar, cell can also be made accessible by up-converting phosphors which today also rely on fluoridic phosphors – desirably on nanosized – materials.

Introduction

Energy-efficient lighting is a contemporary important topic. It is estimated that significant amounts of electricity can be saved when more energy-efficient

In Fluorine-Related Nanoscience with Energy Applications; Nelson, D., et al.;
ACS Symposium Series; American Chemical Society: Washington, DC, 2011.

light sources were used (*1*). Various countries have already or are currently planning to ban conventional incandescent lamps (*2*) which suffer from a poor luminous efficiency since most of the energy is converted to heat and have them replaced by more environmentally benign light sources such as compact fluorescent lamps (CFLs) or light emitting diodes (LEDs). CFLs are currently the most widespread replacements. However, currently the commercial CFLs contain mercury which aside of some technical backdraws is mainly an environmental issue. Possible alternatives in which mercury is replaced by an environmentally safe noble gas rely on phosphors with improved quantum-yield, so-called quantum-cutting phosphors.

Similarly the energy loss connected to the creation of an electron-hole pair with energy greater than the solar cell material can be reduced by quantum-cutting phosphors which convert a photon of more than twice the energy of the solar cell material band gap into two photons which match the band gap energy. In analogy, photons of less energy than the band gap of the solar cell material can be converted by up-conversion phosphors to one photon with the right energy to be absorbed (*3*).

For both applications nano-sized lanthanide fluorides have come into focus (*4*). Intense research efforts are devoted to designing and tuning the emission properties of these materials with respect to the desired application. Fluoride host materials provide some distinct advantages compared to other materials such as oxide and phosphates owing to their very low phonon frequencies, high refractive index, high thermal stability, high ionicity, and wide band gap. Lanthanide ions doped into fluoride hosts display low probabilities for multiphonon relaxation process resulting in long lifetimes of their excited states and high luminescence quantum efficiencies. Different fluoride based materials such as alkali metal rare-earth fluoride ($MLnF_4$), rare-earth fluoride (LnF_3) and for certain applications also rare-earth oxy-fluorides (LnOF) have garnered tremendous attention as host materials.

In this review article, we try to focus on the broader perspective of rare-earth doped nanoparticles including synthesis, optical properties and applications against the background of their application in environmentally benign, modern lighting and energy conversion applications. We have emphasized the development on these materials which occurred in the last 10 years.

Photo-Physical Processes and Their Applications

Quantum-Cutting Phosphors for Compact Fluorescent Lamps and Solar Cells

Currently compact fluorescent lamps (CFLs) are the most popular energy saving lamps. The fluorescent tube is filled with an argon pressure of about 400 Pa and an additional mercury partial pressure of 0.8 Pa. By applying voltage, the cathode emits electrons, which are accelerated and then collide with the mercury atoms to create an excited mercury plasma (Hg*) (Figure 1). In order to release the excessive energy, the excited mercury atoms return to the ground state under emission of UV (ultra-violet) radiation The produced UV light (λ_{max} = 254 nm) is converted by phosphors on the inner side of the light tube to visible light.

Nowadays a mixture of three lanthanide-based phosphors with emission lines in the blue (Eu^{2+}, ~450 nm), green (Tb^{3+}, ~540 nm), and red (Eu^{3+}, ~610 nm) are used to generate white light (*5*).

The overall energy efficiency η of such a low-pressure mercury discharge lamp depends on the mercury discharge efficiency $\eta_{\text{discharge}}$ which is about 70% and the quantum yield which is the ratio between the number of emitted and absorbed photons

$$\eta_{lamp} = \eta_{discharge} \cdot \frac{\lambda_{UV}}{\lambda_{Vis}} \cdot QY$$

Due to the conversion of UV radiation ($\lambda_{UV} = 254$ nm) into visible light (λ_{Vis} ~ 550 nm) an energy loss of 60% is pre-assigned.

One way to improve the overall energy efficiency is to improve the performance of the discharge process. However, the mercury discharge currently is the most efficient process. Two other possibilities to increase the energy efficiency are to choose a pump source with lower photon energy as used in phosphor converted LEDs (see below) or to enhance the quantum yield of the employed phosphor.

It has also to be noted that the use of mercury has several major shortcomings. The most important are the environmental safety and health issues that have to be considered during manufacturing and for the end-of-life of such fluorescent tubes. Many consumers today are unaware of the potential risks of CFLs. Furthermore, mercury based fluorescent light tubes may need up to serveral minutes of start-up time until they reach their full light power as mercury in the tube has to be heated and evaporated first. Thus, they are not well suited to be used in combination with motion sensors. An alternative is the replacement of mercury by noble gases such as xenon in CFLs. The Xe dimer discharge results in a broad UV emission with a maximum at 172 nm. However, the discharge efficiency is lower compared to that of mercury. In addition, conversion of the yet shorter wavelength radiation to visible light results in an even larger energy loss compared to Hg based CFLs. In order to make xenon-based CFLs competitive, a quantum yield of the used phosphors larger than 100 % needs to be achieved. Quantum-cutting is a process in which an incident high energy photon is transformed by a material into more than one lower energy photon.

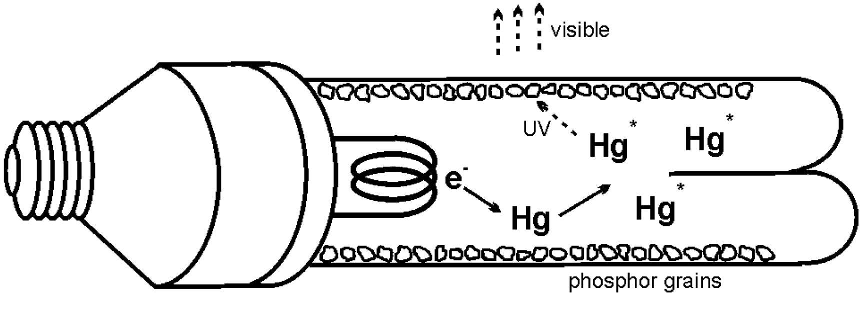

Figure 1. Schematic view of a mercury discharge lamp.

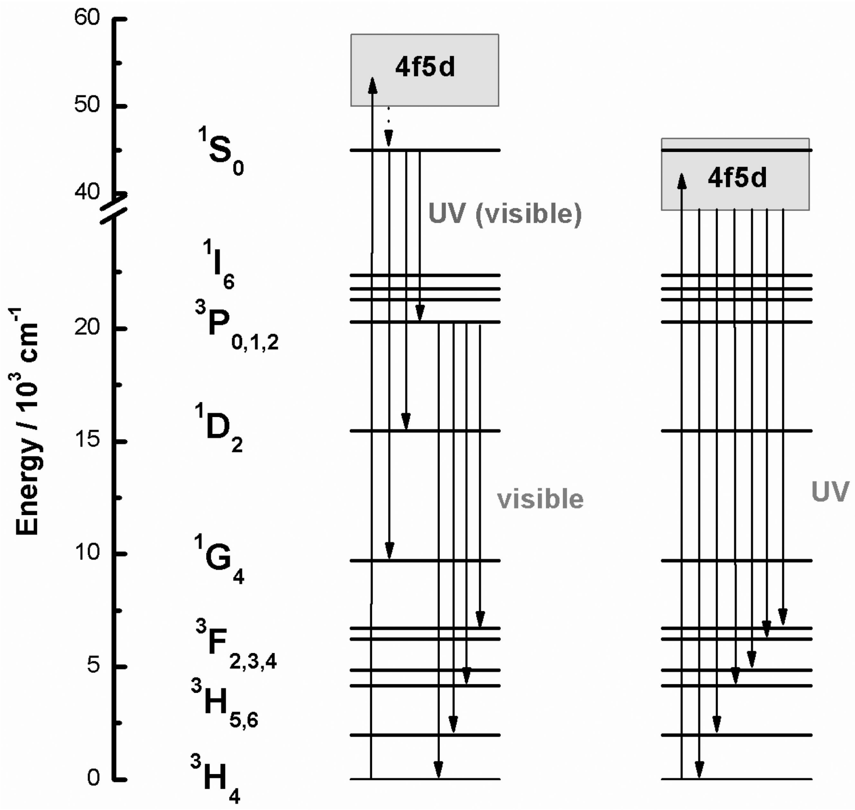

Figure 2. Schematic energy level diagram of Pr^{3+} in different host lattices (left and right), showing the possibility of visible quantum cutting by sequential emission of two photons (left).

In 1974, scientists from Philips and General Electrics independently discovered direct sequential emission of two photons (photon cascade emission) in $YF_3:Pr^{3+}$ and $NaYF_4:Pr^{3+}$ with a quantum efficiency of about 140 % (*6*). Upon irradiation of these materials with short ranged UV light electron excitation into the 4f5d band of Pr^{3+} occurs (Fig. 2; Fig. 4(a)). After non-radiative relaxation to the $^1S_0$ state transitions radiative transitions to the lower f-levels occur. The subsequent first step in the radiative decay mainly proceeds via the $^1S_0 \rightarrow {}^1I_6$, ^3P_J transition, followed by a second emission due to $^3P_0 \rightarrow {}^3H_J$, ^3F_J transitions (Fig 2, left). In spite of the high quantum yield, no applications of Pr^{3+} phosphors have been found as a result of the poor color rendering index of the deep-blue emitted radiation for the human eye. Moreover, the emission process is quite dependent on the host lattice. In many materials, the lowest 4f5d state is energetically below the $^1S_0$ state causing direct transition in the ^3H_J, ^3F_J states (Fig. 2, right). In consequence, no photon cascade emission occurs.

Another quantum cutting makes use of lattice states of wide band gap materials ($E_g > 3.0$ eV) (Figure 3) (*7*). Typical materials showing this effect are $Zn_2SiO_4:Mn^{2+}$ and $Y_2O_3:Eu^{3+}$. Quantum cutting occurs when the exciting energy is at least twice the energy of the host material's band gap. First, an electron is excited to an energy far above the bottom of the conduction band of the host material. Relaxing to the energy at the bottom of the conduction band, the electron transfers part of its energy to another electron, which is promoted over the band gap into the conduction band. Altogether, the process results in the generation of two electron-hole pairs in the valence band. Subsequently, the recombination of these electron-hole pairs on the luminescent centers, the activator sites, entails the emission of two photons in the visible range. However, the excitation energy has to be more than twice the band gap to cause the described Auger interaction, leading to a competition between quantum yield and energy losses in the material. A minimum has been found with an energy of 2.5 times the band gap, which often corresponds to the xenon discharge, but the overall efficiency and, in consequence, the practical application is still limited so that this quantum cutting mechanism is of minor relevance.

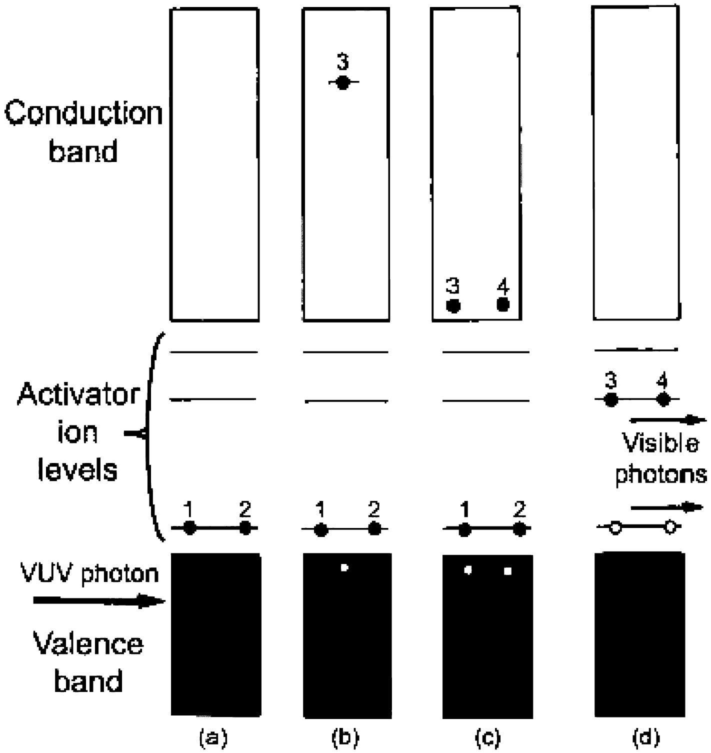

Figure 3. Interband Auger process. (a) Initial configuration before absorption of the VUV photon. Electrons 1 and 2 are the valence electrons of the activator ions. (b) Configuration after VUV absorption and the creation of the first electron-hole pair. (c) Configuration after relaxation of the first electron to the bottom of the conduction band and creation of the second electron-hole pair. (d) Migration of electron-hole pairs to activator sites, leading to recombination and photon emission (62).

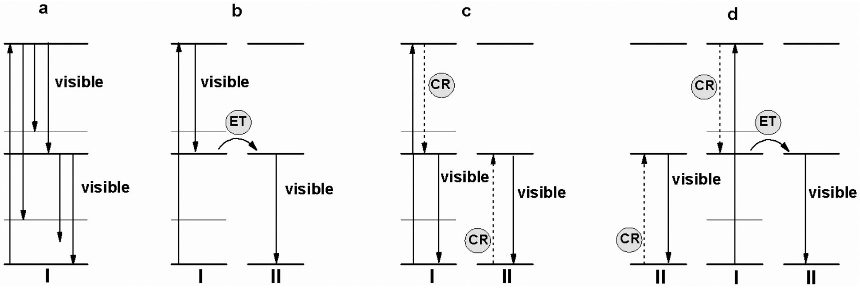

Figure 4. Energy level diagrams for two hypothetical types of rare-earth ions I and II showing the concept of down-conversion. Type I is an ion for which emission from a high-energy level can occur. Type II is an ion to which energy transfer takes place.

A quantum cutting mechanism based on ion pairs has been thought of (*8*). The concept was called down-conversion in analogy to the opposite process, up-conversion. The different, hypothetical, types of downconversion are presented in Fig. 4. In a first step, excitation of ion I to a high-energy level takes place. After energy transfer from ion I to ion II emission of two visible photons from ion II occurs (Fig. 4, (b)). Alternatively, after excitation of ion I cross-relaxation may occur resulting in the emission of one visible photon of ions I and II, respectively (Fig. 4, (c)). In a different scenario, ion I might be able to emit a visible photon from the high lying excited level, and then experience an energy transfer to ion II, which then emits a photon in the visible range (Fig. 4, (d)).

Indeed, for $LiGdF_4:Eu^{3+}$ high quantum efficiency close to theoretical limit of 200% was determined. Upon excitation of Gd^{3+} with a high energy photon, two visible photons can be emitted by Eu^{3+} through an efficient two step energy transfer from Gd^{3+} to Eu^{3+} (*9*).

Down-conversion luminescent materials are also important for plasma display panels (PDPs). A PDP is built of a matrix of xenon plasma discharge cells in between two glass panels, which form a pixel when a red, blue and green cell is combined. Due to a low discharge efficiency of 6% and loss because of highly energetic UV radiation, high performance phosphors are needed for this applications as well. Furthermore down-conversion phosphors can also be used to improve the efficiency of solar cells. In a semiconductor solar cell typically energy loss occurs when an electron-hole pair is created by a photon of higher energy than the band gap of the solar cell material. By quantum-cutting phosphors the high energy UV photon can be profitably converted into two photons of approximately the right energy (*10*).

Up-Conversion and Solar Cells

Another energy loss occurs in the conversion of solar energy to electricity in solar cells related to spectral mismatch: photons of less the band gap energy are not absorbed by a solar cell. Converting two sub-band-gap photons into one photon of the optimum energy by up-conversion helps to increase the solar cell efficiency. Such an up-converting phosphor absorbs the transmitted sub-band-gap photons by sequential ground state absorption/excited state absorption. By this an excited state is generated in the up-converting phosphor from which photons are emitted which can then be absorbed in the solar cell to generate electron-hole pairs (*11*).

The process of photon up-conversion is a way to convert long-wavelength excitation radiation (i.e near-infrared, NIR) into shorter wavelength (vis, visible) output radiation. Up-conversion (UPC) was discovered independently by Auzel (*12*) and Ovsyankin and Feofilov (*13*) in mid 1960s. A number of different mechanisms have been recognized to be involved in up-conversion either alone or in combination (Figure 5).

- Excited State Absorption (ESA)
- Energy Transfer Up-conversion (ETU)
- Co-operative Up-conversion
- Photon Avalanche Effect (PA)

The excited state absorption (ESA) process is sequential absorption of two photons by the same ion. The energy transfer up-conversion (ETU) process is defined as a process where transfer of excitation energy occurs from one ion to another that is already in the excited state. The ETU process is also called APTE effect (for addition de photon par transferts d'energie) (*14*). This process is distinguished from a third process named as cooperative up-conversion which occurs between two ions or between a pair of ions and a third one. Though some aspects similarn to up-conversion by energy transfers, its efficiency is usually much weaker. This is because it involves quasi-virtual pair levels between which transitions have to be described in a higher order of perturbation due to their double-operator nature. The fourth process, photon avalanche (PA) effect is based on sequential energy transfers involving cross-relaxation, whereas the up-conversion step itself is due to ESA.

$NaYF_4$:Er^{3+} up-converting phosphors have shown to be indeed beneficial for enhanced NIR silicon solar cell response (*15*). Today generation of white light has become industrially very much important. Here also up-converting phosphors can be used. For example, it was shown that Yb^{3+}-Ho^{3+}-Tm^{3+} triply doped $NaYF_4$ nano-rods are able to emit white light (*16*). The white up conversion luminescence observed under the excitation with a 980 nm diode laser consists of the blue UPC radiations at 450 and 475 nm corresponding to the $^1D_2$-$^3F_4$ and $^1G_4$-$^3H_6$ transitions of the Tm^{3+} ion, green at 545 nm to the $^5S_2$/$^5F_4$-$^5I_8$ transition of the Ho^{3+} ions and red at 695 nm to the $^3F_3$-$^3H_6$ of Tm^{3+} ion and at 650 nm including both the $^5F_5$-$^5I_8$ transition of the Ho^{3+}ion and the $^3F_2$-$^3H_6$ transition of Tm^{3+} ion was.

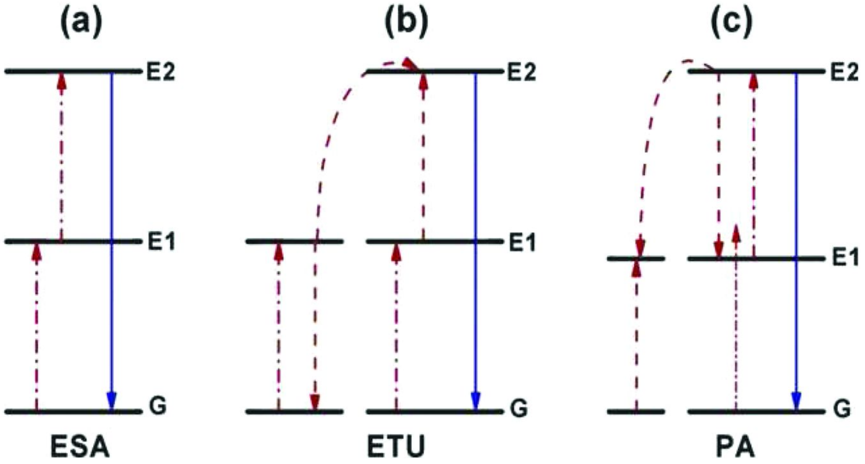

Figure 5. Principal up-conversion processes for lanthanide-doped crystals: (a) excited state absorption, (b) energy transfer upconversion, (c) photon avalanche. The dashed/dotted, dashed, and full arrows represent photon excitation, energy transfer, and emission processes.

Synthesis of Nano-Sized Lanthanide Fluorides

Extensive research is going on to prepare lanthanide doped fluoride materials with controlled phase, morphology, narrow size distribution and surface functionalization. Different methods including thermal decomposition (*17*), a liquid solid two phase approach (*18*), co-precipitation methods (*19*, *20*) complex assisted hydrothermal synthesis (*21*), reverse micelle techniques (*22–24*), microwave synthesis (*25*, *26*) have been demonstrated recently. Not only synthesis routes but also the growth mechanism, (nano-)crystal morphology along with crystal phase tuning (polymorphism) affect the photoluminescence of the dopant ion and their control is currently drawing immense attention (*27–29*).

Hexagonal $NaYF_4$: Yb^{3+}, Ln^{3+}, for example, shows a better UPC efficiency compared to the cubic analogue (*30*). $NaYF_4$: Yb,Er^{3+}, also an up-conversion phosphor, was made by treating YF_3, YbF_3 and ErF_3 in HF gas at 750°, then adding a 20 wt% excess dried NaF and heating for 16 h at 200°C and finally at 1000°C (*31*). Soon after another easy access to the hexagonal $NaYF_4$:Yb,Er^{3+} phosphor got reported (*32*). Micrometer-sized $NaYF_4$:Yb, Pr^{3+} was synthesized through precipitation of first the cubic phase and then conversion to the hexagonal via sand-bath heating of the precipitate (*33*). Due to prolonged heat treatment, the initially formed cubic phase converts to the hexagonal phase. Hexagonal LuF_3 and $NaYF_4$ nano-crystals of different shape can be synthesized via hydrothermal method (*34*). A hydrothermal access to $Na(Y_{1.5}Na_{0.5})F_6$ nano-crystals is also possible (*35*). In a similar solvothermal approach sodium yttrium fluoride nano-crystals where prepared with oleic acid and alcohol as co-solvents to water (*36*). Co-precipitation methods allow generally for a fast and facile access to nano-fluorides and this method was, for example, used to prepare ytterbium and erbium doped sodium yttrium fluoride nano-crystals (*37*). Upconverting $NaYF_4$ nano-crystals can be synthesized via the thermal decomposition of metal trifluoroacetate precursors in the presence of oleic acid and octadecene (*38*). This same technique was used to prepare lanthanide doped LaF_3 and $NaYF_4$ nanoparticles of very small dimension (~5nm) (*39*). Tm^{3+} doped nanoparticles which exhibit 1.47 μm photoluminescence are similarly accessible (*40*). Recently, mono-disperse upconverting nano-material was be prepared by microwave assisted synthesis (*41*). Quantum cutting GdF_3:Eu nano-crystals can be obtained by microwave synthesis using ionic liquid both as the reaction partner and the solvent (*42*). Through a combustion-fluorization method Yb^{3+}-Tm^{3+} co-doped lutetium fluoride nanoparticles are accessible (*43*). A general synthesis of high quality cubic (α-phase) and hexagonal (β phase) $NaLnF_4$ nano-crystals of different shapes by co-thermolysis method was established (*44*). Quite efficient upconverting nanoparticles were prepared using N-(2-hydroxyethyl)-ethylene diamine as the solvent and the ligand (*45*). $NaGdF_4$:Eu nano-crystals with controlled crystal phase and luminescence can be obtained (*46*). Recently, layered fluoride materials where prepared by decomposition of sodium yttrium fluoride and ammonium fluoro-lanthate by sonication and heating (*47*). Crystal phase controlled sodium yttrium fluoride nano-crystals got prepared by a reverse micelle method (*48*). A growth mechanism was proposed for YF_3 nano-crystals forming in the quaternary reverse microemulsion system with water / cetyl trimethyl ammonium bromide/ cyclohexane/ 1- pentanol system (*49*). Solid-state synthesis is also a conventional route to prepare sodium yttrium fluoride nano-crystals (*50*). LaF_3 and CeF_3 nano-crystals can be made using KBF_4 as the fluoride source (*51*). Long thin wires of LnF_3 can be obtained via calcinations of NH_4LnF_4 (*52*).

Surface Modification Including Functionalization

Core-shell particles have attracted a great deal of interest to improve the luminescence efficiency by reducing the surface defects of the nano-crystalline material. Lanthanide dopant luminescence is readily quenched by high energy oscillators arising from weakly bound surface impurities, ligands and solvents due to lack of effective protection by the host lattice (*53*): Excitation energy of the interior ions can also be transferred to the surface through adjacent dopant ions and eventually dissipated non-radiatively. It is generally believed that both the up and down conversion emission of bulk materials can by improved by growing a shell surrounding the emitting core. Both homogeneous and heterogeneous core-shell structures have been synthesized and examined. A homogeneous core-shell structure is favorable because this design can reduce the lattice mismatch between the core and the shell.

Remarkable enhancements of UPC fluorescence of ~ 7 and ~29 times were found for $NaYF_4$: Yb, Er and $NaYF_4$: Yb, Tm respectively after coating with an undoped $NaYF_4$ shell (*54*). Wang et al. also shows the importance of core-shell formation on the enhancements of UPC intensity (*55*). Chow and co-workers have prepared hexagonal phase nanoparticles of $NaYF_4$:Yb, Er (Tm) core and a $NaYF_4$:Yb Er (Tm) /$NaYF_4$ shell (*56*). In a similar way, core-shell $NaYF_4$/

$NaGdF_4$ nano-crystals were prepared and the core-shell formation was proven by X-ray photoelectron spectroscopy data (XPS) measured with tunable synchrotron radiation (*57*).

Silica-coated core/shell LaF_3:Tm/LaF_3 nanoparticles also have been reported (*58*). Silica coating of PVP stabilized $NaYF_4$:Yb/Er nanoparticles with a varying thickness of silica layer from 10 nm to 1 nm can be obtained by controlling the concentration of tetraethoxy silane (TEOS) (*59*). NIR responsive silica coated $NaYbF_4$:Er/Tm/ Ho upconversion fluorescent nanoparticles were synthesized (*60*). A layer-by-layer (LBL) assembly strategy that uses oppositely charged linear polyanions to generate water soluble upconversion nanoparticles was developed and the surface of $NaYF_4$:Yb/Er nanoparticles was coated with stable amino-rich shells by sequential adsorption of positively charged poly (allylamine hydrochloride) (PAH) and negatively charged poly (sodium 4-styrenesulfonate) (PSS) (*61*).

Acknowledgments

This research was supported by the Deutsche Forschungsgemeinschaft within the framework of the collaborative research program SFB 558 “Substrate-catalyst interaction in heterogeneous catalysis” and the European Research Starting Grant “EMIL – Exceptional Materials from Ionic Liquids”. AVM thanks the Fonds der Chemischen Industrie for a Chemiedozenten-Stipendium and PG the Alexander-von-Humboldt foundation for a research fellowship.

References

1. http://www.energiespar-lampen.de/ (accessed Sept. 21st 2009); http://www.energystar.gov/index.cfm?c=cfls.pr_cfls.
2. http://ec.europa.eu/energy/efficiency/ecodesign/doc/committee/2008_12_08_technical_briefing_household_lamps.pdf; http://eur-lex.europa.eu/LexUriServ/LexUriServ.do?uri=OJ:L:2009:076:0003:0016:DE:PDF; http://eur-lex.europa.eu/LexUriServ/LexUriServ.do?uri=OJ:L:2009:076:0017:0044:DE:PDF; http://www.stuff.co.nz/national/764487; http://www.environ.ie/en/Environment/Atmosphere/ClimateChange/News/MainBody,16444,en.htm.
3. (a) Strümpel, C.; McCann, M.; Beaucarne, G.; Arkhipov, V.; Slaoui, A.; Švrček, V.; del Ca~nizo, C.; Tobias, I. *Sol. Energy Mater. Sol. Cells* **2007**, *91*, 238. (b) van der Ende, B. M.; Aarts, L.; Meijerink, A.*Phys. Chem. Chem. Phys.* **2009**, *11*, 11081.
4. (a) Wang, F.; Liu, X. *Chem. Soc. Rev.* **2009**, *38*, 976. (b) Mai, H.-X.; Zhang, Y.-W.; Si, R.; Yan, Z.-G. ; Sun, L.-D.; You, L.-P.; Yan, C.-H. *J. Am. Chem. Soc.* **2006**, *128*, 6426. (c) Ptacek, P.; Schäfer, H.; Kömpe, K.; Haase, M.; *Adv. Funct. Mater.* **2007**, *17*, 3843.
5. Jüstel, T.; Nikol, H.; Ronda, C. *Angew. Chem., Int. Ed.* **1998**, *37*, 3084.

6. (a) Sommerdijk, J. L.; Bril, A. ; de Jager, A. W. *J. Lumin.* **1974**, *8*, 341. (b) Piper, W. W. ; DeLuca, J. A. ; Ham. F. S.*J. Lumin.* **1974**, *8*, 344.
7. Ronda, C. *J. Lumin.* **2002**, *100*, 301.
8. (a) Wegh, R. T.; Donker, H.; Oskam, K. D.; Meijerink, A. *J. Lumin.* **1999**, *82*, 93. (b) Wegh, R. T.; Donker, H.; van Loef, E. V. D.; Oskam, K. D.; Meijerink, A. *J. Lumin.* **2000**, *87−89*, 1017.
9. Wegh, R. T.; Donker, H.; Oskam, K. D.; Meijerink, A. *Science* **1999**, *283*, 663.
10. (a) Strümpel, C.; McCann, M.; Beaucarne, G.; Arkhipov, V.; Slaoui, A.; Švrček, V.; del Ca~nizo, C.; Tobias, I. *Sol. Energy Mater. Sol. Cells* **2007**, *91*, 238. (b) van der Ende, B. M.; Aarts, L.; Meijerink, A.*Phys. Chem. Chem. Phys.* **2009**, *11*, 11081.
11. (a) Strümpel, C.; McCann, M.; Beaucarne, G.; Arkhipov, V.; Slaoui, A.; Švrček, V.; del Ca~nizo, C.; Tobias, I. *Sol. Energy Mater. Sol. Cells* **2007**, *91*, 238. (b) van der Ende, B. M.; Aarts, L.; Meijerink, A.*Phys. Chem. Chem. Phys.* **2009**, *11*, 11081.
12. Auzel, F. *Chem. Rev.* **2004**, *104*, 139.
13. (a) Ovsyankin, V.; Feofilov, P. P. *JETP Lett.* **1966**, *3*, 317. (b) Ghosh, P.; Patra, A. *Pramana* **2005**, *65*, 901.
14. Auzel, F. *Chem. Rev.* **2004**, *104*, 139.
15. Shalav, A.; Richards, B. S.; Truppe, T.; Krämer, K. W.; Güdel, H. U *Appl. Phys. Lett.* **2005**, *86*, 013505.
16. Yang, L. W.; Han, H. L.; Zhang, Y. Y.; Zhong, J. X. *J. Phys. Chem. C* **2009**, *113*, 18995.
17. Boyer, J.-C.; Vetrone, F.; Cuccia, L. A.; Capobianco, J. A. *J. Am. Chem. Soc.* **2006**, *128*, 7444.
18. Wei, Y.; Lu, F.; Zhang, X.; Chen, D. *Chem. Mater.* **2006**, *18*, 5733.
19. (a) Yi, G.; Lu, H.; Zhao, S.; Ge, Y.; Yang, W.; Chen, D.; Guo, L.-H.; *Nano Lett.* **2004**, *4*, 2191. (b) Wang, L.; Li, Y.; *Nano Lett.* **2006**, *6*, 1645. (c) Wang, L.; Li, Y. *Chem. Commun.* **2006**, 2557.
20. (a) Yi, G.-S.; Chow, G.-M. *Chem. Mater.* **2007**, *19*, 341. (b) Yi, G.-S.; Chow, G.-M. *J. Mater.Chem.* **2005**, *15*, 4460.
21. Zeng, J.-H.; Su, J.; Li, Z.-H.; Yan, R.-X.; Li, Y.-D. *Adv. Mater.* **2005**, *17*, 2119.
22. (a) Ghosh, P.; Patra, A. *J. Phys. Chem. C* **2008**, *112*, 19283. (b) Ghosh, P.; Patra, A. *J. Phys. Chem. C* **2008**, *112*, 3223.
23. Ghosh, P.; Kar, A; Patra, A. *J. Phys. Chem. C* **2010**, *114*, 715.
24. Wang, G.; Qin, W.; Zhang, J.; Zhang, J.; Wangyan; Cao, C.; Wang, L.; Wei, G.; Zhu, P.; Kim, R. *J. Phys. Chem. C* **2008**, *112*, 12161.
25. Lorbeer, C; Cybinska, J.; Mudring, A.-V. *Chem. Commun.* **2010**, *46*, 571.
26. Wang, H.-Q.; Nann, T. *ACS Nano* **2009**, *3*, 3804.
27. Mai, H.-X.; Zhang, Y.-W.; Si, R.; Yan, Z.-G.; Sun, L.-D.; You, L.-P.; Yan, C.-H. *J. Am. Chem. Soc.* **2006**, *128*, 6426.
28. (a) Ghosh, P.; Patra, A. *J. Phys. Chem. C* **2008**, *112*, 19283. (b) Ghosh, P.; Patra, A. *J. Phys. Chem. C* **2008**, *112*, 3223
29. Mai, H.-X.; Zhang, Y.-W.; Sun, L.-D.; Yan, C.-H. *J. Phys. Chem. C* **2007**, *111*, 13721.

30. Shan, J.; Ju, Y. *Appl. Phys. Lett.* **2007**, *91*, 123103.
31. Menyuk, N.; Dwight, K.; Pierce, J. W. *Appl. Phys. Lett.* **1972**, *21*, 159.
32. Kano, T.; Suzuki, T.; Minagawa, S. *J. Electrochem. Soc.* **1973**, *120*, C87.
33. Martin, N.; Boutinaud, P.; Mahiou, R.; Cousseinsa, J.-C.; Bouderbal, M. *J. Mater. Chem.* **1999**, *9*, 125.
34. (a) Li, C.; Yang, J.; Yang, P.; Lian, H.; Lin, J. *Chem. Mater.* **2008**, *20*, 4317. (b) Li, C.; Quan, Z.; Yang, P.; Huang, S.; Lian, H.; Lin, J.; *J. Phys. Chem. C* **2008**, *112*, 13395. (c) Li, C.; Yang, J.; Quan, Z.; Yang, P.; Kong, D., Lin, J. *Chem. Mater.* **2007**, *19*, 4933.
35. (a) Wang, L.; Li, Y. *Chem. Mater.* **2007**, *19*, 727. (b) Wang, X.; Li, Y. *Chem. Eur. J.* **2003**, *9*, 5627. (c) Wang, X.; Li, Y. *Angew. Chem., Int. Ed.* **2003**, *42*, 3497.
36. Wang, L.; Li, Y. *Nano Lett.* **2006**, *6*, 1645.
37. Yi, G.; Lu, H.; Zhao, S.; Ge, Y.; Yang, W.; Chen, D.; Guo, L.-H. *Nano Lett.* **2004**, *4*, 2191.
38. Boyer, J.-C.; Vetrone, F.; Cuccia, L. A.; Capobianco, J. A. *J. Am. Chem. Soc.* **2006**, *128*, 7444.
39. (a) Yi, G.-S.; Chow, G.-M. *Chem. Mater.* **2007**, *19*, 341. (b) Yi, G.-S.; Chow, G.-M. *J. Mater.Chem.* **2005**, *15*, 4460
40. (a) Diamente, P. R.; Raudsepp, M.; Van Veggel, F. C. J. M. *Adv. Funct. Mater.* **2007**, *17*, 363. (b) Sivakumar, S.; Van Veggel, F. C. J. M. May, P. S. *J. Am. Chem. Soc.* **2007**, *129*, 620.
41. Wang, H.-Q.; Nann, T. *ACS Nano* **2009**, *3*, 3804.
42. Lorbeer, C; Cybinska, J.; Mudring, A.-V. *Chem. Commun.* **2010**, *46*, 571.
43. Xiao, S.; Yang, X.; Ding, J. W.; Yan, X. H. *J. Phys. Chem. C* **2007**, *111*, 8161.
44. Mai, H.-X.; Zhang, Y.-W.; Si, R.; Yan, Z.-G.; Sun, L.-D.; You, L.-P.; Yan, C.-H. *J. Am. Chem. Soc.* **2006**, *128*, 6426.
45. Schäfer, H.; Ptacek, P.; Kömpe, K.; Haase, M. *Chem. Mater.* **2007**, *19*, 1396.
46. Ptacek, P.; Schäfer, H.; Kömpe, K.; Haase, M. *Adv. Funct. Mater.* **2007**, *17*, 3843.
47. Ghosh, P.; Kar, A; Patra, A. *J. Phys. Chem. C* **2010**, *114*, 715.
48. (a) Ghosh, P.; Patra, A. *J. Phys. Chem. C* **2008**, *112*, 19283. (b) Ghosh, P.; Patra, A. *J. Phys. Chem. C* **2008**, *112*, 3223.
49. Wang, G.; Qin, W.; Zhang, J.; Zhang, J.; Wangyan; Cao, C.; Wang, L.; Wei, G.; Zhu, P.; Kim, R. *J. Phys. Chem. C* **2008**, *112*, 12161.
50. (a) Grzechnik, A.; Bouvier, P.; Crichton, W. A.; Farina, L.; Köhler, J. *Solid State Sci.* **2002**, *4*, 895. (b) Mathews, M. D.; Ambekar, B. R.; Tyagi, A. K.; Kohler, J. *J. Alloys Compd.* **2004**, *377*, 162.
51. (a) Zhu, L.; Meng, I.; Cao, X. Q.; *Eur. J. Inorg. Chem.* **2007**, 3863. (b) Zhu, L.; Li, Q, Liu, X.; Li, J.; Zhang, Y.; Meng, J.; Cao, X. *J. Phys. Chem. C* **2007**, *111*, 5898.
52. Huang, B.; Liu, Z.; Hong, M. J.; Chen, T. X.; Xue, L. Z.; You, Z. X. *J. Cryst. Growth* **2005**, *276*, 613.
53. Wang, F.; Liu, X. *Chem. Soc. Rev.* **2009**, *38*, 976.
54. Yi, G.-S.; Chow, G.-M. *Chem. Mater.* **2007**, *19*, 341.

55. Wang, Y.; Tu, L.; Zhao, J; Sun, Y.; Kong, X.; Zhang, H. *J. Phys. Chem. C* **2009**, *113*, 7164.
56. Yi, G.-S.; Chow, G.-M. *Chem. Mater.* **2007**, *19*, 341.
57. Abel, K. A.; Boyer, J.-C.; Van Veggel, F. C. J. M. *J. Am. Chem. Soc.* **2009**, *131*, 14644.
58. (a) Diamente, P. R.; Raudsepp, M.; Van Veggel, F. C. J. M. *Adv. Funct. Mater.* **2007**, *17*, 363. (b) Sivakumar, S.; Van Veggel, F. C. J. M. May, P. S. *J. Am. Chem. Soc.* **2007**, *129*, 620.
59. Li, Z.; Zhang, Y. *Angew. Chem., Int. Ed.* **2006**, *45*, 7732.
60. Wang, M.; Mi, C.; Zhang, Y.; Liu, J.; Li, F.; Mao, C.; Xu, S. *J. Phys. Chem. C* **2009**, *113*, 19021.
61. Wang, L.; Yan, R.; Huo, Z.; Wang, L.; Zheng, J.; Bao, J.; Wang, X.; Peng, Q.; Li, Y. *Angew. Chem., Int. Ed.* **2005**, *44*, 6054.
62. Yen, W. M.; Shionoya, S.; Yamamoto, H. *Practical Applications of Phosphors*; CRC Press: Boca Raton, FL, 2006.

Downloaded by STANFORD UNIV GREEN LIBR on June 5, 2012 | http://pubs.acs.org
Publication Date (Web): April 27, 2011 | doi: 10.1021/bk-2011-1064.ch007

Chapter 7

Fluorinated Templates for Energy-Related Nanomaterials and Applications

**Mohammed J. Meziani,*,† Fushen Lu,† Li Cao,†
Christopher E. Bunker,*,‡ Elena A. Guliants,¶ and Ya-Ping Sun*,†**

**†Department of Chemistry and Laboratory for Emerging Materials and Technology, Clemson University, Clemson, South Carolina 29634-0973
‡Air Force Research Laboratory, Propulsion Directorate, Wright-Patterson Air Force Base, Ohio 45433-7103
¶University of Dayton Research Institute, Sensors Technology Office, Dayton, Ohio 45469
*Corresponding authors: mmezian@clemson.edu, christopher.bunker@wpafb.af.mil, and syaping@clemson.edu**

Fluorinated ionomer membranes, as represented by the commercially available Nafion films, are macroscopically homogeneous and optically transparent but microscopically inhomogeneous with the presence of nanoscale hydrophilic cavities. These cavities serve as nanoscale reactors for the synthesis of nanoparticles from a variety of materials. The membranes with embedded nanoscale semiconductors, still optically transparent, have been used as sheet-photocatalysts for energy conversion applications, while those with embedded reactive metals used as nano-energetic materials for hydrogen generation and beyond. This chapter provides an overview on the templated synthesis of nanomaterials in fluorinated ionomer membranes and the various energy-related applications of this unique class of nanocomposite materials.

1. Introduction

The combination of fluorinated entities and nanoscale materials has received much recent attention for existing and emerging opportunities in a variety of energy-related applications, such as energy saving (*1*), optoelectronic (lighting)

In Fluorine-Related Nanoscience with Energy Applications; Nelson, D., et al.;
ACS Symposium Series; American Chemical Society: Washington, DC, 2011.

Downloaded by STANFORD UNIV GREEN LIBR on June 5, 2012 | http://pubs.acs.org
Publication Date (Web): April 27, 2011 | doi: 10.1021/bk-2011-1064.ch007

(*2*), catalysis (*3–8*), nanothermite reactions (*9*, *10*), and hydrogen fuel sources (*11*, *12*). Fluorine-containing materials are unique in many desirable properties due to the highest electronegativity and small atomic radius of fluorine. These distinctive properties include high thermal and chemical stability, solvent resistance, low flammability, low moisture absorption, low surface tension/energy, low dielectric constant, and strong oxidant source under energetic conditions (*3*). Among the best-known and most widely used fluorine-containing materials are organic and polymeric compounds with fluorine functional groups (*3*, *10–28*), particularly fluorinated surfactants such as high-molecular weight perfluorinated acids (*3*, *10*, *11*, *13*) and perfluorinated ionomer membranes, with the latter being represented by the commercially available Nafion membrane films (*12*, *14–28*).

Nafion (Scheme 1) is a perfluorinated sulfonic acid polymer with excellent thermal, chemical and mechanical stability and high ionic conductivity (*14*, *16*). Because of these characteristics, Nafion membrane has been the membrane of choice for applications in aggressive chemical environments, such as separators in chloro-alkali cells (*15*, *16*), modern battery and fuel cell technologies (*14–16*), sensors (*15*), and super-acid catalysis for the production of fine chemicals (*17*). For example, Nafion was found to be effective as a membrane for hydrogen/oxygen and direct methanol proton exchange membrane (PEM) fuel cells by permitting hydrogen ion transport while preventing electron conduction, thus providing unparalleled power supply from hydrogen (*14–16*). The Nafion properties are further expanded through its ability to preconcentrate cationic species, making it possible to host a wide range of entities such as redox mediators (*18*) and nanoparticles (*5–8*, *12*, *19–23*) for more efficient catalytic and energetic applications (*5–8*, *12*, *29*). Some of the most exciting developments have been their coupling with nanoscale semiconductor and reactive powders for the photoreduction of CO_2 and evolution of hydrogen (*5–8*, *12*). For example, Nafion membrane was found recently to be an ideal template for the preparation of small and air-stable Al nanoparticles with potential energetic applications (*12*).

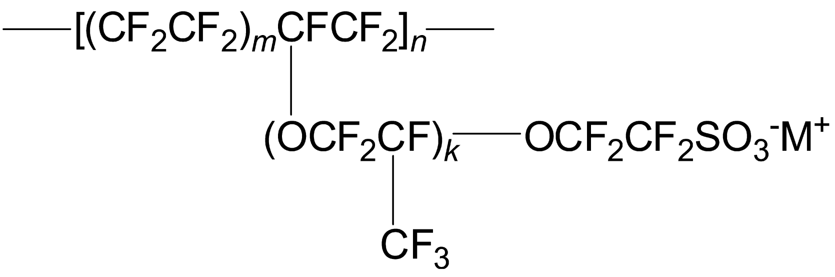

$$-[(CF_2CF_2)_m\underset{\substack{|\\(OCF_2\underset{\substack{|\\CF_3}}{CF})_k-OCF_2CF_2SO_3^-M^+}}{CF}CF_2]_n-$$

Scheme 1. Nafion.

In this chapter, we first provide some background information on and the current understanding of the structure and properties of perfluorinated ionomer membranes, and then highlight recent developments in the use of these membranes for the synthesis of small and size-wise narrowly distributed semiconductor and metal nanoparticles and their selected energy-related applications. We conclude with a brief summary of the challenges and perspectives in this interdisciplinary research field.

2. Fluorinated Ionomer Membranes

Downloaded by STANFORD UNIV GREEN LIBR on June 5, 2012 | http://pubs.acs.org
Publication Date (Web): April 27, 2011 | doi: 10.1021/bk-2011-1064.ch007

Perfluorinated membranes generally refer to ion-exchange membranes with a perfluorinated polymer backbone. These membranes typically exhibit excellent thermal and chemical stability with retention of mechanical properties in highly corrosive and oxidative environments. A representative example is the Nafion membrane (*14–17*), in which the underlying polymer is a sulfonated tetrafluoroethylene-based fluoropolymer-copolymer (Scheme 1). The synthesis of Nafion polymer is achieved via the copolymerization of tetrafluoroethylene (TFE) (the monomer in the widely used Teflon) and a derivative of perfluoro(alkyl vinyl ether) with sulfonyl acid fluoride, followed by the conversion of sulfonyl fluoride into sulfonate groups and then into the acid form. Finally, the polymer solution is cast into thin films via heating in aqueous alcohol at 250 °C in an autoclave (*15*).

The pendant ionic groups interact to form ion-rich aggregates contained in a nonpolar matrix, which strongly influences the polymer properties and applications. Although Nafion polymers in the membrane are not covalently crosslinked, the membrane structure is highly ordered. Microscopically, the structure and properties of perfluorinated ionomer membranes have been understood in terms of a reverse micelle-like ion cluster model developed in the study of Nafion (*4*, *15*, *24*, *25*). According to the model there are essentially three distinctive structural regions in the membrane: the perfluorinated polymer network, hydrophilic cores or ion clusters, and the interfacial domain between the two regions (Scheme 2). The hydrophilic cores or ion clusters are estimated as being on the order of 4 nm in diameter, in part based on experimental results primarily from small-angle X-ray studies (*24*, *25*). The neighboring clusters are interconnected through narrow channels (Scheme 2) (*15*, *25*). While there is some experimental evidence in support of such a structural model, issues including the shape and morphology of the ion clusters, the significance and dimension of the interfacial region, and the general organization of hydrophilic and hydrophobic structural domains in Nafion and related ionomer membranes are still being debated and investigated (*26*, *27*). For example, luminescence spectroscopic methods have been employed to study the structural properties of ionomer membranes, including an evaluation of the ion cluster model illustrated in Scheme 2 (*26–28*). Results from the use of a series of environment-sensitive fluorescent probes such as $Ru(bpy)_3^{2+}$, pyrene with excimer formation, and ethidium bromide have suggested the presence of a substantial interfacial region in perfluorinated ionomer membranes (*26–28*). It was proposed that the interfacial region could be viewed as a heterogeneous mixture of perfluorinated polymer branches and water molecules, where the microscopic environment experienced by the fluorescent molecular probes might effectively be close to those in polar organic solvents (*27*). Results from the luminescence spectroscopic studies have also provided valuable information on the transport-related processes in the ionomer membrane, suggesting considerable mobility throughout the interfacial region, as reflected by the significant diffusional fluorescence quenching for probes in the membrane structural domain (*27*).

The microscopic structure in the ionomer membranes, as described by the ion cluster model (Scheme 2), has major implications to the primary uses of these membranes, such as in fuel cells (*14–16*). Equally significant is the fact that these membrane films are macroscopically homogeneous, uniform and optically highly transparent, but microscopically heterogeneous with hydrophilic ion clusters dispersed in fluorinated polymer backbones, thus offering an excellent platform for templated synthesis of nanoscale materials.

Downloaded by STANFORD UNIV GREEN LIBR on June 5, 2012 | http://pubs.acs.org
Publication Date (Web): April 27, 2011 | doi: 10.1021/bk-2011-1064.ch007

3. Nano-Templating for Energy-Related Applications

The presence of hydrophilic cavities in the ionomer Nafion membrane structure was also supported by experiments in which nanoparticles were prepared by using the cavities in Nafion membrane as templates (*5–8*, *12*, *19–23*). In fact, the incorporation of nanoparticles into the membrane served another purpose by allowing a direct imaging of the hosting cavities in the membrane structure, complementary to the electron microscopy studies of stained Nafion membrane films. For example, Sun and coworkers reported the preparation and characterization of several crystalline semiconductor and metal nanoparticles including PbS, CdS, Ag_2S, and Ag in various perfuorinated ionomer membranes including Nafion and those based on the sulfonimide ionomer and the bis(sulfonyl)methane ionomer (*20*, *21*, *23*). Overall, the nanoparticles were easy to prepare and air-stable, and could easily be handled under ambient conditions.

Experimentally for the preparation of Ag_2S nanoparticles as an example (*20*), a piece of clean Nafion film in the sodium form was soaked in an aqueous solution of $AgNO_3$, followed by rinsing with water to clean the film surface. After the surface was blotted dry, the film containing Ag^+ was immersed in an aqueous solution of Na_2S for the formation of Ag_2S particles under fully hydrated condition. The same procedure and similar experimental parameters were used in the preparation of semiconductor nanoparticles. These nanoparticles could be identified by using UV/vis absorption and luminescence, X-ray powder diffraction (XRD), and transmission electron microscopy (TEM, specimen from cross-sectional slices of the Nafion film loaded with nanoparticles) methods. Examples for the results from characterizations are shown in Figure 1 (*20*, *21*). These nanoparticles were apparently mostly crystalline, small in sizes and with narrow size distributions (*20*, *21*). Microscopically, the nanoparticles were found as being hosted in the membrane structure in an isolated fashion, with no indication of channels-like domains as proposed in the ion cluster model for the ionomer membranes. The results suggested that all of these membrane films contain hydrophilic structural cavities and likely share similar nanoscopic

Downloaded by STANFORD UNIV GREEN LIBR on June 5, 2012 | http://pubs.acs.org
Publication Date (Web): April 27, 2011 | doi: 10.1021/bk-2011-1064.ch007

structures. However, the randomly dispersed Ag_2S nanoparticles were found to be significantly larger than the average size of the reverse micelle-like hydrophilic cavities predicted and/or estimated in the literature for Nafion membrane. A possible explanation for the discrepancy could be that the membrane structure with the ion clusters is somewhat flexible, thus to allow the extra growth of particles (for some materials such as Ag_2S) in the hydrophilic cavities via squeezing the connecting channels.

The nanoscale Ag particles in the structural cavities of Nafion membrane were prepared under similar experimental conditions as those used for Ag_2S, except that $NaBH_4$ was used instead of Na_2S (*23*). The UV/vis absorption spectrum of the membrane post-reaction exhibited the characteristic surface plasmon absorption band of nanoscale Ag (Figure 2). XRD and TEM analyses confirmed the formation of well-dispersed face-centered-cubic crystalline Ag nanoparticles (an average size of 13.4 nm in diameter and a size distribution standard deviation of 2.2 nm, Figure 2). The sizes were comparable to those of the Ag_2S nanoparticles discussed above, again obviously much larger than the predicted and/or estimated average cavity size in the Nafion membrane according to the ion cluster model. The results were also explained such that the hydrophilic cavities and channels must be structurally flexible enough to accommodate the formation of the larger Ag nanoparticles (*23*). More interestingly, the population of Ag nanoparticles in the membrane structure was found to vary with changes in the concentraton of the aqueous $AgNO_3$ solution (Figure 3), but the sizes of these nanoparticles remained generally similar. In fact, the film samples prepared with loading at higher $AgNO_3$ concentrations contained larger populations of Ag nanoparticles (Figure 3) (*23*). The variation of nanoparticle contents in the films was made evident by the UV/vis absorption, XRD, and TEM results. As compared in Figure 3, the characteristic plasmon absorption band obviously increases with the $AgNO_3$ solution concentration used in soaking the film in the nanoparticle preparation. The lower loading of Ag nanoparticles is also obvious in the TEM image shown in Figure 3, in comparison with the image in Figure 2 for the film corresponding to a much more concentrated $AgNO_3$ solution. However, despite the smaller number, the sizes of the Ag nanoparticles remain to be around 13 nm, rather similar to those shown in Figure 2.

These examples discussed above demonstrate that nanoscale semiconductor and metal nanoparticles can be embedded in fluorinated ionomer membranes, specifically in Nafion, to result in composite films. These essentially nanocomposites are generally stable (obviously free from any agglomeration), amenable to a variety of energy-related applications. As highlighted below, their uses as sheet-photocatalysts in energy conversion and as nano-energetic materials are particularly interesting (*5*–*8*, *12*).

Downloaded by STANFORD UNIV GREEN LIBR on June 5, 2012 | http://pubs.acs.org
Publication Date (Web): April 27, 2011 | doi: 10.1021/bk-2011-1064.ch007

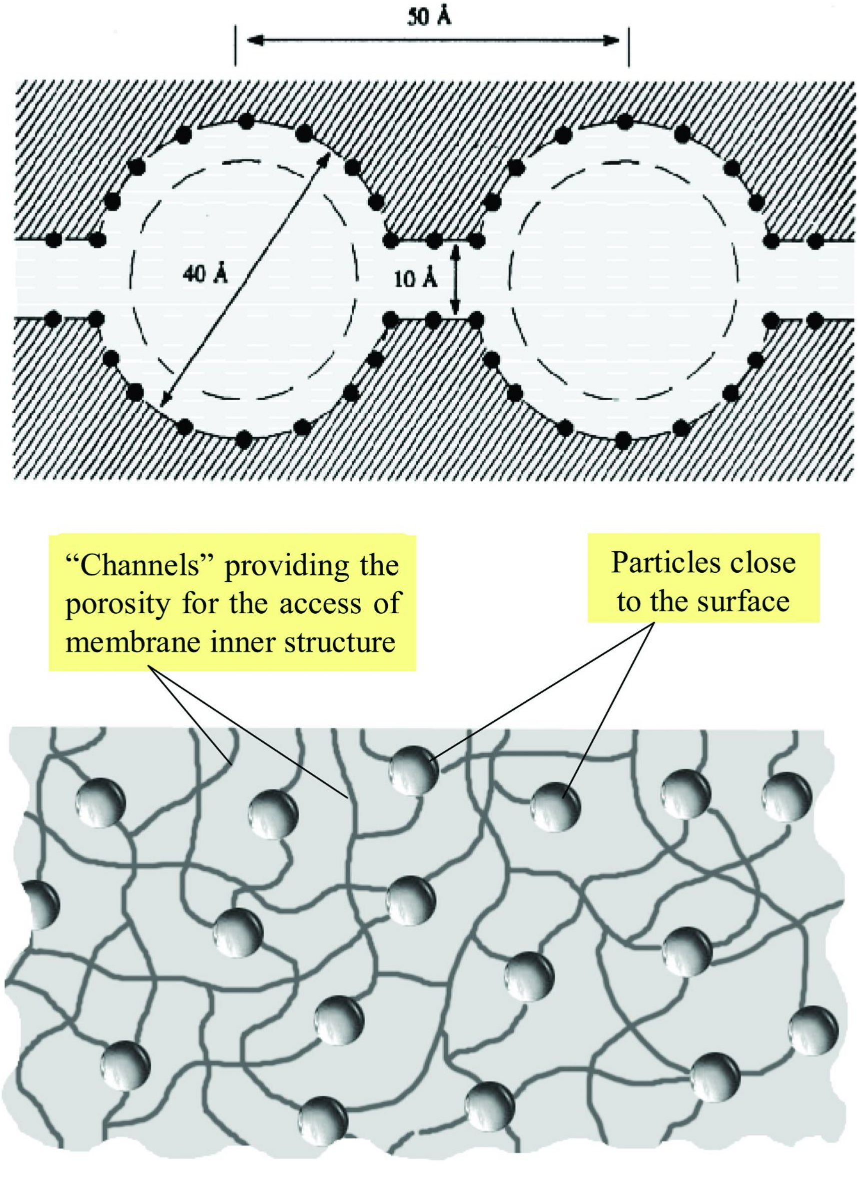
50 Å
40 Å
10 Å
"Channels" providing the porosity for the access of membrane inner structure
Particles close to the surface

Scheme 2. Cartoon illustrations for the proposed structure of ion clusters for perfluorinated ionomer membranes (top) (From ref. (15, 24)) and a cross-sectional view of the Nafion membrane film embedded with nanoparticles (bottom).

Downloaded by STANFORD UNIV GREEN LIBR on June 5, 2012 | http://pubs.acs.org
Publication Date (Web): April 27, 2011 | doi: 10.1021/bk-2011-1064.ch007

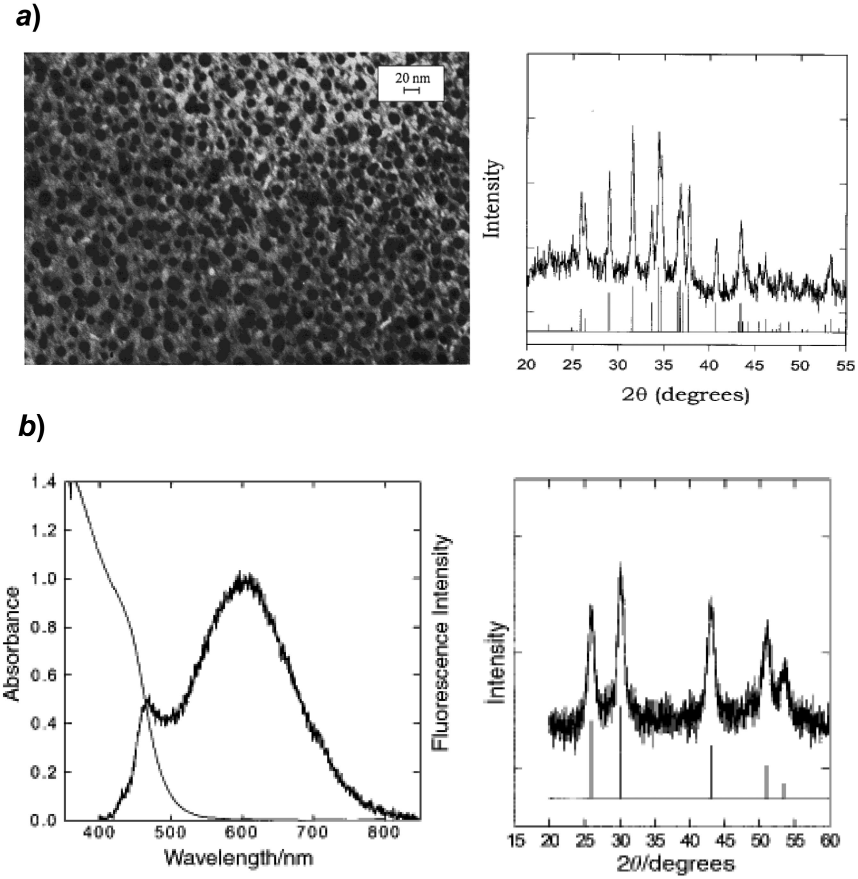

Figure 1. (a) TEM image for a cross-sectional view (left) and X-ray diffraction pattern (right) of Ag_2S nanoparticles embedded in structural cavities of Nafion membrane. (From ref. (20)) (b) Absorption and fluorescence spectra of CdS nanoparticles (left) and the X-ray diffraction pattern of PbS nanoparticles (right) embedded in structural cavities of Nafion membrane. (From ref. (21)).

Downloaded by STANFORD UNIV GREEN LIBR on June 5, 2012 | http://pubs.acs.org
Publication Date (Web): April 27, 2011 | doi: 10.1021/bk-2011-1064.ch007

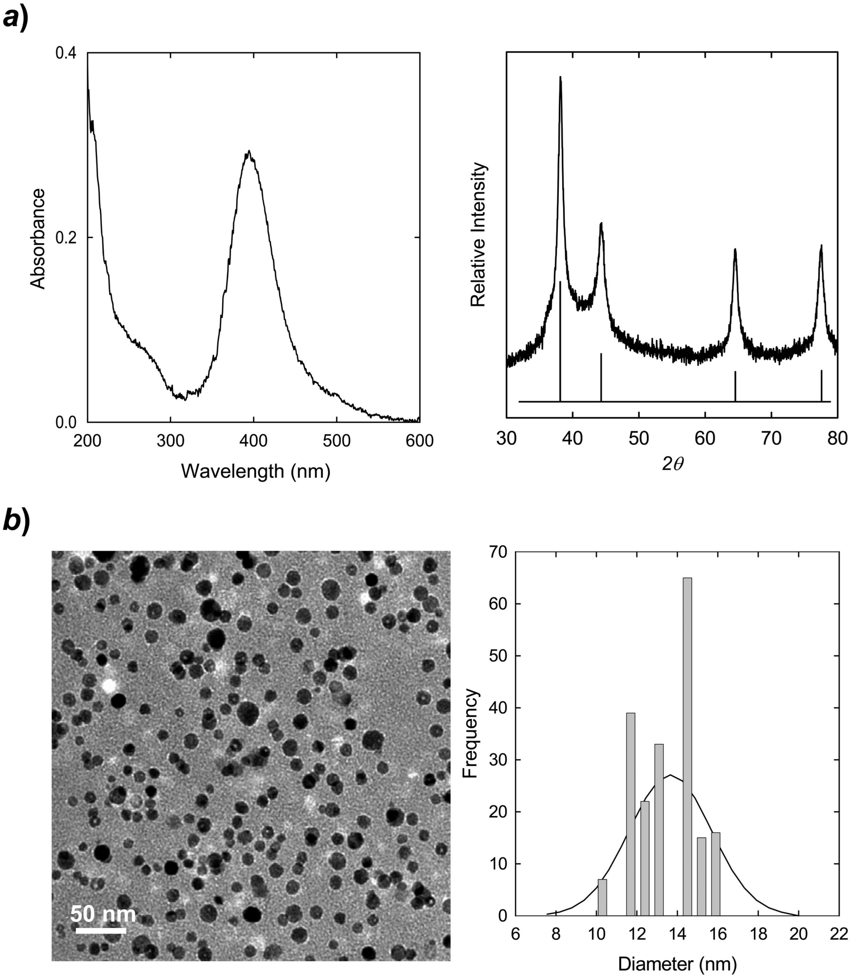

Figure 2. (a) The UV/vis absorption spectrum (left) and the X-ray diffraction pattern (right), and (b) TEM image for a cross-sectional view (left) and a statistical size analysis (right) of silver nanoparticles in Nafion membrane prepared with a more concentrated $AgNO_3$ solution. (From ref. (23)).

Downloaded by STANFORD UNIV GREEN LIBR on June 5, 2012 | http://pubs.acs.org
Publication Date (Web): April 27, 2011 | doi: 10.1021/bk-2011-1064.ch007

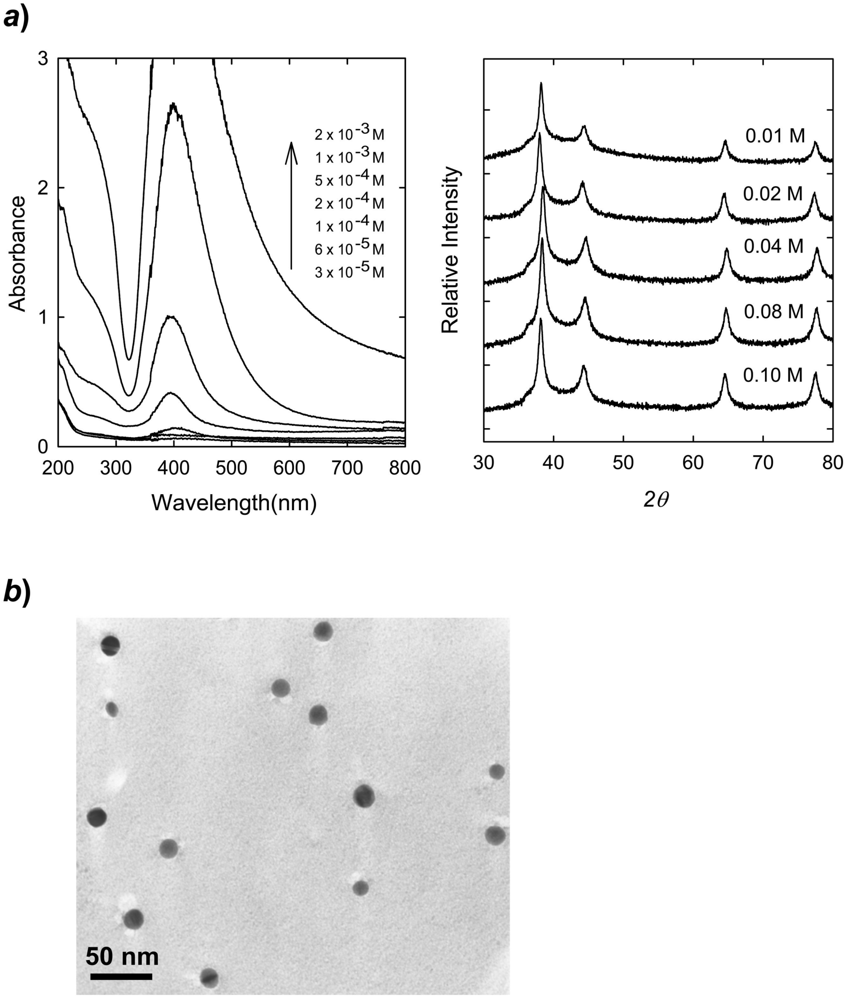

Figure 3. (a) UV/vis absorption spectra (left) and powder X-ray diffraction patterns (right) of silver nanoparticles in Nafion membrane films corresponding to soaking the films in aqueous $AgNO_3$ solutions of different concentrations (as marked) for a constant 30 min. (b) TEM image for a cross-sectional view of silver nanoparticles in the Nafion membrane film corresponding to soaking the film in aqueous $AgNO_3$ solution of 1 mM for 30 min. (From ref. (23)).

Downloaded by STANFORD UNIV GREEN LIBR on June 5, 2012 | http://pubs.acs.org
Publication Date (Web): April 27, 2011 | doi: 10.1021/bk-2011-1064.ch007

3.1. Sheet-Photocatalysts for Energy Conversion

The Nafion films loaded with nanoscale semiconductor particles could remain optically transparent when the nanoparticle population is appropriately controlled. These are effectively semiconductor-based sheet-photocatalysts (*5–8*). The optical transparency of the nanocomposite films as photocatalysts has made it possible to more effectively utilize the incident light and maximize the nanoparticle surface area for high photocatalytic activities (*5–8*). For example, nanoscale semiconductors CdS and TiO_2 and their nanocomposites such as CdS/ZnS and CdS/Pt were prepared in Nafion membrane for evaluations in the photocatalytic production of hydrogen (*5*). In the reported studies, the hydrogen-production efficiencies from water containing a sacrificial electron donor (sulfide ion) were found to be greater than those commonly obtained with unsupported colloidal or powdered semiconductors under similar conditions .

Sun and coworkers studied the photoreduction of CO_2 by using TiO_2 nanoparticles without and with the coated Ag as a co-catalyst embedded in Nafion membrane films (*7*, *8*). For the preparation of TiO_2 and Ag/TiO_2 in nanoscale cavities of Nafion membrane (*7*, *8*, *22*), a clean Nafion film was first soaked in a solution of $Ti(OC_3H_7)_4$ in isopropanol, washed with isopropanol and acetone, and then immersed in boiling water for hydrolysis to form the targeted TiO_2 nanoparticles. The TiO_2-loaded Nafion films appeared similar to the starting blank films, except for a light yellowish color (due to the absorption of the embedded nanoparticles). The TiO_2 nanoparticles embedded in Nafion membrane films were then coated with Ag metal via photolysis (*8*). The resulting film was brownish, consistent with the presence of nanoscale Ag (plasmon absorption), but remained optically transparent. The amount of Ag deposition was found to depend on the concentration of the $AgNO_3$ solution used in the coating. UV/vis absorption and TEM (specimen from cross-sectional microtome) analyses of TiO_2-loaded films without and with the Ag coating are shown in Figure 4. The embedded nanoparticles appeared crystalline and well-dispersed. The nanoparticles became somewhat larger after the Ag coating, 6.5 nm vs 4 nm (Figure 4). The association of Ag with TiO_2 at the nanoscale was also confirmed by the energy dispersive X-ray (EDX) analysis of randomly selected regions in the image, all of which indicated the substantial presence of Ti together with Ag.

The sheet-photocatalysts were evaluated for the photoreduction of liquid CO_2. The configuration of the catalyst films in the high-pressure optical cell of the reaction setup is illustrated in Scheme 3. In a typical experiment, the cell was purged with CO_2 gas for 30 min before it was filled with liquid CO_2 to a pressure of 2,000 psia, followed by photoirradiation with a xenon arc source. Post photoirradiation, the cell was depressurized and water was added to the cell immediately thereafter (*7*, *8*). The resulting aqueous solution contained methanol, acetic acid, and formic acid as the reaction products according to HPLC and ^1H NMR analyses (*7*, *8*). As shown in Figure 5, the results suggest that these sheet-photocatalysts are effective in improving the photocatalytic conversion of CO_2 (in comparison with results from other experimental configurations). The Ag coating apparently enhanced the photoconversion. These sheet-photocatalysts

Downloaded by STANFORD UNIV GREEN LIBR on June 5, 2012 | http://pubs.acs.org
Publication Date (Web): April 27, 2011 | doi: 10.1021/bk-2011-1064.ch007

were also found to be highly stable chemically and photochemically, reusable in repeated photocatalytic reactions (*7*, *8*).

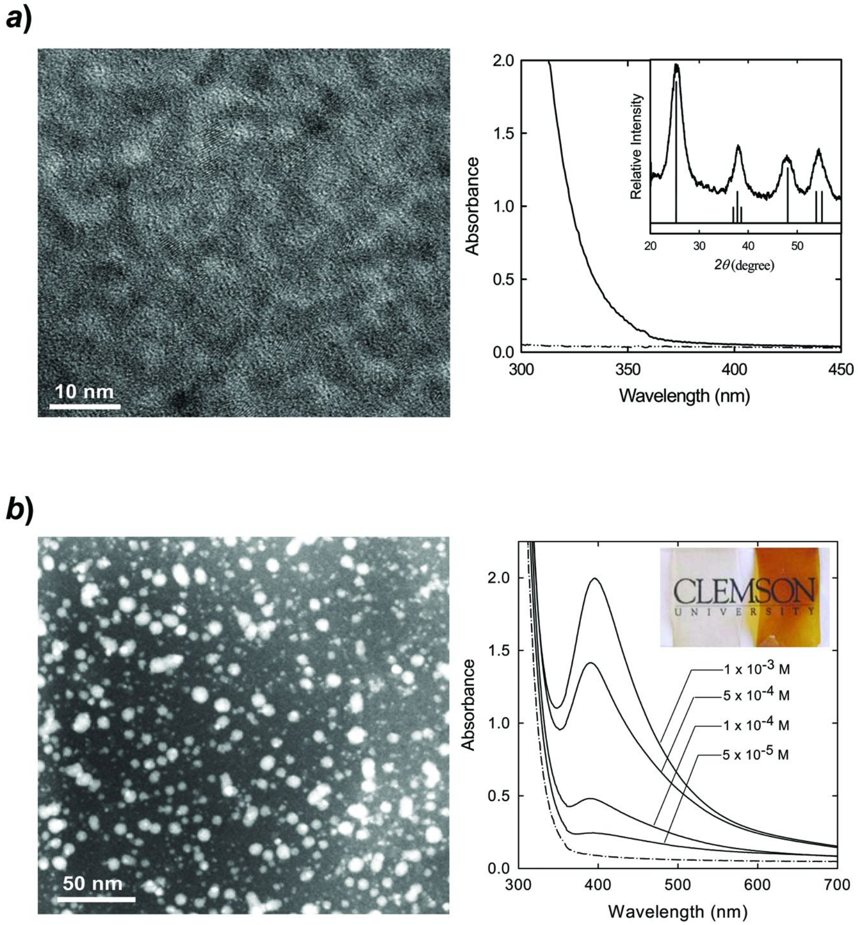

Figure 4. (a) High-resolution TEM image for a cross-sectional view of the TiO_2 nanoparticles in Nafion membrane (left), and UV/vis absorption spectra of Nafion films with (——) and without (— · —) embedded TiO_2 nanoparticles, with the inset showing the powder X-ray diffraction pattern of the TiO_2-loaded Nafion film (right). (From ref. (7) and (22)) (b) Scanning TEM image (in the Z-contrast mode) for a cross-sectional view of the silver-coated TiO_2 nanoparticles in Nafion membrane films (left), and UV/vis absorption spectra of Nafion membrane films containing TiO_2 nanoparticles without (— · —) and with (——) the silver coating (the corresponding silver salt solution concentrations used for the coating as marked), and the inset: photos of the corresponding films (right). (From ref. (8)).

Downloaded by STANFORD UNIV GREEN LIBR on June 5, 2012 | http://pubs.acs.org
Publication Date (Web): April 27, 2011 | doi: 10.1021/bk-2011-1064.ch007

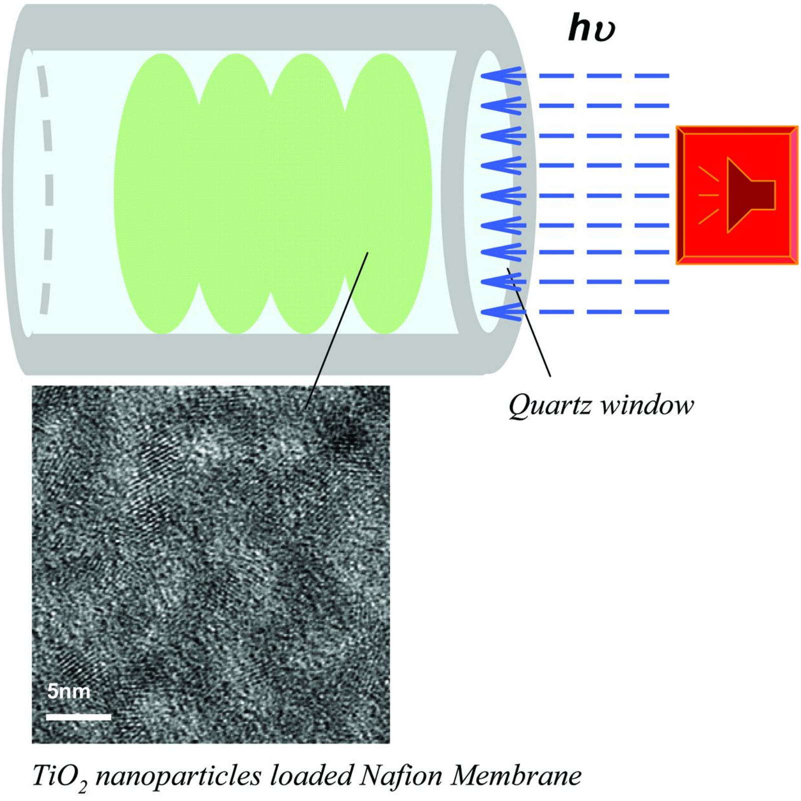

Scheme 3. Experimental setup for the photoreduction of liquid CO_2 with TiO_2-loaded Nafion films as photocatalyst. The TEM image is for a specimen from the cross-sectional microtome of a TiO_2-loaded film. (From ref. (7)).

The facile synthesis of semiconductor nanoparticles in Nafion membrane and the subsequent coating of the nanoparticles with a co-catalyst should be generally applicable to the preparation of other conceptually similar sheet-photocatalysts. In such a configuration, the membrane serves as an optically transparent host for the homogeneous dispersion of the catalytic nanoparticles. These photocatalysts in a uniquely well-dispersed configuration are valuable to various energy conversion applications.

3.2. Energetic Nanoparticles

The characteristic structure and properties of perfluorinated ionomer membranes discussed above and their ability to encapsulate and protect nanoparticles have also made them uniquely applicable in the development of nano-energetic materials. Nanosized (sub-100 nm) Al particles have recently been among the most widely investigated reactive and energetic nanomaterials (*10*, *11*, *30*–*33*). Their large specific surface area and energy density, when coupled or mixed with oxidative species, make them unique combustible additives in propellant formulations, among other fuel-related applications (*34*). Nanoscale Al particles are also studied as high-capacity hydrogen storage materials (*35*). Significant effort has been made on the development of synthetic methodologies for Al nanoparticles of desired properties (*10*, *11*, *30–33*, *36*). The chemical route based on thermal and/or catalytic decomposition of alane in the presence of a surface passivation agent such as perfluorinated carboxylic acids for particle protection and stabilization has been identified as being particularly promising (*10*, *11*). However, this method has generally yielded Al particles of 50 – 200 nm in average sizes. Smaller Al nanoparticles (thus an extremely high surface area) of a narrow size distribution have been pursued for their distinctive advantageous in uses as energetic nanomaterials and for more effective hydrogen generation. However, their bulk production in a consistent fashion and their protection for stability under ambient conditions present special challenges.

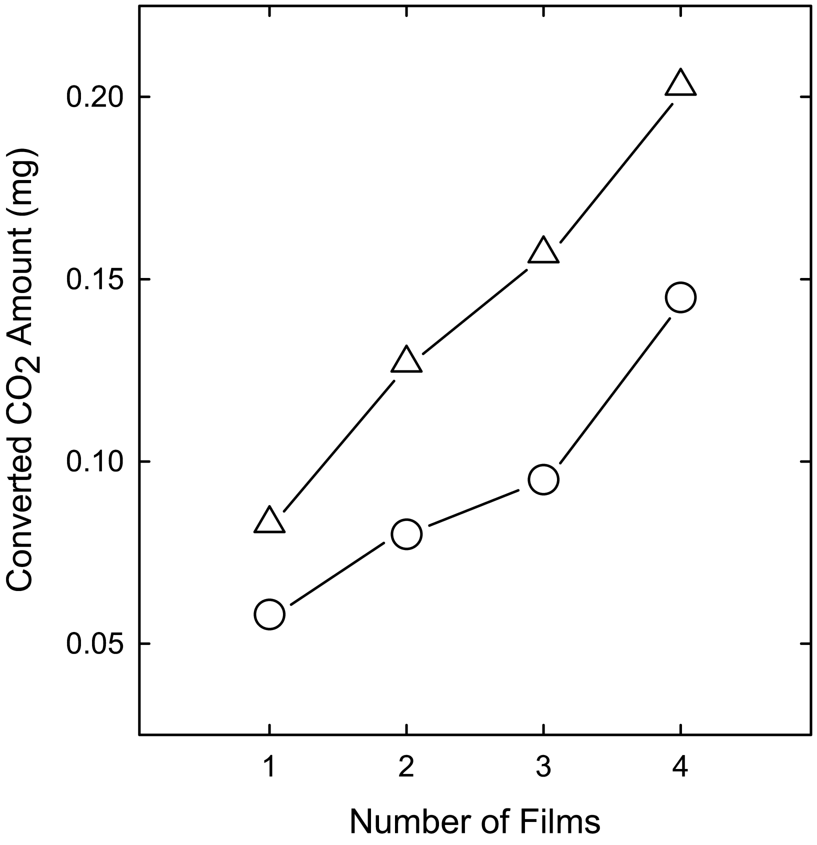

Figure 5. The photoconversion of CO_2 as a function of the number of stacked catalytic films with (Δ) and without (o) the silver coating of the embedded TiO_2 nanoparticles. The reproducibility for the data points was generally within ~3%. (From ref. (8)).

Downloaded by STANFORD UNIV GREEN LIBR on June 5, 2012 | http://pubs.acs.org
Publication Date (Web): April 27, 2011 | doi: 10.1021/bk-2011-1064.ch007

Sun and coworkers reported recently a new strategy in the facile yet controllable synthesis of smaller Al nanoparticles by using nanoscale cavities in Nafion membrane as templates. The nano-templated synthesis was based on the same catalytic alane decomposition chemistry. Experimentally, a piece of Nafion film in the sodium form was soaked in an isopropanol solution of $Ti(OC_3H_7)_4$, rinsed thoroughly to clean the film surface, and then dried. The Nafion film containing the titanium salt was immersed in a THF solution of 1-methylpyrrolidine alane with stirring in a glove-box under nitrogen atmosphere. The film color turned black during the reaction, consistent with the formation of small Al nanoparticles. After the reaction the film was thoroughly washed with THF, dried under vacuum, and then characterized by using a series of techniques. Shown in Figure 6 are low and high resolution TEM images (with the specimen from cross-sectional microtome), a statistical size analysis of particles from multiple TEM images, and also representative results from the EDX analysis (*12*). The randomly dispersed Al nanoparticles appeared crystalline (agreeing well with the face-centered-cubic standard for bulk Al (Figure 6), with an average particle size of 11 nm in diameter and a size distribution standard deviation of 2.5 nm. The EDX results confirmed the presence of large amounts of Al and fluorine (a part of the Nafion membrane structure) and a small amount of titanium from the catalyst. However, there was only a negligible amount of oxygen in the specimen despite the fact that the EDX analysis was performed under ambient conditions, suggesting that the embedded Al nanoparticles were protected by the membrane structure from any significant oxidation (*12*).

More detailed studies on the formation of Al nanoparticles in Nafion membrane suggested that significant variations in the amount of embedded materials in the membrane changed primarily the population of the nanoparticles, but affected much less the sizes of the particles, as suggested by the XRD results (Figure 7) (*12*). The results and conclusion were rather similar to those obtained previously in the systematic study of Ag nanoparticles in perfluorinated ionomer membranes (*23*). The population of Al nanoparticles in the Nafion membrane was increased by using a more concentrated alane solution in the reaction. With the use of high alane concentrations in the particle synthesis, the Nafion membrane films were apparently able to host a substantial amount of Al nanoparticles, as demonstrated by the obvious weight increases of the films post-alane reaction (Figure 8). For example, with alane solutions of 0.5 M and 2 M used in the reaction, the resulting films had weight increases of 14% and 122% (thus the implied Al contents in the films of 12% and 55%), respectively. Both the thermogravimetric analysis (TGA) and hydrogen generation results suggested that the weight increase was due to the amount of reactive Al in the film. For the latter, it was found that the reactive Al contents in the films could be determined accurately by using the films to generate hydrogen gas in a basic aqueous solution (*37*). The experiments were performed in a commercially supplied apparatus to allow precise volumetric measurements of the hydrogen gas generated for the calculation of the reactive Al contents. For the same example, the amounts of Al nanoparticles in the films prepared with 0.5 M and 2 M alane solutions were determined to be 11% and 57% of the film weights, in good agreement with the observed weight increases post-alane reaction discussed above. Results from the

Downloaded by STANFORD UNIV GREEN LIBR on June 5, 2012 | http://pubs.acs.org
Publication Date (Web): April 27, 2011 | doi: 10.1021/bk-2011-1064.ch007

Downloaded by STANFORD UNIV GREEN LIBR on June 5, 2012 | http://pubs.acs.org
Publication Date (Web): April 27, 2011 | doi: 10.1021/bk-2011-1064.ch007

XRD analysis and TEM imaging of the cross-sectional slices of the Al-in-Nafion composite films with high Al loadings suggested that the films were packed with Al nanoparticles, while the particle sizes remained generally similar, suggesting again that the different loadings of Al nanoparticles in the Nafion membrane films are generally decoupled from the average sizes of the nanoparticles.

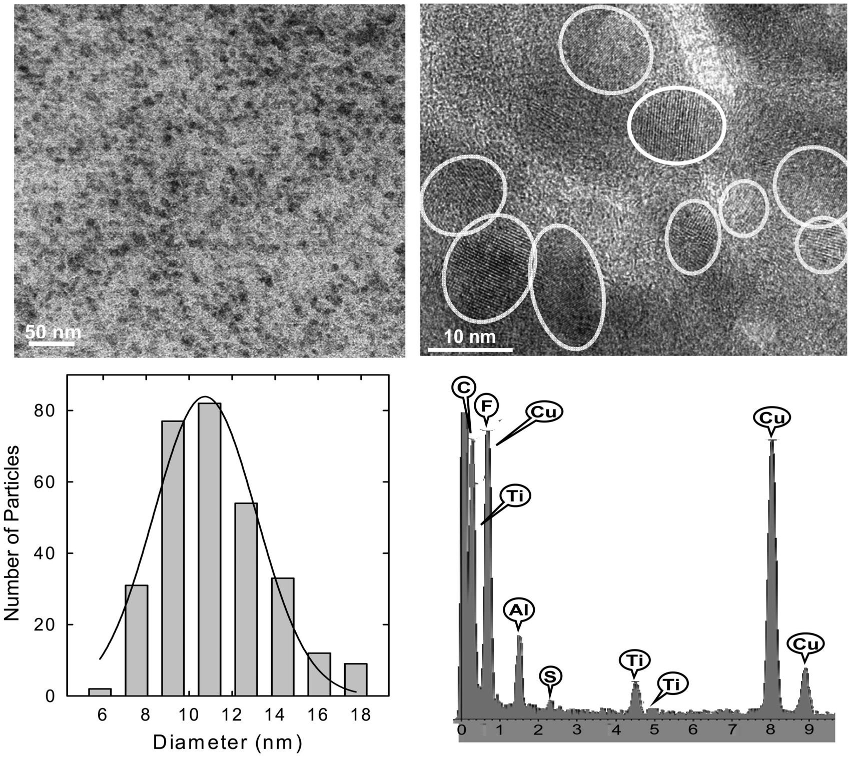

Figure 6. A representative TEM image for the specimen from ultra-microtome of an Al-in-Nafion film (top left), a statistical size analysis of the particles from multiple images (bottom left), and the corresponding high-resolution TEM image for the specimen from ultra-microtome (top right) and the EDX spectrum (bottom right). (From ref. (12)).

Downloaded by STANFORD UNIV GREEN LIBR on June 5, 2012 | http://pubs.acs.org
Publication Date (Web): April 27, 2011 | doi: 10.1021/bk-2011-1064.ch007

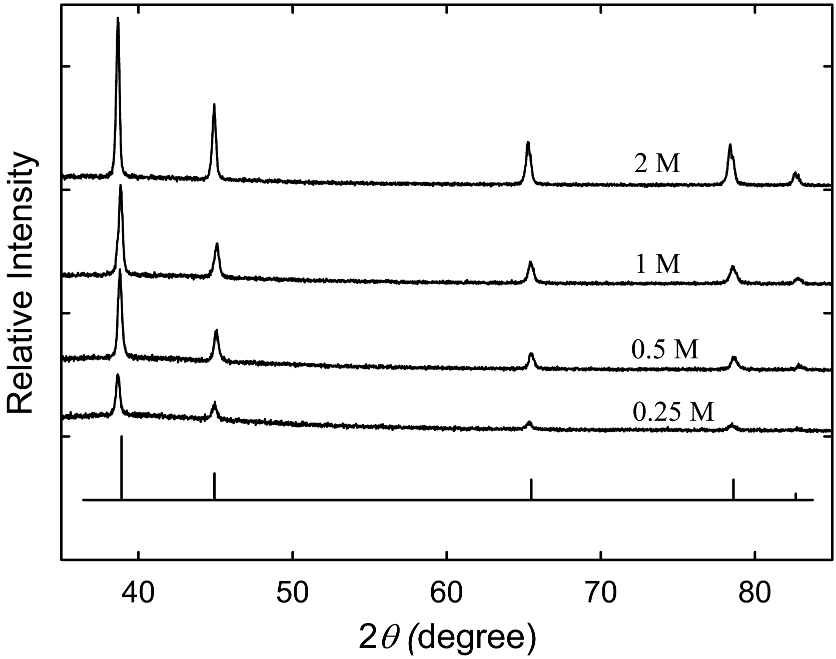

Figure 7. X-ray diffraction patterns of the Al-in-Nafion films prepared with different alane solution concentrations (as marked) are compared with that of bulk fcc aluminum in JCPDS database.

As reported (*12*), all of the Al-in-Nafion film samples were found to be surprisingly stable in ambient air, with the reactive Al contents changed only marginally over time (Figure 9). The relatively more significant initial decrease in the reactive Al content might be attributed to the oxidation of the Al nanoparticles close to the film surface. The small sacrifice of these nanoparticles due to the oxidation probably "sealed off" the composite film as a whole, minimizing any subsequent oxidation. The Nafion membrane structure was apparently not permeable to oxygen under the ambient air conditions, preventing any substantial oxidation of the embedded Al nanoparticles. On the other hand, the Al nanoparticles were fully accessible under the hydrolysis conditions for the nearly quantitative generation of hydrogen gas. Therefore, the Al-in-Nafion composite films may serve as a unique platform for stable energetic materials and/or as materials for energy storage.

Downloaded by STANFORD UNIV GREEN LIBR on June 5, 2012 | http://pubs.acs.org
Publication Date (Web): April 27, 2011 | doi: 10.1021/bk-2011-1064.ch007

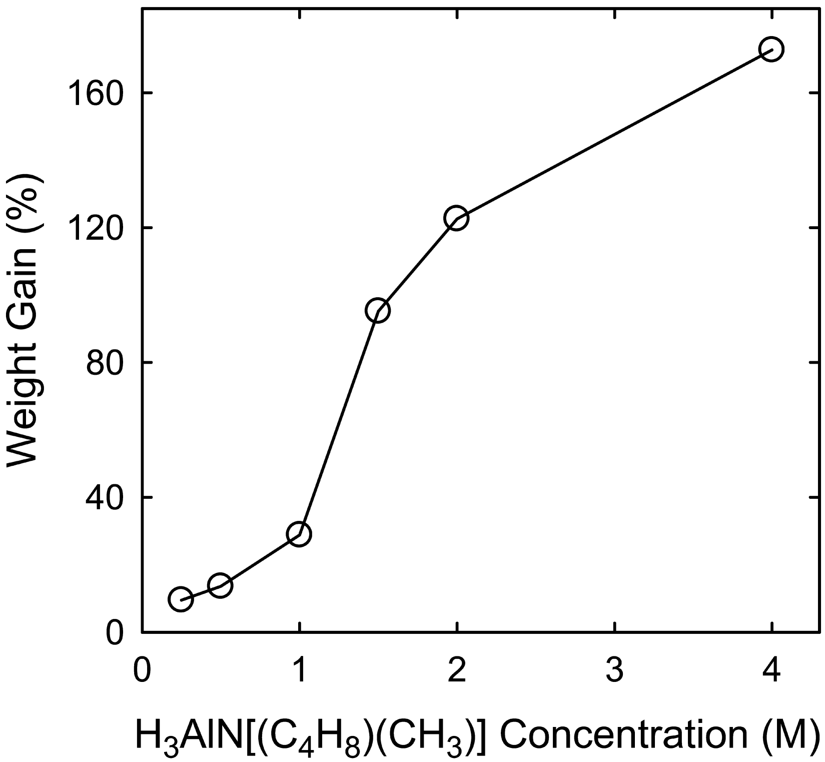

Figure 8. The weight increase in the composites of Al nanoparticles in Nafion membrane as a function of the alane concentration in the reaction for the preparation of these composite films.

The Nafion membrane films embedded with Al nanoparticles, especially those with high loadings, were found to be easily crushed via grinding in a mortar to form black-gray powdery materials. These materials were subsequently dispersed in solvents such as hexane with sonication, though the resulting suspension was unstable (with significant precipitation within a few minutes). Interestingly, however, the Al nanoparticles were largely unaffected in the process, maintaining their sizes and dispersion according to electron microscopy (Figure 10) and XRD results. These powders were essentially Al nanoparticles protected and stabilized by Nafion polymers (disintegrated backbones in the original membrane film).

Downloaded by STANFORD UNIV GREEN LIBR on June 5, 2012 | http://pubs.acs.org
Publication Date (Web): April 27, 2011 | doi: 10.1021/bk-2011-1064.ch007

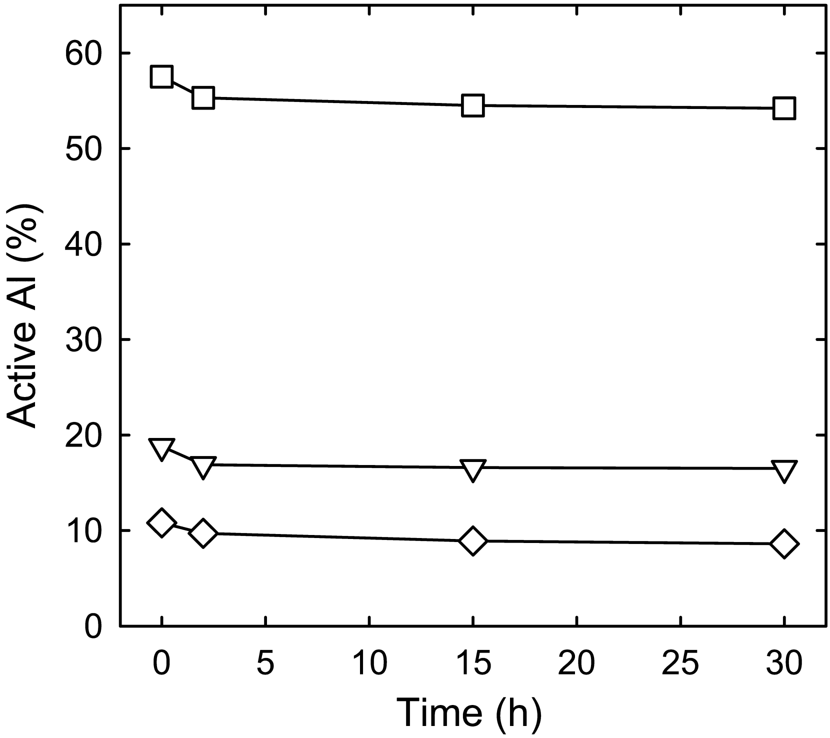

Figure 9. The reactive Al contents in the various Al-in-Nafion films (based on volumetric measurements of the hydrogen gas generated) over time in ambient air. (From ref. (12)).

The reported results on Al nanoparticles in Nafion membrane seem consistent with the same mechanistic picture proposed for Ag and Ag_2S nanoparticles. In the formation of these nanoparticles, the cavities and channels could apparently be rearranged (such as channels connecting two cavities being squeezed out for a larger cavity) to accommodate the growth of the nanoparticles toward their thermodynamically and/or kinetically preferred sizes, but still only up to a limit (likely 15 nm or less) imposed by the much more rigid perfluorinated polymer backbones in the membrane films (*15*, *24*, *25*). There were no dramatic increases in average particle sizes even at very high Al loadings. On the other hand, the high loadings of Al nanoparticles probably strained the membrane films so severely to make them vulnerable to decomposition (via grinding in a mortar, for example, as discussed above).

Downloaded by STANFORD UNIV GREEN LIBR on June 5, 2012 | http://pubs.acs.org
Publication Date (Web): April 27, 2011 | doi: 10.1021/bk-2011-1064.ch007

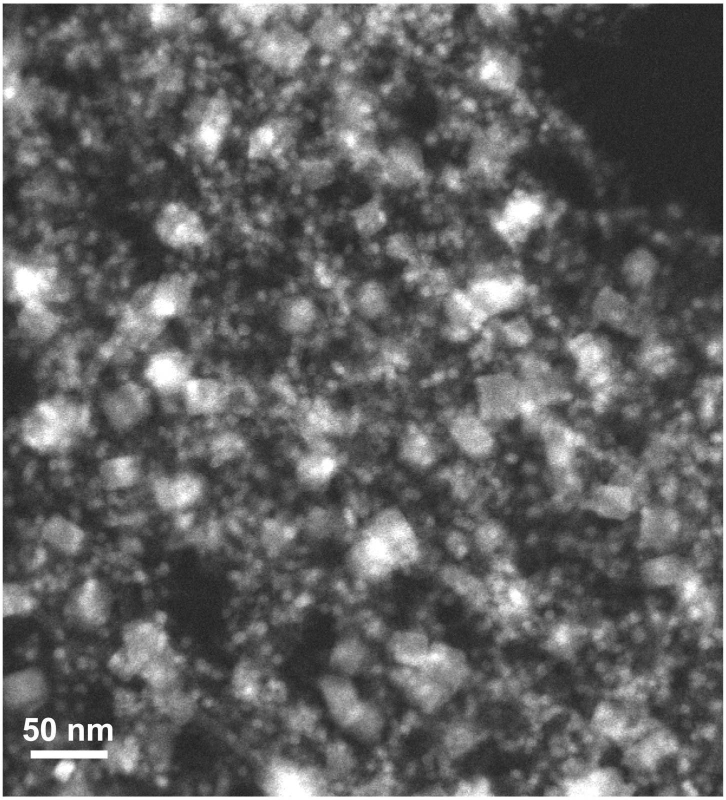

Figure 10. Representative scanning TEM image (in the Z-contrast mode) of the black-gray powdery Al-in-Nafion membrane with high Al loading (from grinding in a mortar and dispersing in hexane).

The nanocomposite-like configuration of nanoscale Al particles in perfluorinated ionomer membrane (Nafion) serves as an excellent platform for nano-energetic materials, similar to or more advantageous than those based on larger Al nanoparticles protected by fluorinated polymers (*10*, *11*). Separately, it also serves as an excellent platform for efficient hydrogen generation under ambient conditions. Further investigations may enable a regeneration of the Al nanoparticles in the nanoscale cavities of the membrane, so as to achieve rechargeable nano-Al systems for energy storage and hydrogen production.

4. Summary and Perspective

The results as examples presented and discussed here suggest that the structural cavities in perfluorinated ionomer membrane films serve as ideal nanoscale templates for facile preparation of well-dispersed small nanoparticles from semiconductors, metals, and other materials. For reactive nanoparticles, in particular, they are surprisingly intact and stable in the membrane films under ambient conditions, yet still accessible by other reactants (such as basic water in the hydrogen generation) under a different set of conditions. The membrane films, which are macroscopically homogeneous and optically clean and transparent, also serve as excellent hosts for the nanoparticles to keep them dispersed. These spatially well-dispersed nanoparticles are unique photocatalysts for photochemically driven energy conversion applications. The membrane hosts are also valuable to another kind of energy conversion, potentially rechargeable reactive metal-based hydrogen production. However, despite the progress already made, the use of perfluorinated ionomer membranes in energy-related nanotechnology is still at the early stage. Further development and optimization are necessary, including a clear understanding of the structural details in the membrane films and the effects of the structure on transport properties of the membrane films (materials in and out of the nanoscale cavities in the membranes). Nevertheless, the nano-templating in these membrane films will find broad applications in energy conversion and beyond.

Downloaded by STANFORD UNIV GREEN LIBR on June 5, 2012 | http://pubs.acs.org
Publication Date (Web): April 27, 2011 | doi: 10.1021/bk-2011-1064.ch007

Acknowledgments

Financial support from the Air Force Research Laboratory through the nanoenergetics program is gratefully acknowledged. Additional supports from the South Carolina Space Grant Consortium (Y.-P.S.), the Air Force Office of Scientific Research (AFOSR) through the program of Dr. Julian Tishkoff (C.E.B.), the American Chemical Society Petroleum Research Fund (Y.-P.S.), the Cente for Advanced Engineering Fibers and Films at Clemson University (Y.-P.S.), and the Defense Threat Reduction Agency (DTRA) through the grant #HDTRA-07-1-0026 (E.A.G.) are also acknowledged.

References

1. (a) Kramer, K. W.; Biner, D.; Frei, G.; Gudel, H. U.; Hehlen, M. P.; Luthi, S. R. *Chem. Mater.* **2004**, *16*, 1244. (b) Shan, J. N.; Ju, Y. G. *Appl. Phys. Lett.* **2007**, *91*, 123103. (c) Shan, J. N.; Ju, Y. G. *Nanotechnology* **2009**, *20*, 275603.
2. Lorbeer, C.; Cybinska, J.; Mudring, A. V. *Chem. Commun.* **2010**, *46*, 571.
3. Gladysz, J. A., Curran, D. P., Horváth, I. T., Eds.; *Handbook of Fluorous Chemistry*; Wiley/VCH: Weinheim, Germany, 2004.
4. (a) Horvath, I. T.; Rabai, J. *Science* **1994**, *266*, 72. (b) Nyffeler, P. T.; Durn, S. G.; Burkart, M. D.; Vincent, S. P.; Wong, C.-H. *Angew. Chem. Int. Ed.* **2005**, *44*, 192. (c) Yang, C.; Wang, X. P.; Omary, M. A. *J. Am. Chem. Soc.* **2007**, *129*, 15454.
5. (a) Krishnan, M.; White, J. R.; Fox, M. A.; Bard, A. J. *J. Am. Chem. Soc.* **1983**, *105*, 7002. (b) Mau, A. W. H.; Huang, C. -B.; Kakuta, N.; Bard, A. J.; Campion, A.; Fox, M. A.; White, J. M.; Webber, S. E. *J. Am. Chem. Soc.* **1984**, *106*, 6537. (c) Kakuta, N.; White, J. M.; Campion, A.; Bard, A. J.; Fox, M. A.; Webber, S. E. *J. Phys. Chem.* **1985**, *89*, 48. (d) Kakuta, N.; Park, K. H.; Finlayson, M. F.; Ueno, A.; Bard, A. J.; Campion, A.; Fox, M. A.; Webber, S. E.; White, J. M. *J. Phys. Chem.* **1985**, *89*, 732. (e) Smotkin,

Downloaded by STANFORD UNIV GREEN LIBR on June 5, 2012 | http://pubs.acs.org
Publication Date (Web): April 27, 2011 | doi: 10.1021/bk-2011-1064.ch007

E. S.; Brown, R. M.; Radenburg, L. K.; Salomon, K.; Bard, A. J.; Campion, A.; Fox, M. A.; Mallouk, T. E.; Webber, S. E.; White, J. M. *J. Phys. Chem.* **1990**, *94*, 7543. (f) Zen, J.-M.; Chen, G. C.; Fan, F.-R. F.; Bard, A. J. *Chem. Phys. Lett.* **1990**, *169*, 23. (g) Li, F.; Bertoncello, P.; Ciani, I.; Mantovani, G.; Unwin, P. R. *Adv. Funct. Mater.* **2008**, *18*, 1685.

6. Premkumar, J.; Ramaraj, R. *J. Photochem. Photobiol. A* **1997**, *110*, 53.
7. Pathak, P.; Meziani, M. J.; Li, Y.; Cureton, L. T.; Sun, Y.-P. *Chem. Commun.* **2004**, 1234.
8. Pathak, P.; Meziani, M. J.; Castillo, L.; Sun, Y.-P. *Green Chem.* **2005**, *7*, 667.
9. (a) Lips, H. R. *J. Spacecraft Rockets* **1977**, *14*, 539. (b) Kubota, N.; Serizawa, C. *J. Propul. Power* **1987**, *3*, 303. (c) Watson, K. W.; Pantoya, M. L.; Levitas, V. I. *Comb. Flame* **2008**, *155*, 619.
10. (a) Jouet, R. J.; Warren, A. D.; Rosenberg, D. M.; Bellitto, V. J.; Park, K.; Zachariah, M. R. *Chem. Mater.* **2005**, *17*, 2987. (b) Jouet, R. J.; Carney, J. R.; Granholm, R. H.; Sandusky, H. W.; Warren, A. D. *Mater. Sci. Technol.* **2006**, *22*, 422.
11. Meziani, M. J.; Bunker, C. E.; Lu, F.; Li, H.; Wang, W.; Guliants, E. A.; Quinn, R. A.; Sun, Y.-P. *ACS Appl. Mater. Interfaces* **2009**, *1*, 703.
12. Li, H.; Meziani, M. J.; Lu, F.; Bunker, C. E.; Guliants, E. A.; Sun, Y.-P. *J. Phys. Chem. C* **2009**, *113*, 20539.
13. (a) Smart, B. E. *Organofluorine Chemistry – Principles and Commercial Applications*; Banks, R. E., Smart, B. E., Tatlow, J. C., Eds.; Plenum Press: New York, 1994, p 57. (b) Kissa, E. *Fluorinated Surfactants and Repellents*; Marcel Dekker, Inc.: New York, 2001. (c) Chambers, R. D. *Fluorine in Organic Chemistry*; Blackwell: Oxford, 2004. (d) Kirsch, P. *Modern Fluoroorganic Chemistry*; Wiley-VCH: Weinheim, Germany, 2004.
14. (a) Young, R. J. *Introduction to Polymers*; Chapman and Hall: New York, 1983, 204. (b) Kreuer, K. D., Paddison, S. J., Spohr, E.; Schuster, M. *Chem. Rev.* **2004**, *104*, 4637. (c) Smitha, B.; Sridhar, S.; Khan, A. A. *J. Membr. Sci.* **2005**, *259*, 10. (d) Cele, N.; Ray, S. S. *Macromol. Mater. Eng.* **2009**, *294*, 719.
15. Heitner-Wirguin, C. *J. Memb. Sci.* **1996**, *120*, 1.
16. Mauritz, K. A.; Moore, R. B. *Chem. Rev.* **2004**, *104*, 4535.
17. (a) Souzy, R.; Ameduri, B.; Boutevin, B.; Gebel, G.; Capron P. *Solid State Ionics* **2005**, *176*, 2839. (b) Gelbard, G. *Ind. Eng. Chem. Res.* **2005**, *44*, 8468.
18. (a) White, H. S.; Leddy, J.; Bard, A. J. *J. Am. Chem. Soc.* **1982**, *104*, 4811. (b) Buttry, D. A.; Saveant, J. M.; Anson, F. C. *J. Phys. Chem.* **1984**, *88*, 3086. (c) DiVirgilio-Thomas, M.; Heineman, W. R.; Seliskar, C. J. *Anal. Chem.* **2000**, *72*, 3461. (d) Bertoncello, P.; Ciani, I.; Li, F.; Unwin, P. R. *Langmuir* **2006**, *22*, 10380. (e) Bertoncello, P.; Ciani, I.; Marenduzzo, D.; Unwin, P. R. *J. Phys. Chem. C* **2007**, *111*, 294. (f) Bertoncello, P.; Dennany, L.; Forster, R. J.; Unwin, P. R. *Anal. Chem.* **2007**, *79*, 7549.
19. (a) Wang, S.; Lin, X. *Electrochim. Acta* **2005**, *50*, 2887. (b) Zhuo, Y.; Yuan, R.; Chai, Y.; Tang, D.; Zhang, Y.; Wang, N.; Li, X.; Zhu, Q. *Electrochem. Commun.* **2005**, *7*, 355. (c) Hrapovic, S.; Liu, Y.; Male, K. B.; Luong, J. H. T. *Anal. Chem.* **2004**, *76*, 1083. (d) Lim, S. H.; Wei, J.; Lin, J.; Li, Q.; You,

J. K. *Biosens. Bioelectron.* **2005**, *20*, 2341. (e) Bertoncello, P.; Peruffo, M.; Unwin, P. R. *Chem. Commun.* **2007**, 1597.

20. Rollins, H. W.; Lin, F.; Johnson, J.; Ma, J. J.; Liu, J. T.; Tu, M. H.; DesMarteau, D. D.; Sun, Y.-P. *Langmuir* **2000**, *21*, 8031.
21. Rollins, H. W.; Whiteside, T.; Shafer, G. J.; Ma, J. J.; Tu, M, H.; Liu, J. T.; DesMarteau, D. D.; Sun, Y.-P. *J. Mater. Chem.* **2000**, *10*, 2081.
22. Liu, P.; Bandara, J.; Lin, Y.; Elgin, D.; Allard, L. F.; Sun, Y.-P. *Langmuir* **2002**, *26*, 10398.
23. Sun, Y.-P.; Atorngitjawat, P.; Lin, Y.; Liu, P.; Pathak, P.; Bandara, J.; Elgin, D.; Zhang, M. Z. *J. Memb. Sci.* **2004**, *245*, 211.
24. Yeo, S. C.; Eisenberg, A. *J. Appl. Polym. Sci.* **1977**, *21*, 875.
25. Gierke, T. D.; Munn, G. E.; Wilson, F. C. *J. Polym. Sci.* **1981**, *19*, 1687. (c) Hsu, W. Y.; Gierke, T. D. *J. Membr. Sci.* **1983**, *13*, 307.
26. (a) Litt, M. H. *Polm. Prepr.* **1997**, *38*, 80. (b) Schmidt-Rohr, K.; Chen, Q. *Nat. Mater.* **2008**, *7*, 75.
27. (a) Bunker, C. E.; Ma, B.; Simmons, K. J.; Rollins, H. W.; Liu, J.-T.; Ma, J.-J.; Martin, C. W.; DesMarteau, D. D.; Sun, Y.-P. *J. Electroanal. Chem.* **1998**, *459*, 15. (b) Bunker, C. E.; Rollins, H. W.; Ma, B.; Simmons, K. J.; Liu, J.-T.; Ma, J.-J.; Martin, C. W.; DesMarteau, D. D.; Sun, Y.-P. *J. Photochem. Photobiol.* **1999**, *126*, 71.
28. (a) Lee, P. C.; Meisel, D. J. *J. Am. Chem. Soc.* **1980**, *102*, 5477. (b) Nagata, I.; Li, R.; Banks, E.; Okamoto, Y. *Macromolecules* **1983**, *16*, 903. (c) Kuczynski, J. P.; Milosavljevic, B. H.; Thomas, J. K. *J. Phys. Chem.* **1984**, *88*, 980. (d) Szentirmay, M. N.; Prieto, N. E.; Martin, C. R. *J. Phys. Chem.* **1985**, *89*, 3017. (e) Robertson, M. A.; Yeager, H. L. *Macromolecules* **1996**, *29*, 5166. (f) Anson, F. C.; Gray, H. B.; Sabatani, E.; Nikol, H. D. *J. Am. Chem. Soc.* **1996**, *118*, 1158.
29. (a) Fendler, J. H. *Nanoparticles and Nanostructured Films: Preparation, Characterisation and Applications*; Wiley-VCH: Weinheim, Germany, 1998. (b) Thomas, J. M.; Johnson, B. F. G.; Raja, R.; Sankar, G.; Midgley, P. A. *Acc. Chem. Res.* **2003**, *36*, 20.
30. (a) Haber, J. A.; Buhro, W. E. *J. Am. Chem. Soc.* **1998**, *120*, 10847. (b) Higa, K. T.; Johnson, C. E.; Hollins, R. A. U. S. Patent 5,885,321, 1999.
31. Foley, T. J.; Johnson, C. E.; Higa, K. T. *Chem. Mater.* **2005**, *17*, 4086.
32. Fernando, K. A. S.; Smith, M. J.; Harruf, B. A.; Lewis, W. K.; Guliants, E. A.; Bunker, C. E. *J. Phys. Chem. C* **2009**, *113*, 500.
33. Mahendiran, C.; Ganesan, R.; Gedanken, A. *Eur. J. Inorg. Chem.* **2009**, *14*, 2050.
34. (a) Mench, M. M.; Kuo, K. K.; Yeh, C. L.; Lu, Y. C. *Combust. Sci. Technol.* **1998**, *135*, 269. (b) Brousseau, P.; Anderson, C. J. *Propellants, Explos., Pyrotech.* **2002**, *27*, 300. (c) Granier, J. J.; Pantoya, M. L. *Combust. Flame* **2004**, *138*, 373.
35. (a) Roach, P. J.; Woodward, W. H.; Castleman, A. W., Jr.; Reber, A. C.; Khanna, S. N. *Science* **2009**, *323*, 492. (b) Wang, H.; Leung. D.; Leung, M.; Ni, M. *Renew. Sustain. Energ. Rev.* **2009**, *13*, 845.
36. (a) Weigle, J. C.; Luhrs, C. C.; Chen, C. K.; Perry, W. L.; Mang, J. T.; Nemer, M. B.; Lopez, G. P.; Phillips, J. *J. Phys. Chem. B* **2004**, *108*, 18601. (b)

Downloaded by STANFORD UNIV GREEN LIBR on June 5, 2012 | http://pubs.acs.org
Publication Date (Web): April 27, 2011 | doi: 10.1021/bk-2011-1064.ch007

Kwon, Y. S.; Gromov, A. A.; Strokova, J. I. *Appl. Surf. Sci.* **2007**, *253*, 5558.

37. Fedotova, T. D.; Glotov, O. G.; Zarko, V. E. *Propellants, Explos., Pyrotech.* **2000**, *25*, 325.

Downloaded by STANFORD UNIV GREEN LIBR on June 5, 2012 | http://pubs.acs.org
Publication Date (Web): April 27, 2011 | doi: 10.1021/bk-2011-1064.ch007

Chapter 8

Synthesis, Functionalization, Characterization, and Application of Controlled Shape Nanoparticles in Energy Production

Simona E. Hunyadi Murph,[*] Steven M. Serkiz, Elise B. Fox, Hector Colon-Mercado, Lindsay Sexton, and Matthew Siegfried

**National and Homeland Security, Savannah River National Laboratory,
Savannah River Site, Aiken, SC 29808
[*]Simona.Murph@srnl.doe.gov**

In this chapter we present recent advances in synthesis, characterization, optical, catalytic and physico-chemical properties of nanoscale materials with potential applications in fuel cells processes. In particular, this review and original research focuses on the catalytic properties of noble metal nanoparticles (e.g., platinum, gold and silver) as a function of particles morphology and composition (e.g., isotropic and anisotropic, solid, hollow and core-shell structures, and mono- and bi- metallic compositions, supported and unsupported).

1. Introduction

One of the greatest challenges in the current global economy is the ability to secure a long-term energy supply. The exponential demand for energy, insufficient fossil fuel supplies, excessive green house gas emissions, efficiency of use, reliability, environmental and climate concerns are critical for development of a sustainable society. It is, therefore essential to develop technologies and materials that enable new, low cost, effective and environmentally friendly energy solutions for clean, renewable sources to meet global energy needs.

The impact and performance of these technologies are intimately connected with the materials properties and applications. With the recent advances in the areas of nanomaterials synthesis, characterization, and application, these materials hold the promise for designing alternative, sustainable and innovative solutions to the current global energy crisis.

Nanomaterials have triggered a great deal of interest recently due to their unique mechanical, electrical, catalytic, mineralogical, and optical properties that differ from the bulk material solely based on their size (*1*). These scale-dependant properties, sometimes referred to as quantum-size effects, have been shown to result from their size being smaller than the mean free path of their electrons (10-100 nm), scattering length and increased surface energy, among other properties. Nanotechnology has introduced new concepts for innovative technology applications in energy research, such as solar energy harvesting, energy storage and conversion, hydrogen production and storage, conversion and use of energy (fuel cells, catalysis, etc.), optical and chemical sensors, photonics, imaging, and drug delivery systems.

In this chapter we review recent advances in synthesis, characterization, optical, catalytic and physico-chemical properties of nanoscale materials with potential energy production applications. In addition, we present original research on studies conducted in the authors' laboratory involving catalytic applications of noble metal nanoparticles in fuel cells processes. More specifically, this review and original research focuses on the catalytic properties of noble metal nanoparticles as a function of particles morphology and composition (e.g., isotropic and anisotropic, solid, hollow and core-shell structures, and mono- and bi- metallic compositions, supported and unsupported).

2. Fuel Cells

Fuel cells (FCs) have been studied and developed extensively throughout the world as one of the most feasible next generation clean energy sources. FCs are electrochemical devices that convert a fuel such as hydrogen, methanol or natural gas directly to electricity through an electro-catalytic process (*2*). Among all types of FCs, which include metal hydride, alkaline, molten carbonate, phosphoric acid, and solid oxide, proton exchange membrane (PEM) FCs are promising for transport applications due to their fast startup, immediate response to changes in the demand for power, and tolerance to shock (*3*). PEMFCs can be further subdivided into direct methanol FCs (DMFC), direct hydrogen FCs (DHFC), and direct formic acid FCs (DFAFC) (*4*).

The DMFC has been considered an ideal FC system because it produces electric power by the direct conversion of the methanol fuel at the anode (Figure 1). When liquid methanol is catalytically oxidized directly at the anode, carbon dioxide, protons, and electrons are produced. Protons diffuse through a PEM, also referred to as a polymer electrolyte membrane, to the cathode, where they combine with the electrons to produce electrical energy and water. There are a number of applications where the DMFCs can provide real benefit based on its high energy density and instantaneous refueling time with the simple exchange of the fuel cartridge. For example, the next generation of high bandwidth mobile devices, battery chargers, and military applications are good niche markets for DMFCs because these applications often require higher power densities than existing batteries can provide.

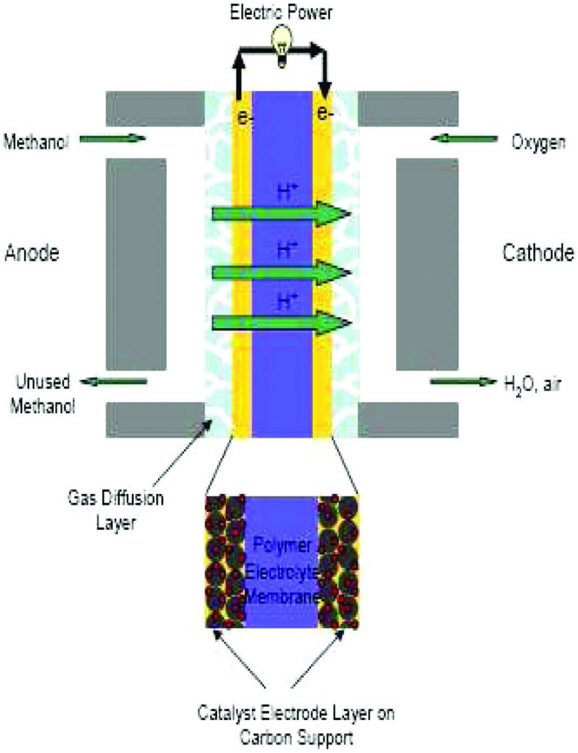
Electric Power
e-
e-
Methanol
Oxygen
H+
H+
H+
Anode
Cathode
Unused
Methanol
H_2O, air
Gas Diffusion
Layer
Polymer
Electrolyte
Membrane
Catalyst Electrode Layer on
Carbon Support

Figure 1. Schematic of DMPEM fuel cell.

DMFCs, however, have several disadvantages including high cost, largely as a result of high precious metal catalyst loading requirements, slow kinetics due to adsorbed carbon monoxide during one of the intermediate steps (*5*), and methanol crossover. In order to overcome these problems there is a need to develop alternative anode and cathode catalysts with high surface area and lower cost to increase the reaction kinetics and lower costs as well as to develop novel membranes that reduce methanol crossover. For example, preliminary studies reported by Jiang (*6*) showed that poly(diallyldimethylammonium chloride) (PDDA) stabilized Pt nanoparticles can block methanol crossover through the Nafion™ electrolyte membrane and enhance the performance of DMFCs.

3. Fuel-Cell Catalysts

Currently, in the scientific community, Pt and Pt alloy-based (e.g. Rh, Ru, Ag, Au, etc.) metals are recognized as the best electrochemical catalysts (*10*, *11*). Platinum also serves as a major catalyst in various organic reactions (Heck and Suzuki reactions) and serves as a catalyst in industrial synthesis of nitric acid and reduction of pollutant gases emitted from automobiles (*7*, *8*). From a practical point of view, Pt is one of the few active and stable noble metals that can withstand harsh environments. However, its high cost often prohibits large-scale commercial application.

Catalysts serve two main functions in a DMFC. They facilitate the oxidation of methanol at the anode (Equation 1) and the reduction of oxygen at the cathode (Equation 2).

$$2CH_3OH + 2H_2O \rightarrow 12H^+ + 2CO_2 + 12e^- \qquad \text{(Eq. 1)}$$

$$3O_2 + 12H^+ + 12e^- \rightarrow 6H_2O \qquad \text{(Eq. 2)}$$

Typically, both catalysts in the DMFC consist of nanoscale Pt particles on high surface area carbon. However, these catalysts still have high activation overvoltages (or voltage losses due to the slow kinetics of reaction) and are plagued by methanol crossover that can lead to poisoning at the cathode. To address these problems Pt alloys have received significant attention in the catalyst development arena.

The US Department of Energy estimates that Pt-based catalysts will require roughly four times less Pt than currently utilized in PEMFC designs to represent a realistic alternative to internal combustion engines (*9*). As a result, one main goal of catalyst design for PEMFCs is to reduce the precious metal loading by producing Pt catalysts with high surface area and low density with increased catalytic performance and utilization efficiency. Decreasing the particle size and creating of nanomaterials with different morphologies, (e.g., solid, porous, hollow materials, supported or unsupported materials, etc.) are expected to boost the performance of the Pt catalyst and reduce the materials cost and overall weight of the FC.

Catalytic activity depends highly on the size, shape, morphology and composition of the nanoparticles (*10*, *11*). Moreover because the crystal shape dictates the interfacial atomic arrangement of the crystal, the shape of a crystal is directly related to its catalytic properties and stability (*12*, *13*). The density and symmetry of atoms in different crystallographic planes are not identical, and neither is their electronic structure, bonding, surface energy or chemical reactivities. Atoms on tips or corners of a crystal have more uncoordinated bonds and tend to be more active. In essence, the same material can act very differently depending on its shape and in recent years a great deal of attention has focused on the shape/property relationships of nanoparticles. The nature and the structure of the electrode material can also affect the adsorption and electro-oxidation/reduction processes, controlling the formation of adsorbed intermediates and the products (*14*).

In summary, due to the larger fraction of atoms at the particle surface, nanometer-sized electrode materials are generally favorable to macroscale electrodes in terms of materials costs alone. Additionally, the electrochemical activity of noble metal catalysts is highly dependent on the size, oxidation state, mineralogy, reaction site distribution (e.g. planar, edge, and corner), and composition of the catalyst. Because many of these properties can only be practically manipulated at the nanoscale, the synthesis and characterization of nanoscale catalysts hold much promise in the development of the next generation of energy technologies.

Considerable progress has already been made toward the design and synthesis of highly active noble metallic catalysts with tunable particle sizes, shapes and compositions for DMFC applications and this work is discussed below in terms of: scale effects; anisotropy; composite nanostructures and catalyst supports.

3.1. Scale Effects

Nanoscale Pt materials have been shown to be more electrochemically active (i.e., catalytic activity on a mass normalized basis) than bulk Pt catalysts (*15*). The smaller the particle size, the larger the fraction of atoms at the surface and, therefore, a higher average binding energy per atom (*10*). Recently, Yamamato's group found that as the size of the Pt clusters decreased to sub-nano scale dimensions, their catalytic activity significantly increased in FC applications (*16*). For example, as the size of the clusters decreased to 12 atoms, the catalytic current produced for the reduction of oxygen increased to 13 times that of commercial Pt nanoparticles (*16*). However, it is believed that the improved performance is probably not due to a simple increase in surface area but to quantum size effects not fully understood yet. Table 1 is a summary and the applications of different size Pt spherical nano-catalysts.

Considerable progress has recently been made toward the design and synthesis of highly active Pt catalysts of different sizes and shapes, in organic solvent or aqueous solutions. However, there are limited synthesis procedures that allow production of monodispersed, tunable Pt nanospheres, with diameters from 1-100 nm, which employ identical ingredients and capping reagents.

Our group has recently demonstrated the ability to produce Pt nanospheres from circa 5 to 85 nm in size by wet chemical synthesis routes. These approaches are facile and straightforward procedures that utilize identical reactants and allow production of large quantities of Pt nanospheres. Two different synthesis routes were employed to control the size of the nanoparticles: citrate reduction (*27*) and seed-mediated (*28*, *29*). Figure 2 shows a general description of these two general routes used to produce Pt nanospheres with controllable diameters.

With the citrate reduction approach, Pt salts, such as H_2PtCl_6 or K_2PtCl_4 were reduced with sodium citrate at 200°C (Figure 2). Small Pt spheres with a diameter of 23±2 nm were prepared (Figure 3a) under these synthesis conditions. In this procedure, citrate serves as a capping and a reducing agent. The formation of Pt nanospheres was easily observed by the color change of the solution from pale yellow to brown (Figure 3b).

In the second method, a seed-mediated synthesis route was used to prepare Pt nanospheres of controlled size by an analogous approach as that reported for Au nanospheres (*28*, *29*). Platinum seed nanoparticles, with a size range of 5±1 nm, were produced by chemical reduction of hydrogen hexachloroplatinate (IV) hydrate (H_2PtCl_6, 99.9%) with a strong reduction agent (sodium borohydride) in the presence of a aqueous solution of sodium citrate at 100°C. The development of a brown solution was an indication that the Pt nanoparticles were produced. These 5 nm seed particles were subsequently used as nucleation centers to grow larger spheres (Figure 2b and Figure 4). Growth solutions containing additional hydrogen hexachloroplatinate (IV) hydrate (H_2PtCl_6, 99.9%), sodium citrate, citric acid, ascorbic acid and 5 nm seed solutions were refluxed at 100°C for 30 minutes.

Table 1. Summary of size controlled Pt-based catalysts

Catalyst	*Synthesis procedure*	*Diameter (nm)*	*Reaction Catalyzed*	*Ref.*
Pt	H_2PtCl_6	3 and 8	Hydrogen oxidation and oxygen reduction reaction	(*17*)
Pt	Sputtering GLAD	100–300	Tested as cathode electrodes in PEM membrane fuel cells	(*18*)
Carbon supported Pt	Commercial grade	1, 2, 5, 30	Formation of OH adlayer, the CO bulk oxidation, and oxygen reduction reaction	(*19*)
Pt - carbon and titania supports	Physical vapor deposition	0.2–2.5	Oxygen reduction reaction	(*20*)
Pt/diamond composite electrode	Galvanostatic deposition	50-350	Oxygen reduction reaction	(*21*)
Pt	Commercial E-Tek	1-10 and >10	Methanol oxidation reaction	(*22*)
carbon-supported Pt	Commercial-grade (E-TEK)	4.6 to 2.3	Oxygen reduction in methanol-containing acid electrolyte	(*23*)
Pt	- tert-butylamine -1,3-diaminopropane - anthranilic acid	- 80 and 100 - 5-8 - 30-50	Oxygen reduction reaction	(*24*)
Pt on mesoporous carbon support	Impregna-tion–reduction method	2.7 to 6.7	Oxygen reduction and methanol oxidation reactions	(*25*)
Pt encapsulated in dendrimer	Dendrimer templating method	1–2	Oxygen reduction reaction	(*26*)

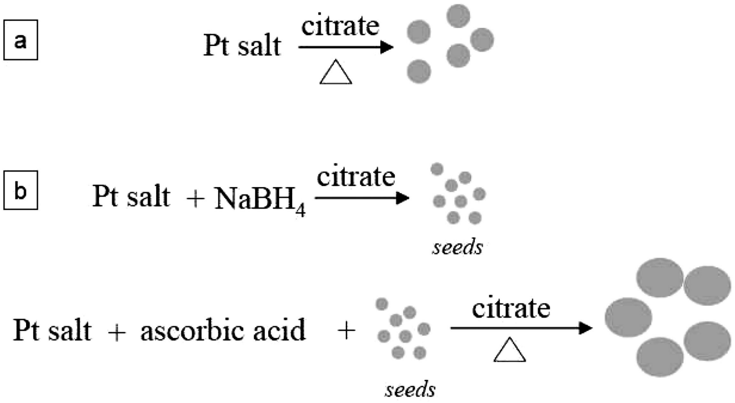

Figure 2. Schematic representation of (a) citrate reduction and (b) seed-mediated synthetic routes to produce Pt nanospheres.

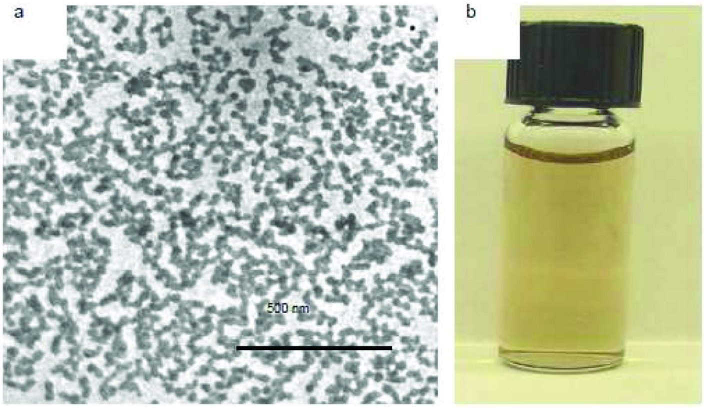

Figure 3. (a)TEM image of 23±2nm Pt nanospheres prepared by a citrate approach, (b) photograph of Pt nanospheres.

This seed-mediated approach allows control on the diameter of the Pt nanospheres simply based on the reactants and the Pt seed concentrations. Controlling reaction conditions (e.g. the Pt salt, reducing agent, seeds concentrations) allows control over the nucleation process and, thereby, the nanosphere sizes (Figure 2b and Figure 4). Generally, by increasing the seed particle concentration, the diameter of the nanospheres decrease. Figure 4 shows a SEM image of uniform 5±1nm, 11±1 nm, 20±1 nm, 45±1 nm, 70±1 nm and 83±1 nm Pt nanospheres.

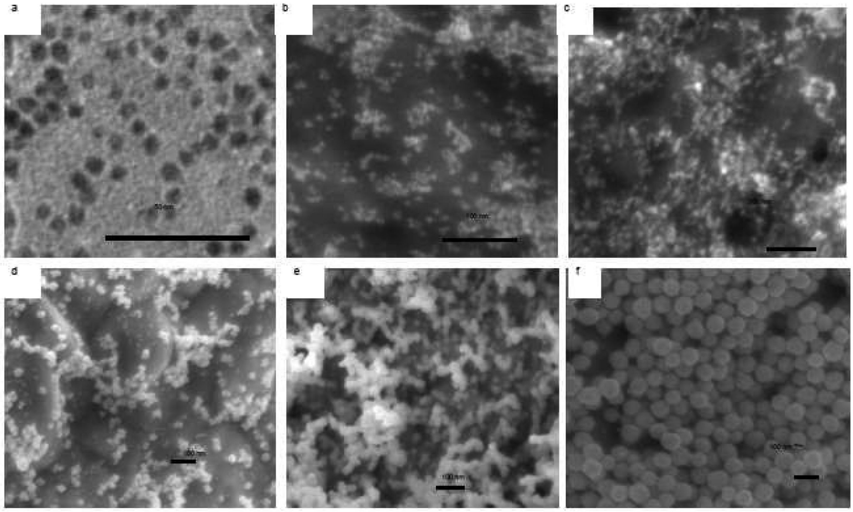

Figure 4. Micrographs of Pt nanoparticles prepared seed-mediated approach (a) "seed" 5±1 nm particles, (b) 11±1 nm, (c) 20±1 nm, (d) 45±1 nm, (e) 70±1 nm and (f) 83±1 nm Pt nanospheres. Scale bar: 500 nm-a, 100 nm-b-f.

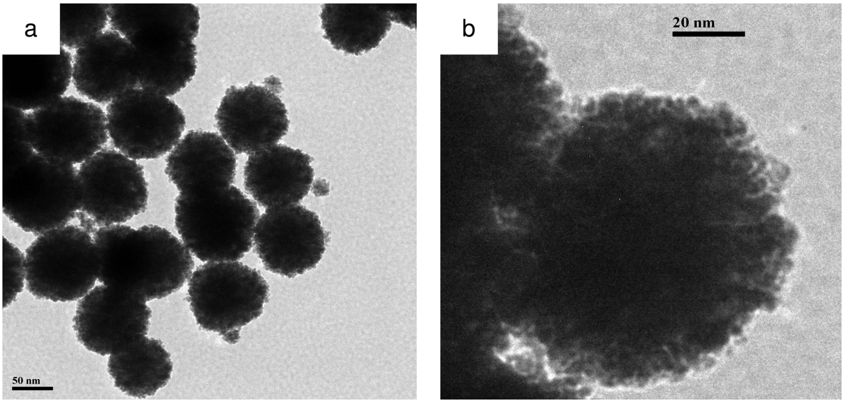

Figure 5. TEM images of 83±1 nm Pt nanoparticles prepared by seed mediated approach. Scale bar (a) 50 nm, (b) 20nm.

The final morphology of the nanoparticles differs based on the synthesis route employed. With citrate reduction, the final product displays a smooth surface with no visible protuberances (Figure 3a), while the seed-mediated approach produces particles with a rough surface with visible individual Pt particulates (4-5 nm) (see Figure 5a and Figure 5b) on the outside of the sphere. While the surface of these nanospheres is quite porous with noticeable protrusions, bumps and pits, they have a highly uniform diameter. The nanospheres are stable and can be separated from the aqueous phase without aggregation.

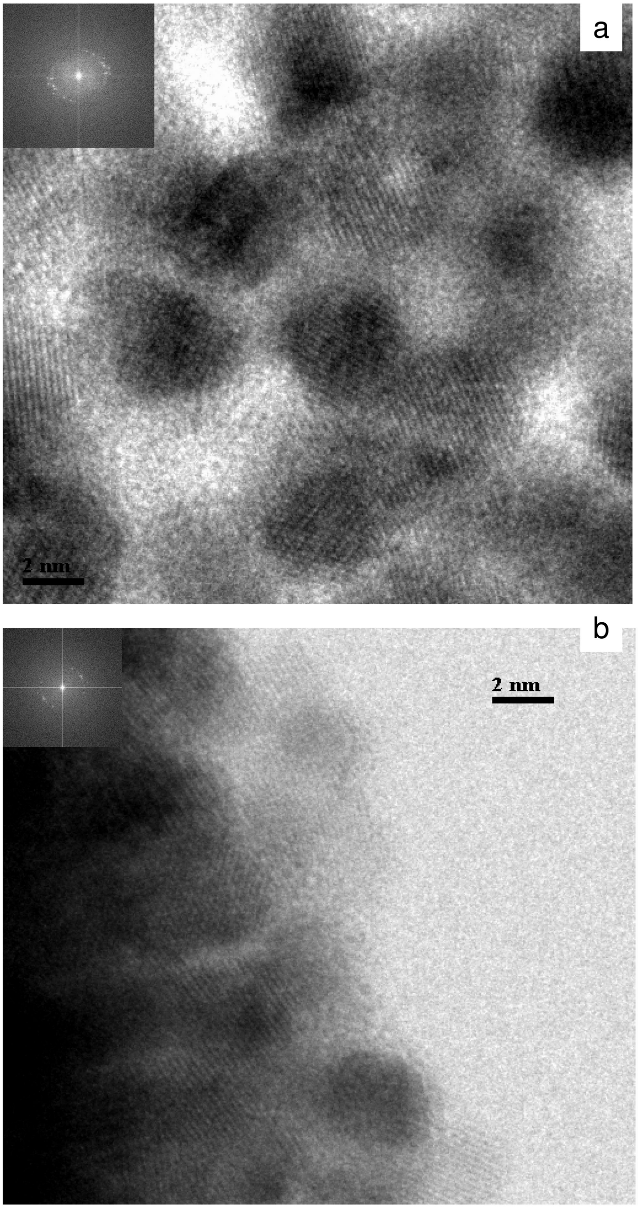

Figure 6. HRTEM of (a) individual 5nm Pt seed nanospheres and (b) 83 nm Pt spheres. Insert shows the diffraction pattern of the Pt nanoparticles. Scale bar: 2 nm – a,b.

High resolution TEM images (Figure 6a,b) and diffraction patterns Figure 6a,b inset) reveal the internal lattice structure of the Pt prepared by seed mediated approach: seeds and grown nanospheres. Both images indicate well defined, parallel, “perfect and infinite,” equally spaced and continuous fringes that suggests single crystalline domains. There are no observable stacking faults, twins or volume dislocations. This is not surprising since twinned structures of Pt rarely form due to high internal strain energy associated with Pt twinned crystals (*30*, *31*). Lattice-fringe imaging indicate a lattice constant of 2.24 Å which is suggestive of [111] facets, in agreement with literature data for spherical Pt nanoparticles (*32*). Pt was confirmed in these nanoparticles using the X-ray energy dispersive microanalysis (data not shown).

The electrochemical activity of Pt nanospheres of varying sizes and synthesis routes (i.e., surface porosity) was investigated by monitoring the oxygen reduction reaction (ORR) using a rotating ring disk electrode (RRDE) cyclic voltammetry. The approach provides information on the kinetics of reactions at the electrode catalyst. Particles were suspended in DI water by sonicating for five minutes. A minimum of 30 μL of the particle suspension was deposited on a glassy carbon electrode (GCE) (5-mm diameter disc) and allowed to dry. The catalyst was then coated with 4 μL of a 20% Nafion™/ethanol solution and allowed to dry. The GCE current output during the potential sweep was used to determine the electrode reactions in 0.5M H_2SO_4 as described in Soderberg et al. (*33*) A graphite carbon rod counter electrode and Ag/AgCl reference electrode were used. Cyclic voltammograms (CVs) were collected under a N_2 blanket at scan rate of 50 mV/s. All potentials were normalized to the standard hydrogen electrode (SHE) and are presented in Figure 7.

The electrochemical activity for the hydrogen reduction reaction (HRR) was determined by the size of the anodic peak on the CV from approximately 0 to 0.25V, which is directly correlated to the electrochemical surface area of the nanoparticle. From the preliminary results below, it appears that, for electrodes impregnated with Pt nanoparticles with a crystalline surface morphology synthesized by citrate reduction or seed mediated approach (seeds), the 5 nm particles have the highest electrochemical surface area (CV "a"), while the 23 nm particles have the lowest (CV "c"). This is also supported by magnitude of Pt reduction, which is the cathodic peak located at approximately 0.75V. It is not surprising that the highest activity is seen on the smallest nanoparticles, as it has previously been determined that the activity should increase with decreasing particle diameter (*34*).

In contrast to the expected size-dependent behavior observed for electrodes made with Pt nanoparticles synthesized by citrate-reduction (i.e., with a smooth and "compacted" surface), the electrode impregnated with 83 nm Pt nanoparticles synthesized by seed-mediated growth was not consistent with this trend. The lower electrochemical activity of the 23 nm particles (CV "c") compared with 83 nm (CV "b") may be explained by the surface roughness of the nanospheres. It is well known that smaller nanoparticles display an enhanced catalytic activity due to the increased surface area. However, the surface protrusions, porosity and compactness of the structures are all factors expected to influence the catalytic activity. It is, therefore, postulated that the enhanced catalytic activity for the 83 nm seed-mediated nanosparticles is due to the additional surface area created by the surface roughness and porosity and, possibly, by an increased activity of these additional sites. For purposes of comparison we assumed that all Pt ions introduced in the reaction are completely reduced to Pt (0) and are entirely converted to nano-spherical Pt materials. The catalyst loading is similar in these experiments. Inductively coupled plasma atomic emission spectroscopy experiments are currently underway to determine the final concentration of the Pt materials. Table 2 is a summary of the total Pt concentration used for each of the synthesis procedures and shows a wide distribution each of the particles produced.

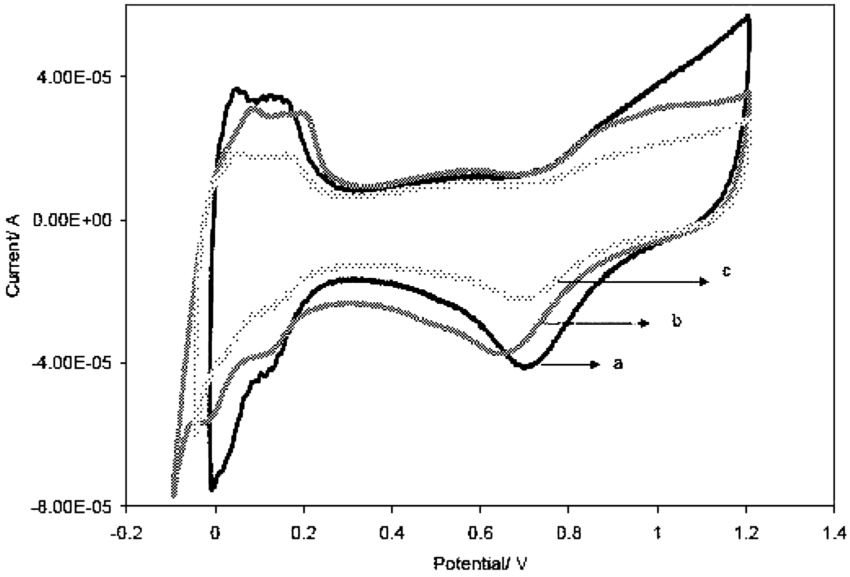

Figure 7. Cyclic voltammograms of electrodes impregnated with Pt nanospheres of varying sizes produced by seed mediated approach (a) 5 nm, (b) 83 nm, and citrate reduction (c) 23 nm.

Table 2. Nominal Pt of concentration nanospheres

Pt spheres size (nm)	*Synthesis procedure*	*Nominal Pt concentration (mM)*
5	Borohydride reduction (seeds)	0.26
23	Citrate reduction	0.11
83	Seed mediated	0.52

Even though the nominal Pt concentration is double for the 83 nm Pt nanospheres, the 5 nm spherical nanoparticles are more active toward the ORR. While the typical drop casting procedure used to impregnate the particles into the electrode is easy and straightforward, it is not the most efficient. For example, this method does not provide the most effective distribution of Pt catalysts on the electrode surface and could obstruct some of the active sites on the catalyst, thereby decreasing the measured catalytic activity. The practical use of Pt catalyst depends largely on the ability to effectively expose the maximum number of active catalysts sites while minimizing the precious metal loading.

3.2. Anisotropic Nanomaterials

The properties of isotropic materials, like those discussed above, are assumed to display the same variations in x, y, and, z space dimensions. While there are likely to be property variations (e.g., surface sites versus core sites, edges and steps) along these dimensions, each space dimension exhibits the same variation functionality. In contrast, anisotropic materials display different spatial and property functionality in the x, y, and, z dimensions. Synthesis of anisotropic nanostructures, therefore, allows access to properties and larger proportions of those properties in nanoscale anisotropic structures than are available at the macroscale. For example, various anisotropic noble metal nanoparticles can be produced in a wide range of shapes (e.g., wire, rod, cube, octahedral, pyramid) (Figure 8) and can be controlled by thermodynamic and kinetic factors. These factors are determined by intrinsic structural properties and reaction parameters such as solvent, capping reagents, reducing agents, temperature, concentration, time, etc. (*28*, *29*, *35*, *36*)

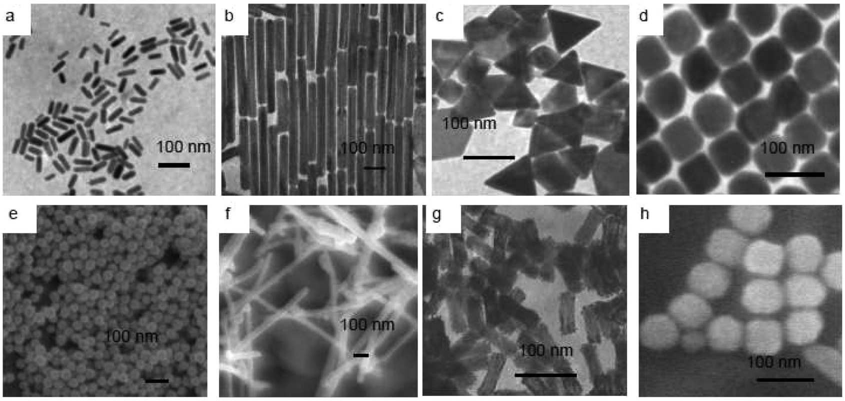

Figure 8. TEM and SEM images of different shaped noble metals. (a-d) Au nanoparticles and (e,f) Pt nanoparticles (g, h) Au-Pt nanoparticles. Scale bar: 100 nm –a-h.

Table 3. Summary of shape controlled Pt-based catalysts

Shape	*Size (nm)*	*Facets*	*Shape Directing Agent*	*Reaction Catalyzed*	*Ref.*
Cubo-octahedral	1.1-5.6	(111) + (100)	Ethylene Glycol	Methanol Oxidation Formic Acid Oxidation	(*40*)
Cubo-octahedral	2-5	(100) + (111)	Ferric Chloride	Oxygen Reduction	(*41*)
Cubo-octahedral	30-40	(100) + (111)	Pulsed laser deposition	Oxygen Reduction	(*42*)
Multipods Discs Hexagons	500 500-1000 2000	---	Electric Potential	Formic Acid Oxidation Ethanol Oxidation	(*43*)
Hollow Spheres	10	---	Electrochemical Removal of Silver Core	Oxygen Reduction	(*44*)
Cubic Tetrahedral Nearly Spherical	7.1 4.8 4.9	(100) (111) (100) + (111)	Polyacrylate PVP PVP	Electron-Transfer Reaction Between Hexacyanoferrate(III) Ions and Thiosulfate Ions	(*45*)
Tetrahexa-hedral	217	{730}, {210}, {530}	Electrochemical Treatment of Pt Nanospheres	Formic Acid Oxidation Ethanol Oxidation	(*46*)

The past decade has witnessed a large amount of research on shape dependent electrocatalytic activity, as presented in Table 3. For example, the activity of Pt surfaces towards catalyzing the ORR in the PEMFC has been shown to be highly dependent on the surface arrangement of atoms and increases in the order of (110) > (111) > (100) planes exposed at the interface (*37*). Thus, Pt particles having a rhombic dodecahedron shape with only (110) planes exposed at the interface are expected to be more active than octahedral and cubic particles having only (111) and (100) planes respectively exposed at the interface (*13*, *38*).

Furthermore, it has been shown that higher index planes of Pt (having a high density of atomic steps, ledges, and kinks serving as active sites for breaking chemical bonds) generally exhibit much higher catalytic activity than the aforementioned low index planes (*39*). Tetrahexahedral Pt crystals enclosed by 24 high indexed facets (such as {730}, {210}, and {520}) have also been shown to be up to 400% more active in the oxidation of ethanol than spherical crystals having the same surface area (*40*). El-Sayed (*12*) investigated the activity of cubic, tetrahedral, and nearly spherical Pt nanoparticles in catalyzing the electron-transfer reaction between hexacyanoferrate (III) ions and thiosulfate ions and found that tetrahedral particles had almost half the activation energy as cubic particles of similar size. Their data showed a strong correlation between catalytic activity and the percentage of surface/corner atoms suggesting that when similarly sized nanoparticles have different shapes the nanoparticles having a higher percentage of atoms on the corners and edges are expected to be more catalytically active. Earlier studies on cubo-octahedral shaped particles suggested that a change in the fraction of crystal lattices on the Pt particle surfaces could be directly correlated to the activity of the catalyst (*13*). If the nanostructure of the Pt particles can be controlled to produce the optimized facet ratios, the catalytic activity of the nanoparticles can be increased, thereby, minimizing the metal loading in the system.

Electrocatalytic reactions are also structure sensitive and their rates vary dramatically with shape or crystallographic facets. For example, in the case of the formic acid and ethanol electro-oxidation, the electrocatalytic performance of Pt tetrahexahedra (THH) nanostructures (80 nm Pt on glassy carbon) have been compared with commercial spherical nanoparticles supported on carbon black (3.2 nm Pt/C on Vulcan XC-72) and 115 nm Pt nanospheres. The results show oxidation currents nearly double for THH Pt compared to that of Pt nanospheres or Pt/C catalysts (*46*).

3.2.1. Nano-Composite Structures

The field of nanocomposite materials is one of the fastest growing areas of research. Nanocomposite can be considered as solid arrangements of repetitive nano-building blocks of different materials that form the structure. These materials typically consist of an inorganic host solid containing an organic component, vice versa or variations and combinations of both. The idea that an assortment of two or more dissimilar materials with disparate functionalities can create fundamentally new structures with improved functionalities and properties offer enormous potential for new applications (*47*). The promise of nanocomposite materials lies within the multifunctionality of nano-building blocks used to design novel structures with properties that are not available in the original component materials. Many chemical and physical interactions are governed by surfaces, surface properties and interfaces (*47*). Therefore, they are vital for fine-tuning nanocomposite properties including: reactivity, stability, electronic structure, melting and boiling point, etc. Despite the extensive research in the area of nanocomposites, the correlation between the catalytic activity synergistic effects of the interfaces, high surface area of nanostructures, composition, spatial arrangement, structure, processing, property relationship, reproducible production routes, etc. is still limited (*48*).

We focus our attention on the synthesis and characterization of three specific types of nanocomposites: core-shell, alloy type and hollow nanocomposite materials where the core is either a metal or silica or vice-versa, or an "emptiness" domain. In many ways, hollow nanoparticles can be considered as nanocomposite structures due the multiphase domain; the hollow can be considered as one phase of "nothingness" that exists at the core of the solid shell nanostructure. While it appears that nanomaterials produced by us (see below) have hollow interiors, it is certainly possible that remnant ions from the synthesis or dispersing/washing solutions, or a combination of both are present inside the structures. By processing metal nanostructures into hollow ones, their performance and efficiency could be further improved because they have a lower material density and a larger fraction of their atoms at the surface, which results in more active sites per mass or mole of metal (*49*).

Generally, the synthesis route used by our group to prepare composite nanostructures was to employ nanostructured materials with different geometries (e.g., spheres, rods, wires, etc.) as "seed" templates. Subsequently, conformal, nonconformal or overgrowth wet chemical procedures were used to produce hollow and bicompositional nanomaterials as presented below.

3.2.1.1. Hollow Nanomaterials

Hollow nanomaterials are an attractive class of functional materials due to their unique physico-chemical properties resulting from their geometries, morphologies, and additional interfaces. They display higher surface-to-volume ratios compared with their solid counterparts, which could be beneficial for applications including energy storage and conversion, catalysis, biomedicine and cell imaging (*50*). This configuration will not only significantly reduces the raw materials cost of the catalyst but is expected to positively affect the weight and performance of FC applications.

For instance, recent studies showed that activity for the oxygen reduction reaction of the hollow Pt shells with nanochannels is higher than that of the commercial catalyst, indicating that additional active catalytic sites and edges are beneficial toward catalytic reactions (*51*).

Hollow nanomaterials can be produced by either template-mediated or galvanic displacement synthesis routes. The template-mediated approaches utilize a sacrificial nano-template coated with a material of interest, followed by complete or partial removal of the template by a post-treatment. Although template-based syntheses can provide good control over nanoparticle dimensions with predetermined geometry, they are commercially limited by the tedious work involved in the removal of the templates. The synthesis steps and the reagents involved in removal of the template can involve harsh procedures that can depreciate and destroy the final morphology, stability, oxidation state, etc. of the resulting nanomaterial.

Galvanic replacement reactions have been used by us and others to synthesize hollow monometallic Au (*52*), Pt (*53*), Pd (*54*) or bimetallic (*55*) nanomaterials starting from Ag (*52*, *53*, *56*), Ge (*57*), and Co (*58*), nanomaterial precursors. By controlling the initial morphology, size, and shape of the sacrificial template, tunable hollow nanomaterials with controllable shell thickness, void size, porosity, and composition can be easily achieved. The galvanic replacement approach, therefore, provides an effective alternative for the production of hollow nanomaterials in large quantities.

We have been able to produce Pt hollow nanospheres and high aspect ratio (i.e., one-dimensional Pt nanotubes) by galvanic replacement reactions with bimetallic Ag-Pt nanomaterials as intermediates (*52*, *53*). Currently, there are very few reports (*59*) in the literature on the synthesis of one-dimensional Pt nanoparticles. For example, the latest attempts to produce long single-crystalline Pt nanorods in solution, through a polyol process under slow reduction in the presence of air and Fe^{2+} or Fe^{3+} ions, mostly yielded aggregates of nanoparticles with the nanorods growing at the surface of the aggregates.

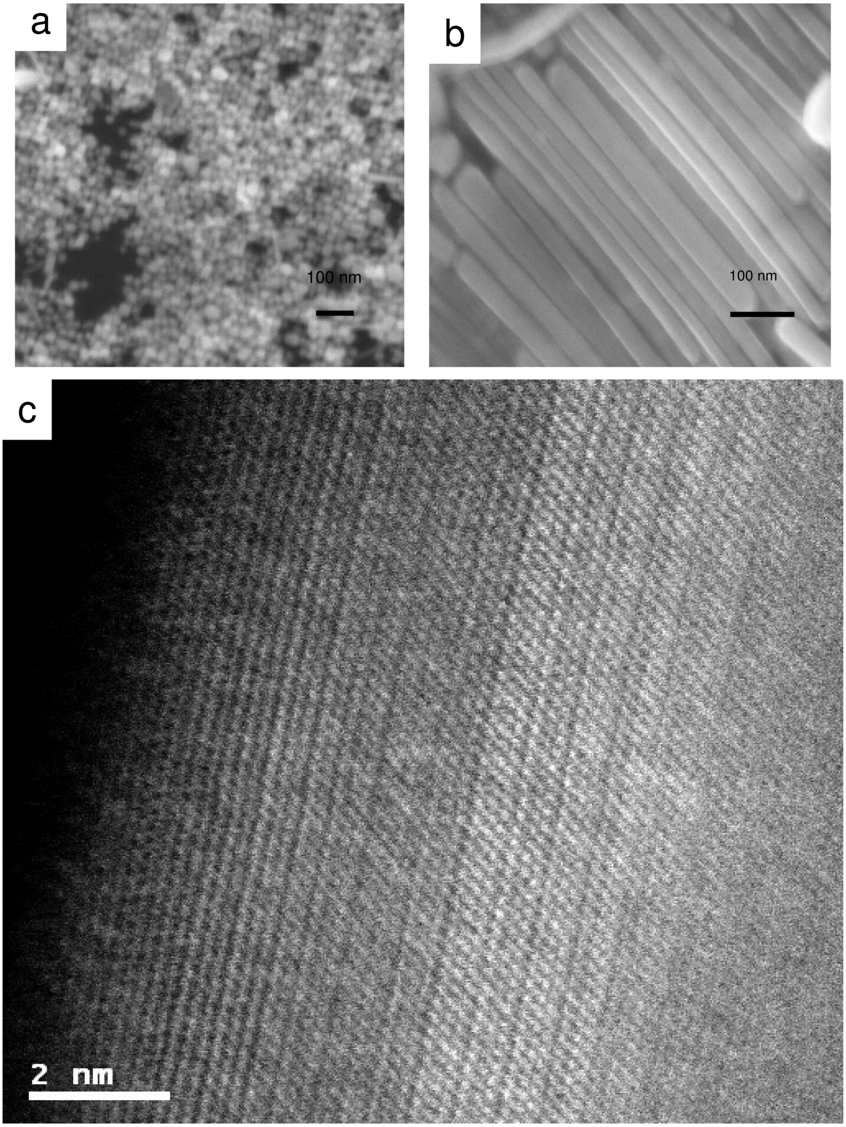

Figure 9. SEM images of (a) 59 nm Ag nanospheres, (b) Ag nanowires, and HRTEM of (c) Ag nanowires used as sacrificial template. Scale bars: 100 nm-a, b and 2 nm-c.

We synthesized and characterized Pt metal hollow nanostructures by replacing Ag atoms in the Ag nanoparticles (acting as a sacrificial template) with Pt cations from the solution phase by controlling the redox conditions of the solution and dissolved ion speciation and concentration, as previously reported (*53*) (see Figure 9a,b). In this process, Ag nanostructures were used both as the source of electrons for the reduction of Pt ions and a physical template around which Pt atoms were deposited during reduction. The control of the Ag sacrificial template size and shape was used for tuning the morphology of Pt hollow nano-structures.

Initially, the sacrificial Ag template nanospheres were prepared by a citrate reduction reaction as reported by Lee et. al. (*60*) The reaction is one in which a Ag salt is reduced to Ag metal, at 100 °C, by sodium citrate. Changes in reactant concentrations can lead to different Ag nanospheres sizes. In this citrate reduction synthesis, sodium citrate performs multiple tasks, as a reducing reagent and as a capping reagent to stabilize the nanoparticle.

Moreover, by boiling aqueous Ag nitrate solutions with aqueous sodium hydroxide solutions, high aspect ratio Ag nanowires can be produced (Figure 9b) (*61*). This reaction produced Ag nanowires with a 30 nm diameter and up to 20 um in length. High resolution transmission electron microscopy (HRTEM) (Figure 9c) performed on the Ag nanowires shows a stacking sequence of the Ag atoms while the diffraction pattern suggests a twinned crystallographic arrangement of the Ag atoms. Molecular dynamic simulation on the Ag nanowires demonstrate that the direction of elongation of the Ag nanowires is [100], with either Ag {100} or Ag {110} faces, or both while each end of the rod is capped with five triangular faces that are Ag {111} (*62*, *63*).

Next, Pt hollow nanospheres and nanowires were produced by a galvanic displacement reaction with Pt (II) followed by Ag dissolution with aqueous ammonia (*53*):

$$2\,\mathrm{Ag(s)} + [\mathrm{PtCl_4}]^{2-}\mathrm{(aq)} \rightarrow 2\,\mathrm{AgCl\ (aq\ or\ s)} + \mathrm{Pt(s)} + 2\,\mathrm{Cl^-(aq)} \qquad \text{Eq. 3}$$

$$4\,\mathrm{Ag(s)} + 2\,\mathrm{NH_3(aq)} + \mathrm{O_2} + 2\,\mathrm{H_2O(l)} \rightarrow [\mathrm{Ag(NH_3)_2}]^+\mathrm{(aq)} + 4\,\mathrm{OH^-(aq)} \qquad \text{Eq. 4}$$

This is similar to the Ag-Au galvanic displacement reaction, in which addition of $HAuCl_4$ to the Ag nanomaterials leads to formation of Au nanomaterials, as reported by us (*52*) and others (*64*). When Pt ions are added to the aqueous solution of Ag nanowires, the displacement reaction occurs rapidly (*53*). At the initiation of the reaction, galvanic replacement takes place on the Ag nanowires surface by Equation 3. As the reaction proceeds, the reduced Pt atoms nucleate on the Ag nanowire surface due to the confinement effect, and grow eventually into a thin shell around the Ag nanowire surface (*52*, *53*).

The size and shape of the Ag nanoparticles control the final morphology of the Pt hollow nanoparticles and the Ag template can be removed from the nanostructure by treatment with ammonia (Equation 4). Electron microscopy was used to monitor the morphological changes and to confirm the hollow appearance of the final nanomaterial (Figure 10 and Figure 11). The TEM images (Figure 10a and Figure 11a) revealed that the smooth and uniform surface of the Ag sacrificial templates nanomaterials becomes rough, porous and uneven following the galvanic displacement reaction. Moreover, the TEM images show noticeable pits, bumps and defects on the nanoparticles surface. The nanomaterials retained their initial shape (wires and spheres) and display a hollow aspect.

Table 4 is a summary of the nanoparticle dimensions before and after the displacement reaction. An average of ~20-25 nm increase in diameter was recorded when a molar equivalent, in terms of nominal Ag, of Pt concentration was added to the Ag nano-template.

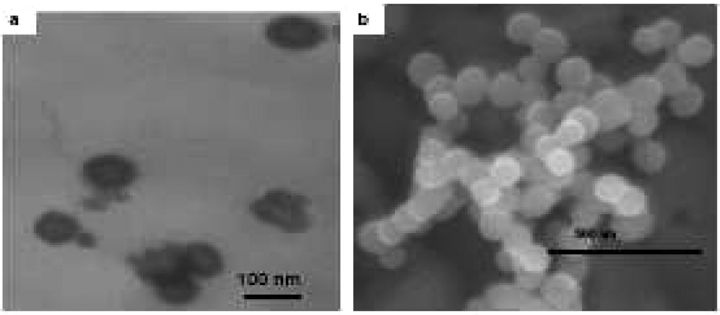

Figure 10. (a) TEM and (b) SEM of hollow platinum nanospheres. Scale bars: (a) 100 nm; and (b) 500 nm.

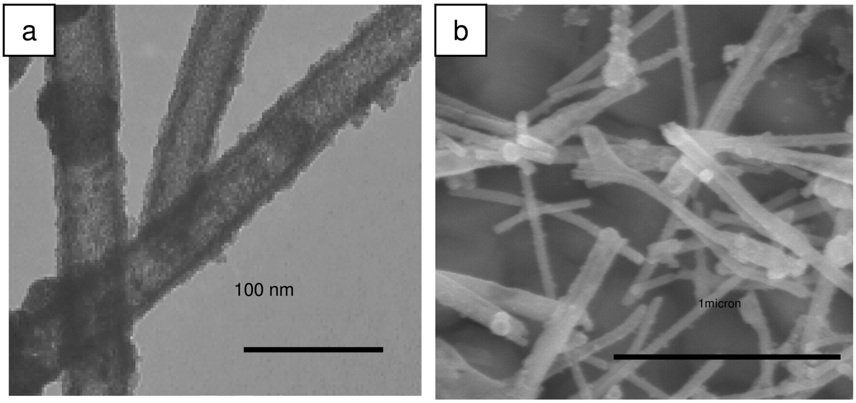

Figure 11. (a) TEM, (b) SEM images of hollow Pt nanowires. Scale bars: (a) 100 nm; and (b) 1000 nm.

Table 4. Ag and Pt nanoparticles dimension in nm

Ag nanosphere	*Pt hollow nanosphere*		*Ag nanowire*	*Pt hollow nanotube*	
Diameter (nm)	Diameter (nm)	Wall thickness (nm)	Diameter (nm)	Diameter (nm)	Wall thick-ness (nm)
59±2	88±2	29±1	30 ± 2	50±2	11±1

The average diameter and wall thickness of Pt hollow spheres and nanowires can be controlled from 9 to 20 nm (wall thickness) and 36 to 74 nm (diameter) by varying the Pt:Ag molar ratios (*53*). The initial morphology of the Ag nanowires was preserved and the size of the hollow core was determined by the dimensions of the Ag nanowires, ~30 nm. The hollow core remained practically unchanged compared to the original Ag nanowire diameter, while the wall dimensions depended on the Pt ion concentration. The monometallic hollow nanoparticles produced by this synthesis route are stable and can be isolated without core aggregation or decomposition. The final morphology and the quantity of material collected are highly dependent on the reaction temperature and the amount and the type of Pt salt used in the galvanic process.

UV-vis spectrophotometry was used to monitor the rate of galvanic displacement reaction. As reaction proceeds, the plasmon band at ~400 nm for Ag nanoparticles completely disappeared indicating that Ag is exchanged after 10-15 minutes (data not shown). After ammonia treatment of the Ag–Pt bimetallic particles, the removal of Ag was complete and confirmed by EDX measurement (data not shown).

Figure 12 shows a representative HRTEMs and associated diffraction patterns for a Pt hollow nanosphere wall (Figure 12a) and the surface of a Pt hollow nanotube (Figure 12b).These data indicate well defined, parallel, “perfect and infinite”, equally spaced and continuous fringes which are parallel to the direction of elongation of the nanotube. The close match in crystal structure and lattice constants (<5%) between Ag and Pt is believed to induce a conformal growth routine, with similar nucleation and growth pattern of Pt at the Ag surface. Analysis of HRTEM images of hollow Pt nanoparticles gave an inter-fringe distance of 0.23 nm for hollow nanospheres and 0.228 nm for hollow nanotubes. The data is in good agreement with the lattice spacing of the (111) plane in the face centered cubic fcc Pt crystal (*65*).

3.2.1.2. Bicompositional Nanostructures

The importance of the relative surface alloying or layering arrangements of metals on single-crystal substrates has been recognized, including the “near surface alloy” model of metal adlayer on metal substrate for the oxygen reduction reaction (*66*).

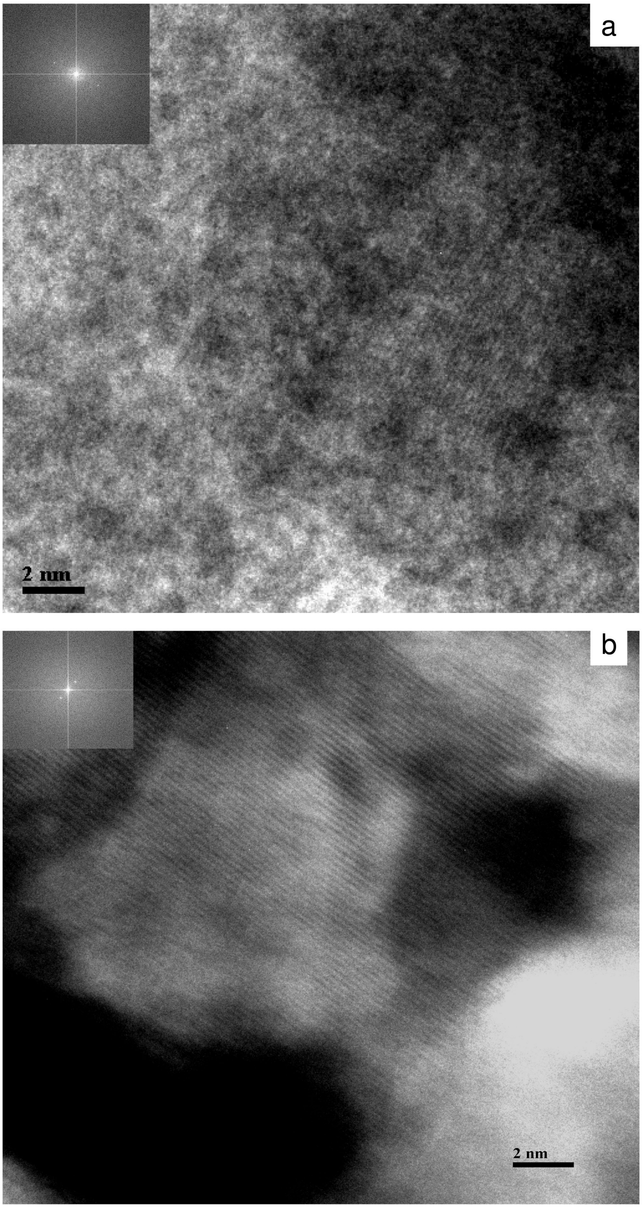

Figure 12. HRTEM of (a) Pt hollow nanospheres wall and (b) Pt hollow nanowire surface. Inset shows electron diffraction pattern. Scale bar: 2nm-a, b.

Bimetallic nanoparticles are of long-standing interest because they can exhibit catalytic (*67*), electronic (*68*), and optical properties (*69*) distinct from either of their constituent monometallic nanoparticles. For instance, a combination of Au and Pt might enable new developments in areas such as optical response modulation (*70*) or even the combination of optical and catalytic properties within a single nanostructure (*71*).

We produced bimetallic core-shell-like Au-Pt nanomaterials, rods and cubes, in a heterogenous epitaxial fashion by a wet chemical approach (*72*). Gold nanorods and cubes were used as “seeds” for Pt growth in the presence of the mild reducing agent ascorbic acid and a cationic surfactant cethyltrimethylammonium bromide (CTAB).

Initially, Au nanorods of different aspect ratios were produced by a seed-mediated growth method developed by the Murphy group (Figure 13) (*27*, *35*, *36*, *73*). These reactions take place in air, and water, at room temperature, and, in principle, and are amenable to scaling up. Basically, metal salts are reduced in water, and in air, at room temperature, with a strong reducing agent (sodium borohydride) to yield 3.5-4 nm spherical "seed" particles. Sodium citrate or CTAB has been used as capping regents to avoid aggregation. Next, growth solutions containing more metal salt, “seed solution”, a structure-directing agent, and a weak reducing agent (ascorbic acid), will produce larger nanoparticles (*35*, *36*). Small changes in reaction conditions such as seed to metal ratio, absence of Ag ions, etc. can be used to control the final morphology and size of the Au nanoparticles. In this study, we produced cubic Au nanoparticles with a side length of 63±2 nm (*73*, *74*). The HRTEM image (Figure 13b) and electron diffraction pattern (Figure 13c) indicate well defined, equally spaced and continuous fringes which are oblique to the direction of elongation of the nanorod. These data suggest that the Au nanorods are single crystalline with no observable stacking faults, twins or volume dislocations. They display facets on side of the rods with {110} and {100} planes, {111} ends, and with a growth direction on the [100] axis (*75*).

Platinum nano-islands were subsequently grown on Au nanorod core in a heterogeneous epitaxial fashion at 40°C in the absence of Ag ions (*72*). TEM images (Figure 14b,c) show the formation of distinct Pt protuberances and islands of ~ 5 nm on the Au nanorods (24±1nm diameter and 73±1nm in length) seed surfaces in a core-shell-like arrangement. The coating is uniform along the whole surface with no significant differences between ends or side of the rods, as shown by the mapping analysis (Figure 14d - f) and confirmed by others (*72*).

Gold and Pt have a lattice mismatch of 4.08% which implies that a non-conformal growth route is favorable (*56*). The high strain energy between the two lattice domains suggests that nanostructures with morphologies that differ from the initial core nanostructures would be produced. However, electron microscopy images (Figure 14 and Figure 15) show that the Au core nanorods shape was preserved after Pt island deposition. HRTEM images and the corresponding electron diffraction pattern of individual Au-Pt nanorods (Figure 15) show their single crystalline structure with a highly ordered continuous, parallel and uniform fringe pattern with interplanar distance of 0.199 nm which suggests a family of planes for Pt of {002}, for a fcc structure (*76*). There are no twinning or defects present on these structures. These results demonstrate that even with a small mismatch (<5%) between lattices domains, conformal growth is possible (*56*, *77*). Recently, Xie suggested that, in addition to a minimal lattice mismatch (<5 %), the metal bond energies of the two components involved in the growth process are vital for conformal growth (*78*). Additionally, it was reported that atomic radius, bond dissociation energy, and electronegativity of the core and shell metals might also be crucial in the conformal and reconstruction routine of these nanostructures (*79*).

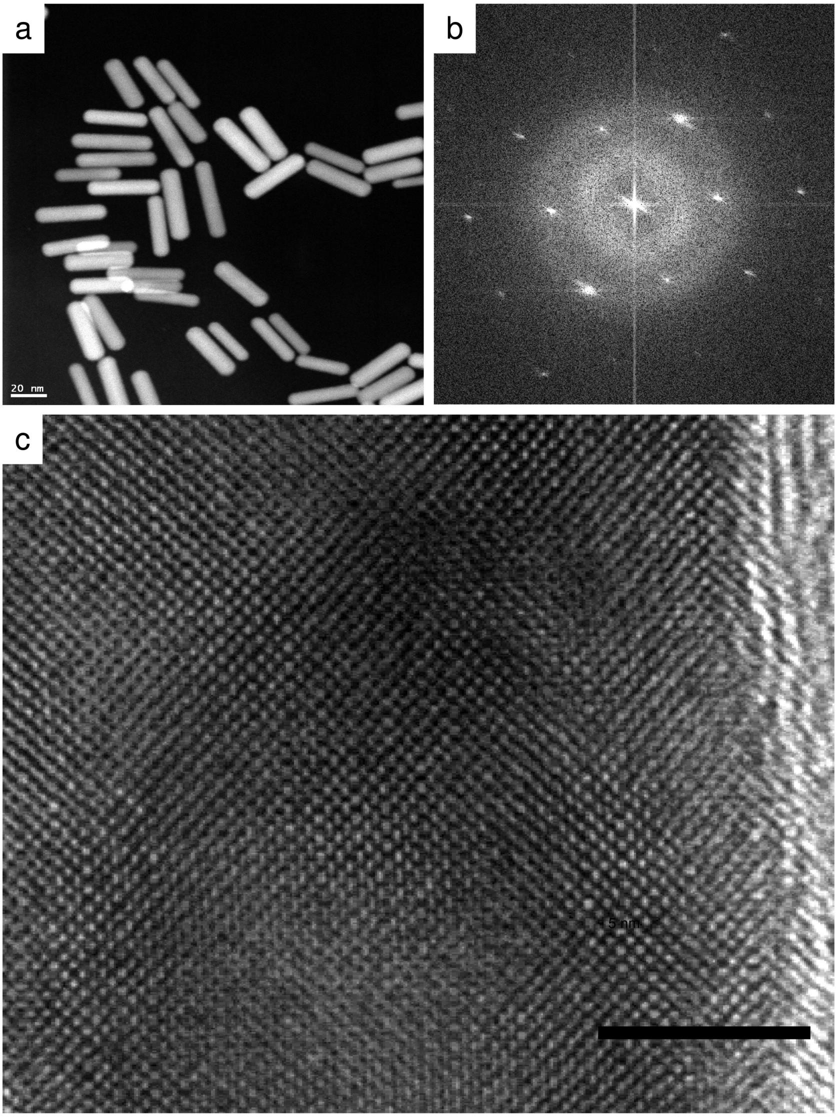

Figure 13. Images of Au nanorods prepared in the presence of Ag ions. (a) SEM, (b) electron diffraction and (c HRTEM). Scale bars: (a) 20 nm; and (c) 5 nm.

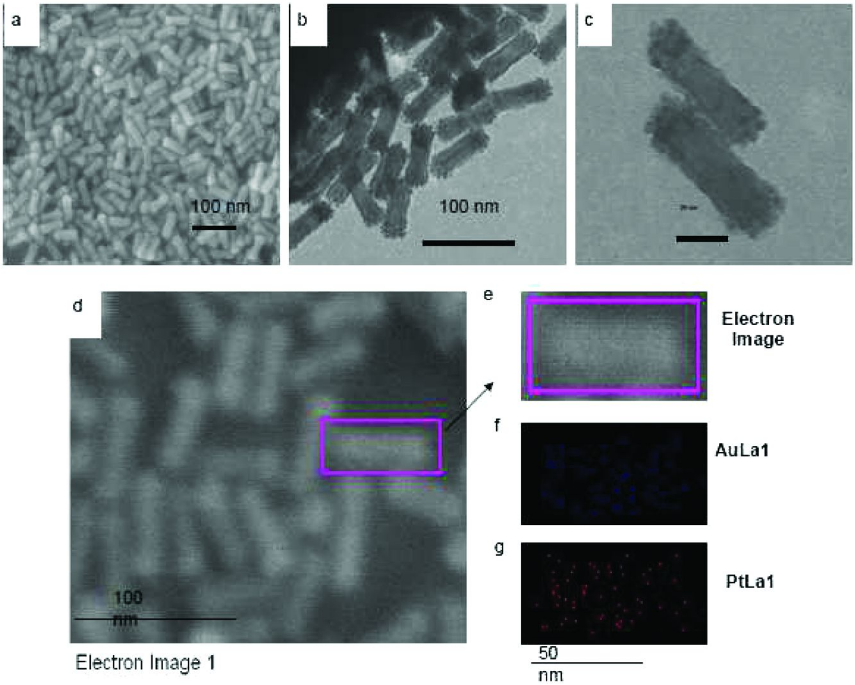

Figure 14. Micrograph of Au-Pt bimetallic nanorods (a) SEM image, (b,c) TEM image, (d) SEM image, (e) SEM image of Individual Au-Pt nanorod and elemental map of Au-Pt bimetallic nanorods (f) AuLa1 (g) PtLa1. Scale bars: 100 nm -a, b,d-g and 20 nm-c.

Figure 16a shows the UV-vis spectra for the Au nanorods. The plasmon band of the nanorods is split in two: the longitudinal plasmon band, corresponding to light absorption and scattering along the long axis of the particle, and the transverse plasmon band, corresponding to light absorption and scattering along the short axis of the particle. Deposition of Pt is nano-island can be also monitored spectroscopically. The overgrowth of a Pt deposit on the Au nanorods induces a red shift of the longitudinal band from ~721nm to ~765nm (Figure 16b). A significant decrease in intensity and a broadening of the peak was recorded after Pt island deposition on the Au nanorod core.

In parallel, Au-Pt nanocubes were prepared by a similar approach and display uniform atomic arrangements with {100} crystallographic facets (Figure 17) (*74*). However, in this case, it appears that Pt island depositions were selectively overgrown on {100} facets (*74*) giving a more “rounded” morphology of the material. This shows that addition of Pt ions produces Au-Pt nanostructures with geometries that are similar with nanospheres, the most energetically stable shape.

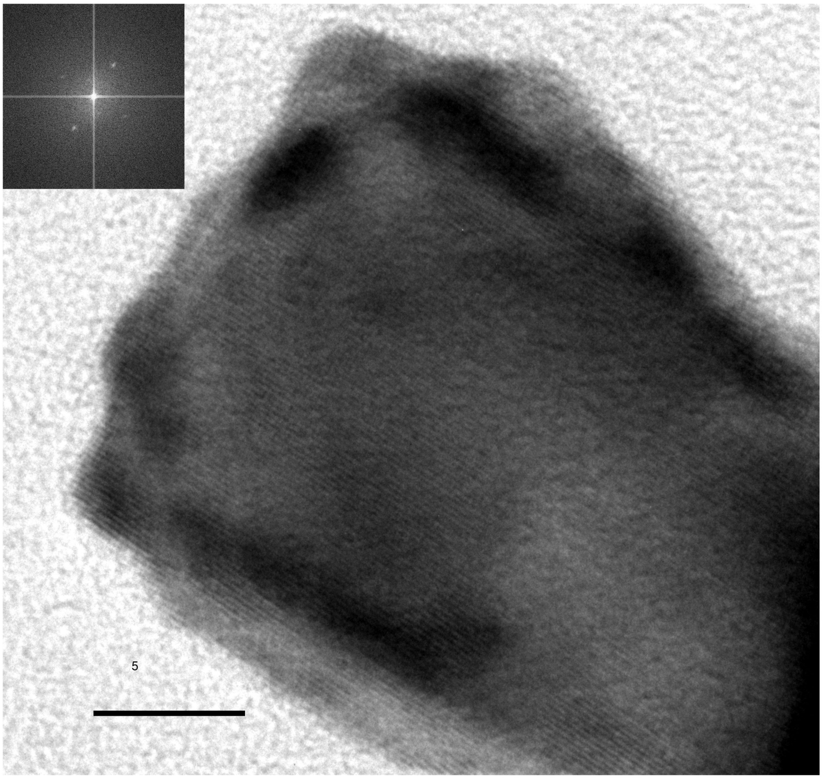

Figure 15. HRTEM and electron diffraction pattern for Au-Pt nanorods. Scale bar: 5nm.

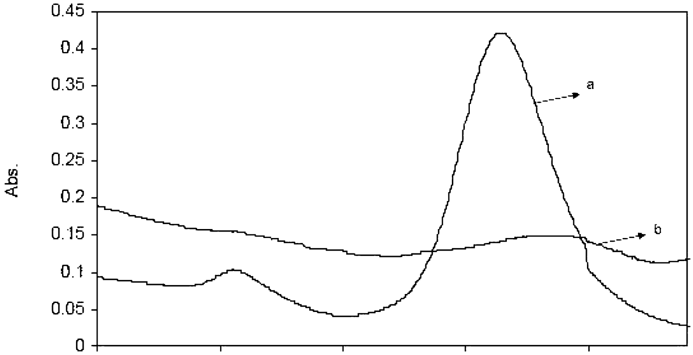

Figure 16. Uv-vis spectra of Au nanorods (a) before and (b) after coating with Pt.

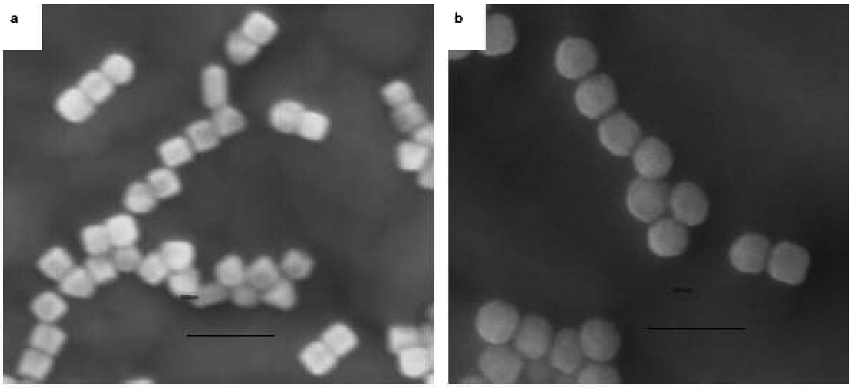

Figure 17. SEM images of (a) Au cubes, (b) Au-Pt cubes. Scale bars: 100 nm a, b.

3.3. Supported Nanomaterials and Their Surface

Over 80% of all commercial chemical production involves the use of catalysts and the vast majority of these catalysts employ a support. Because interactions between the catalyst and support affect durability and reactivity, this topic has received much recent attention. In general, catalysts that are more thermally stable will maintain higher activities and have longer lifetimes. Furthermore, because many catalysts are regenerated at elevated temperatures above process conditions, the development of catalyst-support systems that can undergo regeneration without degradation at high temperature is needed. We report here on the synthesis, characterization and testing of silica and titanate supports decorated with Ag and Au nanoparticles.

In the last decade, numerous catalytic reactions were conducted using noble metals nanoparticles, such as FCs, electron-transfer reactions, oxidations, hydrogenations, reduction, etc. (*80*) Many of these catalytic reactions require elevated temperatures that can hamper the efficient use of nanomaterials. Some of the side effects of these elevated temperatures lead to agglomeration, sintering of the active catalysts, and/or unwanted side reactions. In order to overcome these problems, the nanomaterials could be either (a) encapsulated in “inactive” supports to create core-shell architectures (Figure 19a) or (b) immobilized on inactive/active support (Figure 19c). Ceramic oxide coatings can enhance catalyst reactivity, thus serving both as a chemical as well as a structural role in novel, regenerable catalysts.

The support and the encapsulating materials can be either a semiconductor or insulator material (*81*). The most common supports are: carbon, silica (SiO_2), alumina, titania (TiO_2), grafting onto polymeric support, etc. (*82*). The prerequisites of these encapsulating materials are that the pore channels of the coating must be large enough to allow effective transfer of the reacting molecules, while small enough to prevent the cores from sintering at high temperatures.

One approach to avoid sintering processes and unwanted chemical reactions is *encapsulation* in “inactive” porous materials. Silica is an excellent host material due to the fact that it is a highly porous, easily to functionalize, nontoxic and biocompatible material (*83*). The most popular approach used to synthesized silica nanoparticles is sol-gel process that requires hydrolysis and condensation of a silica precursor (*84*).

Gold nanorods and Ag nanoparticles (e.g. spheres and nanowires) (*85*) were encapsulated with a silica shell through an indirect coating method that involved the use of a bifunctional linker, 3-mercaptopropyl trimethoxysilane ($HS(CH_2)_3Si(OCH_3)_3$, MPTMS), which binds to the Ag or Au (*86*) surface via the thiol group (*85*, *86*). A thin SiO_2 layer is subsequently grown on the MPTMS layer through a modified Stöber method (*84*). Transmission electron microscopy images (Figure 18a,c,d) show that the silica coating is uniform over the entire surface of each nanorod (up to a point), including both ends. The lengths of these silica nanotubes are determined by the original template Au nanorods or Ag nanowires and can be as long as 100 nm and 20 um, for Au and Ag nanoparticles, respectively. The thickness of the silica shell can be controlled from approximately 5 nm to 150 nm by adjusting the growth conditions (*85*).

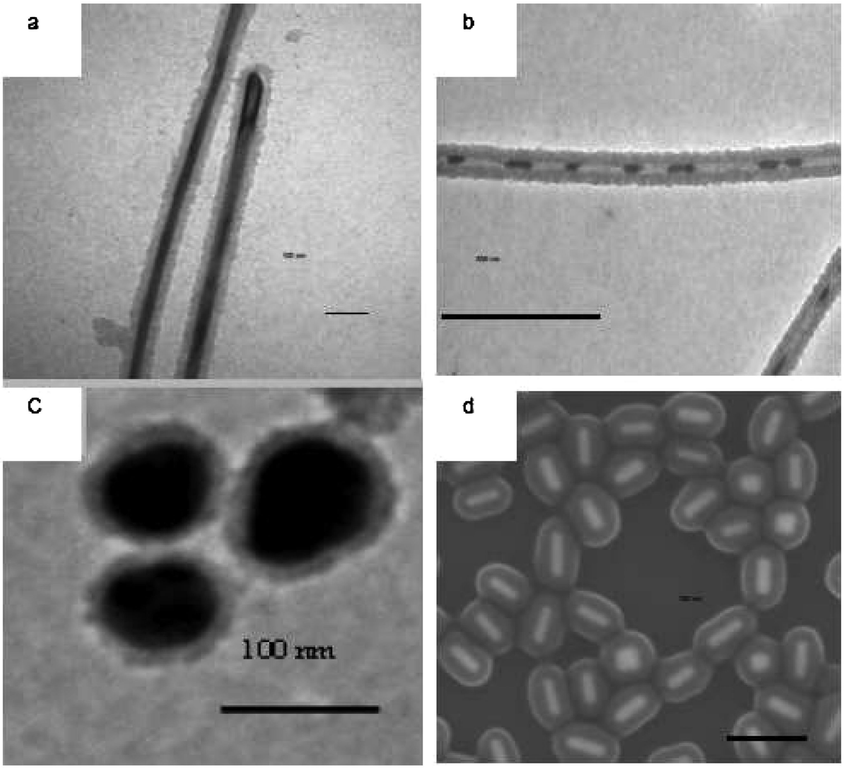

Figure 18. TEM images of core-shell (a) Ag nanowires-silica, (b) Ag-silica nano-peapods, (c) Ag nanospheres-silica, (d) SEM image of Au rods-silica core shell. Scale bar: 500 nm- a, b, and 100 nm- c,d.

Moreover, silica-coated Ag nanowires can be chemically treated to produce a "peapod" architecture in which Ag peas are embedded in silica pods (Figure 18b) (*85*). The Ag "pea" dimension and interparticle spacings are controllable down to ~50 nm. For example, Maier (*87*) reported that electromagnetic energy can be guided coherently down chains of closely spaced metal nanoparticles due to near-field coupling of their plasmons. These structures resemble in principle the architectures of spaced metal nanoparticles that have the potential application in chemical sensing, plasmonics, and catalysis.

Analogous experiments to functionalize Au nanorods with a titania (TiO_2) shell were conducted in our laboratory. Titania as a semiconductor has been regarded as one of the most promising photocatalysts in practical applications, especially water treatment and removal of volatile organic compounds (VOCs) in air (*88*). Moreover, the high catalytic activity of Au clusters on titania oxide has been reported by the Goodman group and was attributed to structural effects (including particle thickness and shape and metal oxidation state), as well as to support effects (*89*).

Additionally, TiO_2 is known as one of the most promising nanomaterial-based photocatalysts and is expected to play a crucial role in solving the energy demand by effective utilization of solar energy based on photovoltaic and water-splitting devices. Titania is extremely attractive due to its low cost, chemical inertness and photostability. The direct band gap for TiO_2 was experimentally determined to be 3.06 and 3.20 eV for the rutile (*90*) and anatase (*91*) forms respectively, and is, therefore, appropriately positioned and sufficiently larger than the 1.23 V required to photocatalytically split water. Fujishima and Honda published the first report using TiO_2 to photocatalytically split water into hydrogen and oxygen (*92*). However, a major drawback to using a wide band gap semiconductor such as TiO_2 for solar applications is the relatively high energy photons required to excite electrons from the valence to conduction band. Consequently unmodified TiO_2 particles can only absorb UV radiation which accounts for only a small fraction of the solar spectrum.

While there is a large amount of literature on TiO_2 and TiO_2-coupled with metallic nanoparticles, most of the research is focused on spherical metallic nanoparticles. Recently, we produced Au nanorods rods with silica/TiO_2 core-shell design, TiO_2 nanospheres, and TiO_2-Au nanorods assemblies, as depicted in Figure 19.

One-dimensional (1-D) metal nanostructures, in which the short axis of the material is in the ~1-100-nm regime but the long axis is up to microns long are especially of interest from fundamental and practical applications (*35*, *36*, *52*, *62*, *63*, *93*). Anisotropic metal nanoparticles can absorb and scatter light along multiple axes; therefore, metal nanorods and nanowires have both longitudinal (along the long axis) and transverse (along the short axis) plasmon bands (*35*, *36*). In the case of Au and Ag nanoparticles, surface plasmons bands are in the visible region of the spectrum and are sensitive to the particles size, shape, environment and dielectric constant (*35*, *36*, *94*).

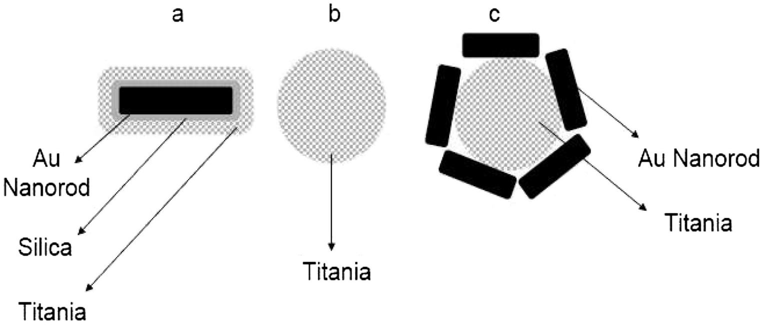

Figure 19. Schematic depiction (a) core-shell Au rod-silica/titania, (b) titania spheres, (c) titania-gold nanorod assemblies.

The thiol-based reactivity of Au nanorods allowed us to attach Au nanorods to spherical TiO_2 nanoparticles and to create core-shell nanostructures. Gold nanorods with a 24±1 nm diameter and 72±2 nm length were encapsulated with a silica shell as described above, followed by the controlled growth of TiO_2 on the silica surface through a sol-gel approach. Bulk TiO_2 is thermally unstable and readily loses its surface area due to sintering at high temperature. In contrast, titania/silica materials have higher thermal stability, surface acidity, and mechanical properties than bulk TiO_2. In addition, the thermal expansion of these oxides does not change to a significant extent over a wide temperature range (*95*).

Growth of the silica/TiO_2 shell was monitored by transmission electron microscopy (TEM) and UV-vis spectroscopy (Figure 20). The silica shell was an average 17±1 nm and was uniform along the entire surface of the Au nanorods surface. After TiO_2 deposition, the shell dimensions increased on average 5±1 nm Energy dispersive X-ray analysis confirmed the presence of titania (Figure 20). Copper peaks in this spectrum are the result of copper grid used to dropcast the sample for TEM analysis. UV-vis spectra was used to monitor conformational changes during the growth process and spectra of the Au-SiO_2-TiO_2 architectures shows a red shifting of the longitudinal plasmon bands from ~690 nm to ~720 due to the dielectric constant of the SiO_2-TiO_2 shell.

In addition to exploring the synthesis routes to prepare core-shell architectures, we investigate attachment of metallic nanoparticles on TiO_2 nanosperes with the structure shown in Figure 19c. In this synthesis, the thiol functionalized Au nanorods were used as template simply by incubating the template particles with titanium(IV) isopropoxide for several hours at room temperature. Figure 21b shows SEM image of these nanocomposite materials. While this procedure is not optimized, and some agglomeration/stacking of Au nanorods are produced, it is believed that changes in reactants concentration and reaction conditions can lead to a more uniform architecture.

Lastly, TiO_2 nanospheres with ~100nm diameter were prepared by a sol-gel procedure and in ethylene glycol at room temperature (Figure 21a) and were used as a baseline catalyst in the dye photodegradation studies described below.

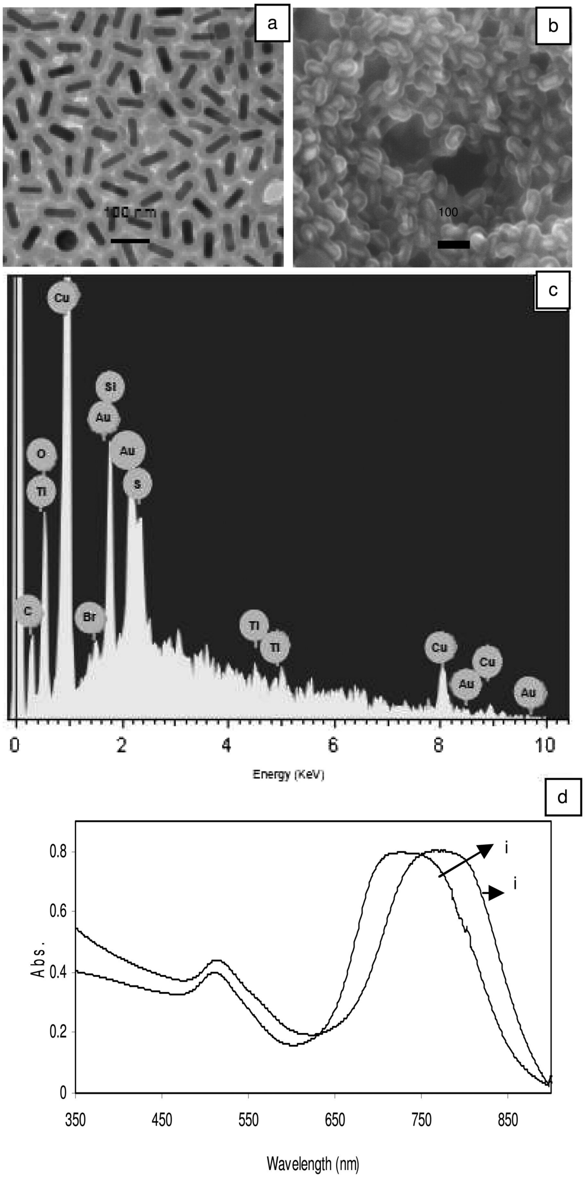

Figure 20. (a) TEM image of Au-silica control (b) SEM image of Au-silica-titania, (c) EDX of Au-silica-titania, (d) UV-vis spectra of (i) Au nanorods and (ii) Au-silica/titania nanorods. Scale bar: 100 nm- a,b.

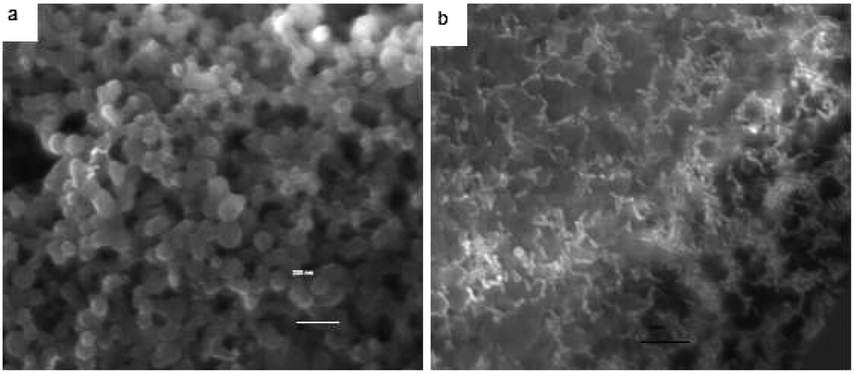

Figure 21. SEM images of (a) titania nanospheres, (b) titania-Au nanorods film. Scale bar: 200 nm-a, 100 nm-b.

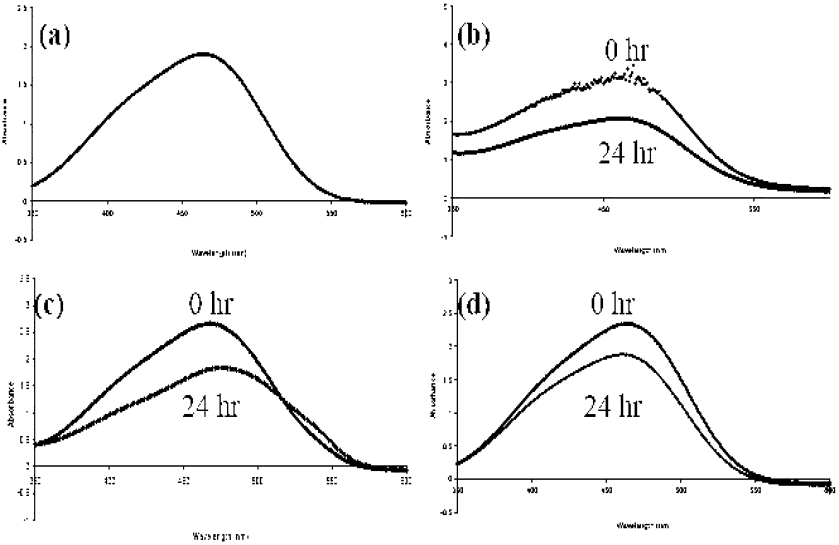

Figure 22. UV-vis spectra of (a) methyl orange and (b) TiO_2, (c) Au- TiO_2 and (d) Au-SiO_2-TiO_2 nanoparticles in solutions of methyl orange before and after 24 hr of Hg lamp irradiation.

As a simple measure of the catalytic activity of Au-SiO_2-TiO_2 and Au-TiO_2 nanoparticles, the photocatalytic decomposition of methyl orange was tested and compared with bare TiO_2 nanoparticles. For this study an aqueous solutions of methyl orange was incubated in the dark for 16 hours with no observable change in the UV-vis spectra indicating that no absorption occurred. Suspensions of each of the three nanoparticles and a blank without particles were then exposed to a mercury lamp of 630 leux intensity. The suspensions were continually stirred and their UV-vis spectrum periodically monitored. The decomposition of methyl orange was very similar for both TiO_2 and Au-TiO_2 particles (33% and 32% reduction of the 470nm peak, respectively) (Figure 22) after 24 hours of lamp exposure. The decomposition of methyl orange in the presence of Au-SiO_2-TiO_2 particles was 20%. While a precise particle concentration is presently unknown, the TiO_2 particles without Au contained 3 orders of magnitude more of the TiO_2 synthetic precursor strongly suggesting the Au nanoparticles play an important role in the reduction of methyl orange.

Another way to avoid sintering processes is to immobilize the nanoparticles on other supports such as silica spheres, nanotubes, or other metals. The size of the support can be nano- or micro-scale. Silica spheres coated with metallic nanoparticles find applications in catalysis and advanced bioimaging techniques (*96*). In general, silica is decorated with Au nanocrystals via an organic linker, an amine or thiol-terminated coupling agent, grafted to the oxide surface that allows metal attachment.

We produced silica nanoparticles of different sizes and shapes and used them as support for further functionalization. The first class of silica support was produced by water-in-oil microemulsion and lead to uniform and monodispersed spherical silica nanospheres (*97*). As silica supports for nanoparticle decoration we used uniform nanospherical silica beads with a 100 nm diameter (Figure 23b), porous walled hollow glass microspheres (Figure 23c) produced by the method described by Wicks et al. (*98*) and uniform silica nanotubes (Figure 23a) synthesized by the approach reported by our group (*85*) by using Ag encapsulated in silica as sacrificial template and subsequent dissolution of Ag core of the silica encapsulated particles using an ammonia treatment.

These silica nanoparticles were incubated with the bifunctional linker MPTMS, for several minutes under slow stirring. The silane function binds to the silica support while the thiol function, with a high affinity toward noble metals, is free to bind the metallic nanostructures. The Au "seed" nanoparticles used in the synthesis were prepared in CTAB solutions by reduction of chloroauric acid with sodium borohydride and used further to grow Au nanorods by a seed mediated procedure. Subsequently, Au nanoparticles were incubated with 3-mercaptopropyl trimethoxysilane and functionalized silica nanostructures. Figure 23c-f shows the attachment of Au nanorods and Au nanospheres on the silica surface.

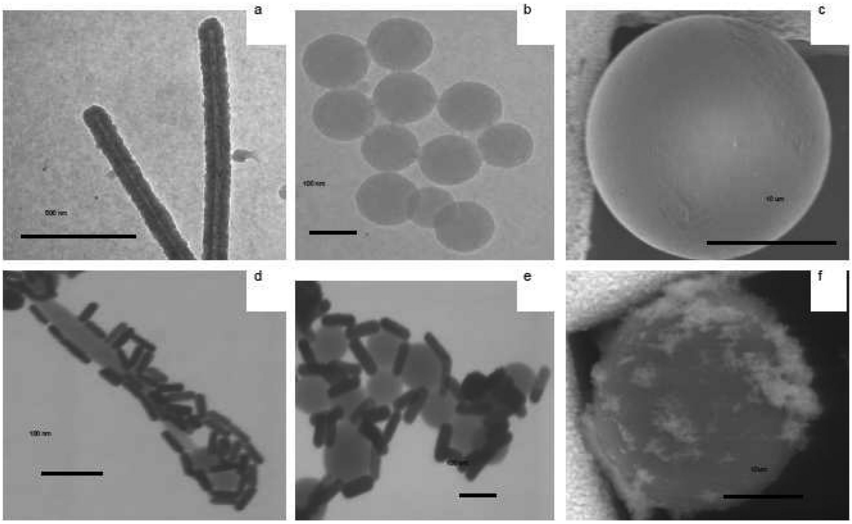

Figure 23. SEM images of metallic nanoparticles attached onto silica supports. (a) silica nanotubes, (b) silica nanospheres, (c) hollow glass microspheres, (d) Au nanorods attached on silica nanowires, (e) Au nanorods attached on the silica spheres and (f) Au nanospheres attached onto the porous glass microspheres. Scale bar: 100 nm-b, d, e, 500 nm-a, 10 um-c, f.

4. Future Challenges and Needs

We illustrate in this study several nanoscale materials that are ideally suited for enhancing the performance and cost of catalysts and electrodes for fuel and solar cell applications. Some materials might provide enhanced activity due to the quantum size effect while others due to particular morphologies and architecture. Incorporation of nanoscale materials with high surface area and high porosity in FCs can reduce the Pt loading in the electrode and the overall cost of the FC. Moreover, the water retention properties of the membranes and conductivity of the membrane could be improved by incorporating nanoscale materials.

Many chemically important reactions such as hydrogenation and the Fischer-Tropsch (FT) synthesis of fuels are relevant only at elevated temperatures. The use of unsupported nanoparticles in catalytic systems, however, is often hampered by temperature stability of the nanoparticles. For example, when elevated temperatures are used catalyst life is often limited due to active metal particle sintering and side reactions such as carbon deposition. To help overcome this limitation, a new class of nanomaterials has been developed where the active metal particle is located at the core of a stable porous ceramic oxide layer, such as silica and titania.

Routine usage of unsupported nanoparticles is also hampered by the limited fundamental understanding of the manner in which the anatomy of nanostructure-based architecture affects overall performance. A major issue has been the reproducible preparation of well defined, stable particles for routine applications in large quantities. The development of new generation of nanomaterials will depend upon on reliable synthetic routes to increasingly complex nanomaterials with highly ordered geometries. These advances in synthetic routes should dramatically improve dependability and repeatability as well as detection limits, selectivity, robustness, reversibility, freedom from interferences, and long term-stability. While we can not predict the magnitude of the application of nanomaterials in the energy arena, it is believed that nanotechnology will likely have a significant impact in the development of efficient materials for energy solutions. To expand the use of clean and renewable energy sources multifunctional catalysts are needed that are active under a variety of reaction conditions and that can be regenerated for continued use. This will create cost and environmental savings by allowing the process to be tailored to the desired product.

Acknowledgments

The research described herein was partially supported by the Savannah River National Laboratory- DOE-LDRD grant. The authors would like to thank Dr. David Hobbs for supplying titanium(IV) isopropoxide material.

References

1. Feldheim, D. L.; Foss, C. A., Jr. In *Metal Nanoparticles: Synthesis, Characterization and Applications*; Marcel Dekker: New York, 2002.
2. Zach, M.; Hagglund, C.; Chakarov, D.; Kasemo, B. *Curr. Opin. Solid State Mater Sci.* **2006**, *10*, 132–143.
3. Shao, Y.; Yin, G.; Wang, Z.; Gao, Y. Z. *J. Power Sources* **2007**, *167*, 235–242.
4. Peng, Z.; Yang, H. *Nano Today* **2009**, *4*, 143–164.
5. McNicol, B. D.; Rand, D. A. J.; Williams, K. R. *J. Power Sources* **1999**, *83*, 15–31.
6. Jiang, P. S.; Liu, Z.; Tang, H. L.; Pan, M. *Electrochim. Acta* **2006**, *51*, 5721.
7. (a) Steele, B. C. H.; Heinzel, A. *Nature* **2001**, *414*, 345. (b) Liu, Z.; Zhao, B.; Guo, C.; Sun, Y.; Xu; Yang, H.; Li, Z. *J. Phys. Chem. C* **2009**, *113*, 16766−16771.
8. (a) Crooks, R. M.; Zhao, M.; Sun, L.; Chechik, V.; Yeung, L. K. *Acc. Chem. Res.* **2001**, *34*, 181. (b) Roucoux, A.; Schulz, J.; Patin, H. *Chem. Rev.* **2002**, *102*, 3757−3769. (c) Williams, K. R.; Burstein, G. T. *Catal. Today* **1997**, *38*, 401−405. (d) Bell, A. T. *Science* **2003**, *299*, 1688−1691.
9. U.S. Department of Energy, *Hydrogen, Fuel Cells & Infrastructure Technologies Program Multi-Year Research, Development and Demonstration Plan*, 2007.
10. Narayanan, R.; Narayanan, R.; El-Sayed, M. A. *J. Phys. Chem. B* **2005**, *109*, 12663–12676.
11. (a) Somorjai, G. A.; Park, J. Y. *Angew. Chem., Int. Ed.* **2008**, *47*, 9212−9228. (b) Somorjai, G. A.; Park, J. Y. *Top. Catal.* **2008**, *49*, 126−135.

12. Burda, C.; Chen, X.; Narayanan, R.; El-Sayed, M. A. *Chem. Rev.* **2005**, *105*, 1025–1102.
13. Narayanan, R.; El-Sayed, M. A. *J. Phys. Chem. B* **2003**, *107*, 12416–12424.
14. Zhou, W. J.; Song, S. Q.; Li, W. Z.; Sun, G. Q.; Xin, Q.; Kontou, S.; Poulianitis, K.; Tsiakaras, P. *Solid State Ionics* **2004**, *175*, 797–803.
15. Baker, L. A.; Jin, P.; Martin, C. R. *Crit. Rev. Solid State Mater. Sci.* **2005**, *30*, 183–188.
16. Yamamoto, K.; Imaoka, T.; Chun, W. J.; Enoki, O.; Katoh, H.; Takenaga, M.; Sonoi, A. *Nat. Chem.* **2009**, *1*, 397–402.
17. Wang, A. L; Sun, Y.; Liang, Z.; Chen, S. *Acta Chim. Sin.* **2009**, *67*, 2554–2558.
18. Gasda, M. D.; Teki, R.; Lu, T. M.; Koratkar, N.; Eisman, G. A.; Gall, D. *J. Electrochem Soc.* **2009**, *156*, B614–B619.
19. Mayrhofer, K. J. J.; Blizanac, B. B.; Arenz, M.; Stamenkovic, V. R.; Ross, P. N.; Markovic, N. M. *J. Phys. Chem. B* **2005**, *109*, 14433–14440.
20. Hayden, B. E.; Pletcher, D.; Suchsland, J. P.; Williams, L. J. *Phys. Chem. Chem. Phys.* **2009**, *11*, 9141–9148.
21. Wang, J.; Swain, G. M. *J. Electrochem. Soc.* **2003**, *150*, E24–E32.
22. Bergamaski, K.; Pinheiro, A. L. N; Teixeira-Neto, E.; Nart, F. C. *J. Phys. Chem. B* **2006**, *110*, 19271–19279.
23. Maillard, F.; Martin, M.; Gloaguen, F.; Leger, J. M. *Electrochim. Acta* **2002**, *47*, 343–3440.
24. Ramírez-Menesesa, E.; Domínguez-Crespoa, M. A.; Montiel-Palmab, V.; Chávez-Herrera, V. H.; Gómezc, E.; Hernández-Tapia, G. *J. Alloys Comp.* **2009**, *483*, 573–577.
25. Joo, S. J.; Kwona, H. K.; You, D. Y.; Paka, C.; Changa, K.; Kimb, J. M. *Electrochim. Acta* **2009**, *54*, 5746–5753.
26. Ye, H.; Crooks, J. A.; Crooks, R. M. *Langmuir* **2007**, *23*, 11901–11906.
27. Hunyadi, S. E. Ph.D. Thesis, University of South Carolina, Columbia, SC, 2007.
28. Jana, N. R.; Gearheart, L.; Murphy, C. J. *Adv. Mater.* **2001**, *13*, 1389–1393.
29. (a) Jana, N.; Gearheart, L.; Murphy, C. J. *Langmuir* **2001**, *17*, 6782 – 6786. (b) Gole, A.; Murphy, C. J. *Chem. Mater.* **2004**, *16*, 3633−3640.
30. (a) Chen, J.; Herricks, T.; Geissler, M.; Xia, Y. *J. Am. Chem. Soc.* 2004, **126**, 10854−10856. (b) Chen, J.; Herricks, T.; Xia, Y. *Angew. Chem.* **2005**, *117*, 2645. (c) Chen, S.; Kimura, K. *J. Phys. Chem. B* **2001**, *105*, 5397−5402.
31. Xia, Y.; Xiong, Y.; Lim, B.; Skrabalak, S. E. *Angew. Chem., Int. Ed.* **2008**, *48*, 60–103.
32. Bigall, N. C.; Haertling, T.; Klose, M.; Simon, P.; Eng, L. M.; Eychmueller, A. *Nano Lett.* **2008**, *8*, 4588–4592.
33. (a) Soderberg, J. N.; Sirk, A. H. C, Campbell, S. A.; Birss, V. I. *J. Electrochem. Soc.* **2005**, *152*, A2017−A2022. (b) Gasteiger, H. A.; Markovic, N. M.; Ross, P. N., Jr. *J. Phys. Chem.* **1995**, *99*, 16757−16767.
34. Tang, Z.; Geng, D.; Lu, G. *J. Colloid Interface Sci.* **2005**, *287*, 159–166.
35. Murphy, C. J.; Sau, T. K.; Gole, A. M.; Orendorff, C. J.; Gao, J.; Gou, L.; Hunyadi, S. E.; Li, T. *J. Phys. Chem. B* **2005**, *109*, 13857–13870.

36. Murphy, C. J.; Gole, A. M.; Hunyadi, S. E.; Orendorff, C. J. *Inorg. Chem.* **2006**, *45*, 7544–7554.
37. Stamenkovic, V. R.; Fowler, B.; Mun, B. J.; Wang, G.; Ross, P. N.; Lucas, C. A.; Markovic, N. M. *Science* **2007**, *315*, 493–497.
38. Valden, M.; Lai, X.; Goodman, D. W. *Science* **1998**, *281*, 1640–1650.
39. Tian, N.; Zhou, Z. Y.; Sun, S. G.; Ding, Y.; Wang, Z. L. *Science* **2007**, *316*, 732–735.
40. Rhee, C. K.; Kim, C. J.; Ham, C.; Kim, Y.-J.; Song, K.; Kwon, K. *Langmuir* **2009**, *25*, 7140–7147.
41. Xia, B. Y.; Wang, J. N.; Wang, X. X. *J. Phys. Chem. C* **2009**, *113*, 18115–18120.
42. Komanicky, V.; Iddir, H.; Chang, K.-C.; Menzel, A.; Karapetrov, G.; Hennessy, D.; Zapol, P.; You, H. *J. Am. Chem. Soc.* **2009**, *131*, 5732–5733.
43. Subhramannia, M.; Ramaiyan, K.; Pillia, V. K. *Langmuir* **2008**, *24*, 3576–3583.
44. Peng, Z.; Wu, J.; Yang, H. *Chem. Mater.* **2010**.
45. Narayanan, R.; El-Sayed, M. A. *Nano Lett.* **2004**, *4*, 1343–1348.
46. Tian, N.; Zhou, Z.-Y.; Sun, S.-G.; Ding, Y.; Wang, Z. L. *Science* **2007**, *316*, 732–735.
47. Ajayan, P. M.; Schadler, L. S.; Braun, P. V. *Nanocomposite Science and Technology*; Wiley-VCH Verlag GmbH & Co. KGaA: Weinheim, Germany, 2003.
48. Zhong, C. J.; Luo, J.; Fang, B.; Wanjala, B. N.; Njoki, P. N; Loukrakpam, R.; Yin, J. *Nanotechnology* **2010**, *21*, 1–20.
49. (a) Guo, S. J.; Fang, Y. X.; Dong, S. J.; Wang, E. K. *J. Phys. Chem. C* **2007**, *111*, 17104. (b) Liang, H.; Guo, Y.; Zhang, H.; Hu, J.; Wan, L.; Bai, C. *Chem. Commun.* **2004**, 1496. (c) Liang, H. P.; Zhang, H. M.; Hu, J. S. Guo, Y. G.; Wan, L. J.; Bai, C. L. *Angew. Chem.* **2004**, *116*, 1566. (d) Chen, G.; Xia, D.; Nie, Z.; Wang, Z.; Wang, L.; Zhang, L.; Zhang, J. *Chem. Mater.* **2007**, *19*, 1840−1845.
50. (a) Umegaki, T.; Yan, J. M.; Zhang, X. B.; Shioyama, H.; Kuriyama, N.; Xu, Q. *J. Power Sources* **2009**, *191*, 209–216. (b) Wang, Y.; Price, A. D.; Caruso F. *J. Mater. Chem.* **2009**, *19*, 6451–6464. (c) Shao, L.; Caruntu, D.; Chen, C. F.; O'Connor, C. J.; Zhou, W. L. *J. Appl. Phys.* **2005**, *97*, 10. (d) Melancon, M. P.; Lu, W.; Yang, Z.; Zhang, R.; Cheng, Z.; Elliot, A. M.; Stafford, J.; Olson, S.; Zhang, J. Z., Li, C. *Mol. Cancer Ther.* **2008**, *7*, 1730−1739.
51. Chen, H. M.; Liu, R. S.; Lo, M. Y.; Chang, S. C.; Tsai, L. D.; Peng, Y. M.; Lee, J. F. *J. Phys. Chem. C* **2008**, *112*, 7522–7526.
52. Hunyadi, S. E.; Murphy, C. J. *J. Mater. Chem.* **2006**, *16*, 3929–3935.
53. Hunyadi, S. E.; Murphy, C. J. *J. Cluster Sci.* **2009**, *20*, 319–330.
54. Liu, Z.; Zhao, B.; Guo, C.; Sun, Y.; Xu, F.; Yang, F.; Li, Z. *J. Phys. Chem. C* **2009**, *113*, 16766–16771.
55. Guo, S. J; Fang, Y. X.; Dong, Y.; Wang, E. K. *J. Phys. Chem. C* **2007**, *111*, 17104.
56. Xia, Y.; Xiong, Y.; Lim, B.; Skrabalak, S. E. *Angew. Chem., Int. Ed* **2009**, *48*, 60–103.
57. Bravo-Vasquez, J. P.; Fenniri, H. *J. Phys. Chem. C* **2009**, *113*, 12897–12900.

58. Park, J. I.; Cheon, J. *J. Am. Chem. Soc.* **2001**, *123*, 5743.
59. Chen, T.; Herricks, M.; Geissler, M.; Xia, Y. *J. Am. Chem. Soc.* **2004**, *126*, 10854–10855.
60. Lee, P. C.; Meisel, D. *J. Phys. Chem.* **1982**, *86*, 3391.
61. Caswell, K. K.; Bender, C. M.; Murphy, C. J. *Nano Lett.* **2003**, *3*, 667–669.
62. Hunyadi, S. E.; Murphy, C. J.; Leach, A.; Gall, K., manuscript in preparation.
63. Tao, C. G.; Cullen, W. G.; Williams, E. D.; Hunyadi, S. E.; Murphy, C. J. *Surf. Sci.* **2007**, *601*, 4939–4943.
64. (a) Sun, Y. G.; Mayers, B. T.; Xia, Y. N. *Nano Lett.* **2002**, *2*, 481−485. (b) Sun, Y. G.; Xia, Y. A. *Nano Lett.* **2003**, 3, 1569−1572.
65. Sun, Y.; Yin, Y.; Mayers, B. T.; Herricks, T.; Xia, Y. *Chem. Mater.* **2002**, *14*, 4736–4745.
66. Zhang, J.; Lima, F. H. B.; Shao, M. H.; Sasaki, K.; Wang, J. X.; Hanson, J.; Adzic, R. R. *J. Phys. Chem. B* **2005**, *109*, 22701–22704.
67. (a) Mizukoshi, Y.; Fujimoto, T.; Nagata, Y.; Oshima, R.; Maeda, Y. *J. Phys. Chem. B* **2000**, *104*, 6028−6035. (b) Schmid, G.; West, H.; Mehles, H.; Lehnert, A. *Inorg. Chem.* **1997**, *36*, 891−900.
68. Harikumar, K. R.; Ghosh, S.; Rao, C. N. R. *J. Phys. Chem. A* **1997**, *101*, 536–541.
69. (a) Michaelis, M.; Henglein, A.; Mulvaney, P. *J. Phys. Chem.* **1994**, *98*, 6212. (b) Mulvaney, P.; Giersig, M.; Henglein, A. *J. Phys. Chem.* **1993**, 97, 7061.
70. Henglein, A. *J. Phys. Chem. B* **2000**, *104*, 2201–2209.
71. (a) Cao, L. Y.; Tong, L. M.; Diao, P.; Zhu, T.; Liu, Z. F. *Chem. Mater.* **2004**, *16*, 3239. (b) Damle, C.; Biswat, K.; Sastry, M. *Langmuir* **2001**, *17*, 7156. (c) Zhang, J.; Lima, F. H. B.; Shao, M. H.; Sasaki, K.; Wang, J. X.; Hanson, J.; Adzic, R. R. *J. Phys. Chem. B* **2005**, *109*, 22701−22706.
72. (a) Grzelczak, M.; Pérez-Juste, J.; Rodríguez-González , B.; Liz-Marzán, L. M. *J. Mater. Chem.* **2006**, *16*, 3946 – 3951. (b) Grzelczak, M.; Pérez-Juste, J.; García de Abajo, F. J.; Liz-Marzán, L. M. *Phys. Chem. C* **2007**, *111*, 6183–6188.
73. Sau, T. K.; Murphy, C. J. *J. Am. Chem. Soc.* **2004**, *126*, 8648–8649.
74. Sisco, P. N.; Murphy, C. J. *J. Phys. Chem. A* **2009**, *113*, 3973–3978.
75. Liu, M.; Guyot-Sionnest, P. **2005**, *109*, 22192–22200.
76. Wang, Z. L.; Ahmad, T. S.; El-Sayed, M. A. *Surf. Sci.* **1997**, *380*, 302–310.
77. Fan, F. R.; Liu, D. Y.; Wu, Y. F.; Duan, S.; Xie, Z. X.; Jiang, Z. Y.; Tian, Z. Q. *J. Am. Chem. Soc.* **2008**, *130*, 6949.
78. Min, M.; Kim, C.; Yang, Y. I; Yib, J.; Lee, H. *Phys. Chem. Chem. Phys.* **2009**, *11*, 9759–9765.
79. Fan, F. R.; Liu, D. Y.; Wu, Y. F.; Duan, S.; Xie, Z. X.; Jiang, Z. Y.; Tian, Z. Q. *J. Am. Chem.Soc.* **2008**, *130*, 6949–6951.
80. (a) Liu, Z.; Ling, X. Y.; Su, X.; Lee, J. Y. *J. Phys. Chem. B* **2004**, *108*, 8234. (b) Bulushev, D. A.; Yuranov, I.; Suvorova, E. I.; Buffat, P. A.; Kiwi-Minsker, L. *J. Catal.* **2004**, *224*, 8. (c) Boudjahem, A. G.; Monteverdi, S.; Mercy, M.; Bettahar, M. M. *J. Catal.* **2004**, *221*, 325. (d) Balint, I.; Miyazaki, A.; Aika, K. *Phys. Chem. Chem. Phys.* **2004**, *6* , 2000.

81. (a) Yang, C.; Kalwei, M.; Schuth, F.; Chao, K. *Appl. Catal. A* **2003**, *254*, 289. (b) Konova, P.; Naydenov, A.; Venkov, C. V.; Mehandjiev, D.; Andreeva, D.; Tabakova, T. *J. Mol. Catal. A: Chem.* **2004**, *213*, 235.

82. (a) Lopez, N.; Janssens, T. V. W.; Clausen, B. S.; Xu, Y.; Mavrikakis, M.; Bligaard, T.; Norskov, J. K. *J. Catal.* **2004**, *223*, 232. (b) Lang, H.; May, R. A.; Iversen, B. L.; Chandler, B. D. *J. Am.Chem. Soc.* **2003**, *125*, 14832. (c) Balint, I.; Miyazaki, A.; Aika, K. *Phys. Chem. Chem. Phys.* **2004**, *6*, 2000. Guczi, L.; Beck, A.; Horvath, A.; Koppany, Z.; Stefler, G.; Frey, K.; Sajo, I.; Geszti, O.; Bazin, D.; Lynch, J. *J. Mol. Catal. A: Chem.* **2003**, *204−205*, 545−549.

83. (a) Hidenori, N.; Yasushi, M. *J. Am. Chem. Soc.* **1995**, *117*, 2651–2652. (b) Kovtyukhova, N. I.; Mallouk, T. E.; Mayer, T. S *Adv. Mater.* **2003**, *15*, 780−783.

84. (a) Brinker, C. J.; Scherer, G. W. In *Sol-Gel Science*; Academic Press, San Diego, CA, 1990. (b) Liz-Marzán, L. M., Giersig, M., Mulvaney, P. *Langmuir* **1996**, *12*, 4329−4335.

85. Hunyadi, S. E.; Murphy, C. J. *J. Phys. Chem. B* **2006**, *110*, 7226–7231.

86. Obare, S. O.; Jana, N. R.; Murphy, C. J. *Nano Lett.* **2001**, *1*, 601–603.

87. Maier, S. A.; Brongersma, M. L.; Kik, P. G.; Meltzer, S.; Requichia, A. A. G.; Atwater, H. *Adv. Mater.* **2001**, *13*, 1501–1505.

88. Wu, X. F.; Song, H. Y.; Yoon, J. M.; Yu, Y. T.; Chen, Y. F. *Langmuir* **2009**, *25*, 6438–6447.

89. Chen, M. S.; Goodman, D. W. *Science* **2004**, *306*, 252–255.

90. Pascual, J.; Camassel, J.; Mathieu, H. *Phys. Rev. B* **1978**, *18*, 5605–5614.

91. Sanjines, R.; Tang, H.; Berger, H.; Gozzo, F.; Margaritondo, G.; Levy, F. *J. Appl. Phys.* **1994**, *75*, 2945–2951.

92. Fujishima, A.; Honda, K. *Nature* **1972**, *37*, 238–241.

93. (a) Cao, G. *Nanostructures and Nanomaterials: Synthesis, Properties and Applications*; Imperial College Press: London, 2004. (b) Hu, J.; Odom, T. W.; Lieber, C. M. *Acc. Chem. Res.* **1999**, *32*, 435- 445. (c) Xia, Y.; Yang, P.; Sun, Y.; Wu, Y.; Mayers, B.; Gates, B.; Yin, Y.; Kim, F.; Yan, H. *Adv. Mater.* **2003**, *15*, 353−389.

94. Murphy, C. J.; Gole, A. M.; Hunyadi, S. E.; Stone, J. W.; Sisco, P. N.; Alkilany, A.; Kinard, B. E.; Hankins, P. *Chem. Commun.* **2008**, *4*, 554–557.

95. Mariscal, R.; Granados, M. L.; Fierro, J. L. G.; Sotelo, J. L.; Martos, C.; Grieken, R. V. *Langmuir* **2000**, *16*, 9460–9464.

96. White, T. J. *Langmuir* **2007**, *23*, 11421–11424.

97. Santra, S.; Zhang, P.; Wang, K.; Tapec, R.; Tan, W. *Anal. Chem.* **2001**, *73*, 4988–4993.

98. Li, S.; Nguyen, L.; Xiong, H.; Wang, M.; Hu, T. C. C.; She, J. X; Serkiz, S. M; Wicks, G. G.; Dynan, W. S. *Nanomed.: Nanotechnol., Biol., Med.* **2009**.

Downloaded by 89.163.35.42 on June 5, 2012 | http://pubs.acs.org
Publication Date (Web): April 27, 2011 | doi: 10.1021/bk-2011-1064.ix002

Subject Index

A

Acetophenone oxime, 34*f*
Ag. *See* Silver
$AgNO_3$ and nafion membrane, 110*f*, 111*f*
Ag_2S nanoparticles and nafion membrane, 109*f*
Alane solution, 118*f*, 119*f*
Al nanoparticles and nafion film, 117*f*, 118*f*, 119*f*, 120*f*, 121*f*
Amides and aminoalcohols association
  ^1H NMR, 31
  SWCNT, 31
2-Aminoethanol and SWCNT, 34*f*, 43*f*
Anisotropic nanomaterials, 138
  biocompositional nanostructures, 145
  hollow nanomaterials, 141
  nano-composite structures, 140
Au. *See* Gold

B

Biocompositional nanostructures, 145
B3LYP/6-311G model chemistry, 23*f*

C

C_{60}
  $TPPF_{20}$, 57
  $TPPF_{100}$, 60*f*, 61*f*
Carbon
  copper substrate, 17*f*
  and fluorinated graphene films
    SiO_2, 25*f*, 26*f*
    SOI, 18*f*, 19*f*, 25*f*, 26*f*
    XeF_2, 19*f*
  lattice, fluorine removal, 23*f*
  nanomaterials, fluorinated, 11
  and XeF_2, 17*f*
Catalysis and nanoparticles, 62
Catalysts
  fuel cells, 129
  Pt-based, 132*t*
CCl_4 and fullerene C_{60}, 61*f*
$CDCl_3$ NMR solvent, 39*f*
CdS nanoparticles and nafion membrane, 109*f*
CF. *See* Perfluorographane
CFL. *See* Compact fluorescent lamps
Chromophores, 58*f*
Citrate
  Pt nanospheres, 15*f*, 137*f*
  reduction, 133*f*, 137*f*
CO_2
  photoconversion and silver-coated TiO_2 nanoparticles, 115*f*
  photoreduction and TiO_2 loaded nafion membrane, 114*s*
Combination ligands and UCNP synthesis, 78*f*
Compact fluorescent lamps, 88
Copper
  fluorinated graphene film, 17*f*
  fluorine and XeF_2, 16*f*
  substrate, 16*f*, 17*f*
Core/shell
  Ag
    nanowires-silica, 152*f*
    and silica nano-peapods, 152*f*
  Au
    rod-silica/titania, 154*f*
    rods-silica, 152*f*
  DCNP, 82*f*
  $NaYF_4$:Yb,Er/NaYF4 nanophosphors, 81*f*
  structured NPs, 80
  titania spheres, 154*f*
  UCNP, 82*f*
Core UCNP, 81*f*, 82*f*
Coronene and fluorines, 21, 23*f*
C_xF. *See* Fluorinated graphene
Cyclohexene oxidation, 63*f*
  Fe(III)$TPPF_{20}$ NPs catalysis, 65*t*

D

DCNP. *See* Downconversion nanophosphors
5-Diethylamino-2-pentanone, 34
Direct methanol FC, 128
DMFC. *See* Direct methanol FC
DMPEM fuel cells, 129
Downconversion nanophosphors
  core and core/shell combining, 82*f*
  core/shell NPs and fluorescence spectroscopy, 80
  emission spectra and NPs, 83*f*
  $NaYF_4$:Eu, 82*f*

  and rare-earth ions, 92*f*

E

EDX. *See* Energy dispersive X-ray
Energy conversion
  sheet-photocatalysts, 112
  solar cells, 87
Energy dispersive X-ray, 117*f*, 155*f*
Energy production and nanoparticles, 127
Energy transfer upconversion, 94*f*
Energy-related nanomaterials and fluorinated templates, 103, 106
Environmentally benign lighting and nanofluorides, 87
ESA. *See* Excited state absorption
ETU. *See* Energy transfer upconversion
Excited state absorption, 94*f*

F

FC. *See* Fuel cells
Fe(III)$TPPF_{20}$ NPs catalysis, 65*t*
Fluorescence spectroscopy and core/shell NPs, 80
Fluorinated carbon nanomaterials, 11
Fluorinated film and Raman spectra, 25*f*
Fluorinated graphene films
  carbon, 19*f*
  copper substrate, 17*f*
  fluorine, 18*f*
  formation, 27
  silicon-on-insulator, 18*f*
  XeF_2, 18*f*
Fluorinated ionomer membranes, 105
Fluorinated porphyrins, 55
Fluorinated templates, 103
Fluorination
  carbon nanomaterials, 11
  graphene, 11
  perfluorographane, 21*f*
  SWCNT, 15*f*
  and XeF_2, 13
Fluorine, 20*f*
  and carbon lattice, 23*f*
  cis and *trans*, 21
  and copper substrate, 16*f*
  and coronene, 21, 23*f*
  and fluorinated graphene films, 18*f*
  relative stability, 21, 23*f*
  SiO_2, 24*f*, 26*f*
  SOI, 18*f*, 24*f*, 26*f*
  and SWCNT, 14*f*
  and XeF_2, 14*f*, 16*f*
Fuel cells, 128
  catalysts, 129
    anisotropic nanomaterials, 138
    scale effects, 131
    supported nanomaterials and their surface, 151
  DMPEM, 129
Fullerene C_{60}
  and CCl_4, 61*f*
  $TPPF_{20}$, 58*f*
  $TPPF_{100}$, 61*f*

G

Gold
  cubes, 151*f*
  nanoparticles, 138*f*
  nanorods, 155*f*
    and Ag ions, 148*f*
    Pt coating, 150*f*
    and silica nanowires, 158*f*
    and silica spheres, 158*f*
  nanospheres and porous glass microspheres, 158*f*
  and Pt
    bimetallic nanorods, 149*f*
    cubes, 151*f*
    nanoparticles, 138*f*
    nanorods, 150*f*
  rods-silica core shell, 152*f*
  silica
    nanorods, 155*f*
    TiO_2 nanoparticles, 156*f*
    titania nanorods, 155*f*
  TiO_2, 156*f*
Graphene, 21*f*
  transfer, 16*f*
  XeF_2 fluorination, 11, 15, 17*f*, 18*f*

H

Hexane, 121*f*
Hg lamp irradiation, 156*f*
High resolution TEM
  Ag nanowires, 142*f*
  Au-Pt nanorods, 150*f*
  Pt
    hollow nanospheres, 146*f*
    seed nanospheres, 135*f*
HiPco SWCNT, 39*f*
^{1}H NMR
  chemical shift

Downloaded by 89.163.35.42 on June 5, 2012 | http://pubs.acs.org
Publication Date (Web): April 27, 2011 | doi: 10.1021/bk-2011-1064.ix002

Downloaded by 89.163.35.42 on June 5, 2012 | http://pubs.acs.org
Publication Date (Web): April 27, 2011 | doi: 10.1021/bk-2011-1064.ix002

    - NMP, 37
    - organonitrogens, 36*t*, 38*t*
    - and SWCNT, 36*t*, 38*t*
  - 1-methyl-2-pyrrolidone, 39*f*
  - representative amides and aminoalcohols, 31
  - SWCNT, 31
- Hollow glass microspheres, 158*f*
- Hollow nanomaterials, 141
- Hollow platinum nanospheres, 144*f*, 146*f*
- Hollow Pt nanowires, 144*f*, 146*f*
- HRTEM. *See* High resolution TEM
- Hydrazine, 26*f*
- Hydrophobic metalloporphyrin nanoparticles, 63*f*

I

- Indium-tin-oxide and TPPF$_{100}$, 60*f*, 61*f*
- Interband Auger process, 91*f*
- ITO. *See* Indium-tin-oxide

J

- JCPDS database, 118*f*

L

- LA. *See* Lauric acid
- Lanthanide
  - doped crystals and up-conversion processes, 94
  - fluorides, nano-sized, 94
- Lauric acid
  - TOP, 75*f*, 76*f*
  - UCNP synthesis, 75*f*, 76*f*, 78*f*
- Ligand effects
  - and NaYF$_4$, 71
    - combination ligands, 77
    - single ligand and combination ligands, 73

M

- Mercury discharge lamp, 89*f*
- Metallic nanoparticles and silica supports, 158*f*
- Metalloporphyrin nanoparticles
  - hydrophobic, 63*f*
  - and water, 63*f*
- Methyl orange, 156*f*
- 1-Methyl-2-pyrrolidone, 39*f*
  - and ^{1}H NMR chemical shift, 37
    - carbonyl and nitrogen electron pairs, association, 42
    - carbonyl versus nitrogen complexation, 42
    - cyclic versus acyclic, 41
    - O to N proximity, effects, 44
    - steric effects and cyclization, 37
  - SWCNT, 34*f*

N

- Nafion, 104*s*
  - film and Al nanoparticles, 117*f*, 118*f*, 119*f*, 120*f*, 121*f*
  - membrane, 108*s*
    - AgNO$_3$, 110*f*, 111*f*
    - Ag$_2$S nanoparticles, 109*f*
    - CdS nanoparticles, 109*f*
    - PbS nanoparticles, 109*f*
    - silver nanoparticles, 110*f*, 111*f*
    - TiO$_2$ nanoparticles, 113*f*, 114*s*
- Nanofluorides
  - energy conversion, 87
  - environmentally benign lighting, 87
  - and solar cells, 87
  - surface modification, 95
- Nanomaterials
  - anisotropic and fuel cells catalysts, 138*f*
  - energy-related, 103
  - fluorinated templates, 103
  - hollow, 141
- Nanoparticles
  - application, 127
  - catalysis, 62
  - challenges and needs, 158
  - characterization, 127
  - controlled shape, 127
  - energetic, 114
  - energy production, 127
  - functionalization, 127
  - metalloporphyrin, 63*f*
  - porphyrin, 63*t*
  - synthesis, 127
- Nanophosphors, 71
  - core/shell structured
    - characterization, 80
    - synthesis, 80
  - downconversion emission spectra, 83*f*
  - sizes, 82*t*
  - upconversion emission spectra, 83*f*

Downloaded by 89.163.35.42 on June 5, 2012 | http://pubs.acs.org
Publication Date (Web): April 27, 2011 | doi: 10.1021/bk-2011-1064.ix002

Nano-sized lanthanide fluorides, 94
Nano-templating
  energy-related applications, 106
    energetic nanoparticles, 114
    sheet-photocatalysts for energy conversion, 112
NaYF$_4$
  based up and downconversion colloidal nanophosphors, 71
  and ligand effects, 71
  shell, 81*f*
  and UCNP core/shell NPs, 80
NaYF$_4$:Eu, 82*f*
NaYF$_4$:Yb,Er, 82*f*
Nitrogen
  SiO$_2$, 26*f*
  SOI, 26*f*
NMP. *See* 1-Methyl-2-pyrrolidone
NMR solvent CDCl$_3$, 39*f*
NMR spectra and SWCNT, 47
N,N-dimethylamides, 34
NP. *See* Nanophosphors

O

OA. *See* Oleic acid
Octadecene, 79*f*
ODE. *See* Octadecene
Oleic acid
  UCNP synthesis
    and TOP, 75*f*
    and TOP/OM, 79*f*
    and TOP/TOPO, 80*f*
Oleylamine, 79*f*
OM. *See* Oleylamine
Organonitrogens
  ^{1}H NMR chemical shift and SWCNT, 36*t*, 38*t*
  SWCNT, 34*f*, 35
Oxidation of cyclohexene, 63*f*

P

PA. *See* Photon avalanche
PbS nanoparticles and nafion membrane, 109*f*
PEM. *See* Proton exchange membrane
Perfluorinated ionomer membranes, 108*s*
Perfluorographane, 15
  fluorination, 21*f*
  formation, 27
Phosphors, 89*f*
Photocatalysts
  energy conversion, 112
  TiO$_2$ loaded nafion membrane, 114*s*
Photon avalanche, 94*f*
Photo-physical processes
  applications
    compact fluorescent lamps, 88
    quantum-cutting phosphors, 88
    solar cells, 88
    up-conversion and solar cells, 92
Photoreduction of CO$_2$ and TiO$_2$ loaded nafion films, 114*s*
Platinum
  coating and Au nanorods, 150*f*
  concentration nanospheres, 137*t*
  hollow nanospheres and HRTEM, 146*f*
  nanoparticles, 138*f*, 145*t*
  nanospheres, 133*f*
    and citrate, 133*f*, 137*f*
    seed-mediated synthetic routes, 134*f*, 137*f*
  nanowires, hollow, 144*f*
  seed nanospheres and HRTEM, 135*f*
Platinum-based catalysts
  shape controlled
  size controlled
Porphine macrocycle, 57*f*
Porphyrins, 58*f*
  catalysis, 55
  fluorinated, 55
  nanoparticles, 63*t*
Pr^{3+}. *See* Phosphors
Proton exchange membrane, 128
Pt. *See* Platinum

Q

Quantum-cutting phosphors
  CFL, 88
  solar cell, 88

R

Raman spectra
  fluorinated film, 25*f*
  SWCNT, 14*f*, 45, 47
Rare-earth ions and down-conversion, 92*f*
Relative stability of fluorines on coronene, 21, 23*f*
Representative amides and aminoalcohols
  ^{1}H NMR, 31
  SWCNT, 31

S

- SA. *See* Stearic acid
- Sacrificial template and Ag nanowires, 142*f*
- Seed-mediated synthetic routes and Pt nanospheres, 133*f*, 134*f*, 137*f*
- Shape controlled Pt-based catalysts, 139*t*
- Sheet-photocatalysts and energy conversion, 112
- Si. *See* Silicon
- Silica, 21*f*
  - carbon, 25*f*, 26*f*
  - fluorine, 24*f*, 26*f*
  - nanospheres, 158*f*
  - nanotubes, 158*f*
  - nanowires and Au nanorods, 158*f*
  - nitrogen, 26*f*
  - supports and metallic nanoparticles, 158*f*
- Silicon
  - crystalline, 20*f*, 21*f*
  - and fluorinated graphene films
    - SOI, 19*f*
    - XeF_2, 19*f*
- Silicon dioxide. *See* Silica
- Silicon-on-insulator, 18*f*
  - carbon, 25*f*, 26*f*
  - carbon and fluorinated graphene films, 19*f*
  - fluorine, 24*f*, 26*f*
  - nitrogen, 26*f*
  - silicon and fluorinated graphene films, 19*f*
- Silver
  - coated TiO_2 nanoparticles
    - CO_2 photoconversion, 115*f*
    - nafion membrane film, 113*f*
  - ions and Au nanorods, 148*f*
  - nanoparticles
    - dimensions, 145*t*
    - and nafion membrane, 110*f*, 111*f*
  - nanospheres, 142*f*, 152*f*
  - nanowires
    - sacrificial template, 142*f*
    - and silica, 152*f*
  - silica nano-peapods core shell, 152*f*
- Single Walled Carbon Nanotubes, 39*f*
  - and 2-aminoethanol, 43*f*
  - association, 31, 45
  - concentrated solution, formation, 35
  - dispersion, 46
  - evaporation, 47
  - fluorination, 13
  - and fluorine, 14*f*
  - formation, 35
  - ^{1}H NMR, 31, 36*t*, 38*t*
  - HiPco, 39*f*
  - 1-methyl-2-pyrrolidone, 34*f*
  - NMR spectra, 47
  - organonitrogens, 34*f*, 35, 36*t*, 38*t*
  - Raman spectra, 14*f*, 45, 47
  - representative amides and aminoalcohols, 31
  - SWeNT, 39*f*
  - wet paste, formation, 37
  - and XeF_2, 13, 14*f*
- SiO_2. *See* Silica
- SOI. *See* Silicon-on-insulator
- Solar cells
  - and nanofluorides, 87
  - photo-physical processes, 88
  - and up-conversion, 92
- Stearic acid
  - UCNP synthesis, 75*f*, 76*f*, 78*f*
    - and TOP, 75*f*, 76*f*
- SWCNT. *See* Single Walled Carbon Nanotubes
- SWeNT SWCNT, 39*f*

T

- Tethering, 40*f*
- 5,10,15,20-Tetrakis-(2,3,4,5,6-pentafluorophenyl)porphyrin, 56, 57*f*
  - and C_{60}, 57, 58*f*
- TiO_2. *See* Titania
- Titania, 156*f*
  - and Au nanorods film, 156*f*
  - CO_2 photoreduction, 114*s*
  - and gold nanorod assemblies, 154*f*
  - loaded nafion films, 114*s*
  - nanoparticles
    - CO_2 photoconversion, 115*f*
    - nafion membrane, 113*f*
    - silver-coated, 113*f*
  - nanospheres, 156*f*
  - spheres, 154*f*
- Toluene, 39*f*
- TOP. *See* Trioctylphosphine
- TOPO. *See* Trioctylphosphine oxide
- $TPPF_{20}$. *See* 5,10,15,20-Tetrakis-(2,3,4,5,6-pentafluorophenyl)porphyrin
- $TPPF_{100}$, 59
  - and C_{60}, 60*f*, 61*f*
  - crystal packing, 60*f*
  - fullerene C_{60}, 61*f*
  - ITO, 61*f*
  - structure, 60*f*
- Trioctylphosphine, 75*f*

Downloaded by 89.163.35.42 on June 5, 2012 | http://pubs.acs.org
Publication Date (Web): April 27, 2011 | doi: 10.1021/bk-2011-1064.ix002

Downloaded by 89.163.35.42 on June 5, 2012 | http://pubs.acs.org
Publication Date (Web): April 27, 2011 | doi: 10.1021/bk-2011-1064.ix002

Trioctylphosphine oxide, 79*f*

U

UCNP. *See* Upconversion nanophosphors
UPC. *See* Up-conversion
Up-conversion
  lanthanide-doped crystals
    energy transfer upconversion, 94*f*
    excited state absorption, 94*f*
    photon Avalanche, 94*f*
  and solar cells, 92
Upconversion nanophosphors
  characterization, 73
  coordination ligands, 75*f*
  core, 81*f*
    and core/shell combining, 82*f*
    shell NPs and fluorescence spectroscopy, 80
  emission spectra, 83*f*
  $NaYF_4$:Yb,Er, 82*f*
  synthesis, 72, 75*f*
    combination ligands, 78*f*
    LA, 75*f*, 76*f*, 78*f*
    LA-TOP, 75*f*, 76*f*
    $NaYF_4$ core/shell NPs, 80
    OA-TOP, 75*f*
    OA/TOP/OM, 79*f*
    OA/TOP/TOPO, 80*f*
    SA, 75*f*, 76*f*, 78*f*
    SA-TOP, 75*f*, 76*f*
    TOPO/OM, 79*f*

W

Water and metalloporphyrin nanoparticles, 63*f*

X

XeF_2
  copper substrate, 17*f*
  fluorination
    graphene, 11, 15, 18*f*, 19*f*
    SWCNT, 13
  and fluorine, 14*f*, 16*f*
  silicon and fluorinated graphene films, 19*f*
  and SWCNT, 13, 14*f*
XPS. *See* X-ray photoelectron spectroscopy
X-ray photoelectron spectroscopy, 14*f*, 16*f*, 17*f*, 18*f*, 19*f*